CELL ADHESION AND MIGRATION IN THE DEVELOPMENT OF MULTICELLULAR ORGANISMS

EDITED BY: Takaaki Matsui, Mitsugu Fujita and Akihiko Ito
PUBLISHED IN: Frontiers in Cell and Developmental Biology

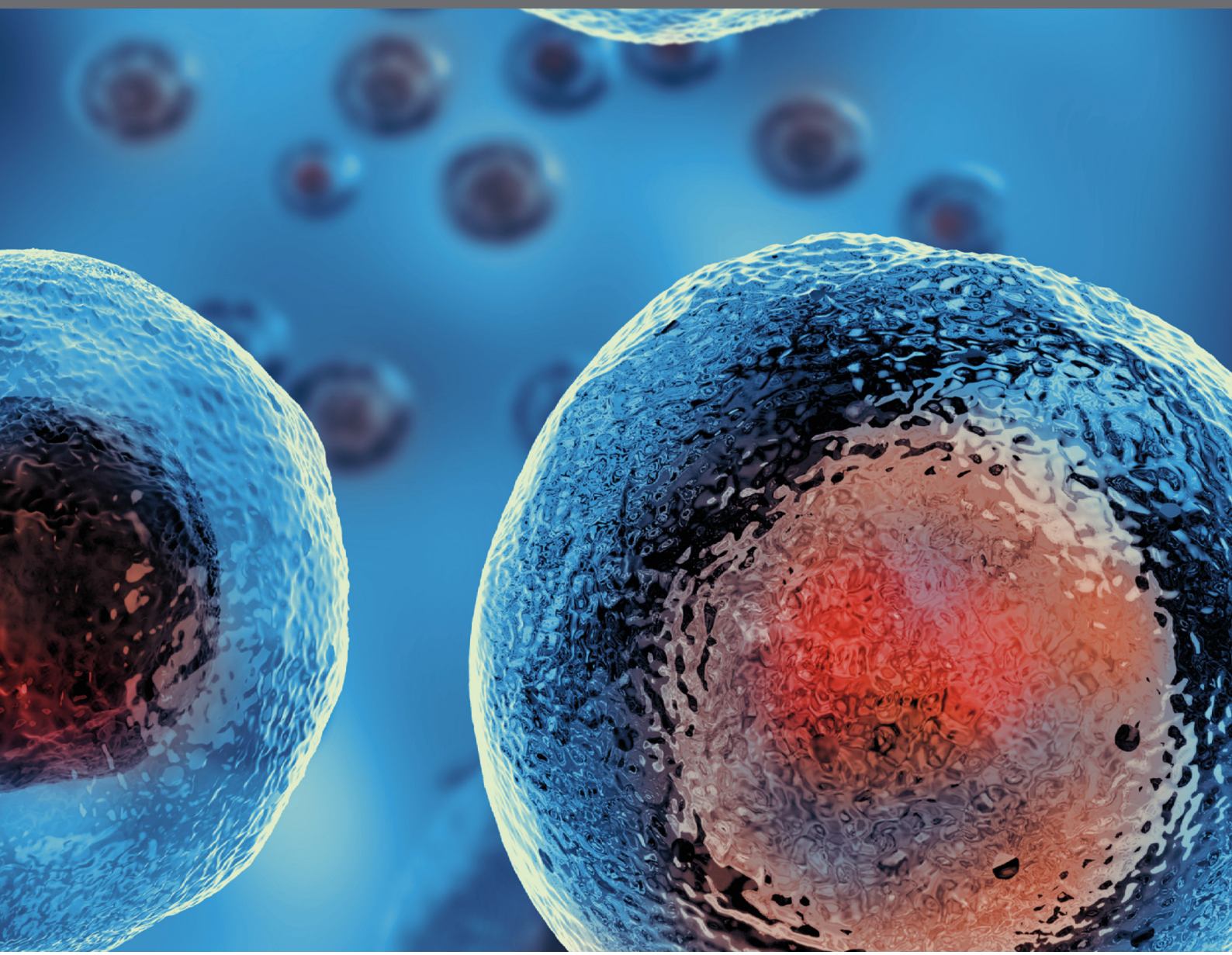

frontiers Research Topics

frontiers

ISSN 1664-8714
ISBN 978-2-88945-694-9
DOI 10.3389/978-2-88945-694-9

About Frontiers

Frontiers is more than just an open-access publisher of scholarly articles: it is a pioneering approach to the world of academia, radically improving the way scholarly research is managed. The grand vision of Frontiers is a world where all people have an equal opportunity to seek, share and generate knowledge. Frontiers provides immediate and permanent online open access to all its publications, but this alone is not enough to realize our grand goals.

Frontiers Journal Series

The Frontiers Journal Series is a multi-tier and interdisciplinary set of open-access, online journals, promising a paradigm shift from the current review, selection and dissemination processes in academic publishing. All Frontiers journals are driven by researchers for researchers; therefore, they constitute a service to the scholarly community. At the same time, the Frontiers Journal Series operates on a revolutionary invention, the tiered publishing system, initially addressing specific communities of scholars, and gradually climbing up to broader public understanding, thus serving the interests of the lay society, too.

Dedication to Quality

Each Frontiers article is a landmark of the highest quality, thanks to genuinely collaborative interactions between authors and review editors, who include some of the world's best academicians. Research must be certified by peers before entering a stream of knowledge that may eventually reach the public - and shape society; therefore, Frontiers only applies the most rigorous and unbiased reviews.
Frontiers revolutionizes research publishing by freely delivering the most outstanding research, evaluated with no bias from both the academic and social point of view. By applying the most advanced information technologies, Frontiers is catapulting scholarly publishing into a new generation.

What are Frontiers Research Topics?

Frontiers Research Topics are very popular trademarks of the Frontiers Journals Series: they are collections of at least ten articles, all centered on a particular subject. With their unique mix of varied contributions from Original Research to Review Articles, Frontiers Research Topics unify the most influential researchers, the latest key findings and historical advances in a hot research area! Find out more on how to host your own Frontiers Research Topic or contribute to one as an author by contacting the Frontiers Editorial Office: researchtopics@frontiersin.org

CELL ADHESION AND MIGRATION IN THE DEVELOPMENT OF MULTICELLULAR ORGANISMS

Topic Editors:
Takaaki Matsui, Nara Institute of Science and Technology, Japan
Mitsugu Fujita, Kindai University, Japan
Akihiko Ito, Kindai University, Japan

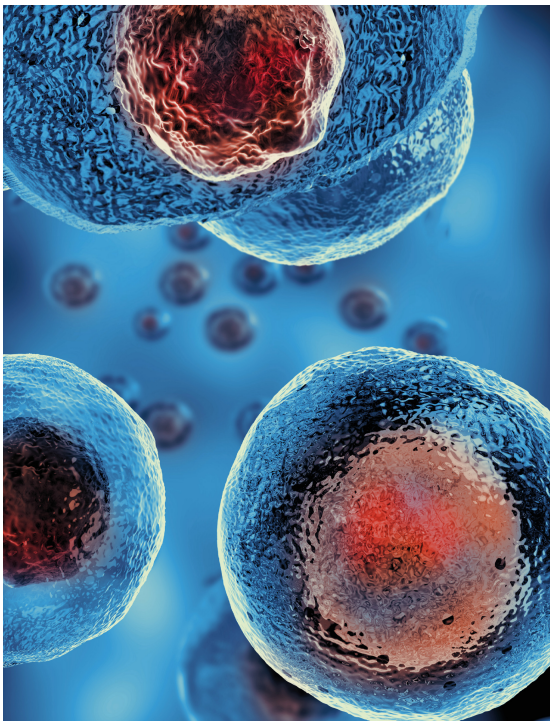

Image: Giovanni Cancemi/Shutterstock.com

During development, cells are generated at specific locations within the embryo and then migrate into their destinations. At their destinations, they assemble together through cell adhesions, eventually leading to the formation of tissues and organs. In some cases, orchestration of cell adhesion and migration produces the global movement of cell groups, called collective cell migration, which is also required for the development of basic tissue structures such as spheres, clusters, and vesicles in the morphogenetic processes of development. Therefore, individual regulation and orchestration of cell adhesion and migration are quite important for appropriate tissue/organ formation during development. However, how cell adhesion and migration are regulated, and orchestrated during development? How cell adhesion and migration affects tissue formation during development? To answer these questions, we assembled several review and research articles in this eBook. By assembling these articles, we could explore the presence of core regulatory mechanisms and deepen the current understanding of cell adhesion and migration during the development of multicellular organisms.

Citation: Matsui, T., Fujita, M., Ito, A., eds. (2019). Cell Adhesion and Migration in the Development of Multicellular Organisms. Lausanne: Frontiers Media. doi: 10.3389/978-2-88945-694-9

Table of Contents

frontiers in Cell and Developmental Biology

EDITORIAL
published: 22 October 2018
doi: 10.3389/fcell.2018.00142

Editorial: Cell Adhesion and Migration in the Development of Multicellular Organisms

*Takaaki Matsui**

Gene Regulation Research, Division of Biological Science, Graduate School of Science and Technology, Nara Institute of Science and Technology, Nara, Japan

Keywords: cell migration, collective cell migration, development, multicellular organisms, cell adhesion

Editorial on the Research Topic

Cell Adhesion and Migration in the Development of Multicellular Organisms

OPEN ACCESS

Edited by:
Akihiko Ito,
Kindai University, Japan

Reviewed by:
Koichi Nishiyama,
Kumamoto University Hospital, Japan

***Correspondence:**
Takaaki Matsui
matsui@bs.naist.jp

Specialty section:
This article was submitted to Cell Adhesion and Migration, a section of the journal Frontiers in Cell and Developmental Biology

Received: *24 August 2018*
Accepted: *04 October 2018*
Published: *22 October 2018*

Citation:
Matsui T (2018) Editorial: Cell Adhesion and Migration in the Development of Multicellular Organisms. Front. Cell Dev. Biol. 6:142. doi: 10.3389/fcell.2018.00142

Cells express many adhesion molecules, cytoskeletons, extracellular matrices, and signal activators/mediators, that are involved in cell adhesion and migration. To generate well-organized tissues during the development of multicellular organisms, expression and/or function of these molecules need to be controlled appropriately in a spatiotemporal manner. In addition, individual regulation and orchestration of cell adhesion and migration are also important. In this research topic, we aimed to understand how cell adhesion and migration are regulated and orchestrated during development and how cell adhesion and migration affect tissue formation during development, and to that end, have put together a collection of articles related to this research area.

On the topic of adhesion molecules, Watanabe produced a review that focuses on the role of gap junction proteins in skin pattern formation and body shape determination, while a review by Togashi touched on the differential and cooperative roles of cadheins and nectins in sensory organ patterning. In another review, Sanghvi-Shah and Weber elaborated on the role of the intermediate filaments in mechanotransduction signaling, and proposed that intermediate filaments act as a centerpiece between mechanical stimuli and directional cell migration.

And along the same line, Hirota and Nakajima; Matsubara et al. also produced interesting reports that focus on signaling mechanisms of cell migration and adhesion in cerebrum and limb, respectively. On the other hand, mechanism of cell-chirality-driven tissue rotation, which is required for proper left-right patterning, is elegantly discussed by Inaki et al. Equally intriguing is the report by Hiraiwa et al. that uses numerical simulation study to show the importance of wave-like propagation of junctional remodeling to collective cell migration.

Using an approach that combined live imaging and computational biology, Sakane et al. and Tsuboi et al. further succeeded in quantifying the fascinating dancing style of collective cell migration and to infer cell mechanics within heterogeneous epithelial tissue, respectively. And in an another advanced technical approach, Nagasaka et al. was able to measure cellular stiffness at the tissue- and single-cell-levels by using an atomic force microscope (AFM) and showed that tissue-level stiffness is determined

not only by mechanical properties of single cells but also by cellular densification, and affects nuclear/somal movements of neuroepithelial cells in cerebrum development. These curated articles showed the variety of opinions that are currently forming in regards to regulation of cell adhesion and migration in various organisms including mouse, ferret, fish, and fly. Nevertheless, they shared the same core points emphasizing that spatial and temporal regulations of expression and/or dynamics of adhesion molecules and cytoskeletons through signal transduction and mechanotransduction are required for proper regulation of cell adhesion and migration, and that mechanical properties of cells and/or mechanical interactions among cells affect cell adhesion and migration during development. In addition, this research topic suggests that interdisciplinary approaches of developmental biology, mathematics, and/or physics would be an excellent system to understand how cell adhesion and migration are regulated and orchestrated during development. By assembling these articles together under this research topic, we hope that it would deepen the current understanding of cell adhesion and migration during the development of multicellular organisms, and serve as the basis for the future works geared to advance this research area.

AUTHOR CONTRIBUTIONS

The author confirms being the sole contributor of this work and has approved it for publication.

ACKNOWLEDGMENTS

The author is appreciative of all the contributors to this research topic, and thanks Dr. Fiqri Dizar Khaidizar for critical reading of the manuscript. The author also thanks the Ministry of Education, Culture, Sports, Science and Technology (MEXT), the Uehara Memorial Foundation, the Nakajima Foundation, the Mochida Memorial Foundation, and the Takeda Science Foundation for past and current support.

Conflict of Interest Statement: The author declares that the research was conducted in the absence of any commercial or financial relationships that could be construed as a potential conflict of interest.

frontiers in Cell and Developmental Biology

MINI REVIEW
published: 21 February 2017
doi: 10.3389/fcell.2017.00013

Gap Junction in the Teleost Fish Lineage: Duplicated Connexins May Contribute to Skin Pattern Formation and Body Shape Determination

Masakatsu Watanabe *

Graduate School of Frontier Biosciences, Osaka University, Suita, Japan

Gap junctions are intercellular channels that allow passage of ions and small molecules between adjacent cells. Gap junctions in vertebrates are composed of connexons, which are an assembly of six proteins, connexins. Docking of two connexons on the opposite cell surfaces forms a gap junction between the cytoplasm of two neighboring cells. Connexins compose a family of structurally related four-pass transmembrane proteins. In mammals, there are ~20 connexins, each of which contributes to unique permeability of gap junctions, and mutations of some connexin-encoding genes are associated with human diseases. Zebrafish has been predicted to contain 39 connexin-encoding genes; the high number can be attributed to gene duplication during fish evolution, which resulted in diversified functions of gap junctions in teleosts. The determination of body shapes and skin patterns in animal species is an intriguing question. Mathematical models suggest principle mechanisms explaining the diversification of animal morphology. Recent studies have revealed the involvement of gap junctions in fish morphological diversity, including skin pattern formation and body shape determination. This review focuses on connexins in teleosts, which are integrated in the mathematical models explaining morphological diversity of animal skin patterns and body shapes.

Keywords: connexin, gap junction, skin pattern, bone shape, zebrafish

OPEN ACCESS

Edited by:
Takaaki Matsui,
Nara Institute of Science and Technology, Japan

Reviewed by:
Igor Jakovcevski,
German Center for Neurodegenerative Diseases (HZ), Germany
Koichi Nishiyama,
Kumamoto University Hospital, Japan

***Correspondence:**
Masakatsu Watanabe
watanabe-m@fbs.osaka-u.ac.jp

Specialty section:
This article was submitted to Cell Adhesion and Migration, a section of the journal Frontiers in Cell and Developmental Biology

Received: *16 December 2016*
Accepted: *07 February 2017*
Published: *21 February 2017*

Citation:
Watanabe M (2017) Gap Junction in the Teleost Fish Lineage: Duplicated Connexins May Contribute to Skin Pattern Formation and Body Shape Determination. Front. Cell Dev. Biol. 5:13. doi: 10.3389/fcell.2017.00013

INTRODUCTION

Gap junctions are intercellular channels that mediate the transfer of small molecules between adjacent cells (Kumar and Gilula, 1996). Because of low size selectivity of molecules transferred through gap junctions (<1,000 Da), it is difficult to determine the biological functions of gap junctions in the organisms. Gap junctions are composed of two hemichannels formed by four-pass transmembrane proteins: connexins and innexins (**Figures 1A,B**; Baranova et al., 2004). Connexins are vertebrate-specific gap junction proteins, whereas innexins are expressed in invertebrates. Connexins as well as innexins form both hemichannels and gap junctions, while pannexins expressed in vertebrates but homologous to invertebrate innexins predominantly exist as hemichannels connecting the intracellular and extracellular space, rather than gap junctions connecting adjacent cells. Curiously, there is no evolutional relationship between connexins and pannexins, although both are expressed in vertebrates. In summary, connexins and innexins are functional homologs, while innexins and pannexins are evolutionary homologs (**Figure 1A**; Scemes et al., 2007).

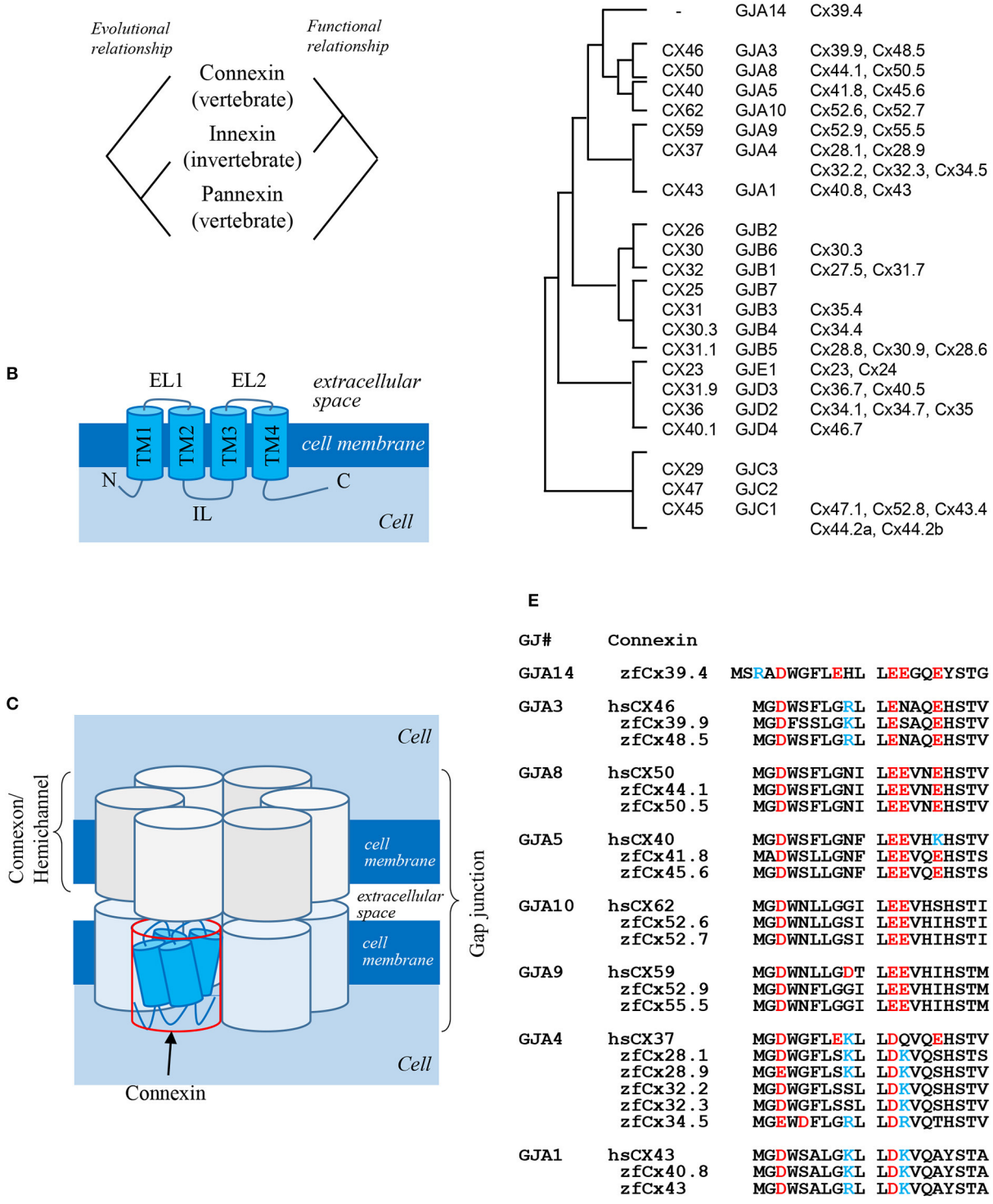

FIGURE 1 | Gap junction proteins. (A) Relationship among three types of gap junction proteins: connexins, innexins, and pannexins (Baranova et al., 2004). **(B)** Structure of connexin proteins. N: N-terminus; TM: transmembrane domain; EL: extracellular loop; IL: intracellular loop; C: C-terminus (Kumar and Gilula, 1996). **(C)** Schematic presentation of a gap junction (Kumar and Gilula, 1996). **(D)** Phylogenic relationship between human and zebrafish connexins (Eastman et al., 2006; Cruciani and Mikalsen, 2007). **(E)** Sequence alignment of N-terminal domains of human and zebrafish alpha-type connexins (Connexin sequences were obtained from genome data base in Sanger Institute, http://www.sanger.ac.uk/).

Six connexin proteins form a hexamer called connexon, which functions as a hemichannel. After docking of two connexons on neighboring cell membranes, a gap junction is formed (**Figure 1C**). Connexins consist of several structural domains: the N-terminus, transmembrane region, extracellular and intracellular loops, and C-terminus (**Figure 1B**; Maeda et al., 2009). The N-terminal domain functions as a plug providing closure of gap junctions (Oshima et al., 2007) and as a voltage sensor of membrane potential (Verselis et al., 1994). The C-terminal domain has several phosphorylation sites which transmit signals to control the opening and closing of gap junctions and are also implicated in other biological pathways (Hebert and Stains, 2013), while extracellular loops are responsible for docking of hemichannels (Kumar and Gilula, 1996).

The number of connexin genes differs depending on animal species. In the human genome, there are 21 connexin genes, whereas in the zebrafish genome, 39 connexin genes are predicted (Hebert and Stains, 2013). Connexin proteins are named according to their molecular weight; for example, connexin 43 (Cx43) is a 43-kDa protein. This system sometimes causes confusion because orthologous genes belonging to different species have different gene symbols; thus, human *CX46* and zebrafish *cx39.9* are orthologous genes (**Figure 1D**). There is also other classification system based on gap junctions which are divided into five families, from gap junction alpha (GJA) to gap junction epsilon (GJE), and all connexins are named according to a specific subfamily (**Figure 1D**, symbol). In this system, orthologous genes in different animal species belong to the same gap junction subfamily. Although this classification makes it easier to understand the relationship between connexins and gap junctions, it has faults, because some connexins have a potential to form gap junctions with different connexin proteins. Thus, gap junctions composed of the same hemichannels consisting of two or more connexins are called heteromeric, while those composed of different hemichannels are called heterotypic. Although the formation of heteromeric-heterotypic gap junctions has been extensively examined in *in vitro* experiments, its role *in vivo* remains largely unknown.

CONNEXINS IN TELEOSTS

There are more connexin-encoding genes in zebrafish than in humans (39 and 21, respectively; Eastman et al., 2006; Cruciani and Mikalsen, 2007). Here, I analyzed the number of connexin genes in six teleost species: zebrafish, herring, catfish, fugu, tilapia, and medaka using Genome Database (Ensembl, Sanger Institute). Zebrafish, herring, and catfish form one sister group, and the other three species form another one (**Figure 2A**). The results show that ∼40 connexin genes exist in the genomes of the examined teleost species, although it is not known whether all the genes are expressed and functional. The duplication of connexin-encoding genes may have occurred in the ancestor of the teleost lineage through chromosome duplication events. After counting the number of connexin genes and categorizing them into the GJA–GJE subfamilies, it appeared that the examined teleost species had similar gene numbers in each subfamily (**Figure 2B**). **Figure 2C** shows the number of connexin genes belonging to the GJA subfamily. For example, *cx39.4* belongs to the GJA14 subfamily and all six species examined have one *cx39.4* ortholog in their genome. In the fugu-tilapia-medaka lineage, connexins of the GJA3 subfamily were duplicated and *cx40.8* and *cx50.5* orthologs were lost in their common ancestor. On the other hand, *cx55.5* might have been lost in catfish and tilapia independently. Connexins belonging to the GJA4 subfamily have three or more paralogous genes. The high copy numbers of GJA4 paralogous genes may be explained by local chromosomal duplications occurred in the ancestor. In addition to the high copy number, the *cx39.4* gene is teleost-specific and is not detected in human, chicken, lizard, or *Xenopus* genomes (**Figures 1D,E**).

CONNEXINS IN ZEBRAFISH

Zebrafish is a small tropical fish with a body 3–4-cm long. Because of its transparent embryo, easy breeding, generation of transgenic lines, and availability of genomic resources through advances in genome sequencing technology, zebrafish is considered an important and convenient model organism for developmental studies in vertebrates. However, knocking out of some connexin gene shows no phenotypes in zebrafish, probably because of gene redundancy or other reasons. To date, the expression of several connexin genes was identified in zebrafish mutants: *cx39.9* in muscle (Hirata et al., 2012), *cx52.6* and *cx55.5* in retina (Klaassen et al., 2011), *cx43* in fins and vertebrae (Iovine et al., 2005; Misu et al., 2016), and *cx36.7* in the heart (Sultana et al., 2008), while *cx41.8* and *cx39.4* were found to be responsible for pigment pattern (Watanabe et al., 2006; Irion et al., 2014).

CONNEXINS IN ZEBRAFISH PIGMENT PATTERN

One of the famous characteristics of zebrafish is "zebra" stripe observed on the skin surface (**Figure 2D**), and the mechanism underlying the generation of the stripe pattern has long been an intriguing question. Sixty years ago, English mathematician Alan M. Turing proposed a mathematical model called the reaction-diffusion (R-D) model, which explained the mechanism underlying pattern formation (Turing, 1952) and which was later applied to biological phenomena (Kondo and Asai, 1995). This mathematical model represents the interaction and diffusion of two hypothetical factors, allowing, by changing the parameters in the equations, to generate various patterns *in silico*. Zebrafish stripes are made of two types of pigment cells, melanophores and xanthophores, and it is shown that interactions between these pigment cells satisfy the condition of the R-D model (Yamaguchi et al., 2007; Nakamasu et al., 2009). Thus, it can be assumed that the zebrafish skin pattern is generated in the R-D manner, which makes zebrafish a model organism for pattern formation studies.

One of the most famous zebrafish skin pattern mutants is *leopard* fish, which has spots instead of stripes (**Figure 2E**). This mutant was originally identified from field and several alleles were isolated from mutagenesis pools (Haffter et al., 1996). Because the spot is a representative pattern of the R-D

A

B

	GJA	GJB	GJC	GJD	GJE
zebrafish	18	8	5	5	2
herring	18	13	5	9	1
catfish	17	12	6	6	1
fugu	16	11	5	7	1
tilapia	17	14	6	8	1
medaka	18	10	5	7	1

C

	GJA14	GJA3		GJA8		GJA5		GJA10		GJA9		GJA4	GJA1	
zfCx	39.4	39.9	48.5	44.1	50.5	41.8	45.6	52.6	52.7	52.9	55.5		43	40.8
zebrafish	+	+	+	+	+	+	+	+	+	+	+	5	+	+
herring	+	+	+	+	+	+	+	+	+	+	+	5	+	+
catfish	+	+	+	+	+	+	+	+	+	+	-	5	+	+
fugu	+	2	2	+	-	+	+	+	+	+	+	3	+	-
tilapia	+	2	2	+	-	+	+	+	+	+	-	5	+	-
medaka	+	2	2	+	-	+	+	+	+	+	+	5	+	-

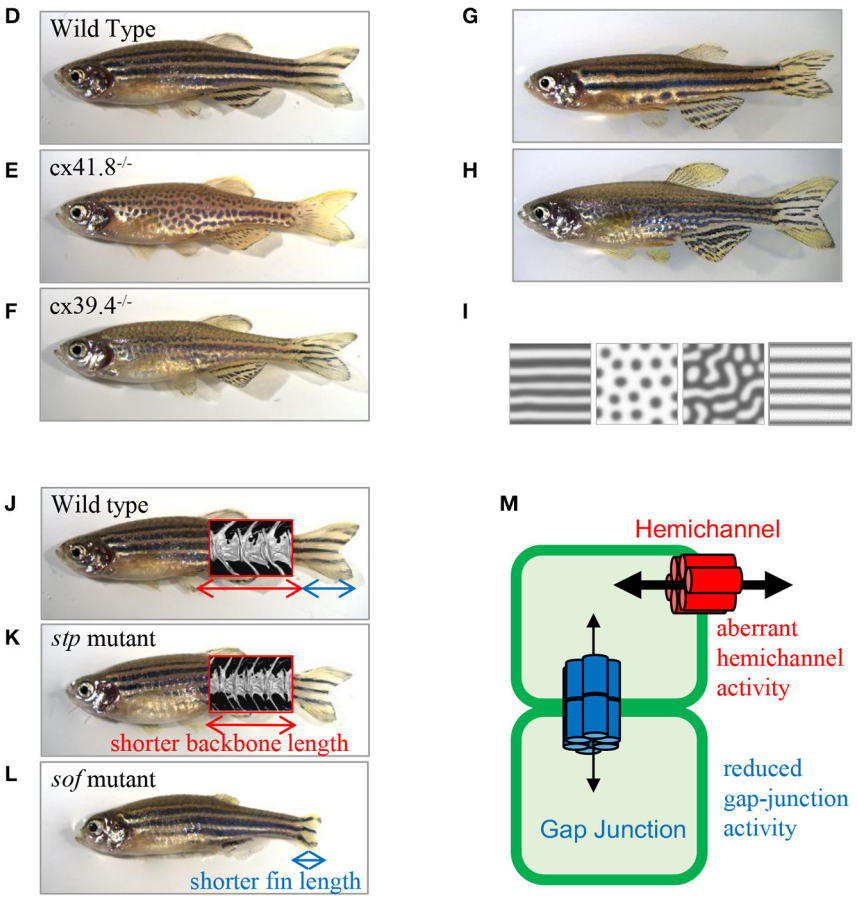

FIGURE 2 | Connexins in teleosts. (A) Phylogenic relationship among six teleost species (Chen et al., 2004). **(B)** The number of connexin-encoding genes in six teleost species. **(C)** The number of genes encoding connexins of the alpha family gap junctions. "zfCx" indicates zebrafish connexins; "+" and "−" indicate the existence or absence, respectively, of an ortholog. If more than one orthologous gene was found, gene numbers are indicated (**B,C**; Connexin sequences were obtained from genome data base in Sanger Institute, http://www.sanger.ac.uk/). **(D–I)** Connexins in zebrafish pigment patterns. Wild-type zebrafish

(Continued)

FIGURE 2 | Continued
(D; Watanabe and Kondo, 2012); *leopard* mutant (**E**; Watanabe and Kondo, 2012); *luchs* mutant (**F**; Irion et al., 2014; Watanabe et al., 2016); transgenic zebrafish Tg(mitfa-cx41.8) >> *leopard* (**G**; Watanabe and Kondo, 2012); transgenic zebrafish Tg(mitfa-cx41.8M7) >> wild-type (**H**; Watanabe and Kondo, 2012); reaction-diffusion (R-D) patterns (**I**; Watanabe and Kondo, 2012). **(J–M)** Connexins in zebrafish bones; micro-CT images of vertebrae are superimposed. Wild-type zebrafish (**J**; Misu et al., 2016), *stp* mutant (**K**; Misu et al., 2016), *sof* mutant (**L**; Iovine et al., 2005; Misu et al., 2016). Schematic presentation of gap junction and hemichannel functions in zebrafish mutants (**M**; Misu et al., 2016). Red font, functional activity of hemichannels in the *stp*-Cx43 mutant; blue font, functional activity of gap junctions in the *sof*-Cx43 mutant.

model (**Figure 2I**), the *leopard* mutant is an important target of pattern formation studies (Asai et al., 1999). Ten years ago, our group identified the gene responsible for the *leopard* pattern, which encoded a gap junction protein Cx41.8 (Watanabe et al., 2006), a zebrafish ortholog of mammalian CX40 and a paralog of zebrafish Cx45.6 (Eastman et al., 2006). Knocking out *cx41.8* results in a spotted skin pattern, whereas knocking out *cx45.6* does not produce a skin phenotype. It should be noted that molecules functioning in cell–cell interaction should participate in stripe-to-spot changes *in vivo* because such changes are predicted by the mathematical model for the interaction between two hypothetical factors. This notion was confirmed when we successfully generated the R-D patterns on zebrafish skin using Cx41.8 mutants (**Figures 2G–I**; Watanabe and Kondo, 2012). To further investigate the role of gap junctions in skin pattern formation, we constructed transgenic fish lines in which connexin-encoding genes were ectopically expressed in pigment cells of the *leopard* fish (Watanabe et al., 2012). The results indicated that, in addition to *cx41.8*, other genes such as *cx44.1*, *cx45.6*, and *cx48.5* rescued the *leopard* phenotype, while *cx27.5*, *cx30.8*, *cx32.2*, or *cx43* did not. Amino acid alignment of N-terminal connexin domains revealed that connexins which rescued the *leopard* phenotype belonged to the GJA14, GJA3, GJA8, and GJA5 subfamilies as evidenced by the presence of the ExxxE motif (**Figure 1E**), a polyamine-binding site important for rectifying properties of gap junctions (Musa et al., 2004).

Polyamines, mainly putrescine, spermidine, and spermine, are small molecules important for cell proliferation and differentiation; they are known to regulate K+ inward-rectifier (Kir) channels through binding to the channel pore (Hibino et al., 2010). We have isolated Kir7.1 from a zebrafish skin pattern mutant, *jaguar*, and shown that the Kir7.1 channel is expressed in melanophores, where it forms resting potential (Iwashita et al., 2006); this hyperpolarization is important for the generation of a clear boundary between melanophores and xanthophores on fish skin (Inaba et al., 2012). Based on this finding, we introduced the *ssat* gene encoding polyamine metabolic enzyme spermidine/spermine N1-acetyltransferaseinto melanophores, and found that the ectopic expression of *ssat* disturbed the stripe pattern of zebrafish (Watanabe et al., 2012). Interestingly, *ssat*-expressing transgenic zebrafish showed a unique phenotype of large spots and wide stripes, which is an intermediate pattern between the *leopard* (*cx41.8*) and *jaguar* (*kir7.1*) mutants (Iwashita et al., 2006; Watanabe et al., 2006, 2012). Furthermore, a recent study showed that spermidine synthase was also involved in skin pattern formation as confirmed by the isolation of spermidine, but not spermine, from melanophores (Frohnhofer et al., 2016). Taken together, these data indicate that spermidine may bind both Kir7.1 and Cx41.8, and control the rectification properties of Kir7.1 as well as of Cx41.8 gap junctions in melanophores. As a result, the expected unidirectional functioning of gap junctions from xanthophores to melanophores would be provided, which is consistent with a previous observation that xanthophores are required for melanophore survival (Nakamasu et al., 2009).

Cx39.4 is another connexin protein shown to be involved in the skin pattern formation of zebrafish. Cx39.4 is the teleost lineage-specific connexin (**Figures 1D,E**) recently isolated from a zebrafish skin pattern mutant, *luchs* (**Figure 2F**) (Irion et al., 2014). We examined the expression of alpha-type connexins in pigment cells and found that the *cx41.8* and *cx39.4* genes were expressed in melanophores and xanthophores, which was also confirmed in transgenic zebrafish carrying a reporter gene under connexin promoters. To compare Cx39.4 and Cx41.8 functions in skin pattern formation, we performed complementation experiments when *cx39.4* was introduced into the *leopard* mutant and *cx41.8* into the *luchs* mutant (Watanabe et al., 2016). None of them was able to rescue each other phenotypes, indicating that Cx41.8 and Cx39.4 have distinct functional activities. Although Cx39.4 contains the N-terminal ExxxE motif important for pattern formation, the sequence of its N-terminus is unique because it is two residues longer than that in other alpha-type connexins and has a basic residue at the third position. Our electrophysiological analysis showed that large voltage-dependent current was absent in Cx39.4-expressing oocytes, indicating that the basic residue at the third position affected the characteristics of gap junctions and accounted for the difference of channeling properties between Cx39.4 and Cx41.8 (Watanabe et al., 2016).

CONNEXINS IN ZEBRAFISH BONES, FINS, AND VERTEBRAE

The variation in body shape among animal species has long been an intriguing question. A century ago, Scottish mathematician and biologist D'Arcy Thompson proposed the theory of transformations suggesting that new body shapes arise by changing angles, extending the length, or enlarging body parts, pointing out correlations between biological forms and mechanical phenomena (Thompson, 1961). Bones determine body shape in vertebrates, and zebrafish fins present a valuable model for the study of bone organogenesis and regeneration because of their rapid growth. Recent advances in transgenic techniques enable the detection of gene expression in bone-producing cells during bone growth and regeneration in live fish. Among the connexin family members expressed in zebrafish,

Cx43 is known to be involved in the formation and regeneration of the fin and in determining vertebra proportions (Iovine et al., 2005; Misu et al., 2016).

Ten years ago, zebrafish Cx43 was identified in the *short-of-fin* (*sof*) mutant who has a short fin segment (**Figure 2L**; Iovine et al., 2005). Four *sof* alleles were isolated from zebrafish mutagenesis pools and amino acid substitutions causing the loss or decrease of Cx43 gap junction functional activity were identified in three mutant alleles. On the other hand, no mutation was found in the coding region of *cx43* in the fourth allele; however, the downregulation of both mRNA and protein expression were detected in the carriers of this allele. Overall, these findings indicate that a decrease of Cx43 gap junction properties produces the short-fin phenotype (**Figure 2L**). In addition, Cx40.8, a paralog of Cx43 in zebrafish is also involved in fin development and regeneration (Gerhart et al., 2009). Interestingly, although the biological function of Cx40.8 is very similar to that of Cx43, its membrane localization is differentially controlled depending on the developmental phases and regeneration status (Gerhart et al., 2012).

To provide deeper understanding of the molecular mechanisms supporting the theory of transformations, our group focused on a zebrafish body-shape mutant named *stoepsel* (*stp*; **Figure 2K**) identified 20 years ago from a zebrafish mutagenesis pool based on reduced body length. Recently, we performed precise analysis of bone shape development in this mutant fish. Micro-CT scanning images revealed that the vertebra shape of the *stp* mutant was almost the same as that of the wild-type fish, although the vertebra size along the anterior-posterior (A-P) axis was decreased (**Figures 2J,K**). Because the vertebra height along the dorsal-ventral (D-V) axis was unchanged, this fish presents a proportion mutant according to the theory of transformations. We also found that the mutant phenotype appeared 50 days post-fertilization, indicating that it is expressed in the adulthood. To disclose the underlying molecular mechanism, we performed positional cloning experiments and identified a point mutation in the *cx43* coding region. Then, we asked a question why mutations occurring in same *cx43* gene caused different phenotypes, i.e., short fin or short vertebra. To address this question, we compared the functions of gap junctions and hemichannels by performing dual-cell voltage clamp experiments and found that the functional activity of *stp*-Cx43 gap junction was decreased similar to that of the *sof*-Cx43 mutant (Misu et al., 2016). Measurements of fin segment length in the *stp* mutant revealed that it was 5% shorter than that of the wild-type fish (Misu et al., 2016), which is consistent with previous findings that shortening of the fin segment is proportional to the reduction in gap junction function (Hoptak-Solga et al., 2007). On the other hand, we detected aberrant increase of *stp*-Cx43 hemichannel activity, while no difference was detected between *sof*-Cx43 and the wild-type Cx43. These findings suggest that malfunctioning of hemichannels results in reduced backbone length, whereas a decrease in gap junction activity causes shortening of the fin segment (**Figure 2M**), although the underlying mechanism remains unclear (Misu et al., 2016).

The mutation in the human *GJA1* gene encoding CX43 is known to be responsible for an extremely rare disease, oculodentodigital dysplasia (ODDD), manifested by small eyes, underdeveloped teeth, and malformation of fingers (Paznekas et al., 2003). As zebrafish Cx43 is an analog of human CX43, zebrafish can present a good experimental model to study ODDD and would help understand the mechanisms controlling bone formation.

MATHEMATICAL MODELS PREDICT GAP JUNCTION FUNCTIONS IN PATTERN FORMATION

It is very interesting that two independent projects which aimed to disclose the molecular mechanism hidden in mathematical models, found the involvement of gap junction proteins: Cx41.8 in the R-D model and Cx43 in the theory of transformation.

In the R-D model, positive interactions between two factors are important. As mentioned above, Cx41.8-gap junctions might be formed between xanthophores and melanophores, and control the directional flow of small molecules from a xanthophore to a melanophore depending on spermidine concentration. In addition, the R-D model predicts that Cx41.8 might be involved in melanophore differentiation. The reduction of basal level synthesis of a factor also causes pattern changes in the R-D model (Asai et al., 1999), and the reduction of the number of melanophores are observed in the *leopard* mutant (**Figure 2E**).

Regarding the theory of transformation, the *stp* mutant might be the simplest example. It is possible that the reduction of osteogenic activity causes the formation of shorter vertebra in the *stp* mutant, although the difference in the mechanisms underlying the formation of shorter vertebra in the *stp* fish and shorter fins in the *sof* fish is unclear. Recent gap junction studies have revealed that hemichannels formed by connexins and/or pannexins function as sensors of mechanical stress (Jiang et al., 2009; Thi et al., 2012), which supports the possibility that gap junctions control body shape variations, including shortening, expanding, and twisting of body frames as predicted by the theory of transformation.

Many questions still remain, including functional differences among connexin proteins, the type of transferred molecules, and the evolutionary events that have led to the acquisition of this intercellular communication system in the animal kingdom. Future mechanistic and genetic studies would address these questions.

AUTHOR CONTRIBUTIONS

The author confirms being the sole contributor of this work and approved it for publication.

ACKNOWLEDGMENTS

This work was supported by the Ministry of Education, Culture, Sports, Science, and Technology in Japan (KAKENHI Grant 26291049).

REFERENCES

Asai, R., Taniguchi, E., Kume, Y., Saito, M., and Kondo, S. (1999). Zebrafish leopard gene as a component of the putative reaction-diffusion system. *Mech. Dev.* 89, 87–92. doi: 10.1016/S0925-4773(99)00211-7

Baranova, A., Ivanov, D., Petrash, N., Pestova, A., Skoblov, M., Kelmanson, I., et al. (2004). The mammalian pannexin family is homologous to the invertebrate innexin gap junction proteins. *Genomics* 83, 706–716. doi: 10.1016/j.ygeno.2003.09.025

Chen, W.-J., Orti, G., and Meyer, A. (2004). Novel evolutionary relationship among four fish model systems. *Trends Genet.* 20, 244–231. doi: 10.1016/j.tig.2004.07.005

Cruciani, V., and Mikalsen, S. O. (2007). Evolutionary selection pressure and family relationships among connexin genes. *Biol. Chem.* 388, 253–264. doi: 10.1515/bc.2007.028

Eastman, S. D., Chen, T. H., Falk, M. M., Mendelson, T. C., and Iovine, M. K. (2006). Phylogenetic analysis of three complete gap junction gene families reveals lineage-specific duplications and highly supported gene classes. *Genomics* 87, 265–274. doi: 10.1016/j.ygeno.2005.10.005

Frohnhofer, H. G., Geiger-Rudolph, S., Pattky, M., Meixner, M., Huhn, C., Maischein, H. M., et al. (2016). Spermidine, but not spermine, is essential for pigment pattern formation in zebrafish. *Biol. Open* 5, 736–744. doi: 10.1242/bio.018721

Gerhart, S. V., Eble, D. M., Burger, R. M., Oline, S. N., Vacaru, A., Sadler, K. C., et al. (2012). The Cx43-like connexin protein Cx40.8 is differentially localized during fin ontogeny and fin regeneration. *PLoS ONE* 7:e31364. doi: 10.1371/journal.pone.0031364

Gerhart, S. V., Jefferis, R., and Iovine, M. K. (2009). Cx40.8, a Cx43-like protein, forms gap junction channels inefficiently and may require Cx43 for its association at the plasma membrane. *FEBS Lett.* 583, 3419–3424. doi: 10.1016/j.febslet.2009.09.054

Haffter, P., Odenthal, J., Mullins, M. C., Lin, S., Farrell, M. J., Vogelsang, E., et al. (1996). Mutations affecting pigmentation and shape of the adult zebrafish. *Dev. Genes Evol.* 206, 260–276. doi: 10.1007/s004270050051

Hebert, C., and Stains, J. P. (2013). An intact connexin43 is required to enhance signaling and gene expression in osteoblast-like cells. *J. Cell. Biochem.* 114, 2542–2550. doi: 10.1002/jcb.24603

Hibino, H., Inanobe, A., Furutani, K., Murakami, S., Findlay, I., and Kurachi, Y. (2010). Inwardly rectifying potassium channels: their structure, function, and physiological roles. *Physiol. Rev.* 90, 291–366. doi: 10.1152/physrev.00021.2009

Hirata, H., Wen, H., Kawakami, Y., Naganawa, Y., Ogino, K., Yamada, K., et al. (2012). Connexin 39.9 protein is necessary for coordinated activation of slow-twitch muscle and normal behavior in zebrafish. *J. Biol. Chem.* 287, 1080–1089. doi: 10.1074/jbc.M111.308205

Hoptak-Solga, A. D., Klein, K. A., DeRosa, A. M., White, T. W., and Iovine, M. K. (2007). Zebrafish short fin mutations in connexin43 lead to aberrant gap junctional intercellular communication. *FEBS Lett.* 581, 3297–3302. doi: 10.1016/j.febslet.2007.06.030

Inaba, M., Yamanaka, H., and Kondo, S. (2012). Pigment pattern formation by contact-dependent depolarization. *Science* 335, 677. doi: 10.1126/science.1212821

Iovine, M. K., Higgins, E. P., Hindes, A., Coblitz, B., and Johnson, S. L. (2005). Mutations in connexin43 (GJA1) perturb bone growth in zebrafish fins. *Dev. Biol.* 278, 208–219. doi: 10.1016/j.ydbio.2004.11.005

Irion, U., Frohnhofer, H. G., Krauss, J., Çolak Champollion, T., Maischein, H. M., Geiger-Rudolph, S., et al. (2014). Gap junctions composed of connexins 41.8 and 39.4 are essential for colour pattern formation in zebrafish. *Elife* 3:e05125. doi: 10.7554/eLife.05125

Iwashita, M., Watanabe, M., Ishii, M., Chen, T., Johnson, S. L., Kurachi, Y., et al. (2006). Pigment pattern in jaguar/obelix zebrafish is caused by a Kir7.1 mutation: implications for the regulation of melanosome movement. *PLoS Genet.* 2:e197. doi: 10.1371/journal.pgen.0020197

Jiang, J. X., Siller-Jackson, A. J., and Burra, S. (2009). Roles of gap junctions and hemichannels in bone cell functions and in signal transmission of mechanical stress. *Front. Biosci.* 12, 1450–1462. doi: 10.2741/2159

Klaassen, L. J., Sun, Z., Steijaert, M. N., Bolte, P., Fahrenfort, I., Sjoerdsma, T., et al. (2011). Synaptic transmission from horizontal cells to cones is impaired by loss of connexin hemichannels. *PLoS Biol.* 9:e1001107. doi: 10.1371/journal.pbio.1001107

Kondo, S., and Asai, R. (1995). A reaction-diffusion wave on the skin of marine angelfish *Pomacanthus*. *Nature* 376, 765–768. doi: 10.1038/376765a0

Kumar, N. M., and Gilula, N. B. (1996). The gap junction communication channel. *Cell* 84, 381–388. doi: 10.1016/S0092-8674(00)81282-9

Maeda, S., Nakagawa, S., Suga, M., Yamashita, E., Oshima, A., Fujiyoshi, Y., et al. (2009). Structure of the connexin 26 gap junction channel at 3.5 A resolution. *Nature* 458, 597–602. doi: 10.1038/nature07869

Misu, A., Yamanaka, H., Aramaki, T., Kondo, S., Skerrett, I. M., Iovine, M. K., et al. (2016). Two different functions of connexin43 confer two different bone phenotypes in zebrafish. *J. Biol. Chem.* 291, 12601–12611. doi: 10.1074/jbc.M116.720110

Musa, H., Fenn, E., Crye, M., Gemel, J., Beyer, E. C., and Veenstra, R. D. (2004). Amino terminal glutamate residues confer spermine sensitivity and affect voltage gating and channel conductance of rat connexin40 gap junctions. *J. Physiol.* 557(Pt 3), 863–878. doi: 10.1113/jphysiol.2003.059386

Nakamasu, A., Takahashi, G., Kanbe, A., and Kondo, S. (2009). Interactions between zebrafish pigment cells responsible for the generation of Turing patterns. *Proc. Natl. Acad. Sci. U.S.A.* 106, 8429–8434. doi: 10.1073/pnas.0808622106

Oshima, A., Tani, K., Hiroaki, Y., Fujiyoshi, Y., and Sosinsky, G. E. (2007). Three-dimensional structure of a human connexin26 gap junction channel reveals a plug in the vestibule. *Proc. Natl. Acad. Sci. U.S.A.* 104, 10034–10039. doi: 10.1073/pnas.0703704104

Paznekas, W. A., Boyadjiev, S. A., Shapiro, R. E., Daniels, O., Wollnik, B., Keegan, C. E., et al. (2003). Connexin 43 (GJA1) mutations cause the pleiotropic phenotype of oculodentodigital dysplasia. *Am. J. Hum. Genet.* 72, 408–418. doi: 10.1086/346090

Scemes, E., Suadicani, S. O., Dahl, G., and Spray, D. C. (2007). Connexin and pannexin mediated cell-cell communication. *Neuron Glia Biol.* 3, 199–208. doi: 10.1017/S1740925X08000069

Sultana, N., Nag, K., Hoshijima, K., Laird, D. W., Kawakami, A., and Hirose, S. (2008). Zebrafish early cardiac connexin, Cx36.7/Ecx, regulates myofibril orientation and heart morphogenesis by establishing Nkx2.5 expression. *Proc. Natl. Acad. Sci. U.S.A.* 105, 4763–4768. doi: 10.1073/pnas.0708451105

Thi, M. M., Islam, S., Suadicani, S. O., and Spray, D. C. (2012). Connexin43 and pannexin1 channels in osteoblasts: who is the "hemichannel"? *J. Membrane Biol.* 245, 401–409. doi: 10.1007/s00232-012-9462-2

Thompson, D. A. (1961). *On Growth and Form. Abridged Edition*. Cambridge: The University Press.

Turing, A. (1952). The chemical basis of morphogenesis. *Philos. Trans. R. Soc. Lond. B* 237, 37–72. doi: 10.1098/rstb.1952.0012

Verselis, V. K., Ginter, C. S., and Bargiello, T. A. (1994). Opposite voltage gating polarities of two closely related connexins. *Nature* 368, 348–351. doi: 10.1038/368348a0

Watanabe, M., Iwashita, M., Ishii, M., Kurachi, Y., Kawakami, A., Kondo, S., et al. (2006). Spot pattern of *leopard Danio* is caused by mutation in the zebrafish connexin41.8 gene. *EMBO Rep.* 7, 893–897. doi: 10.1038/sj.embor.7400757

Watanabe, M., and Kondo, S. (2012). Changing clothes easily: connexin41.8 regulates skin pattern variation. *Pigment Cell Melanoma Res.* 25, 326–330. doi: 10.1111/j.1755-148X.2012.00984.x

Watanabe, M., Sawada, R., Aramaki, T., Skerrett, I. M., and Kondo, S. (2016). The physiological characterization of connexin41.8 and

connexin39.4, which are involved in the striped pattern formation of zebrafish. *J. Biol. Chem.* 291, 1053–1063. doi: 10.1074/jbc.M115.673129

Watanabe, M., Watanabe, D., and Kondo, S. (2012). Polyamine sensitivity of gap junctions is required for skin pattern formation in zebrafish. *Sci. Rep.* 2:473. doi: 10.1038/srep00473

Yamaguchi, M., Yoshimoto, E., and Kondo, S. (2007). Pattern regulation in the stripe of zebrafish suggests an underlying dynamic and autonomous mechanism. *Proc. Natl. Acad. Sci. U.S.A.* 104, 4790–4793. doi: 10.1073/pnas.0607790104

Conflict of Interest Statement: The author declares that the research was conducted in the absence of any commercial or financial relationships that could be construed as a potential conflict of interest.

frontiers in Cell and Developmental Biology

MINI REVIEW
published: 15 September 2016
doi: 10.3389/fcell.2016.00104

Differential and Cooperative Cell Adhesion Regulates Cellular Pattern in Sensory Epithelia

Hideru Togashi *

Division of Molecular and Cellular Biology, Department of Biochemistry and Molecular Biology, Kobe University Graduate School of Medicine, Kobe, Japan

Animal tissues are composed of multiple cell types arranged in complex and elaborate patterns. In sensory epithelia, including the auditory epithelium and olfactory epithelium, different types of cells are arranged in unique mosaic patterns. These mosaic patterns are evolutionarily conserved, and are thought to be important for hearing and olfaction. Recent progress has provided accumulating evidence that the cellular pattern formation in epithelia involves cell rearrangements, movements, and shape changes. These morphogenetic processes are largely mediated by intercellular adhesion systems. Differential adhesion and cortical tension have been proposed to promote cell rearrangements. Many different types of cells in tissues express various types of cell adhesion molecules. Although cooperative mechanisms between multiple adhesive systems are likely to contribute to the production of complex cell patterns, our current understanding of the cooperative roles between multiple adhesion systems is insufficient to entirely explain the complex mechanisms underlying cellular patterning. Recent studies have revealed that nectins, in cooperation with cadherins, are crucial for the mosaic cellular patterning in sensory organs. The nectin and cadherin systems are interacted with one another, and these interactions provide cells with differential adhesive affinities for complex cellular pattern formations in sensory epithelia, which cannot be achieved by a single mechanism.

Keywords: cell adhesion molecules, cadherins, nectins, sensory organs, cell sorting, mosaic cellular pattern, self-organization

OPEN ACCESS

Edited by:
Takaaki Matsui, Nara Institute of Science and Technology, Japan

Reviewed by:
René-Marc Mège, Centre National de la Recherche Scientifique, France
Mitsugu Fujita, Kindai University, Japan

***Correspondence:**
Hideru Togashi
htogashi@med.kobe-u.ac.jp

Specialty section:
This article was submitted to Cell Adhesion and Migration, a section of the journal Frontiers in Cell and Developmental Biology

Received: *01 August 2016*
Accepted: *31 August 2016*
Published: *15 September 2016*

Citation:
Togashi H (2016) Differential and Cooperative Cell Adhesion Regulates Cellular Pattern in Sensory Epithelia. Front. Cell Dev. Biol. 4:104. doi: 10.3389/fcell.2016.00104

INTRODUCTION

Vertebrates possess highly developed sense organs such as the eyes, ears, nose, and tongue. These sense organs detect information about different environments and convert extracellular stimuli into electrical signals. These signals are mediated by specialized sensory epithelia. For example, in vertebrates, the perception of sound is mediated by the auditory epithelium located in the cochlea of the inner ear, and the perception of smell is mediated by the olfactory epithelium inside the nasal cavity. These sensory epithelia are typically composed of sensory cells and non-sensory supporting cells. Interestingly, the same types of sensory cells in the sensory epithelia are separated from one another to form alternating mosaic patterns. These mosaic patterns observed in the sensory organs are evolutionarily conserved among a wide range of species, and are thought to be important for the sensory functions. During the development of the auditory epithelium, sensory hair cells and supporting cells are thought to be segregated through the process of lateral inhibition mediated by

Notch–Delta signaling, and such processes themselves might contribute to the spatial separation of these cells (Zhang et al., 2000; Zine et al., 2001). Expression of Notch 1 and its ligand Jagged 2 is restricted to supporting cells and hair cells, respectively, in the auditory epithelium. In a previous study, genetic inactivation of Notch signaling did not impair the cellular pattern, but did result in an increased number of hair cells (Lanford et al., 1999). These observations suggest that lateral inhibition alone is insufficient to create the checkerboard-like cellular pattern. Recent progress has suggested that cellular rearrangements could also play a role in the mosaic pattern formation in the auditory epithelium. The question then arises as to how cell adhesion molecules regulate the complex and elaborate cellular patterns in the sensory organs. In this review, recent advances in cellular patterning within the sensory epithelia are introduced and discussed.

CELL–CELL ADHESION AND CELLULAR PATTERNING

Cell–cell adhesion systems are involved in many aspects of morphogenesis during development, including not only adhesion, but also movement, proliferation, survival, differentiation, and polarization. Various morphogenetic changes in tissues in developing embryos can be brought about by local cell rearrangements. Differential adhesion and cortical tension have been proposed to promote cell rearrangements and cell sorting in cell aggregates (Foty and Steinberg, 2005; Steinberg, 2007). Steinberg's theory of differential cell adhesion explains cell sorting as follows: when cell adhesion between cells of the same type is stronger than that between cells of different types, the two types of cells should become segregated; conversely, when cell adhesion is stronger between cells of different types, the two types of cells should become intermingled with one another. Although this differential cell adhesion theory suggests roles for self-organized cell movements in various epithelia, it remains unclear how this strategy for cell sorting is used during morphogenesis *in vivo*. Differential mechanical tension also plays an important role in cellular rearrangements (Lecuit, 2005; Heisenberg and Bellaiche, 2013). For example, during *Drosophila* germband extension, junctions are remodeled through the polarized recruitment of myosin II within the epithelium (Bertet et al., 2004). The contractile activity of myosin II creates local tension that orients the disassembly of E-cadherin junctions. In the case of neural-tube closure, polarized constriction of neuroepithelial adherens junctions (AJs) induces the convergence of their apical domains toward the midline of the neural plate (Nishimura et al., 2012). These observations suggest that anisotropic extensions and contractions of cell–cell junctions are used for cellular rearrangements in various epithelia.

ROLES OF CADHERINS AND NECTINS IN CELLULAR PATTERNING

The major cell adhesion molecules at AJs are cadherins and nectins (**Figure 1A**; Takai et al., 2008; Meng and Takeichi, 2009). Cadherins are essential for maintaining multicellular structures, and play a role in vital processes such as embryogenesis, pattern formation, and maintenance of specific tissue architectures. Cadherins are Ca^{2+}-dependent cell–cell adhesion molecules that constitute a superfamily, and are grouped into subfamilies designated classic cadherins and proto-cadherins. Here, for convenience, classic cadherins are simply referred to as cadherins. Cadherin molecules associate with p120 catenin and β-catenin via their cytoplasmic domain, and β-catenin in turn binds to α-catenin. α-Catenin can bind to F-actin, an interaction thought to be crucial for cadherins to create firm cell adhesions (Meng and Takeichi, 2009). The major role of cadherins is to connect cells expressing the same cadherins through homophilic interactions. Through these properties of cadherins, cells in mixed cultures of cell lines expressing E- or N-cadherin were observed to form separate aggregates (Nose et al., 1988; Katsamba et al., 2009), while differential levels of cadherin expression in two transfected cell populations caused one cell population to segregate internally or externally from the other cell population (Friedlander et al., 1989; Steinberg and Takeichi, 1994). The multicellular hexagonal lattice formation of the *Drosophila* retina is thought to arise through a cell-sorting process (Tepass and Harris, 2007). All cells in the retina express DE-cadherin, whereas only the cone cells express DN-cadherin (**Figure 1B**). The cone cell shape is formed by differential cadherin-mediated adhesion (Hayashi and Carthew, 2004). Differential expression of DN-cadherin within cone cells causes these cells to form an overall shape that minimizes their surface contact with surrounding cells. These observations indicated that simple patterned expression of cadherin results in a complex spatial pattern of cells in the visual system of *Drosophila*.

Nectins comprise a family of immunoglobulin-like molecules with four members, nectin-1, -2, -3, and -4. The most important property of this family is that nectins interact with other nectins in homophilic or heterophilic manners. Furthermore, nectins prefer heterotypic partners to homotypic partners, and their heterophilic interactions produce stronger cell–cell adhesions than their homophilic interactions (**Figure 1C**; Fabre et al., 2002; Yasumi et al., 2003; Martinez-Rico et al., 2005; Harrison et al., 2012). Owing to these properties of nectins, cells in mixed cultures of cell lines expressing different nectins became arranged in a mosaic pattern (Togashi et al., 2006, 2011). Several studies have shown that heterophilic interactions of nectins are present in cell–cell adhesions between Sertoli cells and germ cells in the testis (Ozaki-Kuroda et al., 2002; Mueller et al., 2003; Inagaki et al., 2005), between commissural axons and floor plate cells in the neural tube (Okabe et al., 2004), between pigment cell and non-pigment cell layers of the ciliary epithelium in the eye (Inagaki et al., 2005), between ameloblasts and stratum intermedium cells in the developing tooth (Yoshida et al., 2010), and between dendrites and axons of hippocampal neurons during synaptogenesis (Honda et al., 2006; Togashi et al., 2006). These observations suggest that heterophilic interactions of nectins between different cell types are involved in many aspects of organogenesis during development.

The cadherin and nectin systems are associated during cell–cell junction formation through their intercellular interactions

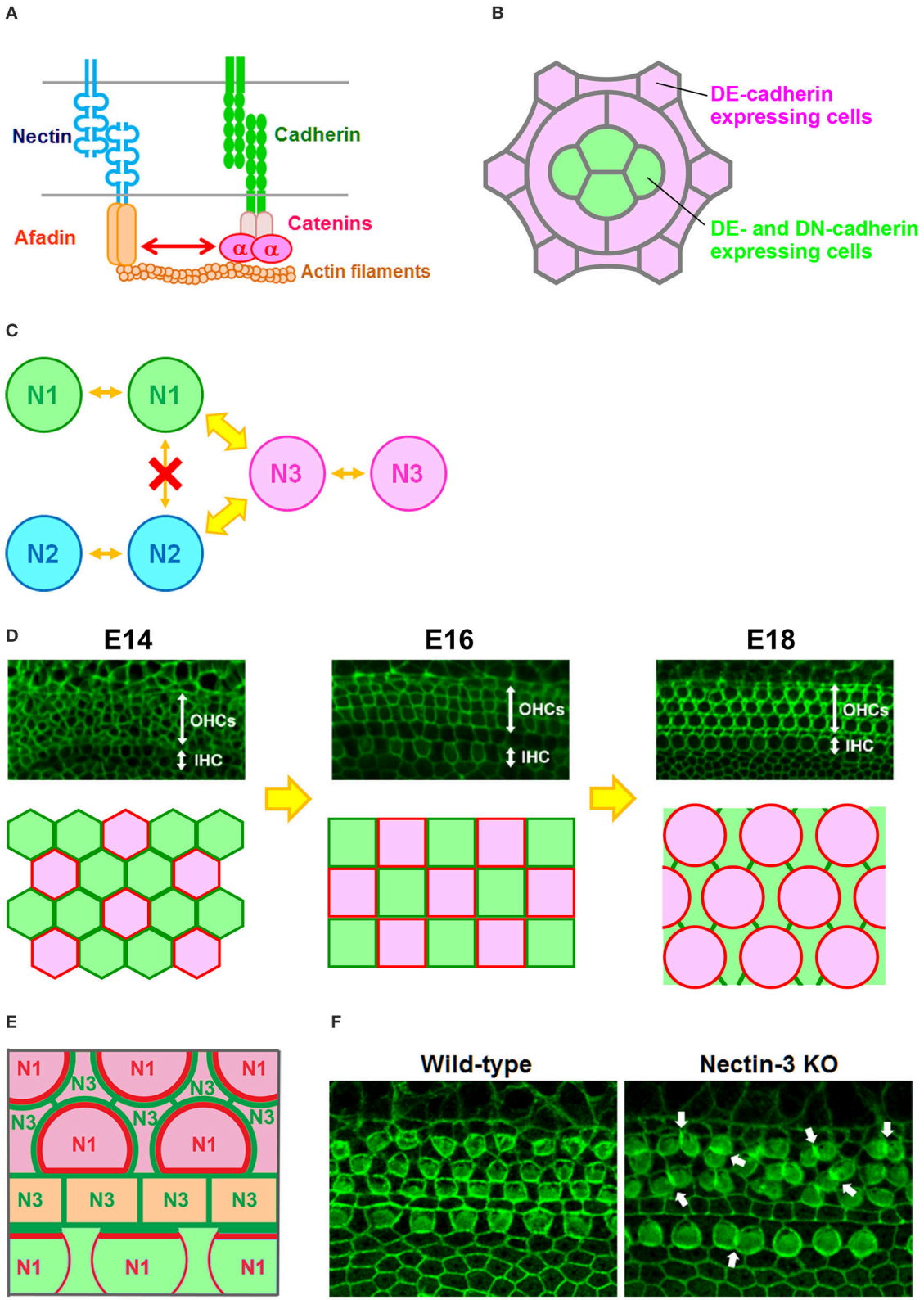

FIGURE 1 | Checkerboard-like cellular pattern in the mouse auditory epithelium. (A) Molecular interactions between nectins and cadherins (Takai and Nakanishi, 2003). α, α-catenin. **(B)** Expression pattern of DE-cadherin and DN-cadherin in the *Drosophila* retina (Hayashi and Carthew, 2004). All cells express

(Continued)

FIGURE 1 | Continued
DE-cadherin, but only cone cells express DN-cadherin. **(C)** Homophilic and heterophilic trans-interactions between nectins (Takai and Nakanishi, 2003). N1, nectin-1; N2, nectin-2; N3, nectin-3. Wide arrows, strong interactions; narrow arrows, weak interactions. **(D)** Cellular rearrangement of the auditory epithelium from embryonic day (E) 14 to E18 (McKenzie et al., 2004; Togashi et al., 2011). (Upper) Localization of ZO-1 at the apical surface of the auditory epithelium. OHCs, outer hair cells; IHC, inner hair cell. (Lower) Schematic illustrations of the cellular rearrangements. Red, differentiated hair cells; green, supporting cells. **(E)** Expression pattern of nectins and cadherins in the auditory epithelium (Simonneau et al., 2003; Togashi et al., 2011). Nectin-1 is expressed in hair cells, while nectin-3 is expressed in supporting cells. E-cadherin is expressed in the region including the outer hair cells (pink), and N-cadherin is expressed in the medial inner hair cell region (light green). Pillar cells express P-cadherin (light yellow). N1, nectin-1; N3, nectin-3. Red or green lines indicate nectin protein localizations at cell–cell boundaries. **(F)** Cellular patterning in the auditory epithelia of wild-type and nectin-3 knockout (KO) mice (Togashi et al., 2011). Arrows point to examples of aberrantly attached hair cells.

(**Figure 1A**). It has been suggested that nectins and afadin initially form cell–cell adhesions and then recruit cadherins to the nectin-based cell–cell adhesion sites to accelerate the formation of cadherin-dependent junctions (Tachibana et al., 2000; Honda et al., 2003). However, it remains unclear which of these molecules results in the recruitment of nectin and cadherin into AJs. It has been reported that cadherins control nectin recruitment into AJs through actin clustering (Troyanovsky et al., 2015). It is possible that both actin bundle formation and adhesion complex clustering mutually regulate cell–cell junction formation. Although both afadin and α-catenin are known to be essential for the associations of nectins and cadherins, the underlying mechanism for how the nectin–afadin system is interacted with the cadherin–catenin system remains unknown (Pokutta and Weis, 2000; Tachibana et al., 2000; Takai and Nakanishi, 2003; Takai et al., 2008).

CHECKERBOARD-LIKE PATTERN FORMATION IN THE AUDITORY EPITHELIUM

The auditory epithelium of the mammalian inner ear consists of inner hair cells, outer hair cells, and at least four different types of supporting cells. The hair cells and supporting cells are organized in a checkerboard-like pattern, such that each hair cell is separated from another hair cell by a supporting cell, forming an alternating mosaic. Cellular rearrangements are a possible mechanism for the patterning in the inner ear. In the developing auditory epithelium, the hair cells and supporting cells continue to change their position and alignment beyond the period of terminal mitoses for cells (**Figure 1D**; Chen et al., 2002; McKenzie et al., 2004). However, the driving force for the cellular rearrangements required for the checkerboard-like patterning is not well understood. Previous studies showed that E- and N-cadherins have complementary expression patterns within the auditory epithelium (Whitlon, 1993; Simonneau et al., 2003; Chacon-Heszele et al., 2012), with E-cadherin detected in the region including the outer hair cells, and N-cadherin restricted to cells in the medial inner hair cell region. Thus, the homophilic adhesive property of cadherins alone cannot explain the mosaic cellular patterning. A mathematical model suggested that the checkerboard-like pattern could be generated by a mixture of two cell types, when their heterotypic cell–cell adhesions dominate over their homotypic cell–cell adhesions (Honda et al., 1986). Our previous study showed that the heterophilic interactions of different nectins regulate the checkerboard-like cellular patterning in the mouse auditory epithelium (Togashi et al., 2011). In the mouse cochlea from an early developmental stage, nectin-1 and nectin-3 are complementarily expressed in hair cells and supporting cells, respectively, and become condensed at heterophilic junctions (**Figure 1E**). Molecular interactions occur between nectin-1 on hair cells and nectin-3 on supporting cells, and the majority of these molecules are recruited to heterophilic binding sites, such that these biased cell–cell adhesions contribute to the checkerboard-like pattern formation. Genetic deletion of nectin-1 or nectin-3 causes the redistribution of their heterophilic partners to ectopic sites and induces aberrant attachments between hair cells, resulting in disruption of the checkerboard-like pattern (**Figure 1F**). These observations indicated that nectins play a key role in the formation of the checkerboard-like pattern of hair cells and supporting cells in the auditory epithelium.

MOSAIC PATTERN FORMATION IN THE OLFACTORY EPITHELIUM

The olfactory epithelium, which is located inside the nasal cavity in mammals, is a specialized sensory epithelium involved in odor perception. The olfactory epithelium is a pseudostratified columnar epithelium composed of olfactory cells, supporting cells, and basal cells. These cells are stereotypically layered from the apical to basal side in the olfactory epithelium. When the luminal surface of the olfactory epithelium is observed from the apical side, ciliated olfactory cells and several types of supporting cells are arranged in a specialized mosaic pattern (**Figure 2A**; Cuschieri and Bannister, 1975; Steinke et al., 2008). The most characteristic aspect of this cellular pattern is that small round olfactory cells are interspersed between hexagonal supporting cells. How is this pattern established? During development, the olfactory cells and supporting cells dynamically arrange themselves to form a mosaic pattern (**Figure 2A**; Katsunuma et al., 2016). The immature olfactory cells are initially clustered at the boundary between neighboring supporting cells at an early development stage. Subsequently, the clustered olfactory cells gradually become separated from one another, and each olfactory cell becomes fully surrounded by supporting cells. These observations imply that cellular rearrangements are required for the mosaic patterning in the olfactory epithelium. However, the cellular rearrangements in the developing olfactory epithelium are unlike those in the developing inner ear. As the initial pattern shows segregation of the olfactory cells from the supporting cells, lateral inhibition is not likely to be involved in

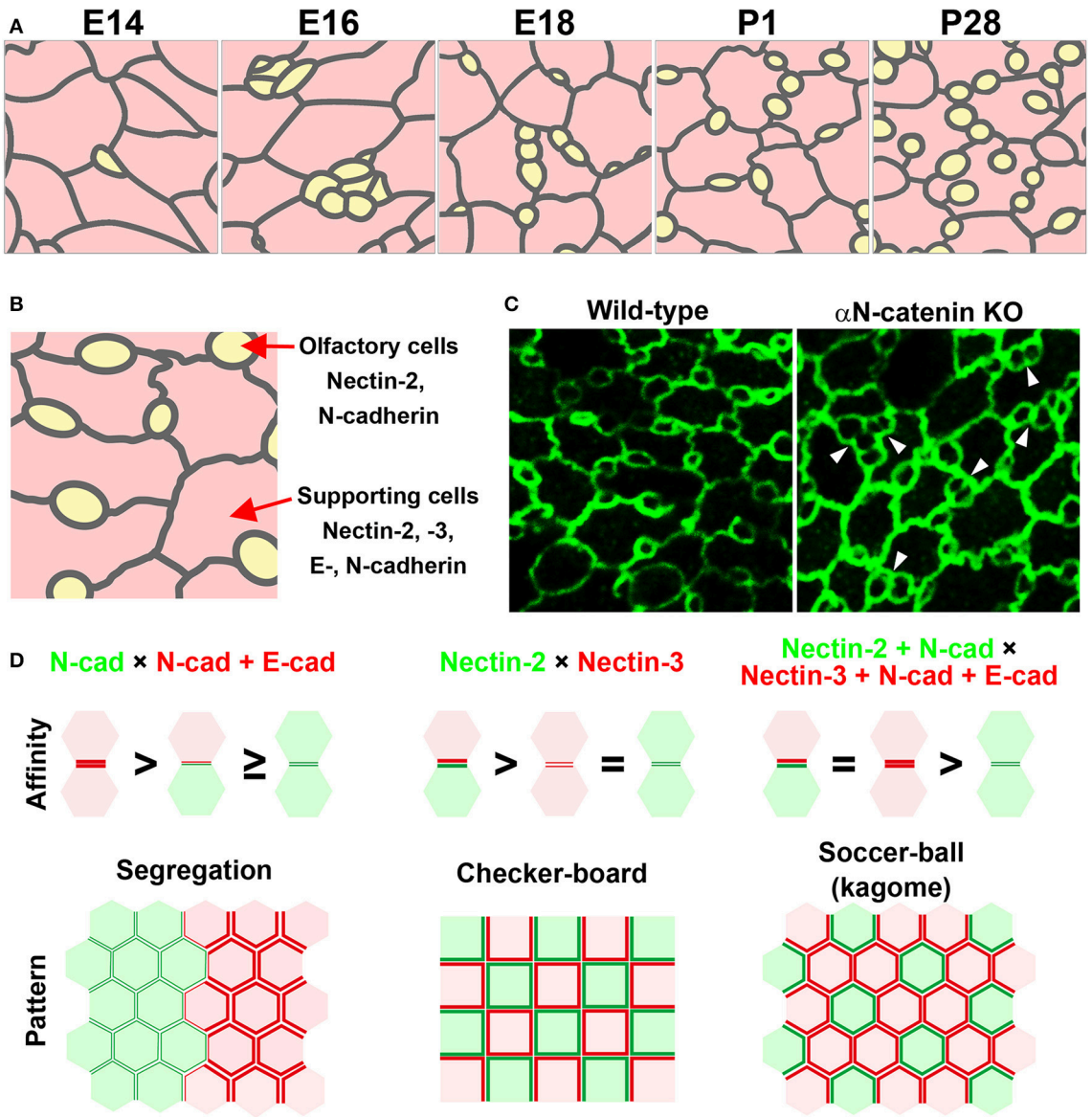

FIGURE 2 | Mosaic cellular pattern in the mouse olfactory epithelium. (A) Schematic illustrations of the apical surface of the mouse olfactory epithelium from embryonic day (E) 14 to postnatal day (P) 28 (Katsunuma et al., 2016). Yellow, olfactory cells; pink, supporting cells. **(B)** Expression pattern of nectins and cadherins in the olfactory epithelium (Katsunuma et al., 2016). **(C)** Cellular patterning in the olfactory epithelia of wild-type and αN-catenin knockout (KO) mice (Katsunuma et al., 2016). Arrowheads point to examples of aberrantly attached olfactory cells. **(D)** Cellular patterns generated by various combinations of cell adhesive affinities (Katsunuma et al., 2016). (Upper) Schematic illustrations of the relative adhesive affinity between the cells. (Lower) Schematic illustrations of the generated cellular patterns.

the mosaic pattern formation. Interestingly, the olfactory cells and supporting cells express different cadherins and nectins (Steinke et al., 2008; Katsunuma et al., 2016). Specifically, the supporting cells express E-cadherin, N-cadherin, nectin-2, and nectin-3, while the olfactory cells express N-cadherin and nectin-2 (**Figure 2B**). What mechanism coordinates the nectin and cadherin adhesion systems in the mosaic cellular patterning? Our recent study showed cooperative actions of nectins and cadherins in the mosaic cellular patterning within the mouse olfactory epithelium. Nectin-2 on olfactory cells interacts with nectin-3 on supporting cells, and this trans-heterophilic interaction promotes homophilic trans-interactions of N-cadherins between the olfactory cells and the supporting cells. The trans-interactions of cadherins at the heterotypic O-S (olfactory cell–supporting cell) boundary are stronger than those at the homotypic O-O (olfactory cell–olfactory cell) boundary, resulting in separation of the olfactory cells. The adhesiveness of the O-S boundary is as strong as that of the S-S (supporting cell–supporting cell)

boundary, because E-cadherin exclusively accumulates in the homophilic S-S junctions. However, the adhesiveness of the O-O boundary is not sufficient to sustain these contacts, resulting in separation of the olfactory cells. Collectively, these findings indicate the involvement of heterophilic binding between nectin-2 on olfactory cells and nectin-3 on supporting cells as well as the selective recruitment of E-cadherin to homophilic interactions between nectin-3-expressing supporting cells. The association of nectins with α-catenin through cytoplasmic interactions is necessary for the efficient clustering of cadherin molecules at cell–cell adhesion sites, and for enhancing the adhesion activity of the clustered cadherin molecules. Genetic deletion of αN-catenin, a subtype of α-catenin that is specifically expressed in the olfactory cells in the olfactory epithelium, causes aberrantly attached of the olfactory cells each other, resulting in disruption of the cellular pattern (**Figure 2C**). The data implicate that intracellular mechanisms implicate in the regulation of the activity of cadherins. Mathematical modeling supports the idea that the strength of adhesion between olfactory cells and supporting cells is greater than that between olfactory cells and equivalent to that between supporting cells, resulting in cellular intercalation of the supporting cells between the olfactory cell junctions. These observations demonstrate that the cooperative action of nectins and cadherins leads to the intercalation of supporting cells between the olfactory cells, resulting in olfactory cell dispersion in the olfactory epithelium, and also suggest that combinatorial expression of nectins and cadherins contributes to the production of the complex cell patterns of sensory organs, which cannot be achieved by a single mechanism (**Figure 2D**).

CONCLUDING REMARKS

Herein, the roles of the cell–cell adhesion molecules nectins and cadherins in the unique cellular pattern formation of sensory organs have been introduced and discussed. Many different types of cells in tissues express various types of cell adhesion molecules. As multiple adhesion systems appear to cooperate at the organogenesis level, it will be of great interest to determine whether they act in parallel or hierarchical manners. As mentioned above, the nectin-dependent differential distribution of cadherins leads to extension or shrinkage of cell–cell junctions, thereby contributing to the cell intercalations and mosaic patterning. However, cooperative mechanisms between nectins, cadherins, and cortical tension are likely to contribute to the production of the complex cell patterns, and our current understanding of the cooperative roles between these mechanisms is insufficient to explain the complex mechanisms underlying cellular patterning. Elucidating the combined mechanisms between differential adhesion and actin–myosin contractility will provide a more detailed picture of cellular patterning. How does the cooperative action of nectins and cadherins regulate actin–myosin contraction and generate differential adhesion? Cell cortical tension is caused by actin–myosin contraction and cell–cell adhesion, and actin cytoskeletal anchoring of cell adhesion molecules is achieved by various actin-binding proteins. Previous studies have shown that mechanical stress on cadherin adhesion complexes modifies their cytoskeletal anchoring strength (Yonemura et al., 2010), and that cadherin oligomerization stiffens these molecules anchored to the actin cytoskeleton (Strale et al., 2015). To understand the mechanism for the production of the complex cell patterns and structures in epithelia, deciphering the intracellular and intercellular signaling mechanisms will provide insights into how the cooperation of cell–cell adhesion and cortical tension contributes to self-organization of cells into tissues.

AUTHOR CONTRIBUTIONS

The author confirms being the sole contributor of this work and approved it for publication.

FUNDING

The author's laboratory was supported by KAKENHI Grant Numbers 25111716, 25127710, 25440107, and 26400205, and by a grant from the Takeda Science Foundation.

ACKNOWLEDGMENTS

The author apologizes to all authors whose work could not be cited because of space constraints. The author thanks S. Katsunuma for critical comments on the manuscript.

REFERENCES

Bertet, C., Sulak, L., and Lecuit, T. (2004). Myosin-dependent junction remodelling controls planar cell intercalation and axis elongation. *Nature* 429, 667–671. doi: 10.1038/nature02590

Chacon-Heszele, M. F., Ren, D., Reynolds, A. B., Chi, F., and Chen, P. (2012). Regulation of cochlear convergent extension by the vertebrate planar cell polarity pathway is dependent on p120-catenin. *Development* 139, 968–978. doi: 10.1242/dev.065326

Chen, P., Johnson, J. E., Zoghbi, H. Y., and Segil, N. (2002). The role of Math1 in inner ear development: uncoupling the establishment of the sensory primordium from hair cell fate determination. *Development* 129, 2495–2505.

Cuschieri, A., and Bannister, L. H. (1975). The development of the olfactory mucosa in the mouse: electron microscopy. *J. Anat.* 119, 471–498.

Fabre, S., Reymond, N., Cocchi, F., Menotti, L., Dubreuil, P., Campadelli-Fiume, G., et al. (2002). Prominent role of the Ig-like V domain in trans-interactions of nectins. Nectin3 and nectin 4 bind to the predicted C-C′-C″-D beta-strands of the nectin1 V domain. *J. Biol. Chem.* 277, 27006–27013. doi: 10.1074/jbc.M203228200

Foty, R. A., and Steinberg, M. S. (2005). The differential adhesion hypothesis: a direct evaluation. *Dev. Biol.* 278, 255–263. doi: 10.1016/j.ydbio.2004.11.012

Friedlander, D. R., Mège, R. M., Cunningham, B. A., and Edelman, G. M. (1989). Cell sorting-out is modulated by both the specificity and amount of different cell adhesion molecules (CAMs) expressed on cell surfaces. *Proc. Natl. Acad. Sci. U.S.A.* 86, 7043–7047. doi: 10.1073/pnas.86.18.7043

Harrison, O. J., Vendome, J., Brasch, J., Jin, X., Hong, S., Katsamba, P. S., et al. (2012). Nectin ectodomain structures reveal a canonical adhesive interface. *Nat. Struct. Mol. Biol.* 19, 906–915. doi: 10.1038/nsmb.2366

Hayashi, T., and Carthew, R. W. (2004). Surface mechanics mediate pattern formation in the developing retina. *Nature* 431, 647–652. doi: 10.1038/nature02952

Heisenberg, C. P., and Bellaïche, Y. (2013). Forces in tissue morphogenesis and patterning. *Cell* 153, 948–962. doi: 10.1016/j.cell.2013.05.008

Honda, H., Yamanaka, H., and Eguchi, G. (1986). Transformation of a polygonal cellular pattern during sexual maturation of the avian oviduct epithelium: computer simulation. *J. Embryol. Exp. Morphol.* 98, 1–19.

Honda, T., Sakisaka, T., Yamada, T., Kumazawa, N., Hoshino, T., Kajita, M., et al. (2006). Involvement of nectins in the formation of puncta adherentia junctions and the mossy fiber trajectory in the mouse hippocampus. *Mol. Cell. Neurosci.* 31, 315–325. doi: 10.1016/j.mcn.2005.10.002

Honda, T., Shimizu, K., Kawakatsu, T., Yasumi, M., Shingai, T., Fukuhara, A., et al. (2003). Antagonistic and agonistic effects of an extracellular fragment of nectin on formation of E-cadherin-based cell-cell adhesion. *Genes Cells* 8, 51–63. doi: 10.1046/j.1365-2443.2003.00616.x

Inagaki, M., Irie, K., Ishizaki, H., Tanaka-Okamoto, M., Morimoto, K., Inoue, E., et al. (2005). Roles of cell-adhesion molecules nectin 1 and nectin 3 in ciliary body development. *Development* 132, 1525–1537. doi: 10.1242/dev.01697

Katsamba, P., Carroll, K., Ahlsen, G., Bahna, F., Vendome, J., Posy, S., et al. (2009). Linking molecular affinity and cellular specificity in cadherin-mediated adhesion. *Proc. Natl. Acad. Sci. U.S.A.* 106, 11594–11599. doi: 10.1073/pnas.0905349106

Katsunuma, S., Honda, H., Shinoda, T., Ishimoto, Y., Miyata, T., Kiyonari, H., et al. (2016). Synergistic action of nectins and cadherins generates the mosaic cellular pattern of the olfactory epithelium. *J. Cell Biol.* 212, 561–575. doi: 10.1083/jcb.201509020

Lanford, P. J., Lan, Y., Jiang, R., Lindsell, C., Weinmaster, G., Gridley, T., et al. (1999). Notch signalling pathway mediates hair cell development in mammalian cochlea. *Nat. Genet.* 21, 289–292. doi: 10.1038/6804

Lecuit, T. (2005). Adhesion remodeling underlying tissue morphogenesis. *Trends Cell Biol.* 15, 34–42. doi: 10.1016/j.tcb.2004.11.007

Martinez-Rico, C., Pincet, F., Perez, E., Thiery, J. P., Shimizu, K., Takai, Y., et al. (2005). Separation force measurements reveal different types of modulation of E-cadherin-based adhesion by nectin-1 and -3. *J. Biol. Chem.* 280, 4753–4760. doi: 10.1074/jbc.M412544200

McKenzie, E., Krupin, A., and Kelley, M. W. (2004). Cellular growth and rearrangement during the development of the mammalian organ of Corti. *Dev. Dyn.* 229, 802–812. doi: 10.1002/dvdy.10500

Meng, W., and Takeichi, M. (2009). Adherens junction: molecular architecture and regulation. *Cold Spring Harb. Perspect. Biol.* 1:a002899. doi: 10.1101/cshperspect.a002899

Mueller, S., Rosenquist, T. A., Takai, Y., Bronson, R. A., and Wimmer, E. (2003). Loss of nectin-2 at Sertoli-spermatid junctions leads to male infertility and correlates with severe spermatozoan head and midpiece malformation, impaired binding to the zona pellucida, and oocyte penetration. *Biol. Reprod.* 69, 1330–1340. doi: 10.1095/biolreprod.102.014670

Nishimura, T., Honda, H., and Takeichi, M. (2012). Planar cell polarity links axes of spatial dynamics in neural-tube closure. *Cell* 149, 1084–1097. doi: 10.1016/j.cell.2012.04.021

Nose, A., Nagafuchi, A., and Takeichi, M. (1988). Expressed recombinant cadherins mediate cell sorting in model systems. *Cell* 54, 993–1001. doi: 10.1016/0092-8674(88)90114-6

Okabe, N., Shimizu, K., Ozaki-Kuroda, K., Nakanishi, H., Morimoto, K., Takeuchi, M., et al. (2004). Contacts between the commissural axons and the floor plate cells are mediated by nectins. *Dev. Biol.* 273, 244–256. doi: 10.1016/j.ydbio.2004.05.034

Ozaki-Kuroda, K., Nakanishi, H., Ohta, H., Tanaka, H., Kurihara, H., Mueller, S., et al. (2002). Nectin couples cell-cell adhesion and the actin scaffold at heterotypic testicular junctions. *Curr. Biol.* 12, 1145–1150. doi: 10.1016/S0960-9822(02)00922-3

Pokutta, S., and Weis, W. I. (2000). Structure of the dimerization and beta-catenin-binding region of alpha-catenin. *Mol. Cell* 5, 533–543. doi: 10.1016/S1097-2765(00)80447-5

Simonneau, L., Gallego, M., and Pujol, R. (2003). Comparative expression patterns of T-, N-, E-cadherins, beta-catenin, and polysialic acid neural cell adhesion molecule in rat cochlea during development: implications for the nature of Kolliker's organ. *J. Comp. Neurol.* 459, 113–126. doi: 10.1002/cne.10604

Steinberg, M. S. (2007). Differential adhesion in morphogenesis: a modern view. *Curr. Opin. Genet. Dev.* 17, 281–286. doi: 10.1016/j.gde.2007.05.002

Steinberg, M. S., and Takeichi, M. (1994). Experimental specification of cell sorting, tissue spreading, and specific spatial patterning by quantitative differences in cadherin expression. *Proc. Natl. Acad. Sci. U.S.A.* 91, 206–209. doi: 10.1073/pnas.91.1.206

Steinke, A., Meier-Stiegen, S., Drenckhahn, D., and Asan, E. (2008). Molecular composition of tight and adherens junctions in the rat olfactory epithelium and fila. *Histochem. Cell Biol.* 130, 339–361. doi: 10.1007/s00418-008-0441-8

Strale, P. O., Duchesne, L., Peyret, G., Montel, L., Nguyen, T., Png, E., et al. (2015). The formation of ordered nanoclusters controls cadherin anchoring to actin and cell-cell contact fluidity. *J. Cell Biol.* 210, 333–346. doi: 10.1083/jcb.201410111

Tachibana, K., Nakanishi, H., Mandai, K., Ozaki, K., Ikeda, W., Yamamoto, Y., et al. (2000). Two cell adhesion molecules, nectin and cadherin, interact through their cytoplasmic domain-associated proteins. *J. Cell Biol.* 150, 1161–1176. doi: 10.1083/jcb.150.5.1161

Takai, Y., Ikeda, W., Ogita, H., and Rikitake, Y. (2008). The immunoglobulin-like cell adhesion molecule nectin and its associated protein afadin. *Annu. Rev. Cell Dev. Biol.* 24, 309–342. doi: 10.1146/annurev.cellbio.24.110707.175339

Takai, Y., and Nakanishi, H. (2003). Nectin and afadin: novel organizers of intercellular junctions. *J. Cell Sci.* 116, 17–27. doi: 10.1242/jcs.00167

Tepass, U., and Harris, K. P. (2007). Adherens junctions in Drosophila retinal morphogenesis. *Trends Cell Biol.* 17, 26–35. doi: 10.1016/j.tcb.2006.11.006

Togashi, H., Kominami, K., Waseda, M., Komura, H., Miyoshi, J., Takeichi, M., et al. (2011). Nectins establish a checkerboard-like cellular pattern in the auditory epithelium. *Science* 333, 1144–1147. doi: 10.1126/science.1208467

Togashi, H., Miyoshi, J., Honda, T., Sakisaka, T., Takai, Y., and Takeichi, M. (2006). Interneurite affinity is regulated by heterophilic nectin interactions in concert with the cadherin machinery. *J. Cell Biol.* 174, 141–151. doi: 10.1083/jcb.200601089

Troyanovsky, R. B., Indra, I., Chen, C. S., Hong, S., and Troyanovsky, S. M. (2015). Cadherin controls nectin recruitment into adherens junctions by remodeling the actin cytoskeleton. *J. Cell Sci.* 128, 140–149. doi: 10.1242/jcs.161588

Whitlon, D. S. (1993). E-cadherin in the mature and developing organ of Corti of the mouse. *J. Neurocytol.* 22, 1030–1038. doi: 10.1007/BF01235747

Yasumi, M., Shimizu, K., Honda, T., Takeuchi, M., and Takai, Y. (2003). Role of each immunoglobulin-like loop of nectin for its cell-cell adhesion activity. *Biochem. Biophys. Res. Commun.* 302, 61–66. doi: 10.1016/S0006-291X(03)00106-2

Yonemura, S., Wada, Y., Watanabe, T., Nagafuchi, A., and Shibata, M. (2010). alpha-Catenin as a tension transducer that induces adherens junction development. *Nat. Cell Biol.* 12, 533–542. doi: 10.1038/ncb2055

Yoshida, T., Miyoshi, J., Takai, Y., and Thesleff, I. (2010). Cooperation of nectin-1 and nectin-3 is required for normal ameloblast function and crown shape development in mouse teeth. *Dev. Dyn.* 239, 2558–2569. doi: 10.1002/dvdy.22395

Zhang, N., Martin, G. V., Kelley, M. W., and Gridley, T. (2000). A mutation in the Lunatic fringe gene suppresses the effects of a Jagged2 mutation on inner hair cell development in the cochlea. *Curr. Biol.* 10, 659–662. doi: 10.1016/S0960-9822(00)00522-4

Zine, A., Aubert, A., Qiu, J., Therianos, S., Guillemot, F., Kageyama, R., et al. (2001). Hes1 and Hes5 activities are required for the normal development of the hair cells in the mammalian inner ear. *J. Neurosci.* 21, 4712–4720.

Conflict of Interest Statement: The author declares that the research was conducted in the absence of any commercial or financial relationships that could be construed as a potential conflict of interest.

frontiers in Cell and Developmental Biology

REVIEW
published: 14 September 2017
doi: 10.3389/fcell.2017.00081

Intermediate Filaments at the Junction of Mechanotransduction, Migration, and Development

*Rucha Sanghvi-Shah and Gregory F. Weber**

Department of Biological Sciences, Rutgers University-Newark, Newark, NJ, United States

Mechanically induced signal transduction has an essential role in development. Cells actively transduce and respond to mechanical signals and their internal architecture must manage the associated forces while also being dynamically responsive. With unique assembly-disassembly dynamics and physical properties, cytoplasmic intermediate filaments play an important role in regulating cell shape and mechanical integrity. While this function has been recognized and appreciated for more than 30 years, continually emerging data also demonstrate important roles of intermediate filaments in cell signal transduction. In this review, with a particular focus on keratins and vimentin, the relationship between the physical state of intermediate filaments and their role in mechanotransduction signaling is illustrated through a survey of current literature. Association with adhesion receptors such as cadherins and integrins provides a critical interface through which intermediate filaments are exposed to forces from a cell's environment. As a consequence, these cytoskeletal networks are posttranslationally modified, remodeled and reorganized with direct impacts on local signal transduction events and cell migratory behaviors important to development. We propose that intermediate filaments provide an opportune platform for cells to both cope with mechanical forces and modulate signal transduction.

Keywords: intermediate filaments, development, migration, mechanotransduction, tension, keratin, vimentin

OPEN ACCESS

Edited by:
Takaaki Matsui, Nara Institute of Science and Technology, Japan

Reviewed by:
Kensaku Mizuno, Tohoku University, Japan
Thomas Magin, Leipzig University, Germany

****Correspondence:***
Gregory F. Weber
gregory.weber@rutgers.edu

Specialty section:
This article was submitted to Cell Adhesion and Migration, a section of the journal Frontiers in Cell and Developmental Biology

Received: *30 June 2017*
Accepted: *30 August 2017*
Published: *14 September 2017*

Citation:
Sanghvi-Shah R and Weber GF (2017) Intermediate Filaments at the Junction of Mechanotransduction, Migration, and Development. Front. Cell Dev. Biol. 5:81. doi: 10.3389/fcell.2017.00081

INTRODUCTION

The last decade has brought a newfound recognition for the role of physical force on stimulating adhesion responses in cells, activating signal transduction pathways, and regulating cellular functions. These physical forces are recognized to be both externally and internally derived. Since the actomyosin machinery is seen as the primary means by which cells generate force, the focus of the research community thus far has largely been on the tripartite relationship between actin-myosin cytoskeleton, physical parameters such as force, and associated signal transduction pathways.

Interestingly, although it is well-accepted that the intermediate filaments provide mechanical integrity to cells, the relationship of intermediate filaments to mechanotransduction processes continues to be a new frontier ripe for exploration. Intermediate filaments remain the least well-understood of the three major cytoskeletal networks. Intermediate filament polymerization-depolymerization regulation, impact to cell signaling pathways and role in tension management within the cell have only just begun to be investigated. Findings to date provide good reason to anticipate an integral role for intermediate filaments in cellular processes where signal transduction and cellular mechanics converge.

In this review article, we provide a summary overview of what is currently known about cytoplasmic intermediate filaments and their regulation. The interplay of intermediate filaments with the cellular adhesive network is highlighted through multicellular behaviors such as migration. These cellular functions are put into physiological context by examining their contributions to embryonic development. We suggest that cytoplasmic intermediate filaments are load-bearing components within cells that both effect and are affected by cells' physical environments. That is, intermediate filaments are a centerpiece intracellular component of cell signaling events due to mechanical stimuli.

CYTOPLASMIC INTERMEDIATE FILAMENTS-GENERAL OVERVIEW

Cytoplasmic intermediate filaments belong to a superfamily of highly conserved proteins (∼65 genes; Hesse et al., 2001) unique to metazoan species (Herrmann and Strelkov, 2011). These members of the intermediate filament family likely originated through the divergence of the more ubiquitously expressed, yet highly conserved, nuclear intermediate filaments—the lamins (Dodemont and Riemer, 1990; Döring and Stick, 1990; Peter and Stick, 2015; Hering et al., 2016). The expression and assembly of these 10–12 nm filament forming cytoplasmic proteins is developmentally regulated in a cell-, tissue-, and context-dependent manner. Based upon their expression pattern, structure, and sequence identity, cytoplasmic intermediate filament proteins are classified into five different gene families (**Table 1**), with a sixth intermediate filament family comprised of lamins which reside in the nucleus (Type V). Type I and II consist of the keratins, which are intermediate filaments highly expressed by epithelia. Notably keratins are also expressed by several non-epithelial cell types and, of particular relevance to this review, are the earliest expressed intermediate filament types during embryogenesis (Franz et al., 1983; Lehtonen et al., 1983). In humans, keratins are encoded by 28 genes for Type I members and 26 genes for Type II members on only two loci (Hesse et al., 2001). While mice have a similar number of keratin genes, the number of keratin genes varies with species, with organisms lower on the phylogenic tree exhibiting fewer keratin genes. For instance, at the other end of the spectrum a single Type I-Type II keratin pair of genes exists in the sea squirt *Ciona intestinalis*, a difference indicative of the evolutionary expansion of keratins through gene duplication (Hesse et al., 2001; Karabinos et al., 2004). Type III intermediate filaments are intermediate filaments, such as vimentin and desmin, that can form homopolymers and also heteropolymers with other Type III intermediate filament proteins. Type IV intermediate filaments are expressed mostly by neurons and muscle and includes the various neurofilament subtypes, nestin and synemin. Type VI includes CP49/phakinin and filensin, which are lens-specific intermediate filaments. Although, CP49 can self-assemble *in vitro*, *in vivo* CP49 and filensin together form heteroligomeric filaments (Goulielmos et al., 1996). Here we will primarily focus on Type I-III cytoplasmic intermediate filaments, with special emphasis on keratin and vimentin, because of the emerging evidence for their influence over signal transduction, cellular function in a wide variety of cell types, and role in embryonic development.

TABLE 1 | General classification of intermediate filament proteins.

Intermediate filament type	General categorization	Intermediate filament protein members
Type I	Acidic Keratins	Acidic Keratins (28 genes in humans)
Type II	Basic Keratins	Basic Keratins (26 genes in humans)
Type III	Homodimerizing intermediate filaments, some capability of heterodimerizing	Vimentin, Desmin, GFAP
Type IV	Intermediate filaments mainly expressed in neurons and muscle	Neurofilaments, Nestin, Synemin
Type V	Nuclear intermediate filaments	Lamins
Type VI	Lens-specific beaded intermediate filaments	Phakinin (CP49), Filensin

All cytoplasmic intermediate filament proteins share a common tripartite molecular structure. Intermediate filament monomers are dominated by a conserved central α-helical domain (∼310 amino acids) flanked by highly variable non-α-helical head and tail domains. Variability in the amino terminal head domain and the carboxy terminal tail domains account for much of the diversity, specificity, and regulation of intermediate filaments. Meanwhile, the central domain is the primary dimerization region. The central rod domain is periodically interrupted by linker domains (L1 and L12) thus forming four helical subdomains (coil 1A, coil 1B, coil 2A, and coil 2B) capable of forming coiled-coils (Geisler and Weber, 1982; Nicolet et al., 2010; Chernyatina et al., 2012). These sub-helices are predominantly rich in heptad repeats $(abcdefg)_n$ where a & d are the small apolar residues (Leu, Ile, Met, or Val). This amphipathic nature of the intermediate filament monomers allows them to readily form highly stable, parallel α-helical coiled-coil dimers without the assistance of any nucleating proteins *in vitro* (Quinlan et al., 1986).

Over the last few decades, several laboratories have elucidated the general mechanism for intermediate filament assembly *in vitro*. Cytoplasmic intermediate filament protein dimers laterally associate in an antiparallel fashion to form apolar tetramers. Once formed, tetramers further align to form unit length filaments (ULF's) that anneal longitudinally to yield long, flexible filaments, and subsequently undergo radial compaction to yield non-polar 10 nm filaments (Herrmann et al., 1996, 1999; Sokolova et al., 2006; Kirmse et al., 2007). Keratins spontaneously form obligate heterodimers from one Type I and one Type II intermediate filament protein (Steinert et al., 1976), whereas vimentin forms homopolymers (Steinert et al., 1981b). In both instances, nucleation and polymerization can occur without aid from co-factors or nucleoside triphosphates (Herrmann et al., 2004). Although, keratin heteropolymers can be formed from any combination of Type I acidic keratins and Type II basic keratins *in vitro*, assembly kinetics do show preferential pairing (Hatzfeld and Franke, 1985). Indeed, specific

pairs of keratins are expressed *in vivo* (Franke et al., 1981) that parallel these assembly preferences. Such *in vitro* assembly studies of intermediate filaments, in addition to their remarkable insolubility in physiological buffers during *in vitro* experiments and resilient mechanical properties, led to the initial notion that intermediate filaments form stable networks in the cytoplasm.

While intermediate filament assemblages certainly have noteworthy physical properties, their assembly and disassembly are hardly static, unregulated, nor inconsequential to cell function. Contrary to *in vitro* assembly observations, *in vivo* pulse chase experiments suggest that intermediate filaments assemble from a soluble pool of tetrameric intermediate filament precursors/subunits (Blikstad and Lazarides, 1983; Soellner et al., 1985; Schwarz et al., 2015). Despite the tendency toward polymerization *in vitro*, in living cells intermediate filament proteins coexist both in filamentous form and as detergent-soluble filament precursors, of various varieties, including tetramers, ULFs, "particles," and "squiggles"-short filamentous structures (Yoon et al., 1998, 2001; Schwarz et al., 2015). Intermediate filament precursors are most apparent in the peripheral region and protrusions of cells (Prahlad et al., 1998; Yoon et al., 1998, 2001; Helfand et al., 2002; Schwarz et al., 2015). As intermediate filament particles are transported, a subset of these are selected to elongate to short filaments otherwise known as squiggles and further assemble into mature filaments, finally incorporating into the network (Yoon et al., 1998; Windoffer et al., 2011; Schwarz et al., 2015). Cytoplasmic intermediate filaments establish complex networks that form a central cage like structure encapsulating the nucleus and further radiates toward the cell periphery (Franke et al., 1978a,b). Strikingly, when both the keratin and vimentin intermediate filaments are expressed in a cell type they display distinct spatial organization of intermediate filament arrays (Osborn et al., 1980). Typically keratin intermediate filaments are packaged into bundles called tonofibrils (Steinert et al., 1981a) and also form bifurcations (Nafeey et al., 2016). On the other hand, vimentin intermediate filaments are loosely arranged in a parallel or crisscross fashion forming a fine mesh network (Goldman et al., 1986). Polymerized filaments either become a part of the existing peripheral keratin intermediate filament network or get disassembled. Depolymerized precursors may be recycled in the cytoplasm and readied for the next cycle of assembly and disassembly or else undergo ubiquitin-mediated proteasomal degradation. Evidence points to a soluble pool of intermediate filament subunits as an important resource for the remodeling of intermediate filament networks. Keratin cycling uses disassembled soluble subunits for filament renewal, since inhibition of protein synthesis does not abolish filament formation nor subunit exchange (Kolsch et al., 2010). Similar cycling mechanisms are also seen for vimentin intermediate filaments, where vimentin precursors are translocated to the peripheral region of the spreading cells and display a stepwise formation of intermediate filaments (Prahlad et al., 1998).

In addition to dynamic assembly of intermediate filaments, established intermediate filament networks are subject to marked remodeling. Live imaging studies highlight the dynamic and motile properties of the intermediate filament networks and clearly show that vimentin and keratin fibrils exhibit undulations while constantly changing their configurations, appearing to collapse, extend, and translocate over relatively short time intervals (Ho et al., 1998; Yoon et al., 1998; Windoffer and Leube, 1999). At the subunit level, the dynamic exchange of intermediate filament dimers is ever more complex. Predictably, severing and end-to-end annealing are major mechanisms for elongation and refurbishment of filaments (Prahlad et al., 1998; Wöll et al., 2005; Winheim et al., 2011; Hookway et al., 2015). Breaking with typical models of filament polymerization however, data show that intermediate filament subunits can also be added and removed from the entire length of the preformed filament as a mechanism for intermediate filament turnover (Ngai et al., 1990; Coleman and Lazarides, 1992; Vikstrom et al., 1992). Microinjection of soluble biotinylated keratin and vimentin (Vikstrom et al., 1989; Miller et al., 1991) and rhodamine-tagged vimentin followed by Fluorescence Recovery After Photobleaching (FRAP) analyses revealed that these subunits can rapidly incorporate in a well-established network (Vikstrom et al., 1992). Exchange of intermediate filament subunits is non-polar and occurs along the entire length of the intermediate filament. Nevertheless, subunit swapping is highly dependent on the availability of a soluble pool. Collectively, this suggests that established intermediate filaments exhibit unique dynamic properties that allow for turnover of subunits, along with severing and end-to end annealing to maintain length and flexibility of the preformed filaments without compromising their structural integrity. Factors regulating and facilitating processes such as severing, reannealing and subunit exchange are largely unknown and the underlying molecular mechanisms demand further attention given the disparate assembly dynamics *in vitro* compared to *in vivo*. As with their actin and microtubule counterparts, we speculate that a host of intermediate filament binding proteins that modulate polymerization are waiting to be elucidated.

Despite the ability of keratin and vimentin to polymerize so readily, cells clearly have regulatory controls that determine when and where intermediate filaments will form. A variety of post-translation modifications (PTMs) of intermediate filaments such as phosphorylation, ubiquitylation, acetylation, and sumoylation are emerging as crucial controllers of intermediate filament dynamics, stability, and function (**Table 2**; for review see Snider and Omary, 2014). Phosphorylation status of cytoplasmic intermediate filaments is modulated by various kinases and phosphatases (Omary et al., 2006) depending upon the intermediate filament protein involved, cell and tissue type and specific physiological condition. Such phosphorylation/dephosphorylation events in general affect their conformation, solubility, filament organization, and interaction with other signaling molecules consequently translating into various cellular functions. Site-specific serine/threonine phosphorylation of the head and tail region of intermediate filaments facilitate their structural reorganization mainly by promoting intermediate filament solubility. Conversely, tyrosine phosphorylation of the rod domain (Tyr 267) of K8 facilitates their proper filament formation and renders them insoluble (Snider et al., 2013b). Different PTMs on intermediate filaments

TABLE 2 | Post-translational modifications of cytoplasmic intermediate filaments.

Post-translational modification	General effect on intermediate filament	References
Ser/Thr phosphorylation	Increases intermediate filament solubility	Omary et al., 2006; Snider and Omary, 2014
Tyr phosphorylation	Promotes keratin insolubility	Snider et al., 2013b
Ser phosphorylation	Induces compartmentalization of intermediate filaments	Chou et al., 1991; Ku et al., 2002; Toivola et al., 2002; Zhou et al., 2006
Sumoylation	Alters filament dynamics	Snider et al., 2011
Acetylation	Promotes formation of dense perinuclear network	Snider et al., 2013a
Glycosylation	Protects against stress and injury	Ku et al., 2010
Ubiquitylation	Regulates intermediate filament degradation and turnover	Ku and Omary, 2000

can serve as docking sites for protein complexes and allow for altered assembly dynamics or rearrangements of the network. For example, the chaperone protein Hsp27 interacts with K8 in a phosphorylation dependent manner (Kayser et al., 2013). Hsp27 manages keratin inter-filament interactions by inhibiting extensive bundling of filaments (Kayser et al., 2013), in essence by acting as a steric "spacer." Such phosphorylation events not only correlate with, but have a functional role in cellular events such as mitosis, cell migration, cell growth, and stress-mediated responses. Spatiotemporal localization of intermediate filaments is phosphorylation dependent. Different forms of intermediate filament proteins (e.g., non-filamentous particles vs. filaments) reside in different subcellular compartments. During distinct cellular processes such as mitosis, site-specific hyperphosphorylation of cytoplasmic intermediate filaments, as determined by phospho-specific antibody labeling, affect their organization and distribution (Chou et al., 1991; Toivola et al., 2002). Epitope-specific phosphorylation can also segregate intermediate filaments to different compartments within a cell. In pancreatic acinar cells, K18 phosphorylated on Ser33 is necessary for specifically basal filament organization while the non-phosphorylated K18 localizes to the apical domain by default (Ku et al., 2002). Moreover, similar site-specific intermediate filament phosphorylation can be limited to specific cells within a tissue. For example, K20 Ser13 phosphorylation occurs specifically in small intestine goblet cells but not in other K20 expressing enterocytes (Zhou et al., 2006).

Phosphorylation of intermediate filaments promotes other PTMs, such as sumoylation of keratins. Both keratins and vimentin are extensively modified by SUMO2 and SUMO3 *in vitro,* at multiple conserved rod domain sites. Monosumoylation of keratin increases protein solubility whereas hypersumoylation decreases it (Snider et al., 2011). Thus, sumoylation similar to phosphorylation is crucial for regulating solubility of cytoplasmic intermediate filaments. Similarly, acetylation of the conserved Lys residue (Lys 207) in the rod domain of K8 also decreases K8 solubility. Acetylation thus promotes the formation of a dense perinuclear intermediate filament network formation altering the mechanical properties of filaments (Snider et al., 2013a). A plausible reciprocal relationship exists between glycosylation and phosphorylation PTMs of intermediate filaments (Ku et al., 1996). Glycosylation of K18 (on Ser30/31/49 in the head domain) behaves as a cytoprotective PTM during stress and injury (Ku et al., 2010), whereas ubiquitylation is frequently detected in the context of hyperphosphorylated intermediate filaments. Ubiquitination of intermediate filament proteins promotes intermediate filament turnover; for example, increased K8 and K18 synthesis and phosphorylation predisposes these proteins to ubiquitination-dependent degradation (Ku and Omary, 2000). Thus, different PTMs by themselves or in combination not only alter the intermediate filament organization but also influence the recruitment of intermediate filament accessory proteins, in a context dependent fashion which subsequently regulate various cellular processes.

INTERMEDIATE FILAMENTS AND THE ESTABLISHMENT OF A CELLULAR ARCHITECTURAL FRAMEWORK

Throughout development, cells both exert and are subject to an array of forces. These physical interactions are initiated not only by the extra-organismal environment, but also by neighboring cells and extracellular matrix. To maintain the integrity of multicellular tissues, cells must (1) avoid rupturing due to mechanical strain and (2) remain adherent to one another. Intermediate filaments have unique features that not only distinguish them from the other two cytoskeletal elements, actin and microtubules, but also make them major contributors in providing mechanical resistance to the cells (**Table 3**). The persistence length of intermediate filaments is much shorter than both actin microfilaments and microtubules, thus classifying them as flexible polymers (Gittes et al., 1993; Mücke et al., 2004; Schopferer et al., 2009; Lichtenstern et al., 2012; Nöding et al., 2014; Pawelzyk et al., 2014). Cytoplasmic filaments along with being flexible and elastic are also highly extensible and can be stretched ∼2.8-fold without rupturing (Kreplak et al., 2005). Microfilaments and microtubules are more fragile and tend to rupture at strains <50% (Janmey et al., 1991). Furthermore, intermediate filaments exhibit strain-induced strengthening without catastrophic failure, making them very suitable as intracellular load bearing springs (Ackbarow et al., 2009; Pawelzyk et al., 2014). Both *in vitro* and *in vivo* analyses corroborate this conceptual model of intermediate filaments as important contributors to cells' elasticity and tensile strength (Janmey et al., 1991; Ma et al., 1999; Fudge et al., 2008; Nolting et al., 2015). The dominant function of intermediate filaments in defining cell stiffness is emphasized in keratinocytes devoid of the entire keratin cytoskeleton (Ramms et al., 2013; Seltmann et al., 2013a). Indirect perturbation of cytoplasmic intermediate filaments likewise has detrimental effects on cell stiffness. Cells exposed to lipids such as sphingosylphosphorylcholine (SPC), induce perinuclear reorganization of keratins through site-specific phosphorylation, leading to a marked decrease in the elastic modulus (Beil et al., 2003). Studies using keratin mutants that either mimic or abrogate phosphorylation of

TABLE 3 | Comparison of the mechanical properties of cytoskeletal elements.

	Keratin intermediate filaments	Vimentin intermediate filaments	Actin filaments	Microtubules
	Lp<L (flexible)		Lp∼L (semi flexible)	Lp>>L (rigid)
Persistence length (Lp)	0.3–0.65 μm Lichtenstern et al., 2012; Pawelzyk et al., 2014	0.4-2 μm Mücke et al., 2004; Schopferer et al., 2009; Lin et al., 2010; Nöding et al., 2014	18 μm Gittes et al., 1993	1,000–5,000 μm Gittes et al., 1993
Contour length	10–20 μm	10–20 μm	≤1 μm	5–15 μm
Extensibility	∼280^{+}% Kreplak et al., 2005	∼300% Qin et al., 2009	∼20% Janmey et al., 1991 ∼200% (native stress fibers) Labouesse et al., 2016	∼50% Janmey et al., 1991

keratins at specific sites further underscore the importance of phosphorylation on the mechanical properties of intermediate filaments (Fois et al., 2013; Homberg et al., 2015). Although tensile strength is most often attributed to the keratin filaments present in epithelial cells, vimentin also contributes to structural integrity, such that cell stiffness is reduced in vimentin depleted or disrupted cells (Wang and Stamenović, 2000; Gladilin et al., 2014; Sharma et al., 2017) and stiffness is increased in cells overexpressing vimentin (Liu et al., 2015). Vimentin further protects fibroblasts against compressive strain (Mendez et al., 2014).

Along with maintaining the general mechanical integrity of the cytoplasmic volume, cytoplasmic intermediate filaments are also vital determinants of intracellular organelle organization. Vimentin plays a critical role in influencing actin and Rac1 driven (Dupin et al., 2011; Matveeva et al., 2015) localization of cytoplasmic organelles such as endoplasmic reticulum, Golgi complex, nucleus, and mitochondria (Gao and Sztul, 2001; Nekrasova et al., 2011; Guo et al., 2013). In *Xenopus laevis,* vimentin intermediate filaments form a cage around melanophores and are involved in their transport and localization at distinct sites within the cells (Chang et al., 2009). Vimentin intermediate filaments are also involved in endoplasm spreading (Lynch et al., 2013). Nuclear position and shape have emerged as important downstream outcomes of mechanical stimuli. Changes in nuclear position relative to other organelles can determine cell polarity, and modulation of nuclear shape influences gene expression and stability. Cytoplasmic intermediate filaments physically link to the nuclear envelope via plectin (an intermediate filament-interacting protein) and SUN/nesprin complexes, also known as Linker of Nucleoskeleton and Cytoskeleton (LINC) complexes (Wilhelmsen et al., 2005; Ketema et al., 2007; Burgstaller et al., 2010). Targeted deletion of nesprin-3 or expression of dominant negative nesprin alters perinuclear intermediate filament organization, cell polarization, and migration (Lombardi et al., 2011; Morgan et al., 2011; Postel et al., 2011). Plectin knockout or plectin mutations related to severe skin blistering disease (epidermolysis bullosa simplex) impair perinuclear keratin architecture, but not the linkages to the nucleus, nonetheless leading to misshapen nuclei and abnormal nuclear deformability (Almeida et al., 2015).

At the cell periphery, adhesions to neighboring cells and the surrounding extracellular matrix provide the interface with which cells interact. Intermediate filaments are most commonly known to be anchored to adjacent cells by desmosomes and to the extracellular matrix by hemidesmosomes. The classic view is that intermediate filaments simply provide internal scaffolding attachments to desmosome and hemidesmosome complexes, adhesive junctions that convey relatively long term associations between a cell and its environment. However, the association of keratin intermediate filaments with desmosomes and hemidesmosomes is also mechanistically supportive of the molecular adhesive complex. That is, keratin filaments can promote the formation and maintenance of desmosomes and hemidesmosomes (Kröger et al., 2013; Seltmann et al., 2015; Loschke et al., 2016). Reciprocally, desmosomal adhesions act as organizing centers for *de novo* keratin network formation in native state tissues (Jackson et al., 1980; Schwarz et al., 2015).

In addition to this classical view of intermediate filaments associating with hemidesmosomes and desmosomes, intermediate filaments interact with cell adhesions often inaccurately believed to be exclusively actin-linked, including junctions mediated by classical cadherins (Kim et al., 2005; Leonard et al., 2008; Weber et al., 2012) and focal adhesions (Tsuruta and Jones, 2003; Windoffer et al., 2006). Association of the intermediate filaments with these otherwise actin-linked adhesions is bolstered in response to physical forces applied to these adhesions (Tsuruta and Jones, 2003; Weber et al., 2012). As with desmosomes and hemidesmosomes, intermediate filaments modify the stability of actin-linked focal adhesions and classical cadherin adhesions. In endothelial cells, vimentin regulates the size and adhesive strength of focal adhesions (Tsuruta and Jones, 2003; Bhattacharya et al., 2009). Vimentin is also implicated in the regulation of vesicular transport of integrin toward the cell membrane (Ivaska et al., 2005).

Intermediate filaments are physically linked to these various adhesion complexes. Vimentin intermediate filaments interact with integrins either directly with binding to β3 integrin tail (Kim et al., 2016) or indirectly via linker proteins including plectin (Bhattacharya et al., 2009; Burgstaller et al., 2010; Bouameur et al., 2014) and BPAG (bullous pemphigoid antigens 1 and 2) by forming dynamic linkages with plakin repeat domains (Fogl et al., 2016). In *X. laevis* mesendoderm (also known as anterior

head mesoderm) cells, plakoglobin acts as recruitment signal for keratin intermediate filament association with cadherins (Weber et al., 2012). Similarly, in endothelial cells p120 catenin recruits vimentin intermediate filaments to cadherins (Kim et al., 2005). Both vimentin and keratin precursor assembly show dependence on focal adhesions as recruitment sites for motile precursors (Burgstaller et al., 2010). Tethering of adhesion complexes to intermediate filaments presents an ideal circumstance wherein intermediate filaments can serve as mediators of both tension and the coincident signaling that we now know occurs as a function of these adhesions.

Although intermediate filaments, microtubules and actin cytoskeletal networks are often viewed as three separate entities, these filamentous arrays cooperatively interact in more ways than not. Actin filaments and microtubules both have impacts on intermediate filament organization through multiple direct, indirect and steric interactions. Bidirectional motility of both mature filaments and their non-filamentous precursors of intermediate filaments can occur on either microtubules or actin microfilaments (Prahlad et al., 1998; Helfand et al., 2002; Liovic et al., 2003; Wöll et al., 2005; Kölsch et al., 2009; Hookway et al., 2015). The filament network used to transport intermediate filament precursors is entirely dependent on context. Neither keratin nor vimentin seems to be exclusively limited to microtubules or actin. Motility of intermediate filament precursors can be both fast and slow, in retrograde and anterograde. Although the mechanism of transport seems to be well-defined in some cases (e.g., entirely dependent on actin or microtubules), defining trends have yet to emerge that reliably predict a mechanism of transport for intermediate filaments. Actin filaments are essential to retrograde motility of keratin precursors in some epithelial cells (Kölsch et al., 2009), yet actin cytoskeleton can restrict microtubule-dependent vimentin precursor movement, establishing a complex three-way cytoskeletal communication (Robert et al., 2014). Perturbing either microtubules, microfilaments, or their associated molecular motors can lead to intermediate filament collapse (Knapp et al., 1983; Wöll et al., 2005). Absence of vimentin intermediate filaments alters the microtubule network orientation, thus suggesting a function of vimentin in organizing the cytoskeletal architecture necessary for cell polarity (Shabbir et al., 2014; Liu et al., 2015). In addition, vimentin filaments, but not "non-filamentous" vimentin negatively regulate actin stress fiber assembly and contractility (Jiu et al., 2017). *In vitro* and *in vivo* studies have highlighted direct interactions between the tail domain of vimentin and actin (Cary et al., 1994; Esue et al., 2006). Furthermore, numerous cytoskeletal linkers have been identified that allow for indirect interaction among the cytoskeletal polymers. These proteins include plectin (Svitkina et al., 1996; Osmanagic-Myers et al., 2015), myosin (Kölsch et al., 2009; Robert et al., 2014), fimbrin (Correia et al., 1999), filamin A (Kim et al., 2010), kinesin (Prahlad et al., 1998; Kreitzer et al., 1999), adenomatous polyposis coli (APC; Sakamoto et al., 2013), dynein, and dynactin (Helfand et al., 2002). Along with distinct cytoskeletal entities interacting with one another, vimentin and keratin intermediate filament networks have been observed to interact at the helical 2B domain of vimentin, and mutations in this region negatively impact collective cell migration (Velez-delValle et al., 2016).

Some data suggest specific roles for each of the cytoskeletal networks in how a cell normally manages different physical forces and stresses. And yet when systems are disrupted, cells often find ways to compensate using the available "protein toolkit." Mechanical probing of fibroblasts shows that actin contributes to cortical stiffness, whereas vimentin dominates cytoplasmic stiffness (Guo et al., 2013). Disruption of vimentin intermediate filaments mandates that cells find other ways of dealing with imposed forces. In some cases, cells compensate to accommodate self-generated forces by increasing actin stress fibers and myosin activity to facilitate ECM substrate traction while exhibiting disruption of cell-cell adherens junctions (Osmanagic-Myers et al., 2015; Jiu et al., 2017). In response to increased externally-derived physical strain and mechanosensing of these forces, keratins can promote stress fiber formation and cell stiffness by activation of ROCK signaling pathway (Bordeleau et al., 2012). These data illustrate great versatility in how cells use the cytoskeletal networks available to facilitate adhesion, cohesion, and balance intracellular tension and externally-derived stresses. In the context of the complex multicellular animal, keratin, and vimentin establish an important scaffolding framework inside the cell. Cytoplasmic intermediate filaments enable the cells to resist deformation, localize organelles, change shape, and are integrally coupled to adhesion complexes (**Figure 1**).

INTERMEDIATE FILAMENTS AND MODULATION OF SIGNAL TRANSDUCTION PATHWAYS

Intriguingly, a wide range of findings suggest that functions of intermediate filaments extend well beyond the mechanical and structural to direct participation in signal transduction. Interactions between cytoplasmic intermediate filaments and other cellular proteins initiate signaling cascades that regulate responses to process such as growth, migration, and apoptosis—all cellular processes fundamental to development and embryogenesis.

Cytoplasmic intermediate filaments differentially regulate cellular adhesions through effecting signaling pathways. Vimentin intermediate filaments promote the formation, maturation, and adhesive strength of maturing focal adhesions (Tsuruta and Jones, 2003; Bhattacharya et al., 2009; Burgstaller et al., 2010; Lynch et al., 2013; Liu et al., 2015). Vimentin regulates VAV2, a Rac1 GEF, phosphorylation, and localizes phosphorylated VAV2 to focal adhesions to promote Rac1-mediated focal adhesion kinase (FAK) stabilization, which further stabilizes focal adhesions (Havel et al., 2015). PKCε-mediated phosphorylation of vimentin governs efficient β1-integrin recycling and motility (Ivaska et al., 2005), whereas Cdc2-mediated vimentin phosphorylation promotes β1-integrin activation, leading to FAK phosphorylation (Chang et al., 2012). Likewise, keratins dynamically regulate focal adhesions through integrin/FAK-dependent signaling mediated either via PKCδ or Akt signaling (Bordeleau et al., 2010; Sankar et al., 2013).

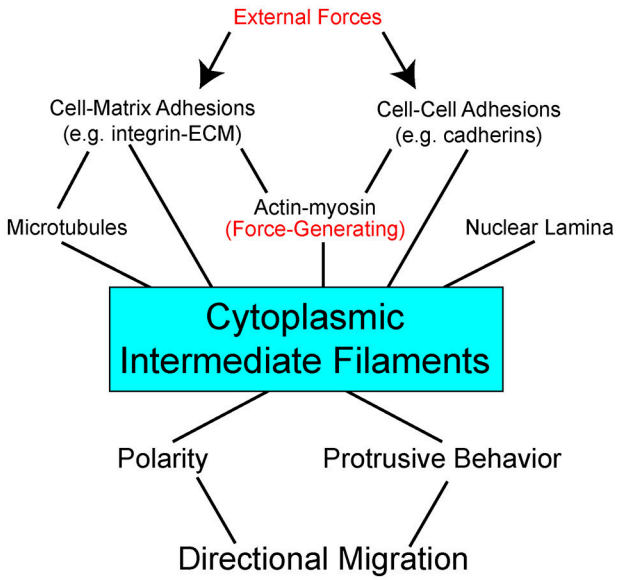

FIGURE 1 | Interdependent network model of cytoplasmic intermediate filaments as a centerpiece between mechanical stimuli and directional cell migration. External forces act on (arrows) adhesion molecules on the cell surface to impact a complex network of bidirectional interactions within the cell (lines). Adhesions are linked to the three major cytoskeletal networks. Of these, actin with its myosin motors is the primary force-generating apparatus. Intermediate filaments can be pre-stressed by actomyosin generated tension. Intermediate filaments also act to resist strains imposed on the cell. Through modulation of cell signaling pathways, direct and indirect, intermediate filaments effect cell polarity and protrusive behavior. Stabilization of distinct subcellular locales promotes persistent directional migration.

Reciprocally, during collective cell migration FAK is required for cadherin-dependent keratin intermediate filament organization (Bjerke et al., 2014). Keratins display isotype-specific signaling functions and unique gene expression patterns of keratins can control stability and dynamics of adhesion complexes. For example, K5/K14 inhibit PKCα-mediated phosphorylation of desmoplakin via RACK1 and thus promote stability and maintenance of desmosomal junctions (Kröger et al., 2013). K6 similarly suppresses cell motility by sequestering Src from being activated and targeting focal adhesions (Rotty and Coulombe, 2012). In contrast, induction of K6/K17 expression produces PKCα-mediated desmosome disassembly (Loschke et al., 2016). Intermediate filaments are tightly coupled with signaling pathways to modulate cellular adhesions.

An ever increasing number of studies implicate intermediate filaments as signaling platforms and as scaffolds for signaling proteins. In fibroblasts, intermediate filament-associated plectin molecules sequester RACK1 on intermediate filaments to modulate PKCδ function (Osmanagic-Myers and Wiche, 2004). Similarly, in keratinocytes, plectin-mediated concentration of RACK1 further regulates ERK1/2 pathway (Osmanagic-Myers et al., 2006). In HER2 positive tumors, a positive feedback loop exists which induces K19 expression via HER2/ERK and further stabilizes HER2 on cell membrane by Akt mediated phosphorylation of K19 on Ser35 (Ju et al., 2015). Keratin 19 is also involved in shuttling β-catenin/Rac1 complex into the nucleus and thus modulating NOTCH signaling pathway in breast cancers (Saha et al., 2017). Collectively, these results support numerous scaffolding roles for keratin intermediate filaments. Vimentin intermediate filaments also function as scaffolds for ERK activation (Kumar et al., 2007). An interesting positive feedback loop exists between vimentin and ROCK2 activation. Activation of ROCK2 causes intermediate filament collapse with simultaneous release of inactive ROCK2. The released ROCK2 is translocated to the periphery where it gets activated again and acts on phosphorylated intermediate filaments (Sin et al., 1998). The vimentin interacting protein Raf-1 associated kinase in concert with other vimentin kinases induce extensive vimentin reorganization (Janosch et al., 2000). It is well-known that intermediate filament architecture is reorganized in response to cell migration stimuli. α-Catulin, a scaffold for the ROCK signalosome (Park et al., 2002), co-localizes with vimentin intermediate filaments and contributes to vascular endothelial cell migration (Bear et al., 2016). In addition, vimentin filaments are also essential for VASP localization and phosphorylation by cGMP dependent kinase in endothelial cells (Lund et al., 2010). Many studies have emphasized the contributions of polymerized intermediate filaments, but a novel role of soluble vimentin precursors has been proposed that is not necessarily related to biogenesis of intermediate filament network. Here, soluble vimentin molecules bind to importin-β and phosphorylated ERK and thus enable their retrograde transport in sensory axons (Perlson et al., 2005, 2006). Polymerized intermediate filaments can function as scaffolds while even intermediate filament precursors can play a role of adaptors to transport signaling molecules.

Cytoplasmic intermediate filaments can also serve as phosphate "sponges or sinks," with broad implications to all signal transduction events. In particular, their head and tail domain have been proposed to buffer excess kinase activity. Such hyperphosphorylation of intermediate filaments can be detrimental or advantageous for the cell depending on the biological context (Lai et al., 1993; Ku and Omary, 2006). Phosphorylated cytoplasmic intermediate filaments can also act as sequestering reservoirs to accommodate stress response or physiological processes. Both phospho-vimentin and keratin provide binding affinity to sequester proteins like 14-3-3 and therefore limit their availability to other target proteins in order to regulate processes like mitosis and signal transduction (Tzivion et al., 2000; Kim et al., 2006; Margolis et al., 2006). Cell proliferation and size are closely coupled to the binding of adaptor proteins and kinases to cytoplasmic intermediate filaments serving as either molecular scaffolds or sequestration sinks. Perhaps the best example of phosphorylated intermediate filaments operating as docking sites for proteins is provided by members of the 14-3-3 protein family. Keratins and vimentin orchestrate the local interaction of 14-3-3 proteins with their multiple binding partners. 14-3-3 proteins bind keratin 18 (K18) at Ser33 in a cell-cycle and phosphorylation-dependent fashion (Ku et al., 1998) and trigger keratin filament solubilization during hepatocyte mitotic progression (Ku et al., 2002). K18 and 14-3-3 interaction is closely coupled to the association

of 14-3-3 proteins with a host of phosphorylated signaling molecules that are involved in mitotic progression, such as Raf1 kinase and Akt (Deng et al., 2012). In the case of Raf, K8/K18 filaments regulate cell signaling via the known K18 and 14-3-3 complex and recruitment of Raf1 kinase by 14-3-3 (Ku et al., 2004). Similarly, phosphorylated vimentin also provides a binding sink for 14-3-3 adaptor proteins (Tzivion et al., 2000). Physical interaction of K10 with Akt and atypical PKCζ inhibits intracellular translocation of these kinases, thus modulating PI-3 kinase signal transduction pathway and enabling K10 to function as a negative modulator cell cycle progression (Paramio et al., 2001). K17/14-3-3 complex has the ability to stimulate Akt/mTOR signaling and influence epithelial cell growth and size by regulating protein synthesis (Kim et al., 2006). Thus, phosphorylation of intermediate filaments has broad impacts to both intermediate filament polymerization status as well as modulation of cell signaling pathways.

ROLE FOR INTERMEDIATE FILAMENTS IN MECHANOTRANSDUCTION

Cellular mechanotransduction is an integration of multiple mechanical cues derived from sensing, transmission of force, and transduction into a biochemical response. There is extensive evidence that cell-cell, cell-ECM, and flow forces are actively sensed in different cellular contexts by the junctional protein complexes (Riveline et al., 2001; Weber et al., 2012; Conway et al., 2013). Different mechanical forces alter the structure, assembly, adhesive strength, function, and signaling of these adhesive complexes, which in turn has consequences to the cytoskeleton. Cytoplasmic intermediate filaments behave as an elastic and conductive network to transmit force and propagate mechanical stimuli within and between cells via adhesion complexes. As we detailed above, cytoplasmic intermediate filaments emerge as modulators of specific signal transduction pathways in a variety of biological contexts. Abundant availability, overall cytoplasmic presence and subcellular reorganization dependent on cellular context, allows the cytoplasmic intermediate filaments to partake in various signaling pathways in a multitude of ways. Such a view presents cytoplasmic intermediate filaments to be apt to transduce mechanical stimuli during development while integrating an ever changing physical environment with cell signaling (**Figure 1**).

Fluid flow shear stress plays important roles in the developing vasculature system. Perhaps more surprisingly fluid flow shear stress is also an important mechanical stimulus in tissues not often intuitively associated with exposure to fluid flow shear stresses, such as bone and glandular epithelia. Fluid flow shear stress studies have shed some light on the role of intermediate filaments in mechanotransduction pathways. Cytoplasmic intermediate filaments alter their network organization most likely by mechanisms such as conformational change, changes in assembly, PTMs and others. Mechanical forces such as shear stress can induce rapid reorganization of vimentin and keratin intermediate filament networks in various cell types, suggesting a role in spatial redistribution of intracellular force (Helmke et al., 2000, 2001; Yoon et al., 2001; Sivaramakrishnan et al., 2008). Shear stress increases the keratin intermediate filament network stiffness in the peripheral region of the cytoplasm (Sivaramakrishnan et al., 2008). Shearing also dramatically transforms the keratin intermediate filaments into more "wavy" tonofibril bundles, a process that is promoted by K8 and K18 phosphorylation on serine residues 73 and 33, respectively (Flitney et al., 2009; Sivaramakrishnan et al., 2009). This phosphorylation dependent reorganization of intermediate filaments is regulated by a variety of protein kinases including PKCδ and PKCζ (Ridge et al., 2005; Sivaramakrishnan et al., 2009). Phosphorylation of keratins in the regulatory head domain (K18 pSer33) recruits binding of 14-3-3, which allow for dynamic exchange and remodeling of the network (Sivaramakrishnan et al., 2009). In order to control against hyperphosphorylation induced disruption, keratin intermediate filaments recruit epiplakin, which perhaps serves as a chaperone during filament reorganization (Spazierer et al., 2008). In addition to the local deformation of the intermediate filaments, there is increased association of vimentin intermediate filaments with β3-integrin focal contacts, further stabilizing cell-matrix adhesions (Tsuruta and Jones, 2003). Similarly, in response to shear stress, endothelial cells trigger a transition from cell-cell adhesion loading on VE-cadherin to interaction of PECAM (Platelet endothelial cell adhesion molecule-1) with vimentin to stabilize cell-cell junctions (Conway et al., 2013). In this manner, mechanical loads may be transferred from one cytoskeletal network to another. Indeed keratin intermediate filaments exhibit less motion when actin-myosin II rigidity is increased, likely a consequence of stress generated by actomyosin being transmitted to pre-stress the keratin intermediate filament network (Nolting and Koster, 2013).

Experimentally introduced physical forces, induced by optical tweezers and fibronectin beads on epithelial cells, promote the modulation of both the K8/K18 intermediate filaments and the actin network through Rho-ROCK pathway (Bordeleau et al., 2012). Tensile forces reinforce stress fibers by joint coordination between Solo protein a RhoA GEF and K8/K18 intermediate filament network (Fujiwara et al., 2016). Actin stress fiber assembly and contractility are likewise modulated by vimentin filament dependent regulation of RhoA and GEF-H1 (RhoA GEF protein; Jiu et al., 2017). Decoupling the intermediate filaments from the mechanotransduction pathway has revealed hitherto unrecognized roles of intermediate filaments in this process. For instance, cells with inhibited vimentin expression display reduced mechanical resistance to the effects of flow (Tsuruta and Jones, 2003). Likewise mutant keratin intermediate filament network is unable to withstand mechanical stress (Ma et al., 2001), with marked reorganization of the filaments into discrete aggregates (Russell et al., 2004). In the absence of vimentin intermediate filaments or their displaced anchorage due to loss of plectin, cells display compromised activation of FAK and its downstream targets Src, ERK1/2, and p38 and thus impaired cell migration. Moreover, exploiting stress conditions in the absence of plectin, triggers prominent fragmentation of the intermediate filament network (Gregor et al., 2014). In agreement with these findings, cytoplasmic intermediate filaments perceive tension relayed

by the upstream mechanosensors and, in response, initiate rearrangements to function as stress buffers. How cytoplasmic intermediate filaments sense tension remains poorly understood. A speculative possibility is that cytoplasmic intermediate filaments alter their conformation or assembly upon stress to reveal cryptic sites crucial for sensing tension. For example, vimentin Cys327 site gets blocked under tension (Johnson et al., 2007; Pérez-Sala et al., 2015). Cytoplasmic intermediate filaments of all types exhibit plasticity in their structural folding which may offer both elasticity and potential for cryptic unmasking. These conformational changes in intermediate filament structure within the polymerized filament could have profound impacts to cell signaling as detailed earlier, and offers a bridge between managing the physical architecture and biochemical signaling.

INTERMEDIATE FILAMENTS AS DETERMINANTS OF MIGRATION

With all of the above in mind, intermediate filaments must be considered as far more than just "intracellular rubberbands." Attention must be given to intermediate filaments' polymerization state, connections to adhesions, and influence on signal transduction pathways. Like their actin and microtubule counterparts, intermediate filaments have profound influence over cellular functions, with migration being amongst the most dynamic.

A traditional view of intermediate filaments, particularly keratins, is that their association with stable adhesions provides for a general inhibition of migratory potential. And indeed, depletion or mutation of keratin alters, often increasing, migration rates of cancer cells which is likely to contribute to metastasis (Busch et al., 2012), affect invasiveness (Fortier et al., 2013), and wound healing (Morley et al., 2003). Additionally, impaired directional migration has been observed in MCF-7, HeLa, and Panc-1 epithelial cells lacking keratin expression (Long et al., 2006). In contrast, upregulation of vimentin is seen during wound healing (Eckes et al., 1998; Gilles et al., 1999; Rogel et al., 2011; Menko et al., 2014) and carcinoma invasion (Dmello et al., 2016). In addition to being an often used general marker of epithelial-mesenchymal transition (EMT), vimentin has a direct role in the migratory phenotype of cells having undergone EMT (Vuoriluoto et al., 2011; Liu et al., 2015), and declining vimentin levels decrease motility during mesenchymal-epithelial transition (MET; Mendez et al., 2010). Furthermore, treatment of cells with diverse bioactive molecules such as withaferin A (Grin et al., 2012; Menko et al., 2014), acrylamide (Eckert, 1985), okadaic acid (Strnad et al., 2001), orthovanadate (Strnad et al., 2002), or sphingolipids (Beil et al., 2003; Hyder et al., 2015) simultaneously disrupts cytoplasmic intermediate filament arrays into to perinuclear collapse or soluble aggregates and alters the migration rates of cells.

The aforementioned view of keratins as inhibiting migration and vimentin as promoting migration, while convenient, greatly oversimplifies the actual role that intermediate filaments play in migration. In fact, some keratins, such as K14, can promote cell migration, and their expression is correlated with both invasive carcinomas and migration during embryonic development (Sun et al., 2010; Cheung et al., 2013, 2016). Still other keratins, like K19, seem to have multiple functionalities that may greatly depend on the expression levels and more nuanced roles in modification of signal transduction pathways (Ohtsuka et al., 2016; Saha et al., 2017). How then might intermediate filaments impact migration when they are doing more than simply resisting motility?

Different modes of migration, whether random or directed, individual or collective, require the cytoskeleton to generate the structures that drive cell movement. Unique cytoskeletal structures determine and differentiate the protrusive cell front and a retracting rear. Akin to the differences that one sees in actin organization in the front vs. the back (branched actin vs. contractile stress fibers), it has become evident in recent years that cytoplasmic intermediate filaments establish a similarly polarized cytoskeletal network that regulates motility of single migratory cells.

Intermediate filaments extend through the rear and the perinuclear region of the cell, whereas vimentin particles are predominantly present in the lamellipodia (Helfand et al., 2011). Consistent with this correlational observation, it has been shown that increased presence of vimentin particles precedes lamellipodia formation (Helfand et al., 2011). Induced disruption of vimentin intermediate filament networks by microinjection of vimentin mimetic peptide (1A or 2B2) induces membrane ruffling at cell edges previously devoid of lamellipodia (Goldman et al., 1996; Helfand et al., 2011). Furthermore, non-filamentous vimentin or ULF's were shown to be in close proximity with smaller FAs while stable vimentin filaments were in vicinity of large FAs (Terriac et al., 2017). This suggests that assembly states of vimentin seems not only affect lamellipodia formation but may also be involved in establishing the anisotropy of focal contacts and focal adhesions to modulate efficient migration.

Notably, roles for intermediate filaments in migration are not limited to vimentin. In isolated keratinocytes, keratin particles primarily reside in the lamellipodia and keratin intermediate filaments extend through the cell body to the trailing edge (Kolega, 1986; Kolsch et al., 2010). Furthermore, these cells also exhibit asymmetric keratin dynamics, keratin particles prominently forming in the lamellipodia, further grow by elongation and fusion until integration into the peripheral network (Kolsch et al., 2010). In some non-epithelial cells that express keratins such as mesodermal cells, the correlation between cell protrusive polarity and reorganization of keratin intermediate filament network remains (Weber et al., 2012). In single multipolar mesodermal cells, lacking a definite protrusive polarity, keratin intermediate filaments span across the cell cytoplasm and yet are notably absent from protrusions (Weber et al., 2012). It remains to be determined whether the location of the keratin filaments *per-se* is a determinant of protrusive activity. However, in support of this hypothesis computational models predict that lamellipodia formation occurs in the direction opposite to keratin network formation (Kim et al., 2012). Keratins mediate stabilization of hemidesmosomes in some cells, and through promotion of these stable contacts, migration is inhibited (Seltmann et al., 2013b). However, not all

cells that express keratins, especially during development while tissues are still establishing themselves, make hemidesmosomes and/or desmosomes. The influence of intermediate filaments on migration may have as much to do with the types of adhesions with which they are associated (focal contacts vs. hemidesmosomes) as it does the intermediate filament subtype expressed (vimentin vs. keratin).

How do intermediate filaments guide migration when cells are moving cohesively? Front-rear polarization depends on mechanical cues exerted at cell-cell junctions. Formation of adherens junctions, but not desmosomes, generates tensile stress in tissues (Harris et al., 2014). Perturbing such intercellular contacts either by function blocking antibodies, chelation of calcium or protein knockdown, attenuates stresses mediated by classical cadherins and collective cell migration (Ganz et al., 2006; Bazellières et al., 2015; Plutoni et al., 2016). Application of local tension on single mesodermal cells induces reorganization of the intermediate filaments at cell-cell adhesion sites via plakoglobin (Weber et al., 2012), coincident with the induction of polarized cell protrusions and directional migratory behavior (Toyoizumi and Takeuchi, 1995; Weber et al., 2012). Similarly, *ex-vivo* embryonic *Xenopus* tissue explants arrange keratin intermediate filaments in a manner similar to single cells under tension (Weber et al., 2012). Reorganization of keratin cytoskeleton is also observed during epithelial sheet migration (Long et al., 2006). Intercellular tissue tension also contributes to integrin mediated traction forces (Dzamba et al., 2009); and conversely, integrin-fibronectin traction forces contribute to tissue tension and affect cell-cell tension by increasing the size of cadherin mediated cell-cell adhesions (Liu et al., 2010; Maruthamuthu et al., 2011). Thus, both cell-cell and cell-ECM interactions establish physicomechanical guidance cues. Extending lamellipodia of repair cells of wound healing are frequently enriched with vimentin particles (Menko et al., 2014). Likewise keratin particles are observed in the leading edge lamellipodia of epithelial cells (Kolsch et al., 2010). Thus, intermediate filaments break the symmetry and are arranged in an asymmetrical array to support polarized migration. We argue that this asymmetry may facilitate establishment of differential front and rear microenvironments necessary for efficient migration.

The small GTPase Rac1 is a probable mechanism for the differential localization of cytoplasmic intermediate filaments, and has direct implications to regulation of migration and polarity. Optimum levels of Rac1 play a critical role in protrusion formation to ensure directional cell migration (Pankov et al., 2005). Spatial and temporal activation of Rac1 is sufficient to promote collective cell migration in different models (Theveneau et al., 2010; Wang et al., 2010; Yoo et al., 2010). Additionally, leader cells of the MDCK collectives not only show elevated levels of Rac1, integrin β1, and PI3k, but also inhibition of any of these molecules disrupt the migratory phenotype. Activation of Rac1 which is downstream of integrin β1 and PI3k drives the collective migration (Yamaguchi et al., 2015). In single migratory fibroblasts, local induction of Rac1, promotes disassembly of vimentin intermediate filaments, locally inducing membrane ruffles, while the assembled filaments are maintained in the rear

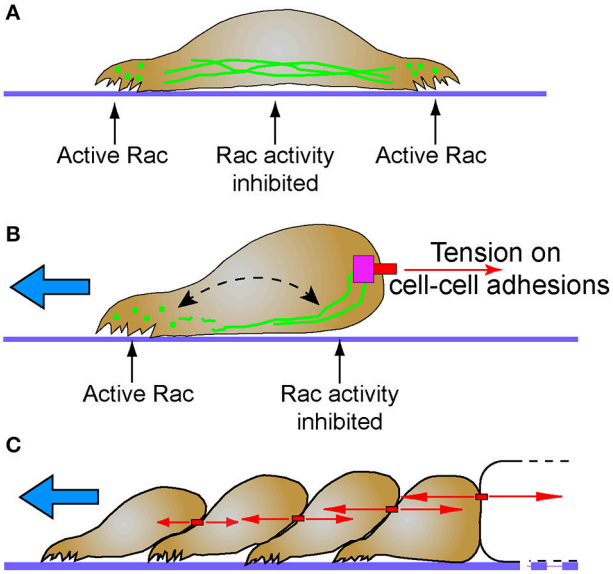

FIGURE 2 | Intermediate filaments and the establishment of cellular subdomains to drive directional migration. **(A)** Intermediate filaments exist in cells as monomer, filament precursors, and mature filaments. While mature intermediate filaments connect to cell adhesions, the nuclear lamina and span across the cell body, they are often notably absent from protrusions. Filament precursors are abundant in protrusions where Rac is active. **(B)** Tension (red arrows) on cell-cell adhesions recruits intermediate filaments. Persistent localization of intermediate filaments proximal to cell-cell adhesions may establish distinct non-protrusive Rac-inhibited zones. Areas of the cell with lesser tension on cell-cell contacts do not recruit intermediate filaments, creating Rac-permissive zones that promote protrusions that lead to directional migration (blue arrow). Despite this subcellular localization, intermediate filaments remain dynamic through non-polar subunit exchange (dashed arrow). **(C)** Stable cell-cell adhesions and the differential intercellular tension present across tissues may promote persistent collective cell migration behavior (blue arrow). Intermediate filaments simultaneously maintain tissue integrity while influencing cell signaling pathways that determine cell polarity and protrusive behavior.

(Helfand et al., 2011). Rac1 activity is negatively regulated by cadherin (Kitt and Nelson, 2011) and plakoglobin (Todorović et al., 2010), proteins which are both intermediate filament interacting molecules. These data suggest that cell-cell contacts may serve a mechanosensing and signaling function by stably recruiting intermediate filaments where they locally suppress Rac activity, and cell protrusions, at the posterior of collectively migrating cells (**Figure 2**).

The antagonistic relationship between cytoplasmic intermediate filaments and Rac1 may act as a mechanochemical switch that determines which of two mutually exclusive signaling states will occur. A similar switch exists between merlin and Rac1. A negative feedback loop between merlin-Rac1 controls the protrusion promoting state in the front end of the cell and protrusion inhibiting state at the rear end of the cells (Das et al., 2015). Stable cell-cell adhesions promote persistent directionality through this negative feedback loop (Das et al., 2015). Interestingly both intermediate filaments and Merlin are associated with stable cadherin-mediated cell-cell contacts.

Perhaps future studies will find a molecular mechanistic link given their common function in regulating polarity of collectively migrating cells.

FUNCTIONAL ROLES FOR INTERMEDIATE FILAMENTS DURING DEVELOPMENT

Elucidating the role of many cytoplasmic intermediate filaments in embryonic development has proven to be challenging due to functional redundancy and complexity within the family. Targeted deletion of K18 failed to block embryonic development in mice because of the presence of K19, demonstrating the functional redundancy within the protein family (Magin et al., 1998). However, double K18/K19 null mice display embryonic lethality due to disruption of the extraembryonic trophectoderm (Hesse et al., 2000). Despite this dominant role in the extraembryonic tissue, various keratin knockouts have surprisingly mild developmental phenotypes considering the known roles intermediate filaments play in adhesion. Knockout of all Type II keratins (KtyII$^{-/-}$) still produces an embryo that survives through neurulation and begins organogenesis (Vijayaraj et al., 2009). Nonetheless it should be noted that there is a significant delay in the early development of these KtyII$^{-/-}$ mice up to E8.5 that rapidly attempts to recover to E9.5 but ultimately ends in embryonic lethality (Vijayaraj et al., 2009). Defects in specific tissues at later stages where keratins are expressed argues a role for keratins in late tissue morphogenesis, homeostasis and physiological function (Bouameur and Magin, 2017), but a role for keratins in early embryogenesis has largely remained elusive in mouse models. As with many of the keratin knockout mice, mice lacking vimentin surprisingly undergo embryonic development quite normally, however, exhibit impaired wound healing (Eckes et al., 2000). In some cases, the role of cytoplasmic intermediate filaments only becomes evident upon mechanical and/or chemical stresses (Bouameur and Magin, 2017).

Genetic mouse models have yet to indicate a role for keratins or vimentin in early embryogenesis, but knockout mice have unequivocally revealed a definitive role for keratins in development and maintenance of skin (Bär et al., 2014; Kumar et al., 2015). The epidermal skin is broadly comprised of proliferative basal, stratified suprabasal, and terminally differentiated cornified layers. Each of these layers expresses a unique combinations of Type I and II keratins. Additional keratins, such as K6, K7, K9, K17, K76, have limited expression in the specialized epidermal regions like the palms and hair follicles. In line with prior data that hemidesmosomes and desmosomes provide for mechanical strength of skin, keratin knockout mice have severely fragile skin and the barrier function of the skin is compromised (Bär et al., 2014; Kumar et al., 2015). What is more, perturbation of keratin expression in these layers also results in the disruption of the homeostasis of the epidermis as it matures into distinct layers. Although functional redundancy may obscure the role of specific keratins (Reichelt et al., 2001; Reichelt and Magin, 2002), dysregulation of cell proliferation is a common theme in several keratin knockouts (e.g., K7$^{-/-}$, K8$^{-/-}$, K9$^{-/-}$, K10$^{-/-}$; Bouameur and Magin, 2017). Keratins also coordinate cell growth and protein biosynthesis by accurate localization of GLUT-1 and -3 and consequentially optimize regulation of mTOR pathway as evidenced by keratin Type II knockout mice (Vijayaraj et al., 2009). Collectively, these data point toward an important role for cytoplasmic intermediate filaments in modulating cell growth and proliferation through their impact on cell signaling pathways.

Cells migrate collectively in a coordinated manner to accomplish various tasks for development of the organism, from gametogenesis to morphogenesis to organogenesis. Collective cell migration allows whole groups of cells to move toward their final destination most efficiently while maintaining tissue cohesivity and tissue-specific characteristics. All the while, these cells can transmit signals to each other and effectively navigate the complex and changing environment within the developing embryo.

Disruption of the keratin network in the amphibian embryo tells quite a different story than mice about the importance of intermediate filaments in early embryogenesis. Disruption of keratin by either targeting protein expression (Heasman et al., 1992; Weber et al., 2012) or filament assembly (Klymkowsky et al., 1992) impairs mesodermal involution and blastopore closure during gastrulation. Pointing to a role in collective migration events, polarized protrusive cell behavior of the mesoderm is lost in the absence of K8 expression in *Xenopus* embryos (Weber et al., 2012).

Collective cell movements are also perturbed in keratin mutant mice, albeit at stages of organogenesis and tissue maintenance. Vimentin plays a role in promoting stemness of mammary epithelial cells which provide the basis for mammary gland growth. Ductal outgrowth is significantly delayed in mammary glands from vimentin knockout mice and the lumen is slightly enlarged (Virtakoivu et al., 2017). Vimentin expression in stromal and basal epithelial layers is accompanied by expression of keratins in the basal (K14) and luminal (K8/18) layers of the mammary epithelia (Sun et al., 2010; Virtakoivu et al., 2017). Both populations of mammary cells are involved in the branching morphogenesis of the tissue. Live cell imaging studies have shown that K8/18+ mammary epithelial cells collectively migrate during this process (Ewald et al., 2008) and other studies have indicated a pro-migratory role of K14 expressing mammary cells in collective invasion at the epithelial-stromal boundary (Cheung et al., 2013). Interestingly during the initial development of the mammary placode in the embryonic mouse, these invasive migratory cells express both K8 and K14 (Sun et al., 2010). Only recently have selective promoters for basal mammary epithelial cells become available. It will be interesting to determine whether knockout of K14 and/or K8 functionally inhibits mammary development.

Morphogenesis of epidermal and muscle tissue in *Caenorhabditis elegans* provides a particular elegant example of the interplay between intermediate filaments and mechanotransduction pathways during development. Muscle-generated tension within the epidermis induces recruitment of the adaptor protein GIT-1 and its partner PIX-1, a Rac GEF, to hemidesmosomes (Zhang et al., 2011). With PIX-1 at the hemidesmosome, Rac is activated, which further

stimulates PAK-1 activity and subsequent phosphorylation of intermediate filaments (Zhang et al., 2011). Phosphorylation of intermediate filaments through this mechanism drives remodeling and maturation of the hemidesmosome and the associated intermediate filament network (Zhang et al., 2011). Hemidesmosomes behave as mechanosensors that further relay the tension by activation of specific signaling pathway that promotes epithelial morphogenesis (Zhang et al., 2011). Indeed, coordination between the epidermis and muscle cells is absolutely essential to epidermal morphogenesis that elongates the worm, and cytoplasmic intermediate filaments are vital to this process (Woo et al., 2004).

Migration driven by cell-cell adhesions has roles very early in development, even as early as development of gametes. Tension sensing through E-cadherin plays a critical role in controlling directionality of migration of border cells in the Drosophila ovary (Cai et al., 2014). As with many collectively migrating cells, asymmetric Rac activity also plays a key role in the steering of these migrating collectives (Wang et al., 2010; Yoo et al., 2010). For some time, cytoplasmic intermediate filaments were believed to be absent from many non-chordates including arthropods. Recently however, it was found that the tropomyosin-1 gene (Tm1) produces a unique isoform, Tm1-I/C, which has many cytoplasmic intermediate filament-like characteristics, including the tripartite head-rod-tail structure and the ability to anneal end-to-end and spontaneously polymerize into filaments of similar diameter to intermediate filaments (Cho et al., 2016). Knockdown of this Tm1 isoform impairs border cell migration, unlike knockdown of other Tm1 isoforms. Moreover, actin stress fiber organization is perturbed in cells lacking Tm1-I/C, despite that Tm1-I/C does not co-localize with actin (Cho et al., 2016). While the inhibition of border cell migration in Tm1-I/C knockdown cells could be entirely structurally related to facilitating adhesions and/or enabling protrusions, it certainly is appealing to speculate that Tm1-I/C, like keratin and vimentin intermediate filaments, tethers to cell adhesions and allows for mechanotransduction between these adhesions and signaling mechanisms regulating cell protrusive behavior.

WHAT IS NEXT FOR INTERMEDIATE FILAMENTS?

Intermediate filaments are the next frontier for understanding how cells cope with mechanical stimuli and integrate these signals with cellular function. Current data bolsters the notion that cytoplasmic intermediate filaments provide a unique scaffolding framework that regulates major mechanotransduction events initiated through cellular adhesions. Moreover, intermediate filaments function in these mechanotransduction processes in a non-redundant manner that cannot be compensated by other cytoskeletal networks during development.

New innovative methods will have to be devised to tackle the details of how intermediate filaments are regulated in terms of turnover, dynamic exchange, and other remodeling events *in vivo*. Although, various signaling pathway relationships to intermediate filaments have been found, the molecular mechanism by which intermediate filaments effect signaling is not always clear. For a few proteins, direct interaction with intermediate filaments are known to exist. The next step will be to determine how strain on intermediate filaments impacts these binding partners and their activity and/or intermediate filament polymerization state. Subcellular compartmentalization of the different intermediate filament polymerization states (i.e., intermediate filament proteins as filaments or particles) is likely to have important consequences to the local cellular activity. Intermediate filament filaments and particles may form a differential composite network that, in coordination with the other cytoskeletal elements, endures and responds to changing physical parameters that cells experience during development.

Significant headway has been made to investigate the relationship between intermediate filaments and the actin and microtubule networks. Still, questions remain particularly related to the *in vivo* functionality of intermediate filament elasticity. If intermediate filaments cannot independently generate force because of the lack of associated motor proteins, is it possible for them to be pre-stressed by nearby actomyosin or microtubule-kinesin/dynein networks? In this regard, intermediate filaments could store substantial potential energy and enable cell contractility through a non-actomyosin mechanism. Both actomyosin and intermediate filaments could work cooperatively as dynamic elastic components. Likewise, nuanced differences between various keratin proteins and vimentin in regulation, turnover rates, and mechanical properties are likely optimized for different cell and tissue-specific functions.

Intermediate filaments as elastic, but resilient, cytoskeletal structures may undergo conformational changes due to mechanical stresses that unmask cryptic binding sites within the polymerized filament. If great enough, these stresses might otherwise rupture a cell or another cytoskeletal component, but intermediate filaments are uniquely suited to cope with these greater forces. For cytoplasmic intermediate filaments, they become a strain sensor- in essence, only permitting certain cell signaling events to occur when strain is applied. Developmental morphogenesis and cell migration are but two processes for which these signals would be important, yet important ones since dramatic tissue shaping occurs on a rapid timescale. As much as intermediate filaments have historically been touted as the keepers of cellular mechanical integrity, investigating them as dynamic components of cellular mechanosensor complexes is demanded.

If we think about different types of adhesions as an interdependent network, then perhaps we can confer a similar thought process to how we think about cytoskeletal networks. Given the coordination in localization, function, and integration with signal transduction pathways, our longstanding conceptual models of discrete adhesive structures with separate cytoskeletal networks may be long overdue for a re-thinking. As much as we have learned about the role of cell adhesions and actomyosin in force-induced signal transduction in the last decade, the potential exists for an equally robust phase of discovery about intermediate filaments and their role in mechanotransduction during development.

AUTHOR CONTRIBUTIONS

RS and GW shared equally in the conceptual development, literature research, and writing of the manuscript.

FUNDING

This work was supported by grant HD084254 from the Eunice Kennedy Shriver National Institute of Child Health and Human Development to GW and by a Rutgers University-Newark Dissertation Fellowship to RS.

ACKNOWLEDGMENTS

We would like to thank the members of the Weber laboratory, especially Shalaka Paranjpe, Richard Mariani, and Huri Mucahit, for helpful discussions leading to the production of this manuscript.

REFERENCES

Ackbarow, T., Sen, D., Thaulow, C., and Buehler, M. J. (2009). Alpha-helical protein networks are self-protective and flaw-tolerant. *PLoS ONE* 4:e6015. doi: 10.1371/journal.pone.0006015

Almeida, F. V., Walko, G., McMillan, J. R., McGrath, J. A., Wiche, G., Barber, A. H., et al. (2015). The cytolinker plectin regulates nuclear mechanotransduction in keratinocytes. *J. Cell Sci.* 128, 4475–4486. doi: 10.1242/jcs.173435

Bär, J., Kumar, V., Roth, W., Schwarz, N., Richter, M., Leube, R. E., et al. (2014). Skin fragility and impaired desmosomal adhesion in mice lacking all keratins. *J. Invest. Dermatol.* 134, 1012–1022. doi: 10.1038/jid.2013.416

Bazellières, E., Conte, V., Elosegui-Artola, A., Serra-Picamal, X., Bintanel-Morcillo, M., Roca-Cusachs, P., et al. (2015). Control of cell-cell forces and collective cell dynamics by the intercellular adhesome. *Nat. Cell Biol.* 17, 409–420. doi: 10.1038/ncb3135

Bear, M. D., Liu, T., Abualkhair, S., Ghamloush, M. A., Hill, N. S., Preston, I., et al. (2016). Alpha-catulin co-localizes with vimentin intermediate filaments and functions in pulmonary vascular endothelial cell migration via ROCK. *J. Cell. Physiol.* 231, 934–943. doi: 10.1002/jcp.25185

Beil, M., Micoulet, A., von Wichert, G., Paschke, S., Walther, P., Omary, M. B., et al. (2003). Sphingosylphosphorylcholine regulates keratin network architecture and visco-elastic properties of human cancer cells. *Nat. Cell Biol.* 5, 803–811. doi: 10.1038/ncb1037

Bhattacharya, R., Gonzalez, A. M., DeBiase, P. J., Trejo, H. E., Goldman, R. D., Flitney, F. W., et al. (2009). Recruitment of vimentin to the cell surface by β3 integrin and plectin mediates adhesion strength. *J. Cell Sci.* 122, 1390–1400. doi: 10.1242/jcs.043042

Bjerke, M. A., Dzamba, B., Wang, C., and DeSimone, D. W. (2014). FAK is required for tension-dependent organization of collective cell movements in Xenopus mesendoderm. *Dev. Biol.* 394, 1–17. doi: 10.1016/j.ydbio.2014.07.023

Blikstad, I., and Lazarides, E. (1983). Vimentin filaments are assembled from a soluble precursor in avian erythroid cells. *J. Cell Biol.* 96, 1803–1808. doi: 10.1083/jcb.96.6.1803

Bordeleau, F., Galarneau, L., Gilbert, S., Loranger, A., and Marceau, N. (2010). Keratin 8/18 modulation of protein kinase C-mediated Integrin-dependent adhesion and migration of liver epithelial cells. *Mol. Biol. Cell* 21, 1698–1713. doi: 10.1091/mbc.E09-05-0373

Bordeleau, F., Lapierre, M. E., Sheng, Y., and Marceau, N. (2012). Keratin 8/18 regulation of cell stiffness-extracellular matrix interplay through modulation of rho-mediated actin cytoskeleton dynamics. *PLoS ONE* 7:e38780. doi: 10.1371/journal.pone.0038780

Bouameur, J.-E., and Magin, T. M. (2017). Lessons from animal models of cytoplasmic intermediate filament proteins. *Subcell. Biochem.* 82, 171–230. doi: 10.1007/978-3-319-49674-0_7

Bouameur, J.-E., Favre, B., Fontao, L., Lingasamy, P., Begré, N., and Borradori, L. (2014). Interaction of plectin with keratins 5 and 14: dependence on several plectin domains and keratin quaternary structure. *J. Invest. Dermatol.* 134, 2776–2783. doi: 10.1038/jid.2014.255

Burgstaller, G., Gregor, M., Winter, L., and Wiche, G. (2010). Keeping the vimentin network under control: cell-matrix adhesion-associated plectin 1f affects cell shape and polarity of fibroblasts. *Mol. Biol. Cell* 21, 3362–3375. doi: 10.1091/mbc.E10-02-0094

Busch, T., Armacki, M., Eiseler, T., Joodi, G., Temme, C., Jansen, J., et al. (2012). Keratin 8 phosphorylation regulates keratin reorganization and migration of epithelial tumor cells. *J. Cell Sci.* 125, 2148–2159. doi: 10.1242/jcs.080127

Cai, D., Chen, S. C., Prasad, M., He, L., Wang, X., Choesmel-Cadamuro, V., et al. (2014). Mechanical feedback through E-cadherin promotes direction sensing during collective cell migration. *Cell* 157, 1146–1159. doi: 10.1016/j.cell.2014.03.045

Cary, R. B., Klymkowsky, M. W., Evans, R. M., Domingo, A, Dent, J., A, and Backhus, L. E. (1994). Vimentin's tail interacts with actin-containing structures *in vivo*. *J. Cell Sci.* 107 (Pt 6), 1609–1622.

Chang, I. A., Oh, M.-J., Kim, M. H., Park, S.-K., Kim, B. G., and Namgung, U. (2012). Vimentin phosphorylation by Cdc2 in Schwann cell controls axon growth via β1-integrin activation. *FASEB J.* 26, 2401–2413. doi: 10.1096/fj.11-199018

Chang, L., Barlan, K., Chou, Y.-H., Grin, B., Lakonishok, M., Serpinskaya, A. S., et al. (2009). The dynamic properties of intermediate filaments during organelle transport. *J. Cell Sci.* 122, 2914–2923. doi: 10.1242/jcs.046789

Chernyatina, A. A., Nicolet, S., Aebi, U., Herrmann, H., and Strelkov, S. V. (2012). Atomic structure of the vimentin central alpha-helical domain and its implications for intermediate filament assembly. *Proc. Natl. Acad. Sci. U.S.A.* 109, 13620–13625. doi: 10.1073/pnas.1206836109

Cheung, K. J., Gabrielson, E., Werb, Z., and Ewald, A. J. (2013). Collective invasion in breast cancer requires a conserved basal epithelial program. *Cell* 155, 1639–1651. doi: 10.1016/j.cell.2013.11.029

Cheung, K. J., Padmanaban, V., Silvestri, V., Schipper, K., Cohen, J. D., Fairchild, A. N., et al. (2016). Polyclonal breast cancer metastases arise from collective dissemination of keratin 14-expressing tumor cell clusters. *Proc. Natl. Acad. Sci. U.S.A.* 113, E854–E863. doi: 10.1073/pnas.1508541113

Cho, A., Kato, M., Whitwam, T., Kim, J. H., and Montell, D. J. (2016). An atypical tropomyosin in Drosophila with intermediate filament-like properties. *Cell Rep.* 16, 928–938. doi: 10.1016/j.celrep.2016.06.054

Chou, Y., Ngai, K., and Goldman, R. (1991). The regulation of intermediate filament reorganization in mitosis. *J. Biol. Chem.* 266, 7325–7328.

Coleman, T. R., and Lazarides, E. (1992). Continuous growth of vimentin filaments in mouse fibroblasts. *J. Cell Sci.* 103(Pt 3), 689–698.

Conway, D. E., Breckenridge, M. T., Hinde, E., Gratton, E., Chen, C. S., and Schwartz, M. A. (2013). Fluid shear stress on endothelial cells modulates mechanical tension across VE-cadherin and PECAM-1. *Curr. Biol.* 23, 1024–1030. doi: 10.1016/j.cub.2013.04.049

Correia, I., Chu, D., Chou, Y. H., Goldman, R. D., and Matsudaira, P. (1999). Integrating the actin and vimentin cytoskeletons: adhesion-dependent formation of fimbrin-vimentin complexes in macrophages. *J. Cell Biol.* 146, 831–842. doi: 10.1083/jcb.146.4.831

Das, T., Safferling, K., Rausch, S., Grabe, N., Boehm, H., and Spatz, J. P. (2015). A molecular mechanotransduction pathway regulates collective migration of epithelial cells. *Nat. Cell Biol.* 17, 276–287. doi: 10.1038/ncb3115

Deng, M., Zhang, W., Tang, H., Ye, Q., Liao, Q., Zhou, Y., et al. (2012). Lactotransferrin acts as a tumor suppressor in nasopharyngeal carcinoma by repressing AKT through multiple mechanisms. *Oncogene* 32, 4273–4283. doi: 10.1038/onc.2012.434

Dmello, C., Sawant, S., Alam, H., Gangadaran, P., Tiwari, R., Dongre, H., et al. (2016). Vimentin-mediated regulation of cell motility through modulation of beta4 integrin protein levels in oral tumor derived cells. *Int. J. Biochem. Cell Biol.* 70, 161–172. doi: 10.1016/j.biocel.2015.11.015

Dodemont, H., and Riemer, D. (1990). Structure of an invertebrate gene encoding cytoplasmic intermediate filament (IF) proteins : implications for the origin and the diversification of IF proteins. *EMBO J.* 9, 4083–4094.

Döring, V., and Stick, R. (1990). Gene structure of nuclear lamin LIII of *Xenopus laevis*; a model for the evolution of IF proteins from a lamin-like ancestor. *EMBO J.* 9, 4073–4081.

Dupin, I., Sakamoto, Y., and Etienne-Manneville, S. (2011). Cytoplasmic intermediate filaments mediate actin-driven positioning of the nucleus. *J. Cell Sci.* 124, 865–872. doi: 10.1242/jcs.076356

Dzamba, B. J., Jakab, K. R., Marsden, M., Schwartz, M. A., and DeSimone, D. W. (2009). Cadherin adhesion, tissue tension, and noncanonical Wnt signaling regulate fibronectin matrix organization. *Dev. Cell* 16, 421–432. doi: 10.1016/j.devcel.2009.01.008

Eckert, B. (1985). Alteration of intermediate filament distribution in PtK1 cells by acrylamide. *Eur. J. Cell Biol.* 37, 169–174.

Eckes, B., Colucci-Guyon, E., Smola, H., Nodder, S., Babinet, C., Krieg, T., et al. (2000). Impaired wound healing in embryonic and adult mice lacking vimentin. *J. Cell Sci.* 113, 2455–2462.

Eckes, B., Dogic, D., Colucci-Guyon, E., Wang, N., Maniotis, A., Ingber, D., et al. (1998). Impaired mechanical stability, migration and contractile capacity in vimentin-deficient fibroblasts. *J. Cell Sci.* 111, 1897–1907.

Esue, O., Carson, A. A., Tseng, Y., and Wirtz, D. (2006). A direct interaction between actin and vimentin filaments mediated by the tail domain of vimentin. *J. Biol. Chem.* 281, 30393–30399. doi: 10.1074/jbc.M605452200

Ewald, A. J., Brenot, A., Duong, M., Chan, B. S., and Werb, Z. (2008). Collective epithelial migration and cell rearrangements drive mammary branching morphogenesis. *Dev. Cell* 14, 570–581. doi: 10.1016/j.devcel.2008.03.003

Flitney, E. W., Kuczmarski, E. R., Adam, S. A., and Goldman, R. D. (2009). Insights into the mechanical properties of epithelial cells: the effects of shear stress on the assembly and remodeling of keratin intermediate filaments. *FASEB J.* 23, 2110–2119. doi: 10.1096/fj.08-124453

Fogl, C., Mohammed, F., Al-Jassar, C., Jeeves, M., Knowles, T. J., Rodriguez-Zamora, P., et al. (2016). Mechanism of intermediate filament recognition by plakin repeat domains revealed by envoplakin targeting of vimentin. *Nat. Commun.* 7:10827. doi: 10.1038/ncomms10827

Fois, G., Weimer, M., Busch, T., Felder, E. T., Oswald, F., Von Wichert, G., et al. (2013). Effects of keratin phosphorylation on the mechanical properties of keratin filaments in living cells. *FASEB J.* 27, 1322–1329. doi: 10.1096/fj.12-215632

Fortier, A. M., Asselin, E., and Cadrin, M. (2013). Keratin 8 and 18 loss in epithelial cancer cells increases collective cell migration and cisplatin sensitivity through claudin1 up-regulation. *J. Biol. Chem.* 288, 11555–11571. doi: 10.1074/jbc.M112.428920

Franke, W. W., Schmid, E., Osborn, M., and Weber, K. (1978a). Different intermediate-sized filaments distinguished by immunofluorescence microscopy. *Proc. Natl. Acad. Sci. U.S.A.* 75, 5034–5038. doi: 10.1073/pnas.75.10.5034

Franke, W. W., Weber, K., Osborn, M., Schmid, E., and Freudenstein, C. (1978b). Antibody to prekeratin. Decoration of tonofilament-like arrays in various cells of epithelial character. *Exp. Cell Res.* 116, 429–445. doi: 10.1016/0014-4827(78)90466-4

Franke, W., Schiller, D., Schmid, R., and Engelbrecht, I. (1981). Diversity of cytokeratins. *J. Mol. Biol.* 153, 933–959. doi: 10.1016/0022-2836(81)90460-5

Franz, J. K., Gall, L., Williams, M. A., Picheral, B., and Franke, W. W. (1983). Intermediate-size filaments in a germ cell: expression of cytokeratins in oocytes and eggs of the frog Xenopus. *Proc. Natl. Acad. Sci. U.S.A.* 80, 6254–6258. doi: 10.1073/pnas.80.20.6254

Fudge, D., Russell, D., Beriault, D., Moore, W., Lane, E. B., and Vogl, A. W. (2008). The intermediate filament network in cultured human keratinocytes is remarkably extensible and resilient. *PLoS ONE* 3:e2327. doi: 10.1371/journal.pone.0002327

Fujiwara, S., Ohashi, K., Mashiko, T., Kondo, H., and Mizuno, K. (2016). Interplay between Solo and keratin filaments is crucial for mechanical force-induced stress fiber reinforcement. *Mol. Biol. Cell* 58, 7250–7257. doi: 10.1091/mbc.E15-06-0417

Ganz, A., Lambert, M., Saez, A., Silberzan, P., Buguin, A., Mège, R. M., et al. (2006). Traction forces exerted through N-cadherin contacts. *Biol. Cell* 98, 721–730. doi: 10.1042/BC20060039

Gao, Y. S., and Sztul, E. (2001). A novel interaction of the Golgi complex with the vimentin intermediate filament cytoskeleton. *J. Cell Biol.* 152, 877–893. doi: 10.1083/jcb.152.5.877

Geisler, N., and Weber, K. (1982). The amino acid sequence of chicken muscle desmin provides a common structural model for intermediate filament proteins. *EMBO J.* 1, 1649–1656.

Gilles, C., Polette, M., Zahm, J. M., Tournier, J. M., Volders, L., Foidart, J. M., et al. (1999). Vimentin contributes to human mammary epithelial cell migration. *J. Cell Sci.* 112(Pt 2), 4615–4625.

Gittes, F., Mickey, B., Nettleton, J., and Howard, J. (1993). Flexural rigidity of microtubules and actin filaments measured from thermal fluctuations in shape. *J. Cell Biol.* 120, 923–934. doi: 10.1083/jcb.120.4.923

Gladilin, E., Gonzalez, P., and Eils, R. (2014). Dissecting the contribution of actin and vimentin intermediate filaments to mechanical phenotype of suspended cells using high-throughput deformability measurements and computational modeling. *J. Biomech.* 47, 2598–2605. doi: 10.1016/j.jbiomech.2014.05.020

Goldman, R. D., Goldman, A. E., Green, K. J., Jones, J. C., Jones, S. M., and Yang, H.-Y. (1986). Intermediate filament networks: organization and possible functions of a diverse group of cytoskeletal elements. *J. Cell Sci. Suppl.* 5, 69–97. doi: 10.1242/jcs.1986.Supplement_5.5

Goldman, R. D., Khuon, S., Chou, Y. H., Opal, P., and Steinert, P. M. (1996). The function of intermediate filaments in cell shape and cytoskeletal integrity. *J. Cell Biol.* 134, 971–983. doi: 10.1083/jcb.134.4.971

Goulielmos, G., Gounari, F., Remington, S., Müller, S., Häner, M., Aebi, U., et al. (1996). Filensin and phakinin form a novel type of beaded intermediate filaments and coassemble *de novo* in cultured cells. *J. Cell Biol.* 132, 643–655. doi: 10.1083/jcb.132.4.643

Gregor, M., Osmanagic-Myers, S., Burgstaller, G., Wolfram, M., Fischer, I., Walko, G., et al. (2014). Mechanosensing through focal adhesion-anchored intermediate filaments. *FASEB J.* 28, 715–729. doi: 10.1096/fj.13-231829

Grin, B., Mahammad, S., Wedig, T., Cleland, M. M., Tsai, L., Herrmann, H., et al. (2012). Withaferin A alters intermediate filament organization, cell shape and behavior. *PLoS ONE* 7:e39065. doi: 10.1371/journal.pone.0039065

Guo, M., Ehrlicher, A. J., Mahammad, S., Fabich, H., Jensen, M. H., Moore, J. R., et al. (2013). The role of vimentin intermediate filaments in cortical and cytoplasmic mechanics. *Biophys. J.* 105, 1562–1568. doi: 10.1016/j.bpj.2013.08.037

Harris, A. R., Daeden, A., and Charras, G. T. (2014). Formation of adherens junctions leads to the emergence of a tissue-level tension in epithelial monolayers. *J. Cell Sci.* 127, 2507–2517. doi: 10.1242/jcs.142349

Hatzfeld, M., and Franke, W. W. (1985). Pair formation and promiscuity of cytokeratins: formation *in vitro* of heterotypic complexes and intermediate-sized filaments by homologous and heterologous recombinations of purified polypeptides. *J. Cell Biol.* 101, 1826–1841. doi: 10.1083/jcb.101.5.1826

Havel, L. S., Kline, E. R., Salgueiro, A. M., and Marcus, A. I. (2015). Vimentin regulates lung cancer cell adhesion through a VAV2-Rac1 pathway to control focal adhesion kinase activity. *Oncogene* 34, 1979–1990. doi: 10.1038/onc.2014.123

Heasman, J., Torpey, N., and Wylie, C. (1992). The role of intermediate filaments in early Xenopus development studied by antisense depletion of maternal mRNA. *Dev. Suppl.* 125, 119–125.

Helfand, B. T., Mendez, M. G., Murthy, S. N. P., Shumaker, D. K., Grin, B., Mahammad, S., et al. (2011). Vimentin organization modulates the formation of lamellipodia. *Mol. Biol. Cell* 22, 1274–1289. doi: 10.1091/mbc.E10-08-0699

Helfand, B. T., Mikami, A., Vallee, R. B., and Goldman, R. D. (2002). A requirement for cytoplasmic dynein and dynactin in intermediate filament network assembly and organization. *J. Cell Biol.* 157, 795–806. doi: 10.1083/jcb.200202027

Helmke, B. P., Goldman, R. D., and Davies, P. F. (2000). Rapid displacement of vimentin intermediate filaments in living endothelial cells exposed to flow. *Circ. Res.* 86, 745–752. doi: 10.1161/01.RES.86.7.745

Helmke, B. P., Thakker, D. B., Goldman, R. D., and Davies, P. F. (2001). Spatiotemporal analysis of flow-induced intermediate filament displacement in living endothelial cells. *Biophys. J.* 80, 184–194. doi: 10.1016/S0006-3495(01)76006-7

Hering, L., Bouameur, J. E., Reichelt, J., Magin, T. M., and Mayer, G. (2016). Novel origin of lamin-derived cytoplasmic intermediate filaments in tardigrades. *Elife* 5:e11117. doi: 10.7554/eLife.11117

Herrmann, H., and Strelkov, S. V. (2011). History and phylogeny of intermediate filaments: now in insects. *BMC Biol.* 9:16. doi: 10.1186/1741-7007-9-16

Herrmann, H., Häner, M., Brettel, M., Ku, N. O., and Aebi, U. (1999). Characterization of distinct early assembly units of different intermediate filament proteins. *J. Mol. Biol.* 286, 1403–1420. doi: 10.1006/jmbi.1999.2528

Herrmann, H., Häner, M., Brettel, M., Müller, S. A., Goldie, K. N., Fedtke, B., et al. (1996). Structure and assembly properties of the intermediate filament protein vimentin: the role of its head, rod and tail domains. *J. Mol. Biol.* 264, 933–953. doi: 10.1006/jmbi.1996.0688

Herrmann, H., Kreplak, L., and Aebi, U. (2004). Isolation, characterization, and *in vitro* assembly of intermediate filaments. *Methods Cell Biol.* 78, 3–24. doi: 10.1016/S0091-679X(04)78001-2

Hesse, M., Franz, T., Tamai, Y., Taketo, M. M., and Magin, T. M. (2000). Targeted deletion of keratins 18 and 19 leads to trophoblast fragility and early embryonic lethality. *EMBO J.* 19, 5060–5070. doi: 10.1093/emboj/19.19.5060

Hesse, M., Magin, T. M., and Weber, K. (2001). Genes for intermediate filament proteins and the draft sequence of the human genome: novel keratin genes and a surprisingly high number of pseudogenes related to keratin genes 8 and 18. *J. Cell Sci.* 114, 2569–2575.

Ho, C. L., Martys, J. L., Mikhailov, A., Gundersen, G. G., and Liem, R. K. (1998). Novel features of intermediate filament dynamics revealed by green fluorescent protein chimeras. *J. Cell Sci.* 111 (Pt 1), 1767–1778.

Homberg, M., Ramms, L., Schwarz, N., Dreissen, G., Leube, R. E., Merkel, R., et al. (2015). Distinct impact of two keratin mutations causing epidermolysis bullosa simplex on keratinocyte adhesion and stiffness. *J. Invest. Dermatol.* 135, 1–29. doi: 10.1038/jid.2015.184

Hookway, C., Ding, L., Davidson, M. W., Rappoport, J. Z., Danuser, G., and Gelfand, V. I. (2015). Microtubule-dependent transport and dynamics of vimentin intermediate filaments. *Mol. Biol. Cell* 26, 1675–1686. doi: 10.1091/mbc.E14-09-1398

Hyder, C. L., Kemppainen, K., Isoniemi, K. O., Imanishi, S. Y., Goto, H., Inagaki, M., et al. (2015). Sphingolipids inhibit vimentin-dependent cell migration. *J. Cell Sci.* 128, 2057–2069. doi: 10.1242/jcs.160341

Ivaska, J., Vuoriluoto, K., Huovinen, T., Izawa, I., Inagaki, M., and Parker, P. J. (2005). PKCepsilon-mediated phosphorylation of vimentin controls integrin recycling and motility. *EMBO J.* 24, 3834–3845. doi: 10.1038/sj.emboj.7600847

Jackson, B. W., Grund, C., Schmid, E., Bürki, K., Franke, W. W., and Illmensee, K. (1980). Formation of cytoskeletal elements during mouse embryogenesis. Intermediate filaments of the cytokeratin type and desmosomes in preimplantation embryos. *Differentiation* 17, 161–179. doi: 10.1111/j.1432-0436.1980.tb01093.x

Janmey, P. A., Euteneuer, U., Traub, P., and Schliwa, M. (1991). Viscoelastic properties of vimentin compared with other filamentous biopolymer networks. *J. Cell Biol.* 113, 155–160. doi: 10.1083/jcb.113.1.155

Janosch, P., Kieser, A., Eulitz, M., Lovric, J., Sauer, G., Reichert, M., et al. (2000). The Raf-1 kinase associates with vimentin kinases and regulates the structure of vimentin filaments. *FASEB J.* 14, 2008–2021. doi: 10.1096/fj.99-0883com

Jiu, Y., Peränen, J., Schaible, N., Cheng, F., and Eriksson, J. E. (2017). Vimentin intermediate filaments control actin stress fiber assembly through GEF-H1 and RhoA. *J. Cell Sci.* 130, 892–902. doi: 10.1242/jcs.196881

Johnson, C. P., Tang, H.-Y., Carag, C., Speicher, D. W., and Discher, D. E. (2007). Forced unfolding of proteins within cells. *Science* 317, 663–666. doi: 10.1126/science.1139857

Ju, J.-H., Oh, S., Lee, K.-M., Yang, W., Nam, K. S., Moon, H.-G., et al. (2015). Cytokeratin19 induced by HER2/ERK binds and stabilizes HER2 on cell membranes. *Cell Death Differ*. 22, 665–676. doi: 10.1038/cdd.2014.155

Karabinos, A., Zimek, A., and Weber, K. (2004). The genome of the early chordate *Ciona intestinalis* encodes only five cytoplasmic intermediate filament proteins including a single type I and type II keratin and a unique IF-annexin fusion protein. *Gene* 326, 123–129. doi: 10.1016/j.gene.2003.10.019

Kayser, J., Haslbeck, M., Dempfle, L., Krause, M., Grashoff, C., Buchner, J., et al. (2013). The small heat shock protein Hsp27 affects assembly dynamics and structure of keratin intermediate filament networks. *Biophys. J.* 105, 1778–1785. doi: 10.1016/j.bpj.2013.09.007

Ketema, M., Wilhelmsen, K., Kuikman, I., Janssen, H., Hodzic, D., and Sonnenberg, A. (2007). Requirements for the localization of nesprin-3 at the nuclear envelope and its interaction with plectin. *J. Cell Sci.* 120, 3384–3394. doi: 10.1242/jcs.014191

Kim, H., Nakamura, F., Lee, W., Shifrin, Y., Arora, P., McCulloch, C. A., et al. (2010). Filamin A is required for vimentin-mediated cell adhesion and spreading. *Am. J. Physiol. Cell Physiol.* 298, 221–236. doi: 10.1152/ajpcell.00323.2009

Kim, J. S., Lee, C. H., Su, B. Y., and Coulombe, P. A. (2012). Mathematical modeling of the impact of actin and keratin filaments on keratinocyte cell spreading. *Biophys. J.* 103, 1828–1838. doi: 10.1016/j.bpj.2012.09.016

Kim, J., Yang, C., Kim, E. J., Jang, J., Kim, S.-J., Kang, S. M., et al. (2016). Vimentin filaments regulate integrin-ligand interactions by binding to the cytoplasmic tail of integrin β3. *J. Cell Sci.* 129, 2030–2042. doi: 10.1242/jcs.180315

Kim, S., Wong, P., and Coulombe, P., a (2006). A keratin cytoskeletal protein regulates protein synthesis and epithelial cell growth. *Nature* 441, 362–365. doi: 10.1038/nature04659

Kim, Y. J., Sauer, C., Testa, K., Wahl, J. K., Svoboda, R. A., Johnson, K. R., et al. (2005). Modulating the strength of cadherin adhesion: evidence for a novel adhesion complex. *J. Cell Sci.* 118, 3883–3894. doi: 10.1242/jcs.02508

Kirmse, R., Portet, S., Mücke, N., Aebi, U., Herrmann, H., and Langowski, J. (2007). A quantitative kinetic model for the *in vitro* assembly of intermediate filaments from tetrameric vimentin. *J. Biol. Chem.* 282, 18563–18572. doi: 10.1074/jbc.M701063200

Kitt, K. N., and Nelson, W. J. (2011). Rapid suppression of activated Rac1 by cadherins and nectins during *de novo* cell-cell adhesion. *PLoS ONE* 6:e17841. doi: 10.1371/journal.pone.0017841

Klymkowsky, M. W., Shook, D. R., and Maynell, L. A. (1992). Evidence that the deep keratin filament systems of the Xenopus embryo act to ensure normal gastrulation. *Proc. Natl. Acad. Sci. U.S.A.* 89, 8736–8740. doi: 10.1073/pnas.89.18.8736

Knapp, L. W., O'Guin, W. M., and Sawyer, R. H. (1983). Rearrangement of the keratin cytoskeleton after combined treatment with microtubule and microfilament inhibitors. *J. Cell Biol.* 97, 1788–1794.

Kolega, J. (1986). Effects of mechanical tension on protrusive activity and microfilament and intermediate filament organization in an epidermal epithelium moving in culture. *J. Cell Biol.* 102, 1400–1411. doi: 10.1083/jcb.102.4.1400

Kölsch, A., Windoffer, R., and Leube, R. E. (2009). Actin-dependent dynamics of keratin filament precursors. *Cell Motil. Cytoskeleton* 66, 976–985. doi: 10.1002/cm.20395

Kolsch, A., Windoffer, R., Wurflinger, T., Aach, T., and Leube, R. E. (2010). The keratin-filament cycle of assembly and disassembly. *J. Cell Sci.* 123, 2266–2272. doi: 10.1242/jcs.068080

Kreitzer, G., Liao, G., and Gundersen, G. G. (1999). Detyrosination of tubulin regulates the interaction of intermediate filaments with microtubules *in vivo* via a kinesin-dependent mechanism. *Mol. Biol. Cell* 10, 1105–1118. doi: 10.1091/mbc.10.4.1105

Kreplak, L., Bär, H., Leterrier, J. F., Herrmann, H., and Aebi, U. (2005). Exploring the mechanical behavior of single intermediate filaments. *J. Mol. Biol.* 354, 569–577. doi: 10.1016/j.jmb.2005.09.092

Kröger, C., Loschke, F., Schwarz, N., Windoffer, R., Leube, R. E., and Magin, T. M. (2013). Keratins control intercellular adhesion involving PKC-α-mediated desmoplakin phosphorylation. *J. Cell Biol.* 201, 681–692. doi: 10.1083/jcb.201208162

Ku, N. O., and Omary, M. B. (2000). Keratins turn over by ubiquitination in a phosphorylation-modulated fashion. *J. Cell Biol.* 149, 547–552. doi: 10.1083/jcb.149.3.547

Ku, N. O., and Omary, M. B. (2006). A disease- and phosphorylation-related nonmechanical function for keratin 8. *J. Cell Biol.* 174, 115–125. doi: 10.1083/jcb.200602146

Ku, N. O., Fu, H., and Omary, M. B. (2004). Raf-1 activation disrupts its binding to keratins during cell stress. *J. Cell Biol.* 166, 479–485. doi: 10.1083/jcb.200402051

Ku, N. O., Liao, J., and Omary, M. B. (1998). Phosphorylation of human keratin 18 serine 33 regulates binding to 14-3-3 proteins. *EMBO J.* 17, 1892–1906. doi: 10.1093/emboj/17.7.1892

Ku, N. O., Michie, S. A., Soetikno, R. M., Resurreccion, E. Z., Broome, R. L., Oshima, R. G., et al. (1996). Susceptibility to hepatotoxicity in transgenic mice that express a dominant-negative human keratin 18 mutant. *J. Clin. Invest.* 98, 1034–1046. doi: 10.1172/JCI118864

Ku, N., Michie, S., Resurreccion, E. Z., Broome, R. L., and Omary, M. B. (2002). Keratin binding to 14-3-3 proteins modulates keratin filaments and

hepatocyte mitotic progression. *Proc. Natl. Acad. Sci. U.S.A.* 99, 4373–4378. doi: 10.1073/pnas.072624299

Ku, N.-O., Toivola, D. M., Strnad, P., and Omary, M. B. (2010). Cytoskeletal keratin glycosylation protects epithelial tissue from injury. *Nat. Cell Biol.* 12, 876–885. doi: 10.1038/ncb2091

Kumar, N., Robidoux, J., Daniel, K. W., Guzman, G., Floering, L. M., and Collins, S. (2007). Requirement of vimentin filament assembly for beta3-adrenergic receptor activation of ERK MAP kinase and lipolysis. *J. Biol. Chem.* 282, 9244–9250. doi: 10.1074/jbc.M605571200

Kumar, V., Bouameur, J. E., Bär, J., Rice, R. H., Hornig-Do, H. T., Roop, D. R., et al. (2015). A keratin scaffold regulates epidermal barrier formation, mitochondrial lipid composition, and activity. *J. Cell Biol.* 211, 1057–1075. doi: 10.1083/jcb.201404147

Labouesse, C., Gabella, C., Meister, J.-J., Vianay, B., and Verkhovsky, A. B. (2016). Microsurgery-aided *in-situ* force probing reveals extensibility and viscoelastic properties of individual stress fibers. *Sci. Rep.* 6:23722. doi: 10.1038/srep23722

Lai, Y. K., Lee, W. C., and Chen, K. D. (1993). Vimentin serves as a phosphate sink during the apparent activation of protein kinases by okadaic acid in mammalian cells. *J. Cell. Biochem.* 53, 161–168. doi: 10.1002/jcb.240530209

Lehtonen, E., Lehto, V. P., Vartio, T., Badley, R. A., and Virtanen, I. (1983). Expression of cytokeratin polypeptides in mouse oocytes and preimplantation embryos. *Dev. Biol.* 100, 158–165. doi: 10.1016/0012-1606(83)90206-3

Leonard, M., Chan, Y., and Menko, A. S. (2008). Identification of a novel intermediate filament-linked N-cadherin/γ-catenin complex involved in the establishment of the cytoarchitecture of differentiated lens fiber cells. *Dev. Biol.* 319, 298–308. doi: 10.1016/j.ydbio.2008.04.036

Lichtenstern, T., Mücke, N., Aebi, U., Mauermann, M., and Herrmann, H. (2012). Complex formation and kinetics of filament assembly exhibited by the simple epithelial keratins K8 and K18. *J. Struct. Biol.* 177, 54–62. doi: 10.1016/j.jsb.2011.11.003

Lin, Y. C., Yao, N. Y., Broedersz, C. P., Herrmann, H., MacKintosh, F. C., and Weitz, D. A. (2010). Origins of elasticity in intermediate filament networks. *Phys. Rev. Lett.* 104, 1–4. doi: 10.1103/PhysRevLett.104.058101

Liovic, M., Mogensen, M. M., Prescott, A. R., and Lane, E. B. (2003). Observation of keratin particles showing fast bidirectional movement colocalized with microtubules. *J. Cell Sci.* 116, 1417–1427. doi: 10.1242/jcs.00363

Liu, C., Lin, H., Tang, M., and Wang, Y. (2015). Vimentin contributes to epithelial-mesenchymal transition cancer cell mechanics by mediating cytoskeletal organization and focal adhesion maturation. *Oncotarget* 6, 15966–15983. doi: 10.18632/oncotarget.3862

Liu, Z., Tan, J. L., Cohen, D. M., Yang, M. T., Sniadecki, N. J., Ruiz, S. A., et al. (2010). Mechanical tugging force regulates the size of cell-cell junctions. *Proc. Natl. Acad. Sci. U.S.A.* 107, 9944–9949. doi: 10.1073/pnas.0914547107

Lombardi, M. L., Jaalouk, D. E., Shanahan, C. M., Burke, B., Roux, K. J., and Lammerding, J. (2011). The interaction between nesprins and sun proteins at the nuclear envelope is critical for force transmission between the nucleus and cytoskeleton. *J. Biol. Chem.* 286, 26743–26753. doi: 10.1074/jbc.M111.233700

Long, H. A., Boczonadi, V., McInroy, L., Goldberg, M., and Määttä, A. (2006). Periplakin-dependent re-organisation of keratin cytoskeleton and loss of collective migration in keratin-8-downregulated epithelial sheets. *J. Cell Sci.* 119, 5147–5159. doi: 10.1242/jcs.03304

Loschke, F., Homberg, M., and Magin, T. M. (2016). Keratin isotypes control desmosome stability and dynamics through PKCα. *J. Invest. Dermatol.* 136, 202–213. doi: 10.1038/JID.2015.403

Lund, N., Henrion, D., Tiede, P., Ziche, M., Schunkert, H., and Ito, W. D. (2010). Vimentin expression influences flow dependent VASP phosphorylation and regulates cell migration and proliferation. *Biochem. Biophys. Res. Commun.* 395, 401–406. doi: 10.1016/j.bbrc.2010.04.033

Lynch, C. D., Lazar, A. M., Iskratsch, T., Zhang, X., and Sheetz, M. P. (2013). Endoplasmic spreading requires coalescence of vimentin intermediate filaments at force-bearing adhesions. *Mol. Biol. Cell* 24, 21–30. doi: 10.1091/mbc.E12-05-0377

Ma, L., Xu, J., Coulombe, P. A., and Wirtz, D. (1999). Keratin filament suspensions show unique micromechanical properties. *J. Biol. Chem.* 274, 19145–19151. doi: 10.1074/jbc.274.27.19145

Ma, L., Yamada, S., Wirtz, D., and Coulombe, P. A. (2001). A "hot-spot" mutation alters the mechanical properties of keratin filament networks. *Nat. Cell Biol.* 3, 503–506. doi: 10.1038/35074576

Magin, T. M., Schröder, R., Leitgeb, S., Wanninger, F., Zatloukal, K., Grund, C., et al. (1998). Lessons from keratin 18 knockout mice: formation of novel keratin filaments, secondary loss of keratin 7 and accumulation of liver-specific keratin 8-positive aggregates. *J. Cell Biol.* 140, 1441–1451. doi: 10.1083/jcb.140.6.1441

Margolis, S. S., Perry, J. A., Forester, C. M., Nutt, L. K., Guo, Y., Jardim, M. J., et al. (2006). Role for the PP2A/B56δ phosphatase in regulating 14-3-3 release from Cdc25 to control mitosis. *Cell* 127, 759–773. doi: 10.1016/j.cell.2006.10.035

Maruthamuthu, V., Sabass, B., Schwarz, U. S., and Gardel, M. L. (2011). Cell-ECM traction force modulates endogenous tension at cell-cell contacts. *Proc. Natl. Acad. Sci. U.S.A.* 108, 4708–4713. doi: 10.1073/pnas.1011123108

Matveeva, E. A., Venkova, L. S., Chernoivanenko, I. S., and Minin, A. A. (2015). Vimentin is involved in regulation of mitochondrial motility and membrane potential by Rac1. *Biol. Open* 4, 1290–1297. doi: 10.1242/bio.011874

Mendez, M. G., Kojima, S.-I., and Goldman, R. D. (2010). Vimentin induces changes in cell shape, motility, and adhesion during the epithelial to mesenchymal transition. *FASEB J.* 24, 1838–1851. doi: 10.1096/fj.09-151639

Mendez, M. G., Restle, D., and Janmey, P. A. (2014). Vimentin enhances cell elastic behavior and protects against compressive stress. *Biophys. J.* 107, 314–323. doi: 10.1016/j.bpj.2014.04.050

Menko, A. S., Bleaken, B. M., Libowitz, A. A., Zhang, L., Stepp, M. A., and Walker, J. L. (2014). A central role for vimentin in regulating repair function during healing of the lens epithelium. *Mol. Biol. Cell* 25, 776–790. doi: 10.1091/mbc.E12-12-0900

Miller, R. K., Vikstrom, K., and Goldman, R. D. (1991). Keratin incorporation into intermediate filament networks is a rapid process. *J. Cell Biol.* 113, 843–855. doi: 10.1083/jcb.113.4.843

Morgan, J. T., Pfeiffer, E. R., Thirkill, T. L., Kumar, P., Peng, G., Fridolfsson, H. N., et al. (2011). Nesprin-3 regulates endothelial cell morphology, perinuclear cytoskeletal architecture, and flow-induced polarization. *Mol. Biol. Cell* 22, 4324–4334. doi: 10.1091/mbc.E11-04-0287

Morley, S. M., D'Alessandro, M., Sexton, C., Rugg, E. L., Navsaria, H., Shemanko, C. S., et al. (2003). Generation and characterization of epidermolysis bullosa simplex cell lines: scratch assays show faster migration with disruptive keratin mutations. *Br. J. Dermatol.* 149, 46–58. doi: 10.1046/j.1365-2133.2003.05493.x

Mücke, N., Kreplak, L., Kirmse, R., Wedig, T., Herrmann, H., Aebi, U., et al. (2004). Assessing the flexibility of intermediate filaments by atomic force microscopy. *J. Mol. Biol.* 335, 1241–1250. doi: 10.1016/j.jmb.2003.11.038

Nafeey, S., Martin, I., Felder, T., Walther, P., and Felder, E. (2016). Branching of keratin intermediate filaments. *J. Struct. Biol.* 194, 415–422. doi: 10.1016/j.jsb.2016.03.023

Nekrasova, O. E., Mendez, M. G., Chernoivanenko, I. S., Tyurin-Kuzmin, P. A., Kuczmarski, E. R., Gelfand, V. I., et al. (2011). Vimentin intermediate filaments modulate the motility of mitochondria. *Mol. Biol. Cell* 22, 2282–2289. doi: 10.1091/mbc.E10-09-0766

Ngai, J., Coleman, T. R., and Lazarides, E. (1990). Localization of newly synthesized vimentin subunits reveals a novel mechanism of intermediate filament assembly. *Cell* 60, 415–427. doi: 10.1016/0092-8674(90)90593-4

Nicolet, S., Herrmann, H., Aebi, U., and Strelkov, S. V. (2010). Atomic structure of vimentin coil 2. *J. Struct. Biol.* 170, 369–376. doi: 10.1016/j.jsb.2010.02.012

Nöding, B., Herrmann, H., and Köster, S. (2014). Direct observation of subunit exchange along mature vimentin intermediate filaments. *Biophys. J.* 107, 2923–2931. doi: 10.1016/j.bpj.2014.09.050

Nolting, J. F., and Koster, S. (2013). Influence of microfluidic shear on keratin networks in living cells. *N. J. Phys.* 15:045025. doi: 10.1088/1367-2630/15/4/045025

Nolting, J. F., Mobius, W., and Koster, S. (2015). Mechanics of individual keratin bundles in living cells. *Biophys. J.* 107, 2693–2699. doi: 10.1016/j.bpj.2014.10.039

Ohtsuka, T., Sakaguchi, M., Yamamoto, H., Tomida, S., Takata, K., Shien, K., et al. (2016). Interaction of cytokeratin 19 head domain and HER2 in the cytoplasm leads to activation of HER2-Erk pathway. *Sci. Rep.* 6:39557. doi: 10.1038/srep39557

Omary, M. B., Ku, N. O., Tao, G. Z., Toivola, D. M., and Liao, J. (2006). "Heads and tails" of intermediate filament phosphorylation: multiple sites and functional insights. *Trends Biochem. Sci.* 31, 383–394. doi: 10.1016/j.tibs.2006.05.008

Osborn, M., Franke, W., and Weber, K. (1980). Direct demonstration of the presence of two immunologically distinct intermediate-sized filament systems

in the same cell by double immunofluorescence microscopy. *Exp. Cell Res.* 125, 37–46. doi: 10.1016/0014-4827(80)90186-X

Osmanagic-Myers, S., and Wiche, G. (2004). Plectin-RACK1 (receptor for activated C kinase 1) scaffolding: a novel mechanism to regulate protein kinase C activity. *J. Biol. Chem.* 279, 18701–18710. doi: 10.1074/jbc.M312382200

Osmanagic-Myers, S., Gregor, M., Walko, G., Burgstaller, G., Reipert, S., and Wiche, G. (2006). Plectin-controlled keratin cytoarchitecture affects MAP kinases involved in cellular stress response and migration. *J. Cell Biol.* 174, 557–568. doi: 10.1083/jcb.200605172

Osmanagic-Myers, S., Rus, S., Wolfram, M., Brunner, D., Goldmann, W. H., Bonakdar, N., et al. (2015). Plectin reinforces vascular integrity by mediating crosstalk between the vimentin and the actin networks. *J. Cell Sci.* 128, 4138–4150. doi: 10.1242/jcs.172056

Pankov, R., Endo, Y., Even-Ram, S., Araki, M., Clark, K., Cukierman, E., et al. (2005). A Rac switch regulates random versus directionally persistent cell migration. *J. Cell Biol.* 170, 793–802. doi: 10.1083/jcb.200503152

Paramio, J. M., Segrelles, C., and Ruiz, S. (2001). Inhibition of protein kinase B (PKB) and PKCζ Mediates keratin K10-induced cell cycle arrest. *Mol. Cell. Biol.* 21, 7449–7459. doi: 10.1128/MCB.21.21.7449-7459.2001

Park, B., Nguyen, N. T., Dutt, P., Merdek, K. D., Bashar, M., Sterpetti, P., et al. (2002). Association of Lbc Rho guanine nucleotide exchange factor with alpha-catenin-related protein, alpha-catulin/CTNNAL1, supports serum response factor activation. *J. Biol. Chem.* 277, 45361–45370. doi: 10.1074/jbc.M202447200

Pawelzyk, P., Mücke, N., Herrmann, H., and Willenbacher, N. (2014). Attractive interactions among intermediate filaments determine network mechanics *in vitro*. *PLoS ONE* 9:e93194. doi: 10.1371/journal.pone.0093194

Pérez-Sala, D., Oeste, C. L., Martínez, A. E., Carrasco, M. J., Garzón, B., and Cañada, F. J. (2015). Vimentin filament organization and stress sensing depend on its single cysteine residue and zinc binding. *Nat. Commun.* 6, 7287.

Perlson, E., Hanz, S., Ben-Yaakov, K., Segal-Ruder, Y., Seger, R., and Fainzilber, M. (2005). Vimentin-dependent spatial translocation of an activated MAP kinase in injured nerve. *Neuron* 45, 715–726. doi: 10.1016/j.neuron.2005.01.023

Perlson, E., Michaelevski, I., Kowalsman, N., Ben-Yaakov, K., Shaked, M., Seger, R., et al. (2006). Vimentin binding to phosphorylated Erk sterically hinders enzymatic dephosphorylation of the kinase. *J. Mol. Biol.* 364, 938–944. doi: 10.1016/j.jmb.2006.09.056

Peter, A., and Stick, R. (2015). Evolutionary aspects in intermediate filament proteins. *Curr. Opin. Cell Biol.* 32, 48–55. doi: 10.1016/j.ceb.2014.12.009

Plutoni, C., Bazellieres, E., Le Borgne-Rochet, M., Comunale, F., Brugues, A., Séveno, M., et al. (2016). P-cadherin promotes collective cell migration via a Cdc42-mediated increase in mechanical forces. *J. Cell Biol.* 212, 199–217. doi: 10.1083/jcb.201505105

Postel, R., Ketema, M., Kuikman, I., de Pereda, J. M., and Sonnenberg, A. (2011). Nesprin-3 augments peripheral nuclear localization of intermediate filaments in zebrafish. *J. Cell Sci.* 124, 755–764. doi: 10.1242/jcs.081174

Prahlad, V., Yoon, M., Moir, R. D., Vale, R. D., and Goldman, R. D. (1998). Rapid movements of vimentin on microtubule tracks: kinesin-dependent assembly of intermediate filament networks. *J. Cell Biol.* 143, 159–170. doi: 10.1083/jcb.143.1.159

Qin, Z., Kreplak, L., and Buehler, M. J. (2009). Hierarchical structure controls nanomechanical properties of vimentin intermediate filaments. *PLoS ONE* 4:e7294. doi: 10.1371/journal.pone.0007294

Quinlan, R. A., Hatzfeld, M., Franke, W. W., Lustig, A., Schulthess, T., and Engel, J. (1986). Characterization of dimer subunits of intermediate filament proteins. *J. Mol. Biol.* 192, 337–349. doi: 10.1016/0022-2836(86)90369-4

Ramms, L., Fabris, G., Windoffer, R., Schwarz, N., Springer, R., Zhou, C., et al. (2013). Keratins as the main component for the mechanical integrity of keratinocytes. *Proc. Natl. Acad. Sci. U.S.A.* 110, 18513–18518. doi: 10.1073/pnas.1313491110

Reichelt, J., and Magin, T. M. (2002). Hyperproliferation, induction of c-Myc and 14-3-3σ, but no cell fragility in keratin-10-null mice. *J. Cell Sci.* 115, 2639–2650.

Reichelt, J., Büssow, H., Grund, C., and Magin, T. M. (2001). Formation of a normal epidermis supported by increased stability of keratins 5 and 14 in keratin 10 null mice. *Mol. Biol. Cell* 12, 1557–1568. doi: 10.1091/mbc.12.6.1557

Ridge, K. M., Linz, L., Flitney, F. W., Kuczmarski, E. R., Chou, Y. H., Omary, M. B., et al. (2005). Keratin 8 phosphorylation by protein kinase c δ regulates shear stress-mediated disassembly of keratin intermediate filaments in alveolar epithelial cells. *J. Biol. Chem.* 280, 30400–30405. doi: 10.1074/jbc.M504239200

Riveline, D., Zamir, E., Balaban, N. Q., Schwarz, U. S., Ishizaki, T., Narumiya, S., et al. (2001). Focal contacts as mechanosensors: externally applied local mechanical force induces growth of focal contacts by an mDia1-dependent and ROCK-independent mechanism. *J. Cell Biol.* 153, 1175–1185. doi: 10.1083/jcb.153.6.1175

Robert, A., Herrmann, H., Davidson, M. W., and Gelfand, V. I. (2014). Microtubule-dependent transport of vimentin filament precursors is regulated by actin and by the concerted action of Rho- and p21-activated kinases. *FASEB J.* 28, 2879–2890. doi: 10.1096/fj.14-250019

Rogel, M. R., Soni, P. N., Troken, J. R., Sitikov, A., Trejo, H. E., and Ridge, K. M. (2011). Vimentin is sufficient and required for wound repair and remodeling in alveolar epithelial cells. *FASEB J.* 25, 3873–3883. doi: 10.1096/fj.10-170795

Rotty, J. D., and Coulombe, P. A. (2012). A wound-induced keratin inhibits Src activity during keratinocyte migration and tissue repair. *J. Cell Biol.* 197, 381–389. doi: 10.1083/jcb.201107078

Russell, D., Andrews, P. D., James, J., and Lane, E. B. (2004). Mechanical stress induces profound remodelling of keratin filaments and cell junctions in epidermolysis bullosa simplex keratinocytes. *J. Cell Sci.* 117, 5233–5243. doi: 10.1242/jcs.01407

Saha, S. K., Choi, H. Y., Kim, B. W., Dayem, A. A., Yang, G.-M., Kim, K. S., et al. (2017). KRT19 directly interacts with β-catenin/RAC1 complex to regulate NUMB-dependent NOTCH signaling pathway and breast cancer properties. *Oncogene* 36, 332–349. doi: 10.1038/onc.2016.221

Sakamoto, Y., Boëda, B., and Etienne-Manneville, S. (2013). APC binds intermediate filaments and is required for their reorganization during cell migration. *J. Cell Biol.* 200, 249–258. doi: 10.1083/jcb.201206010

Sankar, S., Tanner, J. M., Bell, R., Chaturvedi, A., Randall, R. L., Beckerle, M. C., et al. (2013). A novel role for keratin 17 in coordinating oncogenic transformation and cellular adhesion in Ewing sarcoma. *Mol. Cell. Biol.* 33, 4448–4460. doi: 10.1128/MCB.00241-13

Schopferer, M., Bär, H., Hochstein, B., Sharma, S., Mücke, N., Herrmann, H., et al. (2009). Desmin and vimentin intermediate filament networks: their viscoelastic properties investigated by mechanical rheometry. *J. Mol. Biol.* 388, 133–143. doi: 10.1016/j.jmb.2009.03.005

Schwarz, N., Windoffer, R., Magin, T. M., and Leube, R. E. (2015). Dissection of keratin network formation, turnover and reorganization in living murine embryos. *Sci. Rep.* 5:9007. doi: 10.1038/srep09007

Seltmann, K., Cheng, F., Wiche, G., Eriksson, J. E., and Magin, T. M. (2015). Keratins stabilize hemidesmosomes through regulation of β4-integrin turnover. *J. Invest. Dermatol.* 135, 1609–1620. doi: 10.1038/jid.2015.46

Seltmann, K., Fritsch, A. W., Käs, J., a, and Magin, T. M. (2013a). Keratins significantly contribute to cell stiffness and impact invasive behavior. *Proc. Natl. Acad. Sci. U. S. A.* 110, 18507–18512. doi: 10.1073/pnas.1310493110

Seltmann, K., Roth, W., Kröger, C., Loschke, F., Lederer, M., Hüttelmaier, S., et al. (2013b). Keratins Mediate Localization of Hemidesmosomes and Repress Cell Motility. *J. Invest. Dermatol.* 133, 181–190. doi: 10.1038/jid.2012.256

Shabbir, S. H., Cleland, M. M., Goldman, R. D., and Mrksich, M. (2014). Geometric control of vimentin intermediate filaments. *Biomaterials* 35, 1359–1366. doi: 10.1016/j.biomaterials.2013.10.008

Sharma, P., Bolten, Z. T., Wagner, D. R., and Hsieh, A. H. (2017). Deformability of human mesenchymal stem cells is dependent on vimentin intermediate filaments. *Ann. Biomed. Eng.* 45, 1365–1374. doi: 10.1007/s10439-016-1787-z

Sin, W. C., Chen, X. Q., Leung, T., and Lim, L. (1998). RhoA-binding kinase alpha translocation is facilitated by the collapse of the vimentin intermediate filament network. *Mol. Cell. Biol.* 18, 6325–6339. doi: 10.1128/MCB.18.11.6325

Sivaramakrishnan, S., DeGiulio, J. V., Lorand, L., Goldman, R. D., and Ridge, K. M. (2008). Micromechanical properties of keratin intermediate filament networks. *Proc. Natl. Acad. Sci. U.S.A.* 105, 889–894. doi: 10.1073/pnas.0710728105

Sivaramakrishnan, S., Schneider, J. L., Sitikov, A., Goldman, R. D., and Ridge, K. M. (2009). Shear stress induced reorganization of the keratin intermediate filament network requires phosphorylation by protein kinase C zeta. *Mol. Biol. Cell* 20, 2755–2765. doi: 10.1091/mbc.E08-10-1028

Snider, N. T., and Omary, M. B. (2014). Post-translational modifications of intermediate filament proteins: mechanisms and functions. *Nat. Rev. Mol. Cell Biol.* 15, 163–177. doi: 10.1038/nrm3753

Snider, N. T., Leonard, J. M., Kwan, R., Griggs, N. W., Rui, L., and Bishr Omary, M. (2013a). Glucose and SIRT2 reciprocally mediate the regulation of keratin 8 by lysine acetylation. *J. Cell Biol.* 200, 241–247. doi: 10.1083/jcb.201209028

Snider, N. T., Park, H., and Bishr Omary, M. (2013b). A conserved rod domain phosphotyrosine that is targeted by the phosphatase PTP1B promotes keratin 8 protein insolubility and filament organization. *J. Biol. Chem.* 288, 31329–31337. doi: 10.1074/jbc.M113.502724

Snider, N. T., Weerasinghe, S. V. W., Iñiguez-Lluhí, J. A., Herrmann, H., and Omary, M. B. (2011). Keratin hypersumoylation alters filament dynamics and is a marker for human liver disease and keratin mutation. *J. Biol. Chem.* 286, 2273–2284. doi: 10.1074/jbc.M110.171314

Soellner, P., Quinlan, R. A., and Franke, W. W. (1985). Identification of a distinct soluble subunit of an intermediate filament protein: tetrameric vimentin from living cells. *Proc. Natl. Acad. Sci. U.S.A.* 82, 7929–7933. doi: 10.1073/pnas.82.23.7929

Sokolova, A. V, Kreplak, L., Wedig, T., Mücke, N., Svergun, D. I., Herrmann, H., et al. (2006). Monitoring intermediate filament assembly by small-angle x-ray scattering reveals the molecular architecture of assembly intermediates. *Proc. Natl. Acad. Sci. U.S.A.* 103, 16206–16211. doi: 10.1073/pnas.0603629103

Spazierer, D., Raberger, J., Gross, K., Fuchs, P., and Wiche, G. (2008). Stress-induced recruitment of epiplakin to keratin networks increases their resistance to hyperphosphorylation-induced disruption. *J. Cell Sci.* 121, 825–833. doi: 10.1242/jcs.013755

Steinert, P. M., Cantieri, J. S., Teller, D. C., Lonsdale-Eccles, J. D., and Dale, B. A. (1981a). Characterization of a class of cationic proteins that specifically interact with intermediate filaments. *Proc. Natl. Acad. Sci. U.S.A.* 78, 4097–4101. doi: 10.1073/pnas.78.7.4097

Steinert, P. M., Idler, W. W., and Zimmerman, S. B. (1976). Self-assembly of bovine epidermal keratin filaments *in vitro*. *J. Mol. Biol.* 108, 547–567. doi: 10.1016/S0022-2836(76)80136-2

Steinert, P. M., Idler, W. W., Cabral, F., Gottesman, M. M., and Goldman, R. D. (1981b). *In vitro* assembly of homopolymer and copolymer filaments from intermediate filament subunits of muscle and fibroblastic cells. *Proc. Natl. Acad. Sci. U.S.A.* 78, 3692–3696. doi: 10.1073/pnas.78.6.3692

Strnad, P., Windoffer, R., and Leube, R. E. (2001). *In vivo* detection of cytokeratin filament network breakdown in cells treated with the phosphatase inhibitor okadaic acid. *Cell Tissue Res.* 306, 277–293. doi: 10.1007/s004410100455

Strnad, P., Windoffer, R., and Leube, R. E. (2002). Induction of rapid and reversible cytokeratin filament network remodeling by inhibition of tyrosine phosphatases. *J. Cell Sci.* 115, 4133–4148. doi: 10.1242/jcs.00096

Sun, P., Yuan, Y., Li, A., Li, B., and Dai, X. (2010). Cytokeratin expression during mouse embryonic and early postnatal mammary gland development. *Histochem. Cell Biol.* 133, 213–221. doi: 10.1007/s00418-009-0662-5

Svitkina, T. M., Verkhovsky, A. B., and Borisy, G. G. (1996). Plectin sidearms mediate interaction of intermediate filaments with microtubules and other components of the cytoskeleton. *J. Cell Biol.* 135, 991–1007. doi: 10.1083/jcb.135.4.991

Terriac, E., Coceano, G., Mavajian, Z., Hageman, T., Christ, A., Testa, I., et al. (2017). Vimentin levels and serine 71 phosphorylation in the control of cell-matrix adhesions, migration speed, and shape of transformed human fibroblasts. *Cells* 6, 2. doi: 10.3390/cells6010002

Theveneau, E., Marchant, L., Kuriyama, S., Gull, M., Moepps, B., Parsons, M., et al. (2010). Collective chemotaxis requires contact-dependent cell polarity. *Dev. Cell* 19, 39–53. doi: 10.1016/j.devcel.2010.06.012

Todorović, V., Desai, B. V., Patterson, M. J. S., Amargo, E. V., Dubash, A. D., Yin, T., et al. (2010). Plakoglobin regulates cell motility through Rho- and fibronectin-dependent Src signaling. *J. Cell Sci.* 123, 3576–3586. doi: 10.1242/jcs.070391

Toivola, D. M., Zhou, Q., English, L. S., and Omary, M. B. (2002). Type II keratins are phosphorylated on a unique motif during stress and mitosis in tissues and cultured cells. *Mol. Biol. Cell* 13, 1857–1870. doi: 10.1091/mbc.01-12-0591

Toyoizumi, R., and Takeuchi, S. (1995). The behavior of chick gastrula mesodermal cells under the unidirectional tractive force parallel to the substrata. *J. Cell Sci.* 108(Pt 2), 557–567.

Tsuruta, D., and Jones, J. C. (2003). The vimentin cytoskeleton regulates focal contact size and adhesion of endothelial cells subjected to shear stress. *J. Cell Sci.* 116, 4977–4984. doi: 10.1242/jcs.00823

Tzivion, G., Luo, Z. J., and Avruch, J. (2000). Calyculin A-induced vimentin phosphorylation sequesters 14-3-3 and displaces other 14-3-3 partners *in vivo*. *J. Biol. Chem.* 275, 29772–29778. doi: 10.1074/jbc.M001207200

Velez-delValle, C., Marsch-Moreno, M., Castro-Muñozledo, F., Galván-Mendoza, I. J., and Kuri-Harcuch, W. (2016). Epithelial cell migration requires the interaction between the vimentin and keratin intermediate filaments. *Sci. Rep.* 6:24389. doi: 10.1038/srep24389

Vijayaraj, P., Kröger, C., Reuter, U., Windoffer, R., Leube, R. E., and Magin, T. M. (2009). Keratins regulate protein biosynthesis through localization of GLUT1 and -3 upstream of AMP kinase and Raptor. *J. Cell Biol.* 187, 175–184. doi: 10.1083/jcb.200906094

Vikstrom, K. L., Borisy, G. G., and Goldman, R. D. (1989). Dynamic aspects of intermediate filament networks in BHK-21 cells. *Proc. Natl. Acad. Sci. U.S.A.* 86, 549–553. doi: 10.1073/pnas.86.2.549

Vikstrom, K. L., Lim, S. S., Goldman, R. D., and Borisy, G. G. (1992). Steady state dynamics of intermediate filament networks. *J. Cell Biol.* 118, 121–129. doi: 10.1083/jcb.118.1.121

Virtakoivu, R., Peuhu, E., Mai, A., Wärri, A., and Ivaska, J. (2017). Vimentin plays a functional role in mammary gland regeneration. *bioRxiv*. doi: 10.1101/134544. [Epub ahead of print].

Vuoriluoto, K., Haugen, H., Kiviluoto, S., Mpindi, J.-P., Nevo, J., Gjerdrum, C., et al. (2011). Vimentin regulates EMT induction by Slug and oncogenic H-Ras and migration by governing Axl expression in breast cancer. *Oncogene* 30, 1436–1448. doi: 10.1038/onc.2010.509

Wang, N., and Stamenović, D. (2000). Contribution of intermediate filaments to cell stiffness, stiffening, and growth. *Am. J. Physiol. Cell Physiol.* 279, C188–C194.

Wang, X., He, L., Wu, Y. I., Hahn, K. M., and Montell, D. J. (2010). Light-mediated activation reveals a key role for Rac in collective guidance of cell movement *in vivo*. *Nat. Cell Biol.* 12, 591–597. doi: 10.1038/ncb2061

Weber, G. F., Bjerke, M. A., and DeSimone, D. W. (2012). A mechanoresponsive cadherin-keratin complex directs polarized protrusive behavior and collective cell migration. *Dev. Cell* 22, 104–115. doi: 10.1016/j.devcel.2011.10.013

Wilhelmsen, K., Litjens, S. H. M., Kuikman, I., Tshimbalanga, N., Janssen, H., and Van Bout, I., Den, et al. (2005). Nesprin-3, a novel outer nuclear membrane protein, associates with the cytoskeletal linker protein plectin. *J. Cell Biol.* 171, 799–810. doi: 10.1083/jcb.200506083

Windoffer, R., and Leube, R. E. (1999). Detection of cytokeratin dynamics by time-lapse fluorescence microscopy in living cells. *J. Cell Sci.* 112, 4521–4534.

Windoffer, R., Beil, M., Magin, T. M., and Leube, R. E. (2011). Cytoskeleton in motion: the dynamics of keratin intermediate filaments in epithelia. *J. Cell Biol.* 194, 669–678. doi: 10.1083/jcb.201008095

Windoffer, R., Kölsch, A., Wöll, S., and Leube, R. E. (2006). Focal adhesions are hotspots for keratin filament precursor formation. *J. Cell Biol.* 173, 341–348. doi: 10.1083/jcb.200511124

Winheim, S., Hieb, A. R., Silbermann, M., Surmann, E. M., Wedig, T., Herrmann, H., et al. (2011). Deconstructing the late phase of vimentin assembly by total internal reflection fluorescence microscopy (TIRFM). *PLoS ONE* 6:e19202. doi: 10.1371/journal.pone.0019202

Wöll, S., Windoffer, R., and Leube, R. E. (2005). Dissection of keratin dynamics: different contributions of the actin and microtubule systems. *Eur. J. Cell Biol.* 84, 311–328. doi: 10.1016/j.ejcb.2004.12.004

Woo, W. M., Goncharov, A., Jin, Y., and Chisholm, A. D. (2004). Intermediate filaments are required for *C. elegans* epidermal elongation. *Dev. Biol.* 267, 216–229. doi: 10.1016/j.ydbio.2003.11.007

Yamaguchi, N., Mizutani, T., Kawabata, K., and Haga, H. (2015). Leader cells regulate collective cell migration via Rac activation in the downstream signaling of integrin β1 and PI3K. *Sci. Rep.* 5:7656. doi: 10.1038/srep07656

Yoo, S. K., Deng, Q., Cavnar, P. J., Wu, Y. I., Hahn, K. M., and Huttenlocher, A. (2010). Differential regulation of protrusion and polarity by PI(3)K during neutrophil motility in live zebrafish. *Dev. Cell* 18, 226–236. doi: 10.1016/j.devcel.2009.11.015

Yoon, K. H., Yoon, M., Moir, R. D., Khuon, S., Flitney, F. W., and Goldman, R. D. (2001). Insights into the dynamic properties of keratin intermediate filaments in living epithelial cells. *J. Cell Biol.* 152, 503–516. doi: 10.1083/jcb.153.3.503

Yoon, M., Moir, R. D., Prahlad, V., and Goldman, R. D. (1998). Motile properties of vimentin intermediate filament networks in living cells. *J. Cell Biol.* 143, 147–157. doi: 10.1083/jcb.143.1.147

Zhang, H., Landmann, F., Zahreddine, H., Rodriguez, D., Koch, M., and Labouesse, M. (2011). A tension-induced mechanotransduction pathway promotes epithelial morphogenesis. *Nature* 471, 99–103. doi: 10.1038/nature09765

Zhou, Q., Cadrin, M., Herrmann, H., Chen, C. H., Chalkley, R. J., Burlingame, A. L., et al. (2006). Keratin 20 serine 13 phosphorylation is a stress and intestinal goblet cell marker. *J. Biol. Chem.* 281, 16453–16461. doi: 10.1074/jbc.M512284200

Conflict of Interest Statement: The authors declare that the research was conducted in the absence of any commercial or financial relationships that could be construed as a potential conflict of interest.

frontiers in Cell and Developmental Biology

REVIEW
published: 26 April 2017
doi: 10.3389/fcell.2017.00040

Control of Neuronal Migration and Aggregation by Reelin Signaling in the Developing Cerebral Cortex

Yuki Hirota and Kazunori Nakajima *

Department of Anatomy, Keio University School of Medicine, Tokyo, Japan

The mammalian cerebral neocortex has a well-organized laminar structure, achieved by the highly coordinated control of neuronal migration. During cortical development, excitatory neurons born near the lateral ventricle migrate radially to reach their final positions to form the cortical plate. During this process, dynamic changes are observed in the morphologies and migration modes, including multipolar migration, locomotion, and terminal translocation, of the newborn neurons. Disruption of these migration processes can result in neuronal disorders such as lissencephaly and periventricular heterotopia. The extracellular protein, Reelin, mainly secreted by the Cajal-Retzius neurons in the marginal zone during development, plays a crucial role in the neuronal migration and neocortical lamination. Reelin signaling, which exerts essential roles in the formation of the layered neocortex, is triggered by the binding of Reelin to its receptors, ApoER2 and VLDLR, followed by phosphorylation of the Dab1 adaptor protein. Accumulating evidence suggests that Reelin signaling controls multiple steps of neuronal migration, including the transition from multipolar to bipolar neurons, terminal translocation, and termination of migration beneath the marginal zone. In addition, it has been shown that ectopically expressed Reelin can cause neuronal aggregation via an N-cadherin-mediated manner. This review attempts to summarize our knowledge of the roles played by Reelin in neuronal migration and the underlying mechanisms.

Keywords: neocortical development, neuronal migration, Reelin signaling

OPEN ACCESS

Edited by:
Takaaki Matsui,
Nara Institute of Science and Technology, Japan

Reviewed by:
Michael Frotscher,
University of Hamburg, Germany
Seonhee Kim,
Temple University, Japan

***Correspondence:**
Kazunori Nakajima
kazunori@keio.jp

Specialty section:
This article was submitted to Cell Adhesion and Migration, a section of the journal Frontiers in Cell and Developmental Biology

Received: *21 February 2017*
Accepted: *31 March 2017*
Published: *26 April 2017*

Citation:
Hirota Y and Nakajima K (2017) Control of Neuronal Migration and Aggregation by Reelin Signaling in the Developing Cerebral Cortex. Front. Cell Dev. Biol. 5:40. doi: 10.3389/fcell.2017.00040

INTRODUCTION

The mammalian neocortex has a highly organized 6-layered laminar structure, which forms the basis of complex brain functions, including learning, memory, and cognition. During mouse neocortical development, excitatory neurons are generated near the ventricular wall from three types of progenitor cells: radial glia (RG) (Miyata et al., 2001; Noctor et al., 2001) and short neural progenitors (also called apical inter progenitor cells) (Gal et al., 2006) in the ventricular zone (VZ), and the intermediate progenitor cells, also called basal progenitors (BPs), in the subventricular zone (SVZ) (Noctor et al., 2004). RG have a long ascending (basal) fiber and a short apical process, and undergo interkinetic nuclear migration followed by mitosis at the apical surface (Miyata et al., 2001; Noctor et al., 2001). During neurogenic divisions, the RG exhibit asymmetric self-renewing division to generate neurons or BPs. Short neural progenitors possess an apical process and a basal process of variable length that is retracted during mitotic division, and also undergo interkinetic nuclear migration (Gal et al., 2006). Short neural progenitors undergo symmetric self-consuming

division generating two neurons. BPs undergo terminal symmetric division in the SVZ to produce two neurons. Proliferation in the SVZ has expanded evolutionarily in primates. The primate SVZ is thick, consisting of an inner SVZ and outer SVZ (Smart et al., 2002). The human outer SVZ contains outer SVZ radial glia-like (oRG) cells, which possess an ascending basal process and undergo self-renewing asymmetric division (Fietz et al., 2010; Hansen et al., 2010). Subsequently, oRG-like BPs with the morphological features of radial glia were also found in other mammalian species, including rodents. These cells also exist in the inner SVZ of ferrets and marmosets, and are thus called basal RG (bRG) (Englund et al., 2005).

Newborn neurons exhibit multiple migration modes (**Figure 1**). At the beginning of cortical development, the earliest-born neurons form the preplate, a layer of differentiated neurons above the ventricular zone. Neurons subsequently generated in the VZ invade and split the preplate, which results in the formation of two distinct layers: the superficial marginal zone (MZ) and the deep subplate. Then, newborn neurons migrate radially from the VZ, pass through the subplate, and stop beneath the MZ to form the cortical plate (CP). During the early stages of neocortical development, radially migrating neurons destined to become the future deep layer neurons extend leading processes to the MZ, and then shorten their leading processes to move their cell bodies to their final positions. This migration mode is called "somal translocation," in which neurons migrate in a radial glia–independent manner (Nadarajah et al., 2001). During the later stages, the neocortex becomes thick and the neurons begin to migrate in several sequential migration modes. Newborn neurons first remain in the VZ as pin-like cells (Tabata and Nakajima, 2003; Noctor et al., 2004; Tabata et al., 2009, 2012, 2013), and then move out of the VZ toward the brain surface to transform into multipolar cells. The multipolar cells remain just above the VZ, a region called the multipolar cell accumulation zone (MAZ), for about 24 h. In the MAZ, neurons show a unique behavior designated as "multipolar migration," in which they extend and retract multiple processes dynamically while their somata wander (Tabata and Nakajima, 2003; Noctor et al., 2004; Tabata et al., 2009, 2012, 2013). Then, the multipolar cells transform into a bipolar morphology and start directed migration in the intermediate zone (IZ) and CP using the fibers of the RG as the scaffold (Rakic, 1972; Nadarajah et al., 2001). This RG-dependent migration is called "locomotion" (Nadarajah et al., 2001). Locomoting neurons directionally migrate toward the brain surface and when they arrive beneath the primitive cortical zone (PCZ), the outermost cell-dense region of the CP, they transiently pause, switching their migration mode to the "terminal translocation" mode (Sekine et al., 2011), which is morphologically similar to the somal translocation mode. Neurons use terminal translocation as the final migration mode, in which the somata move rapidly in a RG–independent manner to reach just beneath the MZ (Nadarajah et al., 2001) and complete their migration. During these processes, the later-born neurons pass through the early-born neurons at the top of the CP, resulting in a birth-date-dependent "inside-out" pattern, in which the later-born neurons are positioned in the superficial layers, while the early-born neurons reside in the deeper layers of the CP. This "inside-out" arrangement is specifically observed in the mammalian neocortex, suggesting its important roles in the expansion of the neocortex and evolution of the highly complex structure of mammalian brains.

An evolutionally conserved extracellular glycoprotein known as Reelin is now known to be involved in various cellular events in the development and functioning of the mature central nervous system. The most well-known function of Reelin signaling is control of neuronal migration and layer formation during neocortical development. In this review, we focus on the recently described roles of Reelin signaling in neuronal migration and aggregation in the developing neocortex.

CORE COMPONENTS OF REELIN SIGNAL TRANSDUCTION

Reelin was first identified as the responsible gene for the *reeler* mouse, a spontaneous recessive-mutant mouse which shows severe neurological phenotypes, including ataxia and malformations of the cortical layer structure (Bar et al., 1995; D'Arcangelo et al., 1995; Hirotsune et al., 1995). Birth-date labeling analysis revealed that the cortical layers are roughly inverted in these mice (Caviness and Sidman, 1973; Mikoshiba et al., 1980; D'Arcangelo et al., 1995; Ogawa et al., 1995; Boyle et al., 2011), suggesting that Reelin regulates the proper inside-out formation of the mammalian neocortex. Reelin binds to the cell surface receptors apolipoprotein E receptor 2 (ApoER2) and very-low-density lipoprotein receptor (VLDLR), which belong to the low-density lipoprotein receptor family (D'Arcangelo et al., 1999; Hiesberger et al., 1999). Mice with double-knockout of *Apoer2* and *Vldlr* exhibited a roughly inverted laminar cortex, similar to the *reeler* cortex, whereas mice with knockout of either *Apoer2* or *Vldlr* alone showed weak phenotypes (Trommsdorff et al., 1999), suggesting that these genes have redundant functions. Reelin binding to its receptors results in phosphorylation of the intracellular adaptor protein, disabled 1 (Dab1), which binds to the cytoplasmic domain of the same receptors, by the Src-family kinases Fyn and Src (Howell et al., 1999). Mutant mice deficient in *Dab1* showed *reeler*-like phenotypes (Sweet et al., 1996; Sheldon et al., 1997; Ware et al., 1997; Yoneshima et al., 1997; Kojima et al., 2000). Furthermore, double-knockout mice for *Fyn* and *Src* and mutant mice with mutation of all the potential tyrosine phosphorylation sites of Dab1 also exhibit a phenotype similar to the *reeler* mice (Howell et al., 2000; Kuo et al., 2005), lending support to the idea that phosphorylation of Dab1 is required for Reelin signaling. Phosphorylated Dab1 recruits various molecules, including Crk/CrkL (Ballif et al., 2004; Chen et al., 2004; Huang et al., 2004), SOCS3 (Feng et al., 2007), Nckβ (Pramatarova et al., 2003), PI3K (Bock et al., 2003), and Lis1 (Assadi et al., 2003), and transmits the signal to downstream pathways. Dab1 has also been reported to shuttle between the nucleus and cytoplasm, suggesting its possible functions in the nucleus (Honda and Nakajima, 2006, 2016). Thus, a large number of molecules of the Reelin signaling pathway

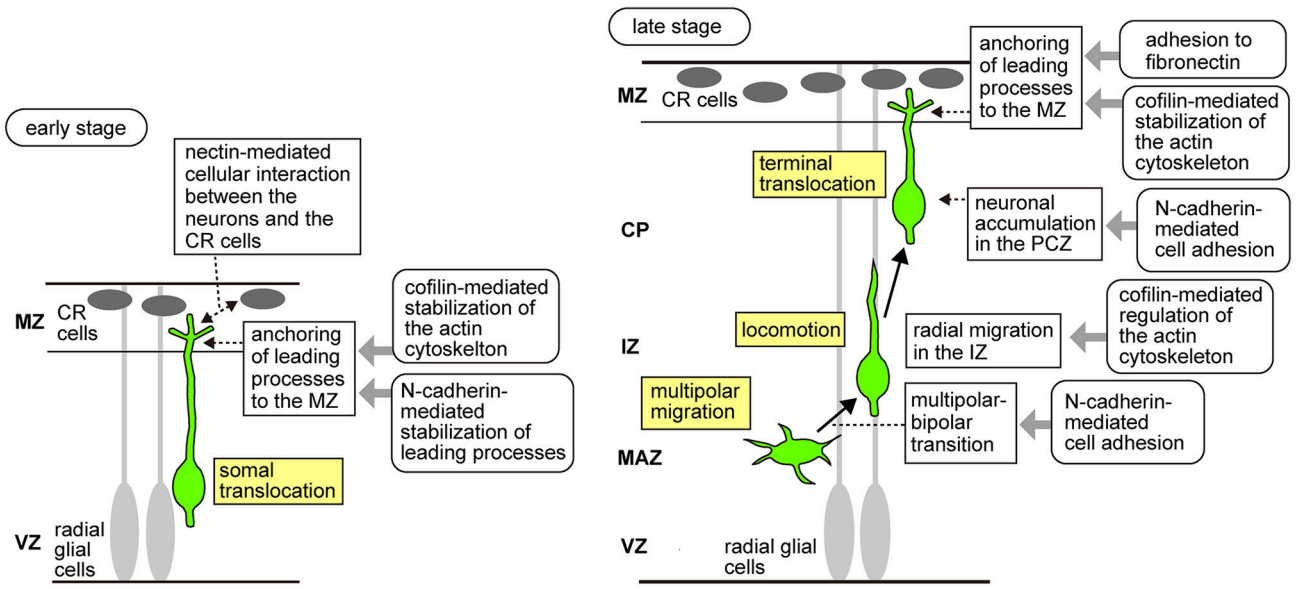

FIGURE 1 | Schema of the migratory modes of the excitatory neurons during neocortical development and molecular mechanisms downstream of Reelin signaling that control neuronal migration. In the early developmental stages **(Left)**, neurons generated from the radial glial cells undergo somal translocation, in which they extend processes to the MZ and shorten their leading processes to move their cell bodies to their final positions just beneath the MZ. During somal translocation, nectin-mediated activation of N-cadherin promotes cellular interaction between the neurons and the CR cells. In addition, n-cofilin expressed in the migrating neurons promotes anchoring of the leading processes to the MZ. N-cadherin also stabilizes the leading processes of the migrating neurons elongating into the MZ. In the later stages **(Right)**, the neurons sequentially change their migratory modes. First, in the MAZ, they exhibit multipolar migration, in which they extend and retract multiple processes dynamically while their somata wander. Multipolar cells then transform into a bipolar morphology. Reelin signaling controls the multipolar-to-bipolar transition via the Rap1/N-cadherin pathway. N-cofilin-mediated regulation of the actin cytoskeleton is involved in the radial migration of the neurons in the IZ. Bipolar neurons show locomotion, in which they directionally migrate in the IZ and CP using radial glial fibers as the scaffold. Finally, when they arrive at the outermost region of the CP, they switch to the terminal translocation mode, in which the somata move rapidly in a radial glia-independent manner to just beneath the MZ to complete migration. N-cadherin promotes neuronal accumulation in the PCZ. Reelin signaling activates integrin α5β1 in the migrating neurons, causing them to adhere to the fibronectin localized in the MZ. LIMK1/n-cofilin and integrin α5β1/fibronectin promote anchoring of the leading processes to the MZ.

have been identified so far. In the following sections, we shall highlight the biological roles of Reelin signaling during neuronal migration.

ROLES OF REELIN SIGNALING IN PREPLATE SPLITTING AND SOMAL TRANSLOCATION

Preplate splitting is the first developmental event during cortical lamination that requires Reelin. In *reeler* mice, the CP neurons fail to split the preplate, resulting in a superficial "superplate," composed of cells normally found in the MZ and subplate (Caviness and Sidman, 1973; Caviness, 1982), suggesting that somal translocation is impaired in the *reeler* mice. Subsequently arriving neurons accumulate beneath the superplate, resulting in an "outside-in" pattern of neuronal alignment, in which the later-born neurons are positioned in the superficial layers, while the earlier-born neurons reside in the deep layers of the CP (Caviness, 1982). Recent reports have shown that Reelin signaling controls somal translocation through distinct mechanisms. Chai et al. showed that Reelin signaling induced stabilization of the actin cytoskeleton during somal translocation. Reelin signaling, through LIMK1 activation, induces phosphorylation of n-cofilin, an actin-depolymerizing protein expressed in the leading processes of the neurons reaching the MZ, which promotes anchoring of these processes to the MZ (Chai et al., 2009). Another mechanism by which Reelin controls somal translocation is that which is mediated by neuronal cadherin, N-cadherin. Using *Dab1* flox mice, Franco et al. showed that Dab1 functions to stabilize the leading processes of the migrating neurons elongated into the MZ in a Rap1/N-cadherin-dependent manner during somal translocation (Franco et al., 2011). Cellular interactions mediated by Reelin signaling during somal translocation were also shown to be important. Gil-Sanz et al. focused on the roles of the immunoglobulin-like adhesion molecule, nectin. They showed that interaction between nectin1, expressed by the Cajal–Retzius (CR) cells, and nectin3, expressed by the migrating neurons, is critical for somal translocation. They also showed that Reelin signaling through the Crk/C3G/Rap1 pathway promotes N-cadherin functions via nectin3 and afadin, an adaptor protein which binds to the cytoplasmic domains of nectin, thus promoting heterotypic cell-cell interactions between the neurons and the CR cells (Gil-Sanz et al., 2013). Taken together, these results suggest that Reelin controls somal translocation via regulation of the actin cytoskeleton and cellular adhesion.

ROLES OF REELIN SIGNALING IN THE RADIAL MIGRATION OF NEURONS IN THE IZ

In the developing cortex, Reelin is mainly secreted by the CR cells in the MZ (D'Arcangelo et al., 1995; Ogawa et al., 1995), however, a small amount of Reelin can also be detected in the lower part of the IZ (Yoshida et al., 2006; Uchida et al., 2009; Hirota et al., 2015). In addition, proteolytic processing of Reelin by neurons was shown to generate a small fragment of Reelin, which diffuses into the deeper part of the CP (Jossin et al., 2007). As for the Reelin receptors, ApoER2 is strongly expressed in the MAZ/lower IZ (Uchida et al., 2009; Hirota et al., 2015). Furthermore, using an alkaline phosphatase fusion protein of the receptor-binding region of Reelin, it was shown that functional Reelin receptors are mainly localized in the IZ/SVZ (Uchida et al., 2009). These findings suggest that Reelin binds to receptors expressed by neurons migrating in the deeper part of the cortex to exert its functions in their early migratory stages. Consistent with this notion, migration defect in the IZ is observed in the *Apoer2* KO and *reeler* mice (Hack et al., 2007; Britto et al., 2011; Hirota et al., 2016), while this radial glia-guided locomotion was not found to be altered when *Dab1* was genetically eliminated using conditional KO mice (Franco et al., 2011), suggesting that Reelin signaling is required for the migration step before locomotion. Lending further support to this idea, exogenous Reelin was shown to influence the migratory behavior of neurons in the VZ/SVZ in cultured brain slices (Britto et al., 2014). Reelin signaling seems to control neuronal migration in the IZ via N-cadherin-mediated cell adhesion. N-cadherin is required for proper polarization and directed radial migration of the neurons in the IZ (Gartner et al., 2012). Several lines of evidence suggest that cell surface expression of N-cadherin is regulated by endosomal trafficking mediated by Rap1, Rab, and Arf6 small GTPases during radial migration (Kawauchi et al., 2010; Jossin and Cooper, 2011; Hara et al., 2016). Expression of a dominant-negative form of the Reelin receptor VLDLR resulted in impaired multipolar-to-bipolar transition, possibly via the Rap1/N-cadherin pathway (Jossin and Cooper, 2011). Regulation of the actin cytoskeleton by Reelin also seems to be involved in the control of neuronal migration in the IZ. As mentioned above, Reelin signaling activates LIMK1, which results in enhanced n-cofilin activation (Chai et al., 2009). A recent study showed that migration defect in the IZ of *reeler* mice was partially rescued by overexpression of LIMK1 or a phosphomimic mutant of cofilin (Chai et al., 2016). These findings suggest that Reelin signaling influences neuronal migration in the IZ. Further studies are required to uncover how the low amount of Reelin protein expressed in the lower part of the IZ regulates this process.

ROLES OF REELIN SIGNALING IN TERMINAL TRANSLOCATION

As mentioned above, Reelin is highly expressed in the MZ of developing cortex, and expression of Reelin receptors at the top of the CP and MZ has been repeatedly reported (Trommsdorff et al., 1999; Uchida et al., 2009; Kubo et al., 2010; Hirota et al., 2015). Since radially migrating neurons complete their migration beneath the MZ, existence of Reelin and its receptors in the MZ suggest a role of Reelin in the late steps of migration. Recent reports have shown important roles of Reelin signaling in terminal translocation. Sekine et al. showed that Reelin-dependent activation of neuronal adhesion to the extracellular matrix is crucial for the eventual birth-date-dependent layering of the neocortex (Sekine et al., 2012). Upon stimulation by Reelin binding to its receptors, Crk adaptor proteins bind to phosphorylated Dab1 and activate GTP exchange factor C3G, followed by activation of Rap1 GTPase. This pathway activates integrin α5β1, thus promoting the anchoring of the leading processes to the fibronectin localized in the MZ to promote terminal translocation (Sekine et al., 2012). Consistent with the morphological similarity between somal translocation and terminal translocation, some common mechanisms may be involved in the regulation of these processes. Reelin signaling has been shown to induce LIMK1/n-cofilin-mediated stabilization of the actin cytoskeleton and Rap1/N-cadherin-mediated stabilization of the leading processes during both terminal translocation and somal translocation (Chai et al., 2009; Franco et al., 2011). Together, these results suggest that Reelin signaling controls terminal translocation via regulating the actin cytoskeleton and cellular adhesion of the leading processes, and that both shared and distinct mechanisms are involved in the regulation of somal and terminal translocation during neuronal migration. It will be interesting to examine whether and how cellular interactions between migrating neurons and/or between neurons and cells in the MZ are involved in the regulation of terminal translocation by Reelin signaling.

ECTOPIC EXPRESSION OF REELIN INDUCES NEURONAL AGGREGATION *IN VIVO*

Recent findings described above indicate that Reelin signaling controls neuronal adhesion by regulating the adhesion of leading processes during translocation. Does Reelin signaling also control other aspects of migration and layer formation via controlling adhesion? Although locomoting neurons migrate individually through the IZ and CP, upon reaching the top of the CP, they seem to accumulate at a high cell density (Ajioka and Nakajima, 2005), suggesting the possibility that accumulation of the neurons in the PCZ may be required for proper layer formation through, for example, cell sorting among the neurons. Although the molecular and cellular mechanisms underlying the accumulation of neurons in the PCZ remain unknown, several lines of evidence suggest involvement of the Reelin signal. When Reelin was overexpressed in the IZ by electroporation into migrating neurons, the ectopically expressed Reelin caused the leading processes of the migrating neurons to assemble in the Reelin-rich region, resulting in ectopic neuronal aggregation *in vivo* (Kubo et al., 2010, **Figure 2**). Transplantation of Reelin-expressing cells into the developing cortex also yielded the same results. The center of the aggregate became cell-body-sparse

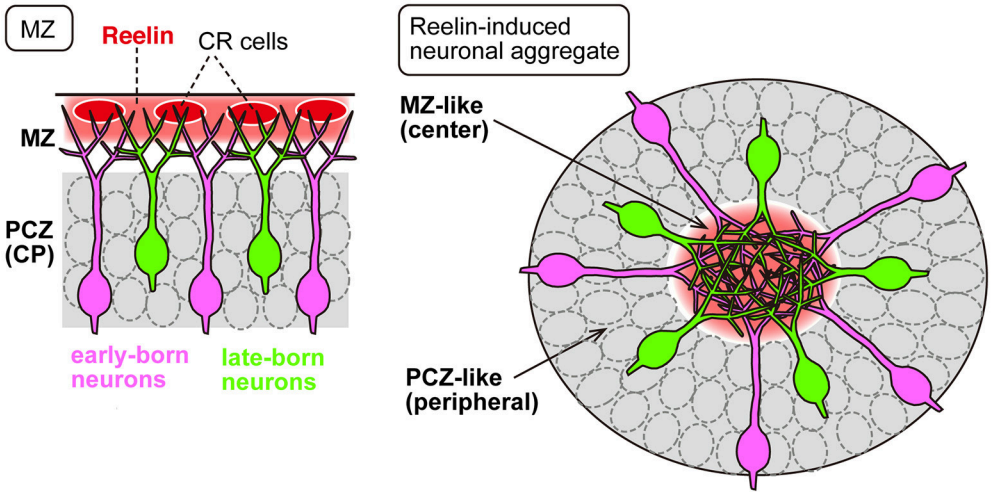

FIGURE 2 | Ectopic expression of Reelin causes neuronal aggregation *in vivo*. In the developing neocortex **(Left)**, Reelin (red) is mainly secreted from the CR cells in the MZ, into which the migrating neurons extend their apical leading processes. The PCZ is densely occupied by neuronal somata (gray). In neuronal aggregation induced by ectopically expressed Reelin **(Right)**, the leading processes of the migrating neurons assemble in the Reelin-rich central region, and the cell bodies are aligned in the PCZ-like peripheral region (gray). In both cases, the migrating neurons exhibit an "inside-out" cell arrangement in which the late-born cells (green) pass by the early-born neurons (magenta).

and dendrite-rich, resembling the structure of the MZ, while the cell bodies were densely packed in the peripheral region of the aggregate, resembling the structure of the PCZ. In addition, sequential labeling of the early and late-born neurons revealed that during the formation of an aggregate, the late-born neurons pass by the early-born neurons to arrive at the cell-body-sparse center of the aggregate (Kubo et al., 2010). It was shown that ectopically expressed Reelin caused neuronal aggregation via binding to the ApoER2 expressed in the migrating neurons, as inhibition of ApoER2 disrupted the aggregate formation (Kubo et al., 2010; Hirota et al., 2016). These results indicate that ectopic Reelin is responsible for the birth-date-dependent "inside-out" pattern of neuronal alignment even in the ectopic cellular aggregates, similar to that which would occur beneath the normal MZ. Thus, this ectopic expression model serves as a useful tool to investigate the roles of Reelin signaling in the cell accumulation or aggregation at the final step of neuronal migration.

Although the results of ectopic Reelin expression described above (Kubo et al., 2010) were intriguing in terms of the cell alignment profile, it was not clear whether Reelin directly promoted adhesion among neurons or rather caused them to form aggregates as a result of being repelled by the surrounding cellular environment. A more recent study showed that Reelin directly promoted adhesion among dissociated neurons in culture (Matsunaga et al., 2017). Moreover, direct measurement of the adhesive forces revealed that Reelin promotes neuronal adhesion to N-cadherin during the aggregate formation (Matsunaga et al., 2017). Consistent with this, inhibition of N-cadherin impaired the neuronal aggregate formation induced by Reelin both *in vivo* and *in vitro*. Interestingly, the Reelin-induced enhancement of N-cadherin-dependent adhesion occurs only transiently (Matsunaga et al., 2017). These results clearly indicate that Reelin directly promotes adhesion among neurons during the aggregate formation. Future studies on the molecular and cellular mechanisms underlying the dynamic changes of N-cadherin-mediated cellular adhesiveness induced by Reelin may be expected to provide a more precise understanding of how appropriate layering of the neocortical neurons is regulated.

What is the physiological significance of the transient neuronal accumulation process observed in the PCZ? One possibility is that the neuronal aggregate itself might produce the physical force needed for the neurons to enter the PCZ. Since the PCZ is already densely packed with the neurons that arrived earlier, the subsequently arriving neurons might need to undergo some cellular changes, such as in their adhesive properties or in the cytoskeletal structure, to intercalate into the crowded environment. Consistent with this idea, migrating neurons start to express various genes when they arrive beneath the PCZ (Tachikawa et al., 2008). Or, neuronal aggregation might help in properly terminating radial migration at the border between the CP and MZ. Previous reports have revealed that the termination of neuronal migration is strictly regulated by the Reelin signal. When neurons reach the top of the CP, Reelin induces degradation of Dab1 via a SOCS7-Cul5-Rbx2-mediated proteasome pathway to inhibit further migration (Arnaud et al., 2003; Feng et al., 2007; Simo et al., 2010; Simo and Cooper, 2013). Multiple lines of evidence have demonstrated that Reelin signaling is required for polarized neurite growth (Niu et al., 2004; Olson et al., 2006; Jossin and Goffinet, 2007; Matsuki et al., 2010; Miyata et al., 2010; Nichols and Olson, 2010; Jossin and Cooper, 2011; O'Dell et al., 2012). A recent study has suggested that Reelin signaling controls migration arrest via polarized dendritogenesis. O'Dell et al. showed, using multiphoton time-lapse imaging, that in *reeler* cortices, a subset of neurons retracted

and reorganized their arbors in an abnormal tangential direction away from the MZ upon completing migration (O'Dell et al., 2015). They also showed that the application of exogenous Reelin to *reeler* explants restored the polarized dendritogenesis, suggesting that Reelin-dependent dendritogenesis is closely related to the migration arrest beneath the MZ (O'Dell et al., 2015). Consistent with this, Reelin receptors are localized in the apical dendrites in the MZ (Hirota et al., 2015). A previous report showed that a large number of cortical neurons exist in the MZ of adult *Vldlr* KO mice, but not in that of *Apoer2* KO mice, suggesting that Vldlr is important for termination of the radial migration of neurons beneath the MZ (Hack et al., 2007). Another recent study reported observation of the overmigration phenotype in neonatal *Apoer2* KO mice (Hirota et al., 2016). Ectopic neurons in the MZ of the *Apoer2* KO mice might be eliminated from the MZ by cell death in the later postnatal stages. Together, accumulating evidence indicates that the Reelin signal is important for termination of the radial migration of neurons in the developing brain. It is important to determine, in a future study, how transient neuronal accumulation in the PCZ contributes to the completion and termination of neuronal migration.

FUTURE DIRECTIONS

In summary, Reelin signaling controls multiple steps of neuronal migration through shared and distinct molecular mechanisms. Reelin signaling has been shown to be involved in LIMK1/n-cofilin activation during somal/terminal translocation and migration in the IZ. Reelin-dependent regulation of the adhesion molecule N-cadherin plays important roles in somal/terminal translocation, multipolar-bipolar transition and cell aggregation. Reelin signaling is also involved in the activation of integrin α5β1, another adhesion molecule, during terminal translocation.

While various downstream key components of Reelin signaling have been identified, it still remains unknown how Reelin signaling controls the multiple processes of neuronal migration and layer formation in the developing brain. Defect in neuronal migration is known to be associated with several neurological disorders, including epilepsy and mental retardation. Lissencephaly is one of the severe developmental disorders that may result from impaired neuronal migration, and is characterized by complete or incomplete agyria of the cerebral cortex. Lissencephaly and cerebellar hypoplasia, a similar phenotype to that observed in the *reeler* mutant mice, have been observed in human patients carrying *reelin* mutations (Hong et al., 2000), suggesting that in both rodents and humans, dysregulated Reelin signaling causes neurological defects. Thus, molecules involved in Reelin signaling could be potential targets for therapeutic intervention against neurological disorders. Further studies of the precise mechanisms underlying the functions of Reelin in various processes of migration of neurons in the developing brain, including neuronal adhesion and aggregation, would increase our understanding of mammalian neocortical development under both physiological and pathological conditions.

AUTHOR CONTRIBUTIONS

All authors listed, have made substantial, direct and intellectual contribution to the work, and approved it for publication.

ACKNOWLEDGMENTS

This work was supported by KAKENHI (JP25440114, JP15H01219, JP15H02355, JP16H06482, JP15H01586) of the Ministry of Education, Culture, Sports, Science, and Technology of Japan (MEXT)/Japan Society for the Promotion of Science (JSPS), Brain Science Foundation, Takeda Science Foundation, Naito Foundation, Keio Gijuku Academic Development Funds, and Fukuzawa Memorial Fund for the Advancement of Education and Research.

REFERENCES

Ajioka, I., and Nakajima, K. (2005). Birth-date-dependent segregation of the mouse cerebral cortical neurons in reaggregation cultures. *Eur. J. Neurosci.* 22, 331–342. doi: 10.1111/j.1460-9568.2005.04214.x

Arnaud, L., Ballif, B. A., and Cooper, J. A. (2003). Regulation of protein tyrosine kinase signaling by substrate degradation during brain development. *Mol. Cell. Biol.* 23, 9293–9302. doi: 10.1128/MCB.23.24.9293-9302.2003

Assadi, A. H., Zhang, G., Beffert, U., McNeil, R. S., Renfro, A. L., Niu, S., et al. (2003). Interaction of reelin signaling and Lis1 in brain development. *Nat. Genet.* 35, 270–276. doi: 10.1038/ng1257

Ballif, B. A., Arnaud, L., Arthur, W. T., Guris, D., Imamoto, A., and Cooper, J. A. (2004). Activation of a Dab1/CrkL/C3G/Rap1 pathway in Reelin-stimulated neurons. *Curr. Biol.* 14, 606–610. doi: 10.1016/j.cub.2004.03.038

Bar, I., Lambert De Rouvroit, C., Royaux, I., Krizman, D. B., Dernoncourt, C., Ruelle, D., et al. (1995). A YAC contig containing the reeler locus with preliminary characterization of candidate gene fragments. *Genomics* 26, 543–549. doi: 10.1016/0888-7543(95)80173-J

Bock, H. H., Jossin, Y., Liu, P., Forster, E., May, P., Goffinet, A. M., et al. (2003). Phosphatidylinositol 3-kinase interacts with the adaptor protein Dab1 in response to Reelin signaling and is required for normal cortical lamination. *J. Biol. Chem.* 278, 38772–38779. doi: 10.1074/jbc.M306416200

Boyle, M. P., Bernard, A., Thompson, C. L., Ng, L., Boe, A., Mortrud, M., et al. (2011). Cell-type-specific consequences of Reelin deficiency in the mouse neocortex, hippocampus, and amygdala. *J. Comp. Neurol.* 519, 2061–2089. doi: 10.1002/cne.22655

Britto, J. M., Tait, K. J., Johnston, L. A., Hammond, V. E., Kalloniatis, M., and Tan, S. S. (2011). Altered speeds and trajectories of neurons migrating in the ventricular and subventricular zones of the reeler neocortex. *Cereb. Cortex* 21, 1018–1027. doi: 10.1093/cercor/bhq168

Britto, J. M., Tait, K. J., Lee, E. P., Gamble, R. S., Hattori, M., and Tan, S. S. (2014). Exogenous Reelin modifies the migratory behavior of neurons depending on cortical location. *Cereb. Cortex* 24, 2835–2847. doi: 10.1093/cercor/bht123

Caviness, V. S. Jr. (1982). Neocortical histogenesis in normal and reeler mice: a developmental study based upon [3H]thymidine autoradiography. *Brain Res.* 256, 293–302. doi: 10.1016/0165-3806(82)90141-9

Caviness, V. S. Jr., and Sidman, R. L. (1973). Time of origin or corresponding cell classes in the cerebral cortex of normal and reeler mutant mice: an autoradiographic analysis. *J. Comp. Neurol.* 148, 141–151. doi: 10.1002/cne.901480202

Chai, X., Forster, E., Zhao, S., Bock, H. H., and Frotscher, M. (2009). Reelin stabilizes the actin cytoskeleton of neuronal processes by inducing n-cofilin phosphorylation at serine3. *J. Neurosci.* 29, 288–299. doi: 10.1523/JNEUROSCI.2934-08.2009

Chai, X., Zhao, S., Fan, L., Zhang, W., Lu, X., Shao, H., et al. (2016). Reelin and cofilin cooperate during the migration of cortical neurons: a quantitative morphological analysis. *Development* 143, 1029–1040. doi: 10.1242/dev.134163

Chen, K., Ochalski, P. G., Tran, T. S., Sahir, N., Schubert, M., Pramatarova, A., et al. (2004). Interaction between Dab1 and CrkII is promoted by Reelin signaling. *J. Cell Sci.* 117, 4527–4536. doi: 10.1242/jcs.01320

D'Arcangelo, G., Homayouni, R., Keshvara, L., Rice, D. S., Sheldon, M., and Curran, T. (1999). Reelin is a ligand for lipoprotein receptors. *Neuron* 24, 471–479. doi: 10.1016/S0896-6273(00)80860-0

D'Arcangelo, G., Miao, G. G., Chen, S. C., Soares, H. D., Morgan, J. I., and Curran, T. (1995). A protein related to extracellular matrix proteins deleted in the mouse mutant reeler. *Nature* 374, 719–723. doi: 10.1038/374719a0

Englund, C., Fink, A., Lau, C., Pham, D., Daza, R. A., Bulfone, A., et al. (2005). Pax6, Tbr2, and Tbr1 are expressed sequentially by radial glia, intermediate progenitor cells, and postmitotic neurons in developing neocortex. *J. Neurosci.* 25, 247–251. doi: 10.1523/JNEUROSCI.2899-04.2005

Feng, L., Allen, N. S., Simo, S., and Cooper, J. A. (2007). Cullin 5 regulates Dab1 protein levels and neuron positioning during cortical development. *Genes Dev.* 21, 2717–2730. doi: 10.1101/gad.1604207

Fietz, S. A., Kelava, I., Vogt, J., Wilsch-Brauninger, M., Stenzel, D., Fish, J. L., et al. (2010). OSVZ progenitors of human and ferret neocortex are epithelial-like and expand by integrin signaling. *Nat. Neurosci.* 13, 690–699. doi: 10.1038/nn.2553

Franco, S. J., Martinez-Garay, I., Gil-Sanz, C., Harkins-Perry, S. R., and Muller, U. (2011). Reelin regulates cadherin function via Dab1/Rap1 to control neuronal migration and lamination in the neocortex. *Neuron* 69, 482–497. doi: 10.1016/j.neuron.2011.01.003

Gal, J. S., Morozov, Y. M., Ayoub, A. E., Chatterjee, M., Rakic, P., and Haydar, T. F. (2006). Molecular and morphological heterogeneity of neural precursors in the mouse neocortical proliferative zones. *J. Neurosci.* 26, 1045–1056. doi: 10.1523/JNEUROSCI.4499-05.2006

Gartner, A., Fornasiero, E. F., Munck, S., Vennekens, K., Seuntjens, E., Huttner, W. B., et al. (2012). N-cadherin specifies first asymmetry in developing neurons. *EMBO J.* 31, 1893–1903. doi: 10.1038/emboj.2012.41

Gil-Sanz, C., Franco, S. J., Martinez-Garay, I., Espinosa, A., Harkins-Perry, S., and Muller, U. (2013). Cajal-Retzius cells instruct neuronal migration by coincidence signaling between secreted and contact-dependent guidance cues. *Neuron* 79, 461–477. doi: 10.1016/j.neuron.2013.06.040

Hack, I., Hellwig, S., Junghans, D., Brunne, B., Bock, H. H., Zhao, S., et al. (2007). Divergent roles of ApoER2 and Vldlr in the migration of cortical neurons. *Development* 134, 3883–3891. doi: 10.1242/dev.005447

Hansen, D. V., Lui, J. H., Parker, P. R., and Kriegstein, A. R. (2010). Neurogenic radial glia in the outer subventricular zone of human neocortex. *Nature* 464, 554–561. doi: 10.1038/nature08845

Hara, Y., Fukaya, M., Hayashi, K., Kawauchi, T., Nakajima, K., and Sakagami, H. (2016). ADP ribosylation factor 6 regulates neuronal migration in the developing cerebral cortex through FIP3/Arfophilin-1-dependent Endosomal trafficking of N-cadherin. *eNeuro* 3:ENEURO.0148-16.2016. doi: 10.1523/ENEURO.0148-16.2016

Hiesberger, T., Trommsdorff, M., Howell, B. W., Goffinet, A., Mumby, M. C., Cooper, J. A., et al. (1999). Direct binding of Reelin to VLDL receptor and ApoE receptor 2 induces tyrosine phosphorylation of disabled-1 and modulates tau phosphorylation. *Neuron* 24, 481–489. doi: 10.1016/S0896-6273(00)80861-2

Hirota, Y., Kubo, K. I., Fujino, T., Yamamoto, T. T., and Nakajima, K. (2016). ApoER2 controls not only neuronal migration in the intermediate zone but also termination of migration in the developing cerebral cortex. *Cereb. Cortex*. doi: 10.1093/cercor/bhw369. [Epub ahead of print].

Hirota, Y., Kubo, K., Katayama, K., Honda, T., Fujino, T., Yamamoto, T. T., et al. (2015). Reelin receptors ApoER2 and VLDLR are expressed in distinct spatiotemporal patterns in developing mouse cerebral cortex. *J. Comp. Neurol.* 523, 463–478. doi: 10.1002/cne.23691

Hirotsune, S., Takahara, T., Sasaki, N., Hirose, K., Yoshiki, A., Ohashi, T., et al. (1995). The reeler gene encodes a protein with an EGF-like motif expressed by pioneer neurons. *Nat. Genet.* 10, 77–83. doi: 10.1038/ng0595-77

Honda, T., and Nakajima, K. (2006). Mouse Disabled1 (DAB1) is a nucleocytoplasmic shuttling protein. *J. Biol. Chem.* 281, 38951–38965. doi: 10.1074/jbc.M609061200

Honda, T., and Nakajima, K. (2016). Proper level of Cytosolic Disabled-1, which is regulated by dual nuclear translocation pathways, is important for cortical neuronal migration. *Cereb. Cortex* 26, 3219–3236. doi: 10.1093/cercor/bhv162

Hong, S. E., Shugart, Y. Y., Huang, D. T., Shahwan, S. A., Grant, P. E., Hourihane, J. O., et al. (2000). Autosomal recessive lissencephaly with cerebellar hypoplasia is associated with human RELN mutations. *Nat. Genet.* 26, 93–96. doi: 10.1038/79246

Howell, B. W., Herrick, T. M., and Cooper, J. A. (1999). Reelin-induced tyrosine [corrected] phosphorylation of disabled 1 during neuronal positioning. *Genes Dev.* 13, 643–648. doi: 10.1101/gad.13.6.643

Howell, B. W., Herrick, T. M., Hildebrand, J. D., Zhang, Y., and Cooper, J. A. (2000). Dab1 tyrosine phosphorylation sites relay positional signals during mouse brain development. *Curr. Biol.* 10, 877–885. doi: 10.1016/S0960-9822(00)00608-4

Huang, Y., Magdaleno, S., Hopkins, R., Slaughter, C., Curran, T., and Keshvara, L. (2004). Tyrosine phosphorylated Disabled 1 recruits Crk family adapter proteins. *Biochem. Biophys. Res. Commun.* 318, 204–212. doi: 10.1016/j.bbrc.2004.04.023

Jossin, Y., and Cooper, J. A. (2011). Reelin, Rap1 and N-cadherin orient the migration of multipolar neurons in the developing neocortex. *Nat. Neurosci.* 14, 697–703. doi: 10.1038/nn.2816

Jossin, Y., and Goffinet, A. M. (2007). Reelin signals through phosphatidylinositol 3-kinase and Akt to control cortical development and through mTor to regulate dendritic growth. *Mol. Cell. Biol.* 27, 7113–7124. doi: 10.1128/MCB.00928-07

Jossin, Y., Gui, L., and Goffinet, A. M. (2007). Processing of Reelin by embryonic neurons is important for function in tissue but not in dissociated cultured neurons. *J. Neurosci.* 27, 4243–4252. doi: 10.1523/JNEUROSCI.0023-07.2007

Kawauchi, T., Sekine, K., Shikanai, M., Chihama, K., Tomita, K., Kubo, K., et al. (2010). Rab GTPases-dependent endocytic pathways regulate neuronal migration and maturation through N-cadherin trafficking. *Neuron* 67, 588–602. doi: 10.1016/j.neuron.2010.07.007

Kojima, T., Nakajima, K., and Mikoshiba, K. (2000). The disabled 1 gene is disrupted by a replacement with L1 fragment in yotari mice. *Brain Res. Mol. Brain Res.* 75, 121–127. doi: 10.1016/S0169-328X(99)00313-7

Kubo, K., Honda, T., Tomita, K., Sekine, K., Ishii, K., Uto, A., et al. (2010). Ectopic Reelin induces neuronal aggregation with a normal birthdate-dependent "inside-out" alignment in the developing neocortex. *J. Neurosci.* 30, 10953–10966. doi: 10.1523/JNEUROSCI.0486-10.2010

Kuo, G., Arnaud, L., Kronstad-O'Brien, P., and Cooper, J. A. (2005). Absence of Fyn and Src causes a reeler-like phenotype. *J. Neurosci.* 25, 8578–8586. doi: 10.1523/JNEUROSCI.1656-05.2005

Matsuki, T., Matthews, R. T., Cooper, J. A., van der Brug, M. P., Cookson, M. R., Hardy, J. A., et al. (2010). Reelin and stk25 have opposing roles in neuronal polarization and dendritic Golgi deployment. *Cell* 143, 826–836. doi: 10.1016/j.cell.2010.10.029

Matsunaga, Y., Noda, M., Murakawa, H., Hayashi, K., Nagasaka, A., Inoue, S., et al. (2017). Reelin transiently promotes N-cadherin-dependent neuronal adhesion during mouse cortical development. *Proc. Natl. Acad. Sci. U.S.A.* 114, 2048–2053. doi: 10.1073/pnas.1615215114

Mikoshiba, K., Kohsaka, S., Takamatsu, K., Aoki, E., and Tsukada, Y. (1980). Morphological and biochemical studies on the cerebral cortex from reeler mutant mice: development of cortical layers and metabolic mapping by the deoxyglucose method. *J. Neurochem.* 34, 835–844. doi: 10.1111/j.1471-4159.1980.tb09655.x

Miyata, T., Kawaguchi, A., Okano, H., and Ogawa, M. (2001). Asymmetric inheritance of radial glial fibers by cortical neurons. *Neuron* 31, 727–741. doi: 10.1016/S0896-6273(01)00420-2

Miyata, T., Ono, Y., Okamoto, M., Masaoka, M., Sakakibara, A., Kawaguchi, A., et al. (2010). Migration, early axonogenesis, and Reelin-dependent layer-forming behavior of early/posterior-born Purkinje cells in the developing mouse lateral cerebellum. *Neural Dev.* 5:23. doi: 10.1186/1749-8104-5-23

Nadarajah, B., Brunstrom, J. E., Grutzendler, J., Wong, R. O., and Pearlman, A. L. (2001). Two modes of radial migration in early development of the cerebral cortex. *Nat. Neurosci.* 4, 143–150. doi: 10.1038/83967

Nichols, A. J., and Olson, E. C. (2010). Reelin promotes neuronal orientation and dendritogenesis during preplate splitting. *Cereb. Cortex* 20, 2213–2223. doi: 10.1093/cercor/bhp303

Niu, S., Renfro, A., Quattrocchi, C. C., Sheldon, M., and D'Arcangelo, G. (2004). Reelin promotes hippocampal dendrite development through the VLDLR/ApoER2-Dab1 pathway. *Neuron* 41, 71–84. doi: 10.1016/S0896-6273(03)00819-5

Noctor, S. C., Flint, A. C., Weissman, T. A., Dammerman, R. S., and Kriegstein, A. R. (2001). Neurons derived from radial glial cells establish radial units in neocortex. *Nature* 409, 714–720. doi: 10.1038/35055553

Noctor, S. C., Martinez-Cerdeno, V., Ivic, L., and Kriegstein, A. R. (2004). Cortical neurons arise in symmetric and asymmetric division zones and migrate through specific phases. *Nat. Neurosci.* 7, 136–144. doi: 10.1038/nn1172

O'Dell, R. S., Cameron, D. A., Zipfel, W. R., and Olson, E. C. (2015). Reelin prevents apical neurite retraction during terminal translocation and dendrite initiation. *J. Neurosci.* 35, 10659–10674. doi: 10.1523/JNEUROSCI.1629-15.2015

O'Dell, R. S., Ustine, C. J., Cameron, D. A., Lawless, S. M., Williams, R. M., Zipfel, W. R., et al. (2012). Layer 6 cortical neurons require Reelin-Dab1 signaling for cellular orientation, Golgi deployment, and directed neurite growth into the marginal zone. *Neural Dev.* 7:25. doi: 10.1186/1749-8104-7-25

Ogawa, M., Miyata, T., Nakajima, K., Yagyu, K., Seike, M., Ikenaka, K., et al. (1995). The reeler gene-associated antigen on Cajal-Retzius neurons is a crucial molecule for laminar organization of cortical neurons. *Neuron* 14, 899–912. doi: 10.1016/0896-6273(95)90329-1

Olson, E. C., Kim, S., and Walsh, C. A. (2006). Impaired neuronal positioning and dendritogenesis in the neocortex after cell-autonomous Dab1 suppression. *J. Neurosci.* 26, 1767–1775. doi: 10.1523/JNEUROSCI.3000-05.2006

Pramatarova, A., Ochalski, P. G., Chen, K., Gropman, A., Myers, S., Min, K. T., et al. (2003). Nck beta interacts with tyrosine-phosphorylated disabled 1 and redistributes in Reelin-stimulated neurons. *Mol. Cell. Biol.* 23, 7210–7221. doi: 10.1128/MCB.23.20.7210-7221.2003

Rakic, P. (1972). Mode of cell migration to the superficial layers of fetal monkey neocortex. *J. Comp. Neurol.* 145, 61–83. doi: 10.1002/cne.901450105

Sekine, K., Honda, T., Kawauchi, T., Kubo, K., and Nakajima, K. (2011). The outermost region of the developing cortical plate is crucial for both the switch of the radial migration mode and the dab1-dependent "inside-out" lamination in the neocortex. *J. Neurosci.* 31, 9426–9439. doi: 10.1523/JNEUROSCI.0650-11.2011

Sekine, K., Kawauchi, T., Kubo, K., Honda, T., Herz, J., Hattori, M., et al. (2012). Reelin controls neuronal positioning by promoting cell-matrix adhesion via inside-out activation of integrin α5β1. *Neuron* 76, 353–369. doi: 10.1016/j.neuron.2012.07.020

Sheldon, M., Rice, D. S., D'Arcangelo, G., Yoneshima, H., Nakajima, K., Mikoshiba, K., et al. (1997). Scrambler and yotari disrupt the disabled gene and produce a reeler-like phenotype in mice. *Nature* 389, 730–733. doi: 10.1038/39601

Simo, S., and Cooper, J. A. (2013). Rbx2 regulates neuronal migration through different cullin 5-RING ligase adaptors. *Dev. Cell* 27, 399–411. doi: 10.1016/j.devcel.2013.09.022

Simo, S., Jossin, Y., and Cooper, J. A. (2010). Cullin 5 regulates cortical layering by modulating the speed and duration of Dab1-dependent neuronal migration. *J. Neurosci.* 30, 5668–5676. doi: 10.1523/JNEUROSCI.0035-10.2010

Smart, I. H., Dehay, C., Giroud, P., Berland, M., and Kennedy, H. (2002). Unique morphological features of the proliferative zones and postmitotic compartments of the neural epithelium giving rise to striate and extrastriate cortex in the monkey. *Cereb. Cortex* 12, 37–53. doi: 10.1093/cercor/12.1.37

Sweet, H. O., Bronson, R. T., Johnson, K. R., Cook, S. A., and Davisson, M. T. (1996). Scrambler, a new neurological mutation of the mouse with abnormalities of neuronal migration. *Mamm. Genome* 7, 798–802. doi: 10.1007/s003359900240

Tabata, H., Hachiya, T., Nagata, K., Sakakibara, Y., and Nakajima, K. (2013). Screening for candidate genes involved in the production of mouse subventricular zone proliferative cells and an estimation of their changes in evolutionary pressure during primate evolution. *Front. Neuroanat.* 7:24. doi: 10.3389/fnana.2013.00024

Tabata, H., Kanatani, S., and Nakajima, K. (2009). Differences of migratory behavior between direct progeny of apical progenitors and basal progenitors in the developing cerebral cortex. *Cereb. Cortex* 19, 2092–2105. doi: 10.1093/cercor/bhn227

Tabata, H., and Nakajima, K. (2003). Multipolar migration: the third mode of radial neuronal migration in the developing cerebral cortex. *J. Neurosci.* 23, 9996–10001.

Tabata, H., Yoshinaga, S., and Nakajima, K. (2012). Cytoarchitecture of mouse and human subventricular zone in developing cerebral neocortex. *Exp. Brain Res.* 216, 161–168. doi: 10.1007/s00221-011-2933-3

Tachikawa, K., Sasaki, S., Maeda, T., and Nakajima, K. (2008). Identification of molecules preferentially expressed beneath the marginal zone in the developing cerebral cortex. *Neurosci. Res.* 60, 135–146. doi: 10.1016/j.neures.2007.10.006

Trommsdorff, M., Gotthardt, M., Hiesberger, T., Shelton, J., Stockinger, W., Nimpf, J., et al. (1999). Reeler/Disabled-like disruption of neuronal migration in knockout mice lacking the VLDL receptor and ApoE receptor 2. *Cell* 97, 689–701. doi: 10.1016/S0092-8674(00)80782-5

Uchida, T., Baba, A., Perez-Martinez, F. J., Hibi, T., Miyata, T., Luque, J. M., et al. (2009). Downregulation of functional Reelin receptors in projection neurons implies that primary Reelin action occurs at early/premigratory stages. *J. Neurosci.* 29, 10653–10662. doi: 10.1523/JNEUROSCI.0345-09.2009

Ware, M. L., Fox, J. W., Gonzalez, J. L., Davis, N. M., Lambert de Rouvroit, C., Russo, C. J., et al. (1997). Aberrant splicing of a mouse disabled homolog, mdab1, in the scrambler mouse. *Neuron* 19, 239–249. doi: 10.1016/S0896-6273(00)80936-8

Yoneshima, H., Nagata, E., Matsumoto, M., Yamada, M., Nakajima, K., Miyata, T., et al. (1997). A novel neurological mutant mouse, yotari, which exhibits reeler-like phenotype but expresses CR-50 antigen/reelin. *Neurosci. Res.* 29, 217–223. doi: 10.1016/S0168-0102(97)00088-6

Yoshida, M., Assimacopoulos, S., Jones, K. R., and Grove, E. A. (2006). Massive loss of Cajal-Retzius cells does not disrupt neocortical layer order. *Development* 133, 537–545. doi: 10.1242/dev.02209

Conflict of Interest Statement: The authors declare that the research was conducted in the absence of any commercial or financial relationships that could be construed as a potential conflict of interest.

frontiers in Cell and Developmental Biology

ORIGINAL RESEARCH
published: 27 December 2016
doi: 10.3389/fcell.2016.00149

Inactivation of Sonic Hedgehog Signaling and Polydactyly in Limbs of Hereditary Multiple Malformation, a Novel Type of *Talpid* Mutant

*Yoshiyuki Matsubara[1†], Mikiharu Nakano[2†], Kazuki Kawamura[1†], Masaoki Tsudzuki[3], Jun-Ichi Funahashi[4], Kiyokazu Agata[5], Yoichi Matsuda[2,6], Atsushi Kuroiwa[1] and Takayuki Suzuki[1]**

[1] Division of Biological Science, Graduate School of Science, Nagoya University, Nagoya, Japan, [2] Avian Bioscience Research Center, Graduate School of Bioagricultural Sciences, Nagoya University, Nagoya, Japan, [3] Laboratory of Animal Breeding and Genetics, Graduate School of Biosphere Science, Hiroshima University, Hiroshima, Japan, [4] Institute of Development, Aging and Cancer, Tohoku University, Sendai, Japan, [5] Department of Biophysics, Graduate School of Science, Kyoto University, Kyoto, Japan, [6] Laboratory of Animal Genetics, Department of Applied Molecular Biosciences, Graduate School of Bioagricultural Sciences, Nagoya University, Nagoya, Japan

OPEN ACCESS

Edited by:
Takaaki Matsui,
Nara Institute of Science and Technology, Japan

Reviewed by:
Minoru Omi,
Fujita Health University, Japan
Joseph Lancman,
Sanford Burnham Prebys Medical Discovery Institute, USA

***Correspondence:**
Takayuki Suzuki
suzuki.takayuki@j.mbox.nagoya-u.ac.jp

[†]These authors have contributed equally to this work.

Specialty section:
This article was submitted to Cell Adhesion and Migration, a section of the journal Frontiers in Cell and Developmental Biology

Received: 08 November 2016
Accepted: 13 December 2016
Published: 27 December 2016

Citation:
Matsubara Y, Nakano M, Kawamura K, Tsudzuki M, Funahashi J-I, Agata K, Matsuda Y, Kuroiwa A and Suzuki T (2016) Inactivation of Sonic Hedgehog Signaling and Polydactyly in Limbs of Hereditary Multiple Malformation, a Novel Type of Talpid Mutant. Front. Cell Dev. Biol. 4:149. doi: 10.3389/fcell.2016.00149

Hereditary Multiple Malformation (HMM) is a naturally occurring, autosomal recessive, homozygous lethal mutation found in Japanese quail. Homozygote embryos ($hmm^{-/-}$) show polydactyly similar to $talpid^2$ and $talpid^3$ mutants. Here we characterize the molecular profile of the $hmm^{-/-}$ limb bud and identify the cellular mechanisms that cause its polydactyly. The $hmm^{-/-}$ limb bud shows a severe lack of sonic hedgehog (SHH) signaling, and the autopod has 4 to 11 unidentifiable digits with syn-, poly-, and brachydactyly. The Zone of Polarizing Activity (ZPA) of the $hmm^{-/-}$ limb bud does not show polarizing activity regardless of the presence of SHH protein, indicating that either the secretion pathway of SHH is defective or the SHH protein is dysfunctional. Furthermore, mesenchymal cells in the $hmm^{-/-}$ limb bud do not respond to ZPA transplanted from the normal limb bud, suggesting that signal transduction downstream of SHH is also defective. Since primary cilia are present in the $hmm^{-/-}$ limb bud, the causal gene must be different from $talpid^2$ and $talpid^3$. In the $hmm^{-/-}$ limb bud, a high amount of GLI3A protein is expressed and GLI3 protein is localized to the nucleus. Our results suggest that the regulatory mechanism of GLI3 is disorganized in the $hmm^{-/-}$ limb bud.

Keywords: sonic hedgehog, polydactyly, quail, Hereditary Multiple Malformation

INTRODUCTION

Avian mutants have often been used to study developmental mechanisms, especially embryonic pattern formation. Some of the most well studied mutant strains in chickens are the *talpids* (*talpid*, $talpid^2$, and $talpid^3$) (Cole, 1942). These three *talpid* mutants are naturally occurring and were independently discovered. The original *talpid* mutation has since been lost, but $talpid^2$ and $talpid^3$ are still maintained in the UK and the USA. Intriguingly, these mutants share a unique phenotype characterized by polydactyly, craniofacial abnormality, autosomal recessive inheritance,

and embryonic lethality. The gene responsible for *talpid*^{2} was identified as *C2CD3* (Chang et al., 2014), whereas the gene responsible for *talpid*^{3} is *KIAA0586* (Davey et al., 2006). These causal genes are both involved in the formation of primary cilia (Yin et al., 2009; Chang et al., 2014).

The primary cilium is thought to be necessary for intermediate sonic hedgehog (SHH) signaling because it provides a location for the processing of the transcriptional factor GLI3 (Besse et al., 2011). SHH is secreted from the Zone of Polarizing Activity (ZPA), which is located at the posterior edge of the limb bud, and determines the limb's anterior-posterior (AP) axis (Riddle et al., 1993). In the absence of SHH, GLI3 is located in the primary cilium and is phosphorylated by protein kinase A (Wang et al., 2000; Hsu et al., 2011). Phosphorylated GLI3 is ubiquitinated, resulting in partial degradation (Bhatia et al., 2006). This short form of GLI3, called GLI3R, inhibits the transcription of target genes (Wang et al., 2000). In the presence of SHH, GLI3 is maintained in a long activator form called GLI3A (Litingtung et al., 2002). GLI3A induces expression of target genes such as *Patched1* (*Ptch1*).

Interestingly, although both C2CD3 and KIAA0586 proteins are necessary for the ciliogenesis pathway to proceed, the *talpid*^{2} and *talpid*^{3} mutants indicate they have different impacts on SHH signaling. In the *talpid*^{2} limb bud, SHH signaling is constitutively activated by the upregulation of GLI3A, which causes anterior expansion of *Ptch1*, *Bmp4*, *Fgf4*, and *Hoxd13* expression (Rodriguez et al., 1996; Caruccio et al., 1999). In contrast, SHH signaling is abolished in the *talpid*^{3} limb bud leading to downregulation of *Ptch1* and *Gli1* expression, but GLI3A is still upregulated (Davey et al., 2006) as in the *talpid*^{2} mutant. It is known that in *Shh* deficient conditions only GLI3R is present, resulting in the formation of only digit 1 in the hindlimb and undetectable expression of *Ptch1* and *Gli1* (Chiang et al., 2001). The *talpid*^{3} mutant is thought to be similar, but it is still unclear why the SHH signaling pathway is defective in the *talpid*^{3} mutant despite up-regulation of GLI3A.

The HMM mutant was reported as a similar mutant phenotype to *talpid* in 1998 (Tsudzuki et al., 1998). It is a naturally occurring, autosomal recessive, homozygous lethal Japanese quail mutant. The gene responsible for *hmm* is still unknown. Homozygote embryos show polydactyly and shortened lower and upper beaks, which is slightly different from the *talpid*^{2} mutant phenotype of an extended lower beak compared to the upper beak (Chang et al., 2014). The HMM mutant also does not display the subcutaneous edema and hemorrhage over the thigh and neck regions found in the *talpid*^{2} and *talpid*^{3} mutants (Tsudzuki et al., 1998). Based on these observations, the developmental causes of the HMM mutant are likely different from the *talpid*^{2} and *talpid*^{3} mutants.

Here we characterize the molecular profile of the HMM mutant and perform a functional analysis of the cellular mechanisms that cause the mutant phenotype. Gene expression patterns indicate that SHH signaling is defective in the homozygous HMM mutant (*hmm*$^{-/-}$), similar to the *talpid*^{3} mutant. However, the limb bud in the *hmm*$^{-/-}$ embryo still has anterior-posterior polarity with restricted anterior marker gene expression. This is different from the limb bud patterning in *talpid*^{2} and *talpid*^{3}. Furthermore, we found that the ZPA in the *hmm*$^{-/-}$ limb bud does not show polarizing activity regardless of the presence of SHH protein expression. The primary cilium was present however, and we observed a high amount of GLI3A protein in the *hmm*$^{-/-}$ limb bud. These results indicate that different molecular pathways than *talpid*^{2} and *talpid*^{3} are defective in the *hmm*$^{-/-}$ limb bud.

MATERIALS AND METHODS

Embryos

The fertilized HMM mutant quail eggs were provided by Avian Bioscience Research center (ABRC) at Nagoya University. Embryos were staged according to Ainsworth et al. (2010). The HMM mutant shows autosomal recessive inheritance, although the causal gene, *hmm*, is still unknown. Heterozygous embryos showed no phenotype and were indistinguishable from wild-type embryos. Therefore we used a mixture of wild-type and heterozygous embryos as a control. Experimental procedures for isolating embryos were performed in accordance with guidelines set forth by the Regulations on Animal Experiments at Nagoya University. The embryo research was approved by Nagoya University Animal Experiment Committee (approval number 17).

Visualization of 3D Image of the Limb Bud by OPT Scanner

Limb buds were fixed with 4% PFA overnight and then embedded in 1% low-melting agarose (Lonza). Excess agarose around the limb was removed with a razor blade. After that, agarose containing the limb buds was attached to the swivel base with Loctite for optical projection tomography (OPT) scanning (Henkel). Limb buds were treated with 100% MeOH for 3 h, and samples cleared in a 1:2 solution of benzyl alcohol (Wako): benzyl benzoate (Wako) overnight. A 3D image was taken with the OPT scanner 3001 (Bioptonics) and visualized by Avizo software (Maxnet).

Skeletal Staining and *In situ* Hybridization

Victoria blue staining was performed as described previously (Suzuki et al., 2008). Embryos were dissected in PBS and fixed in 10% Formalin overnight at room temperature. Embryos were stained overnight with 1% Victoria blue (Sigma) solution containing 1% HCl, and 70% EtOH. Embryos were washed overnight with 1% HCl in 70% EtOH solution following overnight treatment with 100% methylsalicylate to render them transparent.

In situ hybridization was performed as described previously (Suzuki et al., 2008). The following probes were used for *in situ* hybridizations: *Hoxa13* (Yokouchi et al., 1991), *Hoxd13* (Nelson et al., 1996), *Fgf8*, *Gli3*, *Alx4*, *Lhx9*, *Ptch2,* and *Bmp2* (kindly gifted by Dr. John. F. Fallon, University of Wisconsin-Madison), *Hand2* (kindly gifted by Dr. Kazuko Koshiba-Takeuchi, University of Tokyo), *Shh*, *Gli1*, and *Ptch1* (kindly gifted by Dr. Yuki Sato, Kyushu university), *Pax6* (kindly gifted by Dr. Yoshio Wakamatsu, Tohoku university), *Pax3*, *Pax7*, and *Dbx2* (kindly gifted by Dr. Harukazu Nakamura, Tohoku

university), *Islet1* (589–1551 bp, GenBank NM_205414), and *MyoD* (155–1051 bp, GenBank NM_204214).

Implantation of the ZPA

The ZPA was isolated from the posterior side of the donor limb bud with a sharpened tungsten needle. Isolated ZPA was placed in ice-cold Tyrode solution (137 mM NaCl, 2.7 mM KCl, 1 mM $MgCl_2$, 1.8 mM $CaCl_2$, 0.2 mM Na_2HPO_4, 12 mM $NaHCO_3$, 5.5 mM D-glucose) and divided into several pieces. A piece of the ZPA was stained by squirting it with DiI solution (1% DiI dissolved with 70% EtOH) in Tyrode solution, and it was implanted at the anterior side of the host limb bud with a tungsten needle.

Immunohistochemistry

Primary embryonic fibroblasts were isolated from the back region between the forelimb and the hindlimb at St. 35. Back tissues were dissected in PBS. After tissues were minced with a razor blade, they were incubated in 0.25% trypsin-EDTA solution (Wako) for 15 min at 37°C. An equal volume of 100% fetal calf serum was added. The supernatant of the cell suspension was plated on 3.5-cm glass-base tissue culture dish (IWAKI). The next day, cells were fixed with 4% PFA for 10 min at room temperature.

Limb buds were dissected in ice-cold PBS and fixed with 4% PFA for 15 min on ice. The PFA solution was immediately removed and fresh ice-cold PBS was added. The limb buds were treated with 30% sucrose in PBS overnight at 4°C and then embedded in compound for frozen sections (Leica). Samples were then sectioned by cryostat for immunohistochemistry.

Cells in frozen sections or fixed primary fibroblasts were permeabilized by treating with 0.2% TritonX-100 (Wako) for 20 min at room temperature, and then blocked with 3% BSA in PBS for 30 min. Anti-SHH antibody 5E1 (1:100) (DSHB), Anti-GLI3 antibody (1:100) (Santa Cruz sc-20688), and anti-acetylated Tubulin clone 6-11B-1 (1:1000) (Sigma) were diluted in 3% BSA/PBS solution. Samples were incubated overnight at 4°C with the primary antibody. The next day, samples were incubated with the secondary antibody (Alexa Fluor 488) (Thermo Fisher Scientific) diluted at 1:500 in 3% BSA/PBS solution for 2 h at room temperature. After 1 μg/ml of DAPI in PBS was added to the samples for 15 min, the samples were mounted with fluorescein mounting medium (Dako) and fluorescent images were taken with an Olympus FV1000 confocal microscope.

Western Blot Analysis

Fertilized eggs were incubated for 3.5 days. The limb buds of St. 23 embryos were isolated in ice-cold PBS with a tungsten needle and then collected in 1.5 mL collection tubes. After solubilizing the cells with 200 μl of lysis buffer (50 mM HEPES (pH 7.4), 150 mM NaCl, 10 mM EDTA, 1% Triton X-100, 200 mM sodium fluoride, 10% glycerol, 20 mM sodium pyrophosphate, 2 mM phenylmethane sulfonyl fluoride, 4 mM Na_3VO_4, 0.1 mg/ml leupeptin, and 15 mM benzamidine), the cell lysate was centrifuged at 14,000 g for 10 min. The supernatant was assayed for protein content using a Bio-Rad protein assay kit. The proteins were then resolved with SDS-polyacrylamide gel electrophoresis and electrotransferred to polyvinylidene difluoride membranes. After blocking with 5% (w/v) non-fat dry milk in Tris-buffered saline-Tween buffer (20 mM Tris (pH 7.6), 0.14 M NaCl, and 0.1% (w/v) Tween 20), the membranes were treated with primary antibodies, Anti-GLI3 antibody (1:1000) (Santa Cruz sc-20688), and Anti-αTubulin clone B-5-1-2 (1:2500) (Sigma). The proteins were visualized using an ECL Western blotting detection system.

RESULTS

Expanded Expression of *Fgf8* at the AER Is Observed in the *hmm*$^{-/-}$ Limb Bud

We previously reported that the *hmm*$^{-/-}$ embryo shows syndactylous polydactyly (Tsudzuki et al., 1998). It is still unclear how these phenotypes are induced in *hmm*$^{-/-}$ limb bud. In both *talpid*^{2} and *talpid*^{3} mutants, the limb bud is wider in size along the AP axis before cartilage condensation starts (Francis-West et al., 1995; Caruccio et al., 1999). This wider limb bud leads to expansion of the autopod, resulting in polydactyly (Litingtung et al., 2002). Therefore, we first examined the shape of the limb bud in the *hmm*$^{-/-}$ embryo. To compare the shape of the entire limb bud between the mutant and wild-type, we took OPT images (Sharpe et al., 2002) of the hind limb at St. 23, after the limb bud emerged from the body wall (**Figures 1A,B**). The *hmm*$^{-/-}$ limb bud was slightly wider than the *hmm*$^{+/+;+/-}$ (simplified hereafter as *hmm*$^{+/-}$) limb bud along the AP axis (**Figure 1A**). The *hmm*$^{-/-}$ limb bud was also expanded along the dorso-ventral (DV) axis compared to the *hmm*$^{+/-}$ limb bud (**Figure 1B**). To elucidate the mechanisms underlying the expansion of the limb bud along the AP axis, we compared the limb field's AP width between *hmm*$^{+/-}$ and *hmm*$^{-/-}$ embryos. We found that the anterior boundary of the *hmm*$^{-/-}$ forelimb bud (FLB) was expanded cranially compared to that of the *hmm*$^{+/-}$ FLB (**Figures 1C,E**). The AP width of the hindlimb bud (HLB) appeared to be the same in both *hmm*$^{+/-}$ and *hmm*$^{-/-}$ embryos (**Figures 1D,F**), implying that a different mechanism is involved in the expansion of the hindlimb along the AP axis. In the *talpid*^{2} mutant, the expansion of *Fgf8* expression at the apical ectodermal ridge (AER) along the AP axis is observed along with formation of a wider limb bud (Caruccio et al., 1999). Therefore, we checked the expression of *Fgf8* at St. 23 and St. 26 in the *hmm*$^{-/-}$ limb bud, and found that it was expanded into both the anterior and posterior ends close to the body wall (**Figures 1G–J**). Expansion of *Fgf8* expression was continued into St. 26, along with wider autopod formation in the *hmm*$^{-/-}$ embryo (**Figures 1K–N**). Taken together, these results suggest that mesenchymal cells of the *hmm*$^{-/-}$ limb bud propagate more than in the wild-type and give rise to a wider limb bud with an extended AER along the AP axis. In addition, the anterior boundary of the forelimb field is expanded in the *hmm*$^{-/-}$ embryo when the FLB is initiated.

Anterior-Posterior Polarity Is Disrupted in the *hmm*$^{-/-}$ Limb Bud

In the autopod of the *hmm*$^{-/-}$ embryo many of the digits are shortened during development (Tsudzuki et al., 1998). We

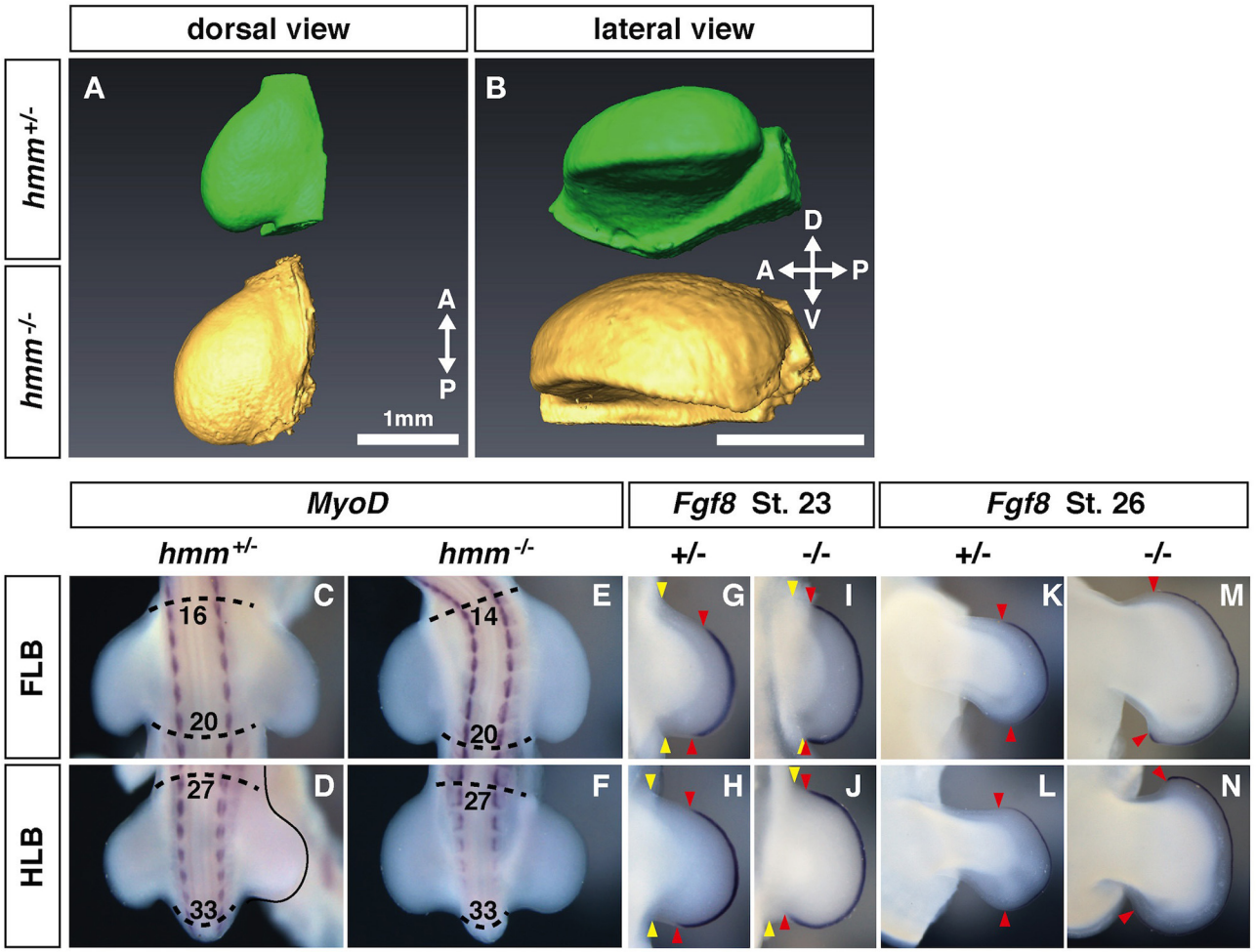

FIGURE 1 | Expression of *Fgf8* at the apical ectodermal ridge (AER) is expanded along the anterior-posterior (AP) axis in the *hmm*$^{-/-}$ limb bud. (A,B) Morphology of the limb at St. 22 as scanned by OPT. Dorsal view **(A)** and lateral view **(B)** of the *hmm*$^{+/-}$ (green) and *hmm*$^{-/-}$ (yellow) hindlimb buds. The scale bar indicates 1 mm. **(C–F)** *In situ* hybridization of *MyoD*. The dotted line shows the anterior and posterior end of the limb buds. Numbers indicate the position of the somite starting with the first somite. **(G–N)** *In situ* hybridization of *Fgf8*. Yellow arrowheads indicates the boundary between the limb bud and the body wall. Red arrowheads indicate the anterior and posterior boundaries of *Fgf8* expression at the AER. A, anterior; P, posterior; D, dorsal; V, ventral; FLB, forelimb bud; HLB, hindlimb bud.

therefore analyzed detailed patterns of polydactylous digits along the AP axis. In the *hmm*$^{+/-}$ HLB, digital rays 1, 2, 3, and 4 are formed correctly to their unique full lengths along the AP axis (**Figure 2A**). In contrast, we observed indistinguishable shortened digital rays in the *hmm*$^{-/-}$ HLB. We also found webbing along the AP axis of the digital ray sequence in the *hmm*$^{-/-}$ HLB. These results imply that anterior-posterior polarity is disrupted in the *hmm*$^{-/-}$ limb bud.

In order to identify the specific region where anterior-posterior polarity is disrupted, we performed victoria blue staining to visualize condensing cartilage at St. 35 (**Figure 2B**). In the forelimb, the *hmm*$^{-/-}$ embryo has four to eight digits with syn-, poly-, and brachdactyly, whereas the *hmm*$^{+/-}$ embryo has three digits (**Table 1**). The forelimb of *hmm*$^{-/-}$ has one shortened, thick humerus in the stylopod and an unidentifiable ulna/radius in the zeugopod. The hindlimb of the *hmm*$^{-/-}$ embryo also has one shortened, thick femur in the stylopod and an unidentifiable fibula/tibia in the zeugopod. The autopod of the *hmm*$^{-/-}$ hindlimb has seven to eleven digits (**Table 1**). Based on the morphological criteria of digit identity (number, size, and shape of the phalanges Suzuki, 2013), we assumed that the *hmm*$^{-/-}$ autopod has lost digit identity. We also found that the metacarpal/metatarsal bones were fused and the metacarpal/metatarsal-phalangeal joints were missing in the *hmm*$^{-/-}$ autopod (**Figure 2B** arrowhead). We observed the phalangeal joint in both the forelimb and the hindlimb, but its formation was incomplete. These results indicate that anterior-posterior polarity of both the forelimb and the hindlimb is disrupted in the *hmm*$^{-/-}$ embryo.

To understand the molecular mechanisms of anterior-posterior pattering deficiency in *hmm*$^{-/-}$ limbs, we next examined gene expression patterns of marker genes specifically expressed at the anterior/posterior sides. Genetic antagonism between *Hand2* and *Gli3* is necessary to establish AP polarity at

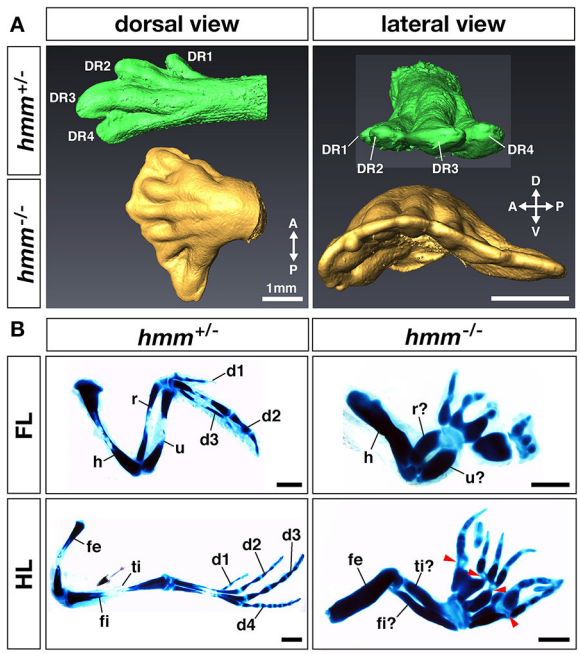

FIGURE 2 | Anterior-posterior polarity is disrupted in the *hmm*$^{-/-}$ limb bud. (A) Morphology of the limb at St. 34 as scanned by OPT. Dorsal view and lateral view of the *hmm*$^{+/-}$ (green) and *hmm*$^{-/-}$ (yellow) hindlimb buds are shown. The scale bar indicates 1 mm. **(B)** The skeletal pattern of the limb at St. 36. All images are oriented with the anterior side up and the posterior side down. Red arrowheads indicate immature metatarsal-phalangeal joints. The scale bar indicates 1 mm. A, anterior; P, posterior; D, dorsal; V, ventral; DR, digital ray; FL, forelimb; HL, hindlimb; d1-d4, digit 1-digit 4; h, humerus; r, radius; u, ulna; fe, femur; ti, tibia; fi, fibula.

TABLE 1 | Skeletal pattern of the autopod in HMM mutant.

Limb	Embryo	Number of metacarpals/ metatarsals	Number of digits	Number of phalanges
Right forelimb	Wild-type	3	3	221
	a	3	8	22211311
	b	3	4	2222
	c	3	7	11121nn
	d	4	5	n2222
	e	4	6	2212nn
	f	2	5	222nn
	g	3	6	22n2nn
Left forelimb	Wlid-type	3	3	221
	a	3	5	22211
	b	3	4	1122
	c	3	5	2122n
	d	4	6	1nn221
	e	2	6	1212nn
	f	4	5	1222n
	g	4	7	1nnn1nn
Right hindlimb	Wild-type	4	4	2345
	a	7	9	333322211
	b	4	8	32213233
	c	5	9	323221321
	d	6	11	32323213423
	e	5	7	3223423
	f	6	8	32233223
	g	5	8	32333424
Left hindlimb	Wild-type	4	4	2345
	a	8	10	3321212332
	b	4	8	32333233
	c	5	8	32333222
	d	6	10	3232133333
	e	6	8	32333333
	f	5	7	3333434
	g	5	8	31424224

n, non-countable.

the early limb bud stage (te Welscher et al., 2002a). We found that expression of *Hand2* was restricted at the posterior side in the *hmm*$^{+/-}$ limb bud. In contrast, in the *hmm*$^{-/-}$ limb bud we observed strong expression of *Hand2* at the posterior side and weak expression at the anterior side (**Figures 3A–D**). In the *hmm*$^{+/-}$ limb bud, *Gli3* was not expressed at the posterior side where *Hand2* was expressed (**Figures 3E,F**). In contrast, *Gli3* was expressed throughout the limb bud at the early stages in the *hmm*$^{-/-}$ limb bud (**Figures 3G,H**). *Alx4* was expressed at the anterior mesoderm at St. 23 in the *hmm*$^{+/-}$ limb bud (**Figures 3I,J**), but its expression was downregulated though still detectable in the *hmm*$^{-/-}$ limb bud (**Figures 3K,L**). At St. 25, *Alx4* was continuously expressed at the anterior side of the stylopod and zeugopod in the *hmm*$^{+/-}$ limb bud (**Figures 3I′,J′**). In the *hmm*$^{-/-}$ limb bud, its expression was still observed in the FLB (**Figure 3K′**) but not detectable in the HLB (**Figure 3L′**). *Lhx9* was expressed at the anterior side at St. 22 (**Figures 3M,N**) and at the anterior autopod at St. 25 (**Figures 3M′,N′**). In contrast to the expression of *Alx4*, expression of *Lhx9* was expanded to the posterior side in the *hmm*$^{-/-}$ limb bud (**Figures 3O–P′**). In particular, *Lhx9* expression was observed at the posterior end of the *hmm*$^{-/-}$ hindlimb autopod (**Figure 3P′**). Expression of *Hoxd13* was restricted to the posterior side in the *hmm*$^{+/-}$ limb bud at St. 22 (**Figures 3Q,R**), and at St. 25 its expression was observed at the posterior mesoderm in the autopod (**Figures 3Q′,R′**). Expression of *Hoxd13* was similarly restricted to the posterior side in the *hmm*$^{-/-}$ limb bud (**Figures 3S–T′**). We checked the autopod area for *Hoxa13* expression in the contra-lateral side (**Figures 3U–X**), and we saw that the autopod expanded along the AP axis in the *hmm*$^{-/-}$ limb bud at St. 25 (**Figures 3W,X**). However, expression of *Hoxd13* was still restricted to the posterior side (**Figures 3S′,T′**), the same as in the *hmm*$^{+/-}$ autopod (**Figures 3Q′,R′**). At St. 29 *Hoxd13* was expressed throughout the *hmm*$^{+/-}$ autopod except on the anterior side of digit 1 (**Figures 3Y,Z**). However, it was expressed all the way to the anterior end of the *hmm*$^{-/-}$ autopod (**Figures 3a,b**) along with *Hoxa13* (**Figures 3c–f**). From these results, we conclude that the *hmm*$^{-/-}$ limb bud partially

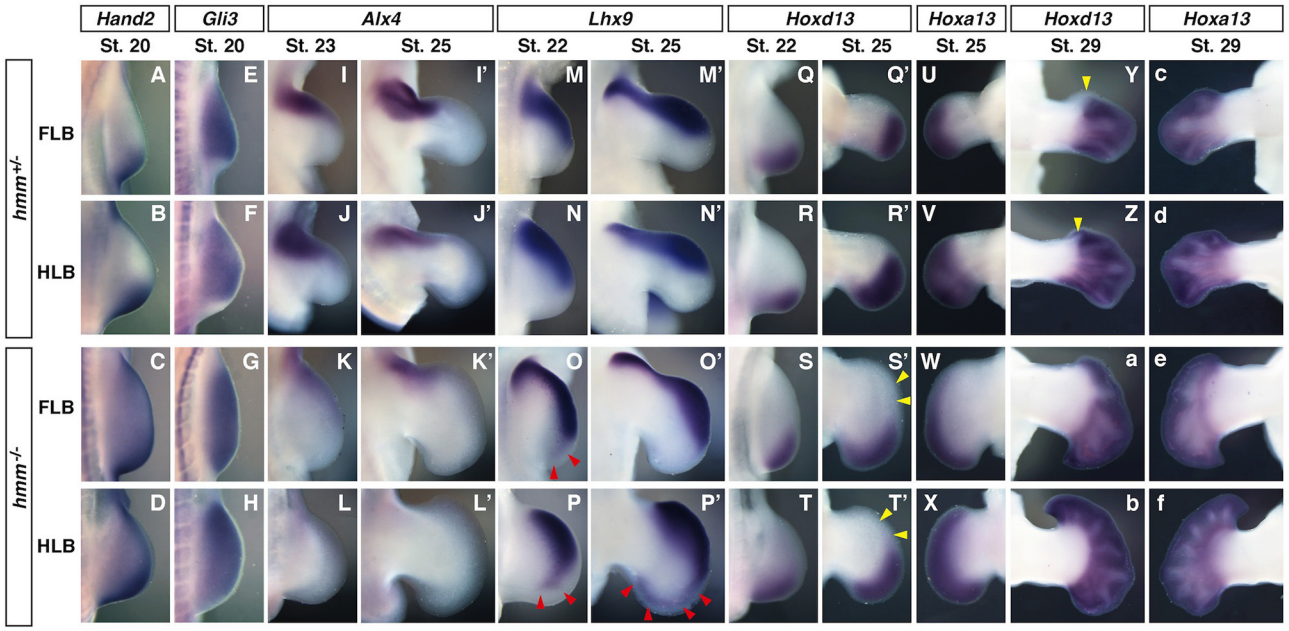

FIGURE 3 | Anterior-posterior polarity is partially maintained at the limb bud stage in the *hmm*$^{-/-}$ embryo. *In situ* hybridization of *Hand2* **(A–D)**, *Gli3* **(E–H)**, *Alx4* **(I–L′)**, *Lhx9* **(M–P′)**, *Hoxd13* **(Q–T′,Y–b)** and *Hoxa13* **(U–X,c–f)**. All images are oriented with the anterior side up and the posterior side down. **(O,P,P′)** Red arrowheads indicate the expanded expression domain of *Lhx9* on the posterior side. **(S′,T′)** Yellow arrowheads indicate the region where *Hoxd13* is not expressed in the autopod. **(Y,Z)** Yellow arrowheads indicate the region where *Hoxd13* is not expressed on the anterior side of the digit 1 primordium. FLB, forelimb bud; HLB, hindlimb bud.

maintains AP polarity at the limb bud stage (St. 20–25), but loses AP polarity at the late autopod stage (St. 29).

SHH Signaling is Reduced in the *hmm*$^{-/-}$ Limb Bud

As described above, AP polarity in the limb bud is disrupted in the *hmm*$^{-/-}$ embryo. It is known that expression of *hand2*, *Gli3*, and *Alx4* is altered by SHH signaling, which establishes anterior-posterior polarity in the limb (Takahashi et al., 1998; te Welscher et al., 2002a). We therefore examined the expression patterns of target genes downstream of SHH in the limb bud. Expression of *Shh* was restricted to the posterior edge of the *hmm*$^{+/-}$ limb bud (**Figures 4A,B**). In the *hmm*$^{-/-}$ limb bud, *Shh* was expressed at the posterior mesoderm; however, expression was restricted to a more proximal region of the FLB than in the *hmm*$^{+/-}$ limb bud (**Figure 4C**). On the other hand, the expression domain of *Shh* was expanded proximally in the HLB (**Figure 4D**).

Gli1, *Ptch1*, *Ptch2,* and *Bmp2* are known to be downstream target genes of SHH signaling that are expressed in response to SHH signaling (Chiang et al., 2001). In the *hmm*$^{+/-}$ limb bud, the expression domain of *Gli1* was expanded to the middle part of the limb bud along the anterior-posterior axis (**Figures 4E,F**). In contrast, *Gli1* was expressed uniformly at very low levels throughout the *hmm*$^{-/-}$ limb bud (**Figures 4G,H**). Similarly, *Ptch1* was expressed at the posterior half of the *hmm*$^{+/-}$ limb bud (**Figures 4I, J**), but in the *hmm*$^{-/-}$ limb bud was expressed uniformly at very low levels along the anterior-posterior axis (**Figures 4K,L**). In the *hmm*$^{+/-}$ limb bud *Ptch2* was expressed at the posterior mesoderm similarly to *Ptch1* (**Figures 4M,N**), but expression was not detected in the *hmm*$^{-/-}$ limb bud (**Figures 4O,P**). In the *hmm*$^{-/-}$ limb bud, expression of *Bmp2* was observed at the posterior edge in the FLB only, but in *hmm*$^{+/-}$ limb buds expression was observed at the posterior mesoderm in both the FLB and the HLB (**Figures 4Q–T**). The expression of *Gli1*, *Ptch1*, *Ptch2,* and *Bmp2* is reduced or lost in the limb bud of the *Shh*$^{-/-}$ mouse embryo (Litingtung et al., 2002), therefore SHH signaling must be substantially reduced despite the detection of *Shh* expression in the *hmm*$^{-/-}$ limb bud. Reduction of SHH signaling was also observed in the neural tube of the *hmm*$^{-/-}$ embryo (**Figure S1A**).

We next examined limb bud expression of *Gli3*, a transcriptional factor that mediates SHH signaling. In the *hmm*$^{+/-}$ limb bud *Gli3* was expressed in the mesenchyme in a complementary pattern to *Shh* expression (**Figures 4A,B,U,V**). In contrast, in the *hmm*$^{-/-}$ limb bud *Gli3* was strongly expressed throughout the limb bud, including in the *Shh*-expressing region (**Figures 4C,D,W,X**). We therefore concluded that the syndactylous polydactyly phenotype in the *hmm*$^{-/-}$ limb bud does not result simply from a loss of SHH signaling due to a defect in *Gli3* expression.

ZPA Derived from *hmm*$^{-/-}$ Limb Bud Does Not Have Polarizing Activity

In *hmm*$^{-/-}$ embryos, cells in the limb bud showed a reduction in SHH signaling despite expression of *Shh* (**Figure 4**). We therefore hypothesized that cells in the *hmm*$^{-/-}$ embryo might have lost

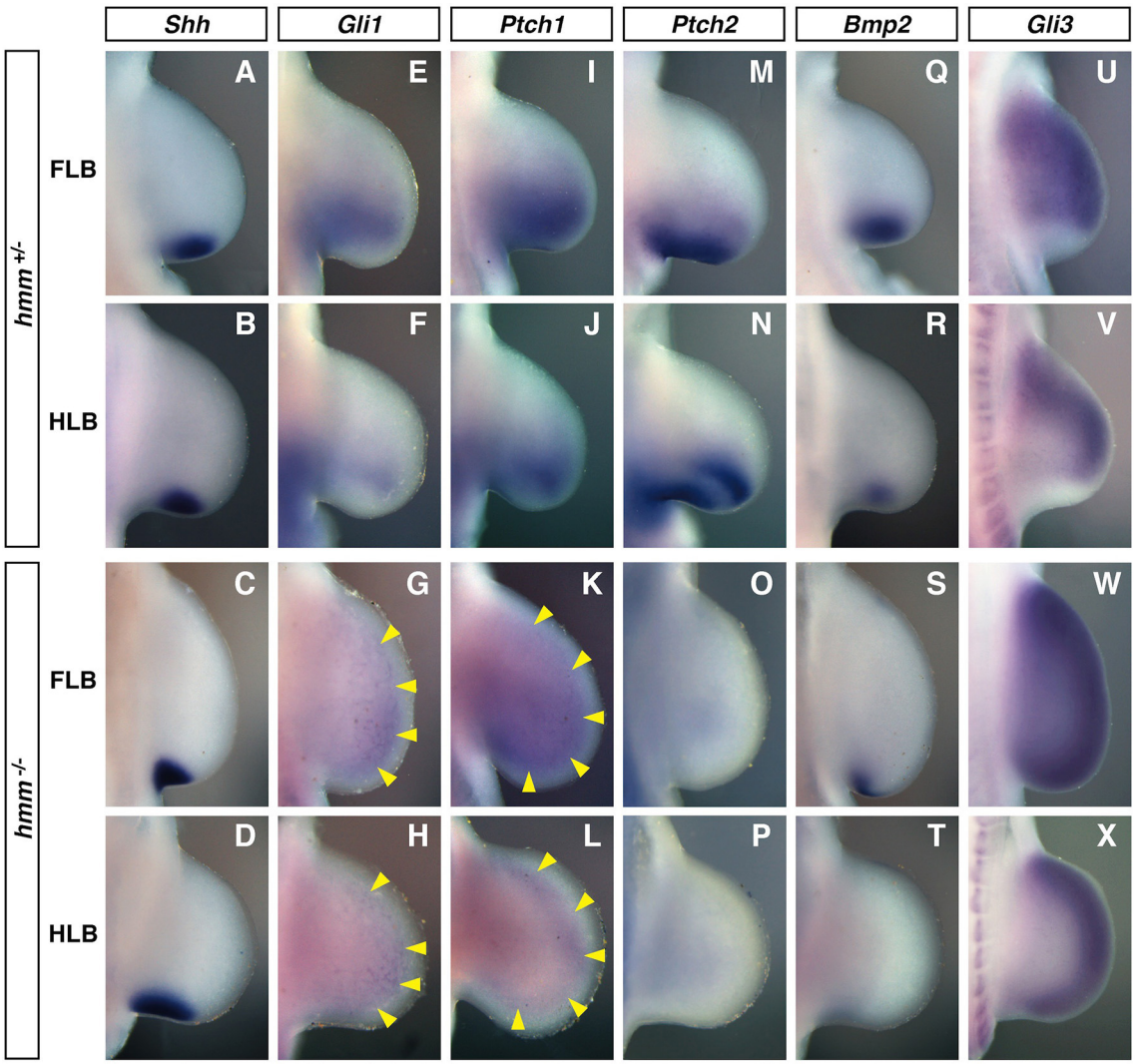

FIGURE 4 | SHH signaling is reduced in the *hmm*$^{-/-}$ limb bud. *In situ* hybridization of *Shh* **(A–D)**, *Gli1* **(E–H)**, *Ptch1* **(I–L)**, *Ptch2* **(M–P)**, *Bmp2* **(Q–T)**, and *Gli3* **(U–X)** at St. 22/23. All images are oriented with the anterior side up and the posterior side down. **(G–L)** Yellow arrowheads indicate the weak expression of *Gli1* and *Ptch1*. FLB, forelimb bud; HLB, hindlimb bud.

SHH protein activity or the ability to respond to SHH protein. To test these hypotheses, we analyzed the polarizing activity of the *hmm*$^{-/-}$ limb bud. When we grafted ZPA from the *hmm*$^{+/-}$ FLB to the anterior side of the *hmm*$^{+/-}$ FLB at St. 20, strong ectopic *Ptch2* expression was observed (83%, $n = 6$) (**Figure 5A**). In contrast, implantation of ZPA from the *hmm*$^{+/-}$ FLB to the *hmm*$^{-/-}$ FLB did not induce ectopic *Ptch2* expression (0%, $n = 4$) (**Figures 5B,C**). We next grafted ZPA from the *hmm*$^{-/-}$ FLB to the *hmm*$^{+/-}$ FLB. Unexpectedly, ectopic *Ptch2* expression was not induced (0%, $n = 8$) (**Figures 5D,E**). These results show that mesenchymal cells in the *hmm*$^{-/-}$ limb bud do not respond to SHH protein. Furthermore, despite the presence of *Shh* expression (**Figures 4C,D**), ZPA derived from the *hmm*$^{-/-}$ limb bud cannot induce expression of SHH signaling downstream targets.

We next examined the presence of SHH protein using immunohistochemistry. We found that the protein was detectable by anti-SHH antibody in the limb bud and the notochord in both *hmm*$^{+/-}$ (**Figures 6A,B**, **Figure S1B**) and *hmm*$^{-/-}$ (**Figures 6C,D**, **Figure S1B**) embryos. These observations raise the following possibilities in the *hmm*$^{-/-}$ embryo: first, the secretion pathway of the SHH protein is defective; second, the SHH protein is dysfunctional; and third, the SHH signaling pathway in the target tissues is disrupted.

High Expression of GLI3A Is Observed in the Presence of Primary Cilia in *hmm*$^{-/-}$ Limb Bud

It was recently reported that loss of primary cilia induces constitutive activation of SHH signaling through high expression

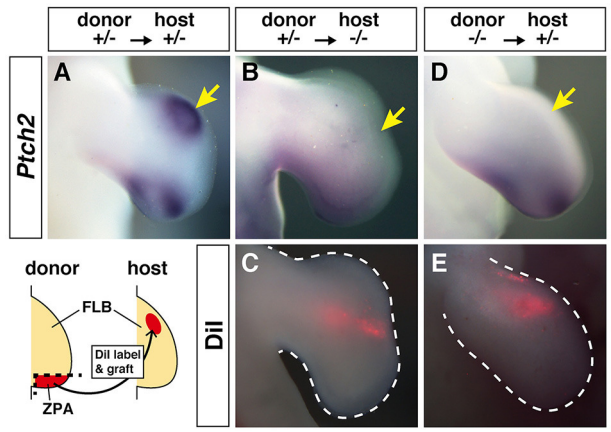

FIGURE 5 | Zone of Polarizing Activity (ZPA) derived from the *hmm*$^{-/-}$ limb bud does not have polarizing activity. (A,B,D) *In situ* hybridization of *Ptch2* after ZPA was implanted into the anterior limb bud. **(C,E)** Fluorescence of the implanted ZPA labeled with DiI is shown. The schematic drawing shows the grafting protocol of ZPA from the donor limb bud (*hmm*$^{+/-}$ or *hmm*$^{-/-}$) to the host limb bud (*hmm*$^{+/-}$ or *hmm*$^{-/-}$). The yellow arrows indicate the position of the implanted ZPA. FLB, forelimb bud.

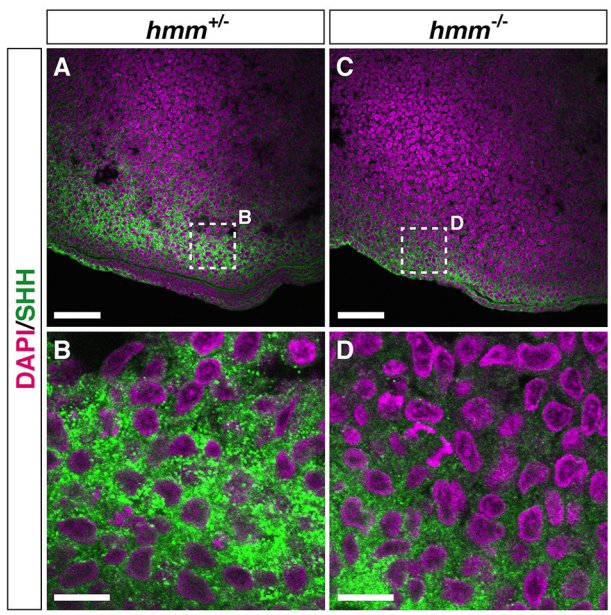

FIGURE 6 | SHH protein is detectable by immunohistochemistry in the *hmm*$^{-/-}$ limb bud. Immunohistochemistry of SHH protein at the posterior limb bud of the St. 23 embryo is shown with fluorescent green. The nucleus is stained with DAPI. Frontal sections are oriented with the anterior side up and the posterior side down. **(B,D)** Higher magnification of the area enclosed by the dotted square in **A** and **C**. Scale bars, 50 μm **(A,C)**, 10 μm **(B,D)**.

of GLI3A in both *talpid*^{2} and *talpid*^{3} mutants (Davey et al., 2006; Chang et al., 2014). Therefore, we visualized the primary cilia using immunohistochemistry targeting acetylated tubulin. However, we found that primary cilia were still present in both the *hmm*$^{+/-}$ and *hmm*$^{-/-}$ limb buds (**Figure 7**), suggesting

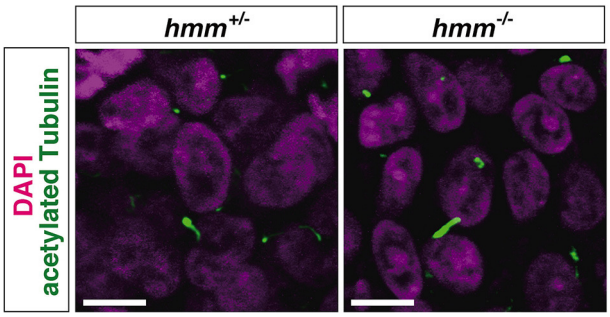

FIGURE 7 | The primary cilium is present in *hmm*$^{-/-}$ limb bud. Immunohistochemistry of acetylated tubulin in the limb bud cells at St. 23 is shown with fluorescent green. The nucleus is stained with DAPI. Scale bars, 10 μm.

that loss of primary cilia is not a cause of the *hmm*$^{-/-}$ phenotype. We next performed western blotting for the GLI3 protein (**Figure 8A**), and found that the active form of GLI3, GLI3A, was highly expressed in both the anterior and posterior halves of the *hmm*$^{-/-}$ limb bud compared to the *hmm*$^{+/-}$ limb bud. In particular, high expression of GLI3A was observed on the anterior side of the *hmm*$^{-/-}$ limb bud where *Shh* is not expressed. Expression of GLI3R was not detected in our experiments. This result raises the possibility that GLI3A protein does not function normally in the *hmm*$^{-/-}$ limb bud.

Finally, we examined whether transport of the GLI3 protein from the cytoplasm to the nucleus is disrupted in the *hmm*$^{-/-}$ embryo using immunohistochemistry. We observed that GLI3 protein is localized to the nucleus in both *hmm*$^{+/-}$ and *hmm*$^{-/-}$ primary fibroblast cells (**Figure 8B**). Taken together, our results imply that despite the presence of GLI3 protein in the nucleus, SHH signaling is abolished in the *hmm*$^{-/-}$ embryo due to a loss of function of the GLI3 protein.

DISCUSSION

In this study, we examined the developmental properties of the *hmm*$^{-/-}$ limb bud. We found that the abnormalities of the *hmm*$^{-/-}$ limb bud develop through a different mechanism than those of the *talpid*^{2} and the *talpid*^{3} limb buds (**Table 2**). The *hmm*$^{-/-}$ embryo showed disruption of SHH signaling in both the limb bud and the neural tube as in *talpid*^{3} (Davey et al., 2006), whereas in the *talpid*^{2} limb bud constitutive activation of SHH signaling is observed (Caruccio et al., 1999). While the *hmm*$^{-/-}$ limb bud shows a similar phenotype to the *talpid*^{3} limb bud in terms of the SHH signaling pathway in the cells, several phenotypes are different between them. Expression of ectopic *Hoxd13* was observed uniformly from the posterior to anterior mesenchyme in the *talpid*^{3} limb bud (Francis-West et al., 1995), whereas its expression was restricted posteriorly in the *hmm*$^{-/-}$ limb bud as it is in the wild-type (**Figures 3S,S′,T,T′**). This phenotype is unique to the *hmm*$^{-/-}$ limb bud compared to the *talpid*^{2} (Rodriguez et al., 1996) and *talpid*^{3} limb buds, indicating that the HMM mutant is a novel type of *talpid* mutant. It has been

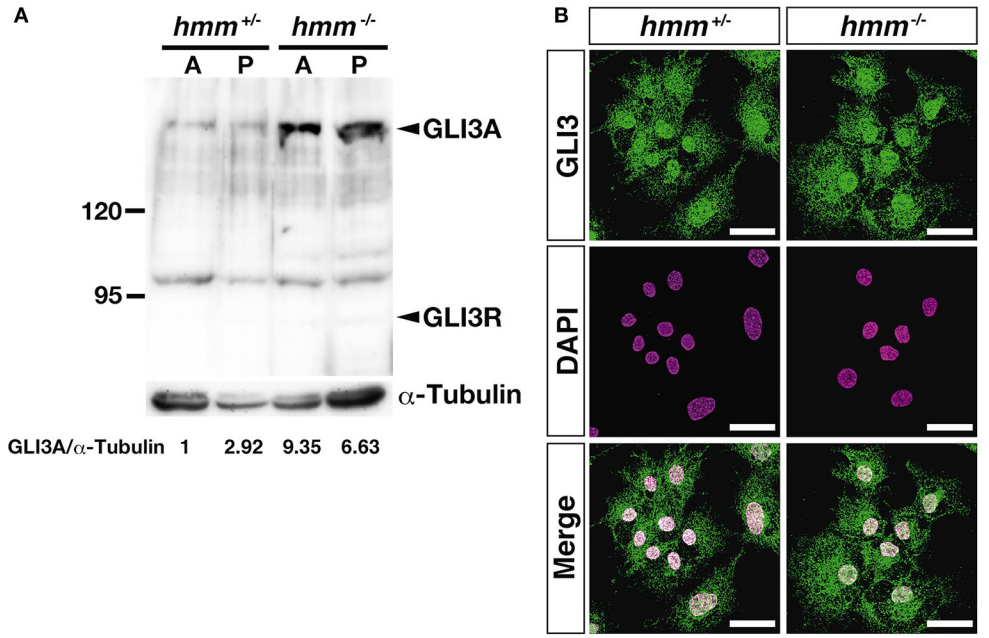

FIGURE 8 | High amounts of GLI3A protein are expressed in the *hmm*$^{-/-}$ limb bud. (A) Western blotting of GLI3 protein and α-tubulin in the limb is shown. A and P indicate samples extracted from anterior and posterior limb buds. Relative ratio of GLI3A/α-Tubulin is shown at the bottom. **(B)** Immunohistochemistry of GLI3 protein in primary fibroblasts is shown with fluorescent green. The nucleus is stained with DAPI. Scale bars, 30 μm.

TABLE 2 | Typical phenotypes of three talpid mutants in the limb bud.

	talpid^2	*talpid*^{3}	HMM mutant
Ptch1 expression	Expanded to the anterior border (Caruccio et al., 1999)	Uniformly expressed at very low level throughout mesenchyme (Lewis et al., 1999)	Similar to *talpid*^{3}
ZPA graft	–	High level *Ptch1* was induced (Lewis et al., 1999)	*Ptch1* was not Induced
Anterior graft	Induced digit duplication without *Shh* expression (Caruccio et al., 1999)	*Ptch1* was induced (Lewis et al., 1999)	–
Bmp2 expression	Expanded throughout AP axis (Caruccio et al., 1999)	Uniformly expressed under the AER along the AP axis (Francis-West et al., 1995)	Downregulated
Hoxd13 expression	Expanded throughout AP axis (Rodriguez et al., 1996)	Expressed in the anterior mesenchyme (Francis-West et al., 1995)	Expressed only at the posterior side as same as wild-type
Primary cilia	Disrupted (Chang et al., 2014)	Lack of primary cilia (Bangs et al., 2011)	Exist
Responsible gene	*C2CD3*	*KIAA0586*	not identified
Gli3 expression	Expanded to the posterior side (Caruccio et al., 1999)	Expanded to the posterior side (Lewis et al., 1999)	Similar to *talpid*^{2} and *talpid*^{3}
GLI3 protein	Functional high GLI3A expression(Chang et al., 2014)	No functional high GLI3A expression (Davey et al., 2006)	No functional high GLI3A expression
Gli1 expression	Expanded to the antetior side (Caruccio et al., 1999)	Expressed very weakly throughout the limb except distally under the AER (Lewis et al., 1999)	Similar to *talpid*^{3}
SHH protein	–	Wide spreaded than normal (Davey et al., 2006)	Expressed as same as wild-type
Skeletal pattern	Short broad radius and narrower ulna (Dvorak and Fallon, 1992)	Radius and ulna were fused (Ede and Kelly, 1964)	Indistinguishable same size of short radius and ulna
	Claw was formed in the leg (Litingtung et al., 2002)	Claw was not observed due to severe syndactyly (Bangs et al., 2011)	Claw was formed in some leg digits

reported that the expression level of GLI3R regulates the *Hoxd13* expression pattern along the AP axis (te Welscher et al., 2002b). The expression of *Hoxd13* in the limb is downregulated in the absence of *Shh* expression (Ros et al., 2003) because only GLI3R is present. When GLI3R is expressed at half the wild-type level, expression of *Hoxd13* can be faintly observed at the posterior

side of the limb (te Welscher et al., 2002b). In the *Gli3*$^{-/-}$ limb bud, expression of *Hoxd13* is expanded to the anterior side due to a lack of GLI3R protein, the same as in *talpid*^{3} mutants (Davey et al., 2006). Based on these observations, one possible reason for the different expression domains of *Hoxd13* between the *talpid*^{3} and the *hmm*$^{-/-}$ limb bud is that a lower amount of GLI3R is expressed in the *talpid*^{3} limb bud than the *hmm*$^{-/-}$ limb bud due to the lack of primary cilia in the *taplid*^{3} mutant. This could result in a high expression level of GLI3A (Bangs et al., 2011) and thus expanded expression of *Hoxd13* to the anterior side. In contrast, the expression level of GLI3R in the *hmm*$^{-/-}$ limb bud would be slightly higher than the *talpid*^{3} limb bud because the primary cilium is still present. These results imply that the expression level of GLI3R might be dependent on the presence or absence of the primary cilia among *talpid* family mutants. In our experiments, we could not detect GLI3R expression by western blotting (**Figure 8A**), suggesting the possibility that the antibody we used does not cross-react with quail GLI3R. Further study is needed to examine the expression level of GLI3R among *talpid* family mutants using different antibodies in the future.

We showed that the *hmm*$^{-/-}$ limb bud partially retained AP polarity at the limb bud stage in the absence of SHH signaling (**Figure 3**). Previous reports in the mouse embryo suggested that the antagonization of *Hand2* by *Gli3* specifies anterior-posterior polarity of the limb bud at early stages before *Shh* expression starts (te Welscher et al., 2002a). After *Hand2/Gli3* specifies the anterior-posterior polarity in the limb bud, SHH expression in the ZPA establishes the anterior-posterior axis. We infer that immature AP polarity could be maintained downstream of the *Hand2*/*Gli3* system in the *hmm*$^{-/-}$ limb bud.

In the *hmm*$^{-/-}$ limb bud, target genes downstream of SHH signaling (*Hoxd13,* and *Bmp2)* were expressed at much lower levels than in the *talpid*^{2} and *talpid*^{3} limb buds (**Figures 3**, **4**, **Table 2**). The *hmm*$^{-/-}$ limb bud showed severe lack of SHH signaling activity despite high expression levels of the activator form of GLI3, GLI3A. We therefore assume that the function of GLI3 as a transcriptional factor is affected in the *hmm*$^{-/-}$ limb bud. Previous work has shown mice with a conditional knockout of *Sufu* in the limbs have polydactyly with severe hypoplasia of the humerus, distal phalanges, and a short radius and ulna. In addition, a high level of GLI3A expression was observed in the *Sufu*$^{-/-}$ limb bud (Zhulyn and Hui, 2015), but *Gli1* expression was downregulated (Zhulyn et al., 2014). These phenotypes are reminiscent of the *hmm*$^{-/-}$ limb bud. Given that high levels of GLI3A expression were observed in the *hmm*$^{-/-}$ limb bud, the regulatory system of GLI3A as mediated by proteins such as SUFU might be disorganized in the *hmm*$^{-/-}$ limb bud. However, we examined expression of *Sufu* by *in situ* hybridization, and the expression appeared to be the same in both the *hmm*$^{+/-}$ and *hmm*$^{-/-}$ limb buds (data not shown). The binding of SUFU to the GLI3A/KIF7 complex leads to GLI3R formation, but this is inhibited by the SMO/KIF3A/β-ARRESTIN complex in the presence of SHH, resulting in GLI3A formation (Kovacs et al., 2008). These results suggest that the function of SUFU protein might be disorganized in the *hmm*$^{-/-}$ limb bud. When we examined the coding sequence of *Gli3* derived from reverse-transcribed mRNA from the *hmm*$^{-/-}$ limb bud, we saw several abnormal splicing variants at the N-terminus and full-length ORF sequence of *Gli3* (data not shown). Prior work reports that the Polydactyly Nagoya (*Pdn*) mouse mutant has several abnormal splicing variants of *Gli3* at the N-terminus due to integration of a retrotransposon (Thien and Rüther, 1999). Homozygous *Pdn* mice show severe polydactyly. It is possible that the abnormal splicing variants of *Gli3* we observed in the *hmm*$^{-/-}$ limb bud interfere with GLI3A activity as a dominant negative variant of GLI3.

On the other hand, our results indicate that SHH protein is dysfunctional in the *hmm*$^{-/-}$ limb bud (**Figure 5**) even though it was detectable by immunohistochemistry (**Figure 6**). In contrast, SHH protein is functional in the *talpid*^{3} limb bud (Lewis et al., 1999) (**Table 2**). These results also suggest that the gene responsible for *hmm* is different from the cause of the *talpid*^{3} mutant. We suggest that post-translational modification of SHH protein might be disrupted in the *hmm*$^{-/-}$ limb bud. After the full length of SHH protein is synthesized, autoproteolytic cleavage is induced concomitantly with cholesterol modification of the N-terminal region of SHH protein (SHH-N). After that, SHH-N is palmitoylated by skinny hedgehog (SKI) (Briscoe and Thérond, 2013) and secreted from the cells. When we examined the coding sequence of *Shh* expressed in the *hmm*$^{-/-}$ limb bud, it was normal. Further, ZPA derived from the *hmm*$^{-/-}$ limb bud did not induce expression of *Ptch2* near the implanted region (**Figure 5D**). These results imply that the secretion of SHH-N protein might be disrupted by a defect in palmitoylation. Future work needs to determine if SHH-N is palmitoylated in the *hmm*$^{-/-}$ limb bud.

Altogether, our results suggest that both SHH secretion and GLI3 function are disrupted in the HMM mutant. Interestingly, mice lacking both *Shh* and *Gli3* show similar phenotypes in both the limb bud and neural tube. The *Gli3*$^{-/-}$ limb bud still has normal expression levels of *Ptch1,* whereas the *Shh*$^{-/-}$; *Gli3*$^{-/-}$ limb bud shows no expression (Litingtung et al., 2002). The *hmm*$^{-/-}$ limb bud showed very low expression of *Ptch1* (**Figure 4**). This phenotype is more similar to the *Shh*$^{-/-}$; *Gli3*$^{-/-}$ limb bud rather than the *Gli3*$^{-/-}$ limb bud, suggesting that the *hmm*$^{-/-}$ limb bud is not just caused by *Gli3* deficient conditions. Furthermore, expression of *Hoxd13* is not observed in the *Shh*$^{-/-}$ limb bud, whereas the *Shh*$^{-/-}$; *Gli3*$^{-/-}$ limb bud has high expression of *Hoxd13*. The *hmm*$^{-/-}$ limb bud also showed *Hoxd13* expression, suggesting that the *hmm*$^{-/-}$ limb bud is not caused by just *Shh* deficient conditions. In terms of neural tube development, *Shh*$^{-/-}$; *Gli3*$^{-/-}$ mice show a milder dorsalization phenotype (Litingtung and Chiang, 2000; Persson et al., 2002) than *Shh*$^{-/-}$ mice (Chiang et al., 1996; Pierani et al., 1999). This phenotype is like the one observed in the *hmm*$^{-/-}$ neural tube (**Figure S1**). These observations support the idea that both SHH and GLI3 activity would be disrupted in the HMM mutant as in *Shh*$^{-/-}$; *Gli3*$^{-/-}$ mice. In the autopod, the function of GLI3 downstream of Indian hedgehog (IHH) is necessary for cartilage growth in the digits (St-Jacques et al., 1999). Therefore, the unidentifiable, malformed digits in the *hmm*$^{-/-}$ limb bud likely result from the disruption of GLI3 function during both digit patterning and digital cartilage formation.

Shh$^{-/-}$; *Gli3*$^{-/-}$ mice show polydactyly with unidentifiable digits similar to the *hmm*$^{-/-}$ limb bud. Recently, it was reported that *Gli3*, *Hoxa13*, and *Hoxd13* triple mutant mice show more severe polydactyly than *Gli3*$^{-/-}$ mice (Sheth et al., 2012). Previous reports indicated that HoxA13 regulates cell adhesion in the chick limb bud (Yokouchi et al., 1991). It is possible that the cell adhesion molecule downstream of GLI3/HoxA13/HoxD13 is involved in the determination of digit number. In the *hmm*$^{-/-}$ limb bud, expression of *Hoxd13* is expanded in the autopod (**Figure 3**) with a disruption of GLI3 function, resulting in irregularly spaced digital ray sequence (**Figure 2**). We propose that we can elucidate the mechanisms of regulating the distance between digital rays under the control of cell adhesion molecule using the HMM mutant. Furthermore, it was reported that the expression of the cell adhesion molecule N-CAM is altered in the *talpid*^{2} limb bud (Chuong et al., 1993), which implies that it contributes to the aberrant condensation and bunching of digits in this mutant (McGlinn et al., 2005). Thus, adhesion molecules are thought to be important for the pattern formation and cartilage differentiation of the digits in the autopod. Studying the HMM mutant could be especially useful for determining how cell adhesion plays a role in the development of digit number and morphology.

In conclusion, we revealed several molecular characteristics of the *hmm*$^{-/-}$ limb bud that distinguish it from the *talpid*^{2} and *talpid*^{3} limb buds. These mutants all show the common phenotype of high amounts of GLI3A expressed in the limb, but the expression of SHH downstream target genes is unique in each mutant. We need further study to understand why SHH signaling is abolished in the *hmm*$^{-/-}$ limb bud despite the presence of a high amount of GLI3A, and why the SHH protein is dysfunctional in the *hmm*$^{-/-}$ limb bud. Several new SHH signaling components and their functions have been recently reported, including IFT proteins, the Cos2-Fu system, an enzyme for Hh processing, and regulators of GLI activity like DYRK2 and MAP3K10 (Ramsbottom and Pownall, 2016). These reports indicate that the SHH signaling pathway is more complex than previously thought. We propose that further analysis of the HMM mutant will provide new insight into the SHH signaling pathway. It can also serve as a useful model system for studying pattern formation like the *talpid*^{2} and *talpid*^{3} mutants did for vertebrate morphogenesis.

AUTHOR CONTRIBUTIONS

YosM, MN, KK, AK, and TS conceived the project and designed the experiments. YosM performed gene-expression studies and the ZPA grafting; MN maintained HMM mutant; KK performed the immunohistochemistry. JF, KK, and TS. performed the OPT scanning. TS performed the western blot analysis. KA contributed the isolation of quail cDNA. YosM, MN, KK, MT, YoiM, AK, and TS wrote the paper.

FUNDING

This work was supported by KAKENHI grant no. 25111710 and 25291050.

ACKNOWLEDGMENTS

We thank Dr. Yo-ichi Yamamoto Shiraishi for discussions; Dr. Kaori Tsujino for collecting the quail embryos; and researchers in the Avian Bioscience Research Center for kind assistance.

SUPPLEMENTARY MATERIAL

The Supplementary Material for this article can be found online at: http://journal.frontiersin.org/article/10.3389/fcell.2016.00149/full#supplementary-material

Supplemental Information

Shh is also expressed at the notochord and floor plate, and determines the dorsal-ventral polarity of the neural tube. To check whether SHH signaling is disrupted in other tissues, we examined the expression pattern of genes downstream of SHH signaling in the neural tube (**Figure S1A**). In the *hmm*$^{-/-}$ embryo, *Shh* was expressed in the notochord but not in the floor plate. *Ptch2* was expressed around the notochord in *hmm*$^{+/-}$ embryo and in the ventricular zone located in the ventral neural tube. However, this expression was not observed in the *hmm*$^{-/-}$ embryo, indicating that SHH signaling is disrupted in the neural tube as it is in the limb bud. We further checked the expression patterns of transcription factors that determine neuronal identity along the DV axis under SHH signaling (Davey et al., 2006). The expression patterns of dorsal markers *Pax3* and *Pax7* were not distinguishable between the *hmm*$^{+/-}$ and *hmm*$^{-/-}$ embryos. In contrast, expression of the intermediate marker *Pax6* was expanded ventrally in the *hmm*$^{-/-}$ embryo. *Dbx2* is also expressed at an intermediate level in the *hmm*$^{+/-}$ embryo, but its expression was reduced in the *hmm*$^{-/-}$ embryo. *Islet1* expression was normally observed in the ventral spinal cord but not in the floor plate. It is notable that *Islet1* expression was expanded to the most ventral region of the spinal cord in the *hmm*$^{-/-}$ embryo. These observations of dorsalization and downregulation of genes downstream of SHH indicate that SHH signaling is also disrupted in the spinal cord and neighboring tissue in *hmm*$^{-/-}$ embryos.

Figure S1 | SHH signaling is reduced in the *hmm*$^{-/-}$ spinal cord. (A) *In situ* hybridization of *Shh, Ptch2, Pax3, Pax7, Pax6, Dbx2,* and *Islet1* on the transverse sections of the spinal cord at St. 25. All images are oriented with the dorsal side up and the ventral side down. The red arrowhead in the *Pax6* figure indicates expanded *Pax6* expression at the ventral side. The yellow arrowhead in the *Dbx2* figure indicates the region where expression of *Dbx2* is downregulated. The red arrowhead in the *Islet1* figure indicates expanded *Islet1* expression at the floor plate. **(B)** Immunohistochemistry of SHH protein at the notochord and neural tube is shown with fluorescent green. The nucleus is stained with DAPI. Transverse sections are oriented with the dorsal side up and the ventral side down.

REFERENCES

Ainsworth, S. J., Stanley, R. L., and Evans, D. J. R. (2010). Developmental stages of the Japanese quail. *J. Anat.* 216, 3–15. doi: 10.1111/j.1469-7580.2009.01173.x

Bangs, F., Antonio, N., Thongnuek, P., Welten, M., Davey, M. G., Briscoe, J., et al. (2011). Generation of mice with functional inactivation of talpid3, a gene first identified in chicken. *Development* 138, 3261–3272. doi: 10.1242/dev.063602

Besse, L., Neti, M., Anselme, I., Gerhardt, C., Rüther, U., Laclef, C., et al. (2011). Primary cilia control telencephalic patterning and morphogenesis via Gli3 proteolytic processing. *Development* 138, 2079–2088. doi: 10.1242/dev.059808

Bhatia, N., Thiyagarajan, S., Elcheva, I., Saleem, M., Dlugosz, A., Mukhtar, H., et al. (2006). Gli2 is targeted for ubiquitination and degradation by beta-TrCP ubiquitin ligase. *J. Biol. Chem.* 281, 19320–19326. doi: 10.1074/jbc.M513203200

Briscoe, J., and Thérond, P. P. (2013). The mechanisms of Hedgehog signalling and its roles in development and disease. *Nat. Rev. Mol. Cell Biol.* 14, 416–429. doi: 10.1038/nrm3598

Caruccio, N. C., Martinez-Lopez, A., Harris, M., Dvorak, L., Bitgood, J., Simandl, B. K., et al. (1999). Constitutive activation of sonic hedgehog signaling in the chicken mutant talpid(2): Shh-independent outgrowth and polarizing activity. *Dev. Biol.* 212, 137–149. doi: 10.1006/dbio.1999.9321

Chang, C.-F., Schock, E. N., O'Hare, E. A., Dodgson, J., Cheng, H. H., Muir, W. M., et al. (2014). The cellular and molecular etiology of the craniofacial defects in the avian ciliopathic mutant talpid2. *Development* 141, 3003–3012. doi: 10.1242/dev.105924

Chiang, C., Litingtung, Y., Harris, M. P., Simandl, B. K., Li, Y., Beachy, P. A., et al. (2001). Manifestation of the limb prepattern: limb development in the absence of sonic hedgehog function. *Dev. Biol.* 236, 421–435. doi: 10.1006/dbio.2001.0346

Chiang, C., Litingtung, Y., Lee, E., Young, K. E., Corden, J. L., Westphal, H., et al. (1996). Cyclopia and defective axial patterning in mice lacking Sonic hedgehog gene function. *Nature* 383, 407–413. doi: 10.1038/383407a0

Chuong, C. M., Widelitz, R. B., Jiang, T. X., Abbott, U. K., Lee, Y. S., and Chen, H. M. (1993). Roles of adhesion molecules NCAM and tenascin in limb skeletogenesis: analysis with antibody perturbation, exogenous gene expression, talpid mutants and activin stimulation. *Prog. Clin. Biol. Res.* 383B, 465–474.

Cole, R. K. (1942). The' talpid lethal' in the domestic fowl. *J. Hered.* 33, 82–86.

Davey, M. G., Paton, I. R., Yin, Y., Schmidt, M., Bangs, F. K., Morrice, D. R., et al. (2006). The chicken talpid3 gene encodes a novel protein essential for Hedgehog signaling. *Genes Dev.* 20, 1365–1377. doi: 10.1101/gad.369106

Dvorak, L., and Fallon, J. F. (1992). The talpid2 chick limb has weak polarizing activity and can respond to retinoic acid and polarizing zone signal. *Dev. Dyn.* 193, 40–48. doi: 10.1002/aja.1001930107

Ede, D. A., and Kelly, W. A. (1964). Developmental abnormalities in the trunk and limbs of the talpid3 mutant of the fowl. *J. Embryol. Exp. Morphol.* 12, 339–356.

Francis-West, P. H., Robertson, K. E., Ede, D. A., Rodriguez, C., Izpisúa-Belmonte, J. C., Houston, B., et al. (1995). Expression of genes encoding bone morphogenetic proteins and sonic hedgehog in talpid (ta3) limb buds: their relationships in the signalling cascade involved in limb patterning. *Dev. Dyn.* 203, 187–197. doi: 10.1002/aja.1002030207

Hsu, S.-H. C., Zhang, X., Yu, C., Li, Z. J., Wunder, J. S., Hui, C.-C., et al. (2011). Kif7 promotes hedgehog signaling in growth plate chondrocytes by restricting the inhibitory function of Sufu. *Development* 138, 3791–3801. doi: 10.1242/dev.069492

Kovacs, J. J., Whalen, E. J., Liu, R., Xiao, K., Kim, J., Chen, M., et al. (2008). Beta-arrestin-mediated localization of smoothened to the primary cilium. *Science* 320, 1777–1781. doi: 10.1126/science.1157983

Lewis, K. E., Drossopoulou, G., Paton, I. R., Morrice, D. R., Robertson, K. E., Burt, D. W., et al. (1999). Expression of ptc and gli genes in talpid3 suggests bifurcation in Shh pathway. *Development* 126, 2397–2407.

Litingtung, Y., and Chiang, C. (2000). Specification of ventral neuron types is mediated by an antagonistic interaction between Shh and Gli3. *Nat. Neurosci.* 3, 979–985. doi: 10.1038/79916

Litingtung, Y., Dahn, R. D., Li, Y., Fallon, J. F., and Chiang, C. (2002). Shh and Gli3 are dispensable for limb skeleton formation but regulate digit number and identity. *Nature* 418, 979–983. doi: 10.1038/nature01033

McGlinn, E., van Bueren, K. L., Fiorenza, S., Mo, R., Poh, A. M., Forrest, A., et al. (2005). Pax9 and Jagged1 act downstream of Gli3 in vertebrate limb development. *Mech. Dev.* 122, 1218–1233. doi: 10.1016/j.mod.2005.06.012

Nelson, C. E., Morgan, B. A., Burke, A. C., Laufer, E., DiMambro, E., Murtaugh, L. C., et al. (1996). Analysis of Hox gene expression in the chick limb bud. *Development* 122, 1449–1466.

Persson, M., Stamataki, D., te Welscher, P., Andersson, E., Böse, J., Rüther, U., et al. (2002). Dorsal-ventral patterning of the spinal cord requires Gli3 transcriptional repressor activity. *Genes Dev.* 16, 2865–2878. doi: 10.1101/gad.243402

Pierani, A., Brenner-Morton, S., Chiang, C., and Jessell, T. M. (1999). A sonic hedgehog-independent, retinoid-activated pathway of neurogenesis in the ventral spinal cord. *Cell* 97, 903–915. doi: 10.1016/S0092-8674(00)80802-8

Ramsbottom, S. A., and Pownall, M. E. (2016). Regulation of Hedgehog Signalling Inside and Outside the Cell. *J. Dev. Biol.* 4, 23. doi: 10.3390/jdb4030023

Riddle, R. D., Johnson, R. L., Laufer, E., and Tabin, C. (1993). Sonic hedgehog mediates the polarizing activity of the ZPA. *Cell* 75, 1401–1416. doi: 10.1016/0092-8674(93)90626-2

Rodriguez, C., Kos, R., Macias, D., Abbott, U. K., and Izpisúa Belmonte, J. C. (1996). Shh, HoxD, Bmp-2, and Fgf-4 gene expression during development of the polydactylous talpid2, diplopodia1, and diplopodia4 mutant chick limb buds. *Dev. Genet.* 19, 26–32. doi: 10.,1002/(SICI)1520-6408(1996)19:1<26::AID-DVG3>3.0.CO;2-2

Ros, M. A., Dahn, R. D., Fernandez-Teran, M., Rashka, K., Caruccio, N. C., Hasso, S. M., et al. (2003). The chick oligozeugodactyly (ozd) mutant lacks sonic hedgehog function in the limb. *Development* 130, 527–537. doi: 10.1242/dev.00245

Sharpe, J., Ahlgren, U., Perry, P., Hill, B., Ross, A., Hecksher-Sørensen, J., et al. (2002). Optical projection tomography as a tool for 3D microscopy and gene expression studies. *Science* 296, 541–545. doi: 10.1126/science.1068206

Sheth, R., Marcon, L., Bastida, M. F., Junco, M., Quintana, L., Dahn, R., et al. (2012). Hox genes regulate digit patterning by controlling the wavelength of a Turing-type mechanism. *Science* 338, 1476–1480. doi: 10.1126/science.1226804

St-Jacques, B., Hammerschmidt, M., and McMahon, A. P. (1999). Indian hedgehog signaling regulates proliferation and differentiation of chondrocytes and is essential for bone formation. *Genes Dev.* 13, 2072–2086. doi: 10.1101/gad.13.16.2072

Suzuki, T. (2013). How is digit identity determined during limb development? *Dev. Growth Differ.* 55, 130–138. doi: 10.1111/dgd.12022

Suzuki, T., Hasso, S. M., and Fallon, J. F. (2008). Unique SMAD1/5/8 activity at the phalanx-forming region determines digit identity. *Proc. Natl. Acad. Sci. U.S.A.* 105, 4185–4190. doi: 10.1073/pnas.0707899105

Takahashi, M., Tamura, K., Büscher, D., Masuya, H., Yonei-Tamura, S., Matsumoto, K., et al. (1998). The role of Alx-4 in the establishment of anteroposterior polarity during vertebrate limb development. *Development* 125, 4417–4425.

te Welscher, P., Fernandez-Teran, M., Ros, M. A., and Zeller, R. (2002a). Mutual genetic antagonism involving GLI3 and dHAND prepatterns the vertebrate limb bud mesenchyme prior to SHH signaling. *Genes Dev.* 16, 421–426. doi: 10.1101/gad.219202

te Welscher, P., Zuniga, A., Kuijper, S., Drenth, T., Goedemans, H. J., Meijlink, F., et al. (2002b). Progression of vertebrate limb development through SHH-mediated counteraction of GLI3. *Science* 298, 827–830. doi: 10.1126/science.1075620

Thien, H., and Rüther, U. (1999). The mouse mutation Pdn (Polydactyly Nagoya) is caused by the integration of a retrotransposon into the Gli3 gene. *Mamm. Genome* 10, 205–209. doi: 10.1007/s003359900973

Tsudzuki, M., Nakane, Y., and Wada, A. (1998). Hereditary multiple malformation in Japanese quail: a possible powerful animal model for morphogenetic studies. *J. Hered.* 89, 24–31. doi: 10.1093/jhered/89.1.24

Wang, B., Fallon, J. F., and Beachy, P. A. (2000). Hedgehog-regulated processing of Gli3 produces an anterior/posterior repressor gradient in the

developing vertebrate limb. *Cell* 100, 423–434. doi: 10.1016/S0092-8674(00)80678-9

Yin, Y., Bangs, F., Paton, I. R., Prescott, A., James, J., Davey, M. G., et al. (2009). The Talpid3 gene (KIAA0586) encodes a centrosomal protein that is essential for primary cilia formation. *Development* 136, 655–664. doi: 10.1242/dev.028464

Yokouchi, Y., Sasaki, H., and Kuroiwa, A. (1991). Homeobox gene expression correlated with the bifurcation process of limb cartilage development. *Nature* 353, 443–445. doi: 10.1038/353443a0

Zhulyn, O., and Hui, C.-C. (2015). Sufu and Kif7 in limb patterning and development. *Dev. Dyn.* 244, 468–478. doi: 10.1002/dvdy.24249

Zhulyn, O., Li, D., Deimling, S., Vakili, N. A., Mo, R., Puviindran, V., et al. (2014). A switch from low to high Shh activity regulates establishment of limb progenitors and signaling centers. *Dev. Cell* 29, 241–249. doi: 10.1016/j.devcel.2014.03.002

Conflict of Interest Statement: The authors declare that the research was conducted in the absence of any commercial or financial relationships that could be construed as a potential conflict of interest.

frontiers in Cell and Developmental Biology

REVIEW
published: 03 April 2018
doi: 10.3389/fcell.2018.00034

Cell Chirality Drives Left-Right Asymmetric Morphogenesis

*Mikiko Inaki, Takeshi Sasamura and Kenji Matsuno**

Department of Biological Sciences, Graduate School of Science, Osaka University, Osaka, Japan

Most macromolecules found in cells are chiral, meaning that they cannot be superimposed onto their mirror image. However, cells themselves can also be chiral, a subject that has received little attention until very recently. In our studies on the mechanisms of left-right (LR) asymmetric development in *Drosophila*, we discovered that cells can have an intrinsic chirality to their structure, and that this "cell chirality" is generally responsible for the LR asymmetric development of certain organs in this species. The actin cytoskeleton plays important roles in the formation of cell chirality. In addition, *Myosin31DF* (*Myo31DF*), which encodes *Drosophila* Myosin ID, was identified as a molecular switch for cell chirality. In other invertebrate species, including snails and *Caenorhabditis elegans*, chirality of the blastomeres, another type of cell chirality, determines the LR asymmetry of structures in the body. Thus, chirality at the cellular level may broadly contribute to LR asymmetric development in various invertebrate species. Recently, cell chirality was also reported for various vertebrate cultured cells, and studies suggested that cell chirality is evolutionarily conserved, including the essential role of the actin cytoskeleton. Although the biological roles of cell chirality in vertebrates remain unknown, it may control LR asymmetric development or other morphogenetic events. The investigation of cell chirality has just begun, and this new field should provide valuable new insights in biology and medicine.

Keywords: cell chirality, left-right asymmetry, F-actin, Myosin I, *Drosophila*

OPEN ACCESS

Edited by:
Takaaki Matsui,
Nara Institute of Science and Technology (NAIST), Japan

Reviewed by:
Hidetaka Shiratori,
Kyoto Sangyo University, Japan
Makoto Sato,
Kanazawa University, Japan

****Correspondence:***
Kenji Matsuno
kmatsuno@bio.sci.osaka-u.ac.jp

Specialty section:
This article was submitted to Cell Adhesion and Migration, a section of the journal Frontiers in Cell and Developmental Biology

Received: *17 November 2017*
Accepted: *14 March 2018*
Published: *03 April 2018*

Citation:
Inaki M, Sasamura T and Matsuno K (2018) Cell Chirality Drives Left-Right Asymmetric Morphogenesis. Front. Cell Dev. Biol. 6:34. doi: 10.3389/fcell.2018.00034

INTRODUCTION

The directional left-right (LR) asymmetry of body structures and functions is found in animals across phyla. In this review, directional LR asymmetry is called "LR asymmetry." LR asymmetry is a fundamental property of animal development, and the mechanisms of LR asymmetric development are a topic of strong interest in various biological and medical fields. To explain the molecular basis of LR asymmetric development, Walport proposed the "F molecule" hypothesis (Brown and Wolpert, 1990). In this hypothesis, the F molecule is chiral and can be arranged along the anterior-posterior and dorsal-ventral axes. An object is chiral if it cannot be superposed onto its mirror image. By virtue of these properties, the F molecule can direct the LR axis based on its chirality. This idea is supported by findings on the molecular mechanisms of LR asymmetric development in mouse.

In mouse, motile cilia in the node, which is a small pit located in the ventral side of the early embryo, rotate clockwise and induce a leftward flow of extra-embryonic fluid, named the "nodal flow" (Nonaka et al., 1998). The nodal flow is the first cue that breaks the LR symmetry of the mouse embryo. The nodal flow induces left-side-specific gene expression, which leads to subsequent LR asymmetric development (Nonaka et al., 1998, 2002; Okada and Hirokawa, 1999). In addition to their ventral location, the nodal cilia slant posteriorly, which helps them to generate the leftward fluid flow (Nonaka et al., 2005). Thus, the nodal cilia are arranged in a polar manner along both the anterior-posterior and dorsal-ventral axes. The nodal cilia also have intrinsic chirality, because they rotate clockwise (Nonaka et al., 1998). Therefore, the nodal cilia satisfy the requirements of the F molecule (Brown and Wolpert, 1990). In this case, the molecular origin of LR asymmetric development is traced back to the chiral structure and motion of cilia, which is still a subject of active investigation (Okada and Hirokawa, 2009; Nonaka, 2013).

CELL CHIRALITY DRIVES LR ASYMMETRIC MORPHOGENESIS IN *DROSOPHILA*

Drosophila melanogaster is another organism in which the mechanisms of LR asymmetric development have been extensively studied (Hozumi et al., 2006; Spéder et al., 2006; González-Morales et al., 2015; Inaki et al., 2016). In this organism, chirality at the level of cells, rather than molecules, was found to contribute to LR asymmetric development for the first time (Taniguchi et al., 2011; Inaki et al., 2016). The embryonic hindgut first forms LR symmetrically along the midline, then rotates counterclockwise 90° as viewed from the posterior, and eventually exhibits a LR asymmetric morphology (**Figure 1**). Before the rotation, the hindgut has a hook-like shape that points ventrally, and its most posterior part is stably connected to the anus (**Figure 1**). The hindgut then twists, causing the hook-like shape to point rightward (**Figure 1**).

Before the rotation, the anterior-posterior axis direction of the hindgut epithelial tube can be readily defined and used as a reference in analyzing the LR asymmetry of each cell. Taniguchi et al. discovered that before rotation onset, the hindgut epithelial cells show LR asymmetry in their apical surface, which faces the lumen of the hindgut tube (**Figure 2**; Taniguchi et al., 2011). In these cells, leftward-tilting cell boundaries are found more frequently than rightward-tilting ones (**Figure 2**). In addition, the hindgut epithelial cells have apical-basal polarity, like other epithelial cells. Therefore, the three-dimensional hindgut epithelial cells are chiral, because their shape cannot be superimposed onto their mirror image (**Figure 3**). This property of cells was called "cell chirality" (Taniguchi et al., 2011; Inaki et al., 2016). The chirality of these cells eventually disappears as the rotation progresses, and the cell shape becomes achiral (LR symmetric) when the rotation is completed (Taniguchi et al., 2011).

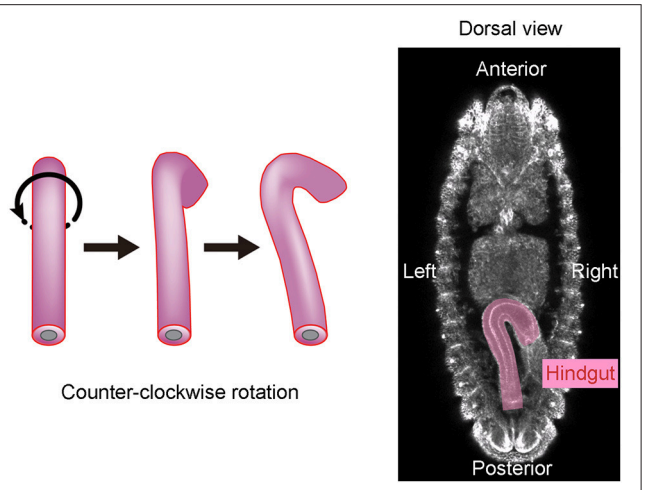

FIGURE 1 | The *Drosophila* embryonic hindgut rotates 90° counterclockwise. **(Left)** The embryonic hindgut first forms as a bilaterally symmetric structure that curves ventrally **(Left)**. It rotates 90° counterclockwise from the posterior view **(Middle)**, and consequently curves to the right **(Right)**. **(Right)** The embryonic gut curves rightward at stage 12 in wild-type *Drosophila*. This figure is partly adapted from Inaki et al. (2016) with permission.

A computer simulation demonstrated that the introduction and subsequent dissolution of cell chirality is sufficient to induce the counterclockwise rotation of a model epithelial tube (Taniguchi et al., 2011). The results of this model study were also consistent with previous observations that cell proliferation and cell death do not occur during hindgut rotation, suggesting that cell rearrangement and/or deformation alone is responsible for the hindgut rotation (Lengyel and Iwaki, 2002; Wells et al., 2013).

MYOSIN31DF IS A SWITCH FOR CELL CHIRALITY AND LR ASYMMETRY

Although the mechanisms of cell-chirality formation remain unclear, important clues emerged from the genetic identification of *Drosophila Myosin31DF* (*Myo31DF*) mutants, in which the LR asymmetry of various organs is reversed (Hozumi et al., 2006; Spéder et al., 2006). *Myo31DF* is the *Drosophila* ortholog of *Myosin1D*, which encodes an evolutionarily conserved class I myosin (Hozumi et al., 2006; Spéder et al., 2006). In loss-of-function *Myo31DF* mutants, the hindgut rotates 90° in the opposite direction to that of wild type in more than 80% of the flies, resulting in a hindgut in which the hook-like shape points leftward (**Figure 2**; Hozumi et al., 2006). *Myo31DF* mutants are homozygous viable and fertile, suggesting that the role of *Myo31DF* is highly specific for LR asymmetric development (Hozumi et al., 2006; Spéder et al., 2006). In addition, the chiral hindgut epithelial cells in these mutants are the mirror image of their wild-type counterparts (Taniguchi et al., 2011). The forced expression of wild-type *Myo31DF* in the hindgut epithelium of these mutants rescues both the reversed hindgut rotation and the reversed cell chirality. These observations indicated that the default states of LR asymmetry and cell chirality are the mirror

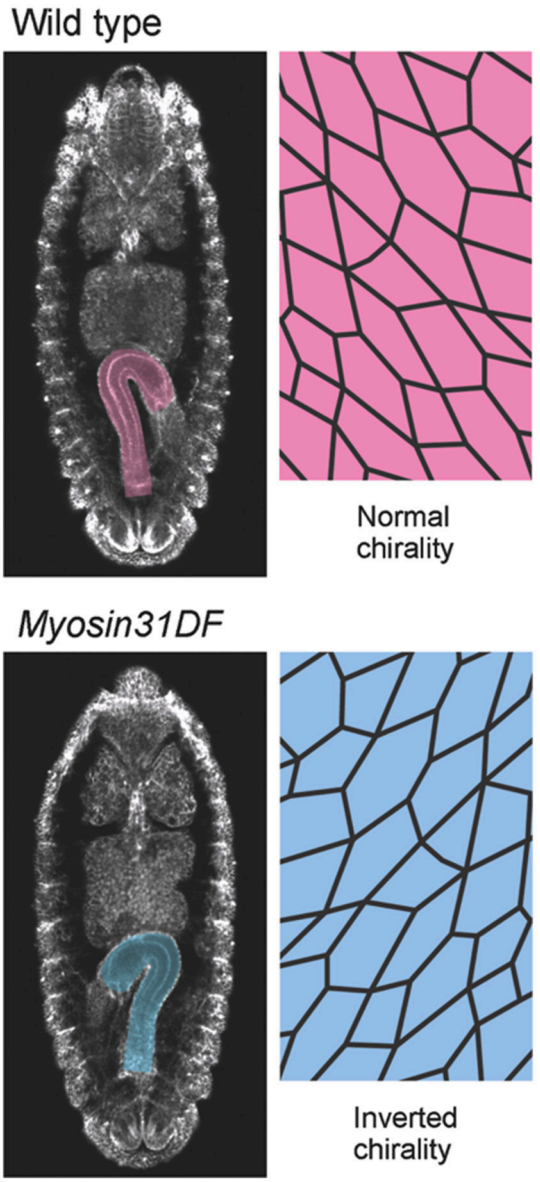

FIGURE 2 | *Myosin31DF* mutation reverses the cell chirality and hindgut rotation. **(Top)** A wild-type *Drosophila* embryo shows normal cell chirality and a rightward-pointing hindgut. **(Bottom)** In the *Myosin31DF* mutant, the cell chirality and hindgut laterality are the mirror images of those in its wild-type counterpart. This figure is partly adapted from Inaki et al. (2016) with permission.

image of wild type, and that *Myo31DF* acts to reverse them to the wild-type direction (Hozumi et al., 2006; Taniguchi et al., 2011).

A genetic mosaic analysis of *Myo31DF* suggested that cell chirality is generated intrinsically in each cell, but is also under some influence of neighboring cells, probably through mechanical force (Hatori et al., 2014). These findings collectively suggest that *Myo31DF* acts as a switch for cell chirality and determines the direction of *Drosophila* hindgut rotation.

CELL-CHIRALITY-DRIVEN LR ASYMMETRIC MORPHOGENESIS IN VARIOUS *DROSOPHILA* ORGANS

In addition to the embryonic hindgut, *Myo31DF* mutants in *Drosophila* show LR inversion in various other organs, including the male genitalia, testes, and adult gut, indicating that *Myo31DF* determines the LR asymmetry in these organs, as well (Hozumi et al., 2006; Spéder et al., 2006). Among these organs, cell chirality is known to contribute to the LR asymmetric development of the male genitalia and adult gut (González-Morales et al., 2015; Sato et al., 2015a). Thus, cell chirality appears to be a common strategy for driving the LR asymmetric morphogenesis of tissues in *Drosophila*.

The male genitalia in *Drosophila* undergo a 360° clockwise rotation as viewed from the posterior during the pupal stage, achieved by a combination of 180° rotations in two adjacent segments, A8a and A8p (Suzanne et al., 2010; Kuranaga et al., 2011). Just before the rotation begins, A8a epithelial cells show cell chirality (**Figure 4**; Sato et al., 2015a). In this tissue, Myosin II (MyoII) is concentrated along the rightward tilting cell boundaries (**Figure 4**; Sato et al., 2015a). This chiral distribution of MyoII is maintained during the rotation and appears to drive LR asymmetric cell intercalation (Sato et al., 2015a). A computer simulation suggested that these LR asymmetric cell interactions give rise to the directional rotation of the male genitalia (Sato et al., 2015a). The cell chirality in the male genitalia is also inverted in *Myo31DF* mutants, consistent with the idea that cell chirality drives the LR directional rotation of this organ (Sato et al., 2015a).

Although cell chirality is also responsible for the LR asymmetric development of the adult gut, the mechanism by which *Myo31DF* and cell chirality contribute to the LR asymmetric morphogenesis of this organ may be different from that of the embryonic hindgut and male genitalia. *Drosophila* undergoes complete metamorphosis, and the adult gut develops from its primordium during the pupal stage (Robertson, 1936; Fox and Spradling, 2009). The adult gut primordium consists of two segments, H1 and H2 (Murakami and Shiotsuki, 2001; González-Morales et al., 2015). The epithelial cells in H2 proliferate to become the adult gut, while the H1 segment is eliminated during the pupal stage. *Myo31DF* is required only in H1 during late larval stage, and cell chirality is observed only in H2 after H1 is eliminated (**Figure 4**; González-Morales et al., 2015). To explain these observations, it was proposed that polarity determined by *Myo31DF* in H1 is propagated to H2 as cell chirality (**Figure 4**; González-Morales et al., 2015). In addition, evidence suggested that this propagation of cell chirality is mediated by the unconventional cadherins, Dachsous and Fat (**Figure 4**; González-Morales et al., 2015). Dachsous and Fat are components of the planer cell polarity (PCP) pathway (Yang et al., 2002). A connection between MyoID, which is an ortholog of Myo31DF, and the PCP pathway was also found in rat (Hegan et al., 2015). The *MyoID* mutation in rat results in the elimination of PCP in multi-ciliated tracheal and brain-ependymal epithelial cells (Hegan et al., 2015). Therefore, some aspects of the relationship between

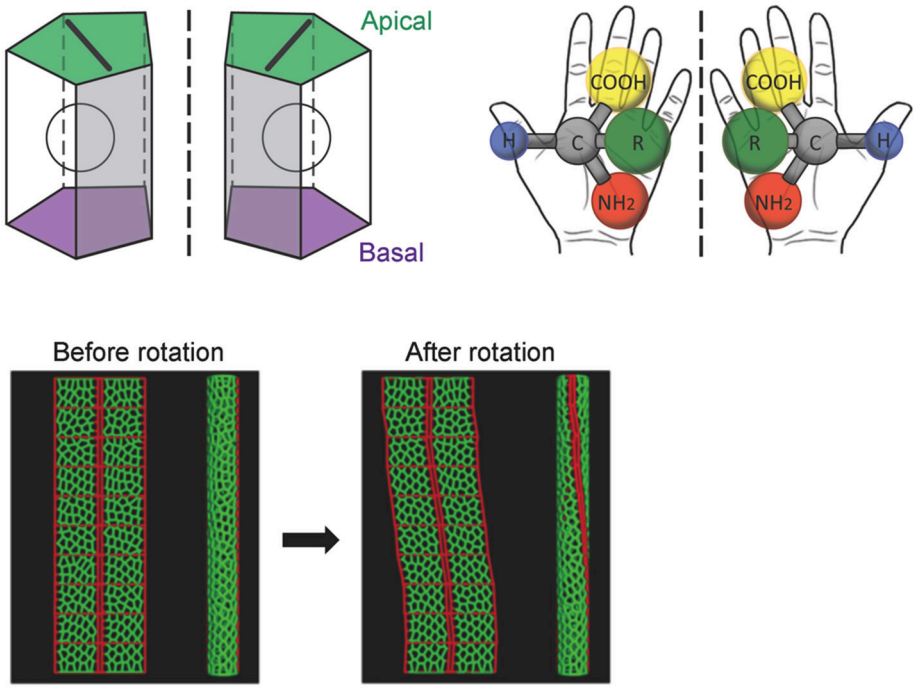

FIGURE 3 | A computer simulation recapitulates the cell-chirality-driven counterclockwise rotation of the hindgut. **(Top)** The shape of the apical surface of hindgut epithelial cells is LR-asymmetric **(Left)**. Considering that these cells also have apical-basal polarity, they show chirality. This property is illustrated by left-handed and right-handed chiral amino acids **(Right)**. **(Bottom)** To test whether cell chirality alone could induce the axial rotation of the hindgut epithelial tube, a computer simulation based on a vertex model was performed. The introduction of LR bias to the contraction of the cell boundary was sufficient to recapitulate the cell chirality found *in vivo*. The introduction and subsequent release of cell chirality were sufficient to induce the LR-asymmetric rotation of the model epithelial tube (Taniguchi et al., 2011). These figures are partly adapted from Inaki et al. (2016) and Taniguchi et al. (2011) with permissions.

MyoID and PCP may be conserved between *Drosophila* and mammals.

MOLECULAR FUNCTION OF MYOSIN31DF IN LR ASYMMETRIC DEVELOPMENT

The biochemical functions of the Myosin I family have been studied extensively, and their roles in membrane tension generation, membrane dynamics, and mechanosignal transduction are well-documented (McConnell and Tyska, 2010). Myo31DF is an F-actin-based motor protein, and therefore is likely to exert its function through the actin cytoskeleton; however, the molecular links between cell chirality and Myo31DF remain largely unknown (Hozumi et al., 2006; Taniguchi et al., 2011). To date, a chiral distribution of Myo31DF has not been observed in the *Drosophila* hindgut epithelial cells (Hatori et al., 2014). It may be necessary to observe the dynamics of Myo31DF's localization or activity to understand the biochemical basis of chirality formation.

Potential insight into the connection between the Myosin I family and cell chirality was obtained from an elegant biochemical study of a mammalian Myosin I family protein (Pyrpassopoulos et al., 2012). In this experiment, Myosin1c, a mouse Myosin I family protein (also known as Myosin IC), powered actin motility on fluid-supported lipid bilayers, and this motility was observed to occur along curved paths in a counterclockwise direction (Pyrpassopoulos et al., 2012). Thus, Myosin I family proteins may have an intrinsic chiral property that causes actin to move in a chiral manner. In addition, the actin cytoskeleton has important roles in the chirality of the hindgut epithelial cells in *Drosophila*. Overexpressing a dominant-negative form of Rho1 (Rho1 N19) or Rac1 (Rac1 N17), which is known to regulate F-actin, causes these epithelial cells to become achiral (Taniguchi et al., 2011). Therefore, F-actin dynamics may be important for the formation of cell chirality though Myo31DF.

The *Drosophila* E-Cadherin (*D*E-cad) may also functionally interact with Myo31DF. In *DE-cad* mutants, epithelial cells of the embryonic hindgut become achiral, and the embryonic hindgut rotates in a random direction or does not rotate (Taniguchi et al., 2011). *DE-cad* is also required for the male genitalia rotation (Petzoldt et al., 2012). Genetic analyses suggested that *DE-cad* functions downstream of *Myo31DF* in both organs (Taniguchi et al., 2011; Petzoldt et al., 2012). Myo31DF physically interacts with β-catenin and forms a complex with *D*E-cad, indicating that Myo31DF might regulate *D*E-cad through a β-catenin/cadherin complex (Petzoldt et al., 2012). In the embryonic hindgut, *D*E-cad chirally localizes to adherens junctions, and in *Myo31DF* mutants, this chiral localization of *D*E-cad is the mirror image

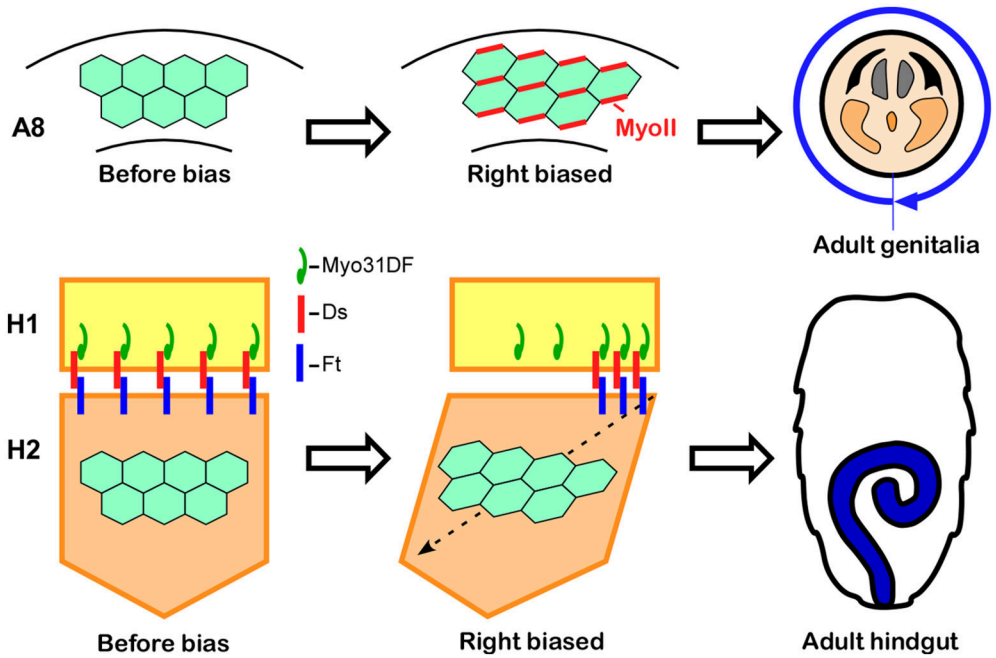

FIGURE 4 | Cell chirality drives LR asymmetric morphogenesis in various *Drosophila* organs. **(Top)** In wild-type *Drosophila* males, the genitalia rotate clockwise as viewed from the posterior. Just before rotation begins, genital epithelial cells in the A8 segment show a chiral cell shape and an asymmetric Myosin II (MyoII) distribution **(Middle)**. This cell chirality drives the 360° rotation of the genitalia **(Right)**. **(Bottom)** The wild-type adult *Drosophila* gut develops from the H2 segment during the pupal stage, while gut laterality is determined by *Myo31DF* expressed in the H1 segment during the larval stage **(Middle)**. Cell chirality is observed only in the H2 segment after the H1 segment is eliminated during metamorphosis. The handedness determined by *Myosin31DF* in the H1 segment is propagated to the H2 segment, leading to the LR-directional looping of the adult hindgut **(Right)**. The atypical cadherins Dachsous (Ds) and Fat (Ft) are thought to be involved in this process. Dachsous is reported to bind *Myo31DF* **(Middle)**. These figures are partly adapted from Inaki et al. (2016) with permission.

of that in wild-type (Taniguchi et al., 2011). However, it is not known how Myo31DF, which does not show a chiral distribution in hindgut epithelial cells, controls the chiral localization of DE-cad.

UPSTREAM REGULATION OF *MYOSIN31DF* IN *DROSOPHILA*

By a genetic screen, the *Abd-B* gene was identified as a dominant enhancer of the *Myo31DF* mutation in *Drosophila* (Coutelis et al., 2013). The knockdown of Abd-B by RNA interference in the male genital discs stops the rotation of genitalia (Coutelis et al., 2013). The *Myo31DF* expression in the male genital discs is almost abolished under this condition, and the no-rotation phenotype is rescued by overexpressing *Myo31DF* (Coutelis et al., 2013). The knockdown of *Abd*-B in the embryonic hindgut also stops the hindgut rotation (Coutelis et al., 2013). These results indicate that *Abd-B* acts upstream of *Myo31DF*.

In *Myo31DF* mutants, the embryonic gut and male genitalia still rotate in the reverse direction, suggesting that a "default" pathway exists that drives the inverse rotation of these organs (Hozumi et al., 2006; Spéder et al., 2006). In contrast, *Abd-B* knockdown results in no-rotation phenotypes in these organs. Therefore, the default pathway of LR asymmetric development is also under the control of *Abd-B* (Coutelis et al., 2013). Further experiments are needed to uncover this default pathway. In any case, these results indicate that *Abd-B* may be a master controller of LR asymmetric development in *Drosophila*.

ROLES OF OTHER TYPE I MYOSINS IN LR ASYMMETRIC DEVELOPMENT IN *DROSOPHILA*

Drosophila has three type I myosin family proteins: Myo31DF (also known as MyoID), Myo61F (also known as MyoIC), and Myo95E (most similar to MyoIB in vertebrates) (Tzolovsky et al., 2002; Okumura et al., 2015). In addition to *Myo31DF*, potential roles of the other two Myosin I family proteins in LR asymmetric development have been investigated in *Drosophila*. *Myo61F* was proposed to have antagonistic functions to *Myo31DF*, because overexpressing *Myo61F* causes LR inversion of the embryonic gut and male genitalia, reminiscent of the *Myo31DF* loss-of-function phenotypes (Hozumi et al., 2006). Furthermore, these inversion phenotypes induced by *Myo61F* overexpression are suppressed by additionally overexpressing *Myo31DF* (Hozumi et al., 2006; Petzoldt et al., 2012). *Myo61F* inhibits the physical interaction between Myo31DF and the β-catenin/DE-cadherin complex, suggesting how Myo61F may

antagonize Myo31DF (Petzoldt et al., 2012). However, the null *Myo61F* mutant alone is homozygous viable and does not show LR defects in the embryonic hindgut or genital disc (Okumura et al., 2015). Thus, the LR-reversing activity of Myo61F overexpression may not reflect its physiological function (Okumura et al., 2015). On the other hand, the *Myo61F* null mutant recessively enhances the clockwise (wild type) genitalia rotation of the *Myo31DF* mutant, suggesting that *Myo61F* and *Myo31DF* have a redundant function in promoting the dextral LR rotation of the male genitalia (Okumura et al., 2015).

Regarding Myo95E, a null mutant of *Myo95E* is homozygous viable and does not show any detectable LR defects (Okumura et al., 2015). In addition, *Myo95E* overexpression results in no obvious LR defects (Okumura et al., 2015). *Myo95E* does not enhance the phenotype of Myo31DF, suggesting that *Myo95E* is not involved in LR asymmetric development (Okumura et al., 2015). Unexpectedly, triple homozygotes for *Myo31DF*, *Myo61F*, and *Myo95E* lacking their maternal contributions are viable and fertile, and show no obvious developmental defects, except for the LR defects due to the *Myo31DF* mutation (Okumura et al., 2015). Therefore, none of the Myosin I family genes are essential for viability in *Drosophila* (Okumura et al., 2015).

CHIRALITY OF BLASTOMERES IS AN EVOLUTIONARILY CONSERVED MECHANISM FOR BREAKING THE LR SYMMETRY

In addition to *Drosophila*, the mechanisms of LR asymmetric development have been well studied in other invertebrate species, including air-breathing snails (Pulmonata) and *Caenorhabditis elegans* (*C. elegans*), which are model organisms used to study developmental biology in Ecdysozoa and Lophotrochozoa, respectively (Inaki et al., 2016). In Pulmonata and *C. elegans*, the LR asymmetry of blastomeres at the very early stages of embryogenesis plays central roles in the subsequent LR asymmetric development (Wood, 1991; Bergmann et al., 2003; Shibazaki et al., 2004). These LR asymmetric blastomeres are chiral, given that their shape cannot be superimposed onto its mirror image. In these cases, the chirality of the blastomeres defines the LR asymmetric axis of the next blastomere cleavage, which consequently introduces LR asymmetry into the arrangement of blastomeres (Wood, 1991; Bergmann et al., 2003; Shibazaki et al., 2004). Strikingly, in *Lymnaea stagnalis* (a Pulmonata species) and *C. elegans*, reversing the LR asymmetry in the arrangement of blastomeres by artificial manipulations inverses the entire subsequent LR asymmetric development (Wood, 1991; Kuroda et al., 2009). These results suggest that LR asymmetry in the relative position of blastomeres contains all of the information for the LR axis polarity in the subsequent development.

In Pulmonata, the initial LR asymmetry is observed as cell chirality of the blastomeres at the four-cell stage (Shibazaki et al., 2004). This chirality leads to LR slanting of the cleavage axes of the four blastomeres, which results in a helical shift of the micromeres that are generated by the next cleavage, in a particular direction (Shibazaki et al., 2004). This LR asymmetric rearrangement of macromeres is fully responsible for the entire LR asymmetric development that subsequently occurs, including the coiling direction of the shell and the laterality of the visceral organs (Shibazaki et al., 2004). Notably, in *L. stagnalis*, a maternal *D* mutant that dominantly determines the clockwise (wild type) coiling of the shell in the offspring was identified in a natural population (Pelseneer, 1920; Rolan-Alvarez and Rolan, 1995). In this mutant embryo, the chirality of blastomeres at the four-cell stage disappears, and the blastomeres become radially symmetric, which subsequently leads to the reversed LR asymmetry in the configuration of the eight-cell-stage blastomeres (Shibazaki et al., 2004). Recently, the *D* gene of *L. stagnalis* was found to be a homolog of *formin* (Davison et al., 2016). Formin belongs to a group of proteins that associate with the barbed end of actin filaments and are involved in actin polymerization (Pruyne et al., 2002). These results demonstrate that the actin cytoskeleton is important in the formation of blastomere chirality in this snail.

Actin also plays an important role in the blastomere chirality in *C. elegans*. In this organism, the initial LR asymmetry is detected as a chiral rotation of the actomyosin cortex in the one-cell-stage embryo (Naganathan et al., 2014). This chiral flow is created by turning forces that are generated by myosin under the control of Rho GTPase signaling (Naganathan et al., 2014). In the *C. elegans* embryo, handedness is determined at the four-cell stage (Wood, 1991). The chiral turning force in these blastomeres probably causes a LR asymmetric skewing of the mitotic spindle direction at the four-cell stage, which is responsible for the subsequent LR asymmetric development of the entire body (Wood, 1991; Bergmann et al., 2003).

In summary, the chirality of blastomeres plays critical roles in the LR asymmetric development of these two representative model organisms of Ecdysozoa and Lophotrochozoa. Given that the chirality of blastomeres is a specific version of cell chirality found during early cleavage stages, cell chirality may have general and evolutionarily conserved roles in LR asymmetric development.

CELL CHIRALITY IN VERTEBRATES

Although cell chirality and blastomere chirality have been found *in vivo* only in invertebrates, many vertebrate cells demonstrate various indications of cell chirality under certain culture conditions (**Figure 5**; Xu et al., 2007; Wan et al., 2011; Chen et al., 2012; Tee et al., 2015; Worley et al., 2015; Yamanaka and Kondo, 2015; Raymond et al., 2016). Cell lines including mouse myoblasts (C2C12), human umbilical vein endothelial cells (hUVEC), and canine kidney epithelial cells (MDCK) exhibit a chiral cell shape when cultivated on ring or stripe micro-patterns of adhesive substrates (**Figure 5**; Wan et al., 2011; Chen et al., 2012; Worley et al., 2015; Raymond et al., 2016). Cell chirality is also found in cellular behaviors under certain culture conditions. For example, human

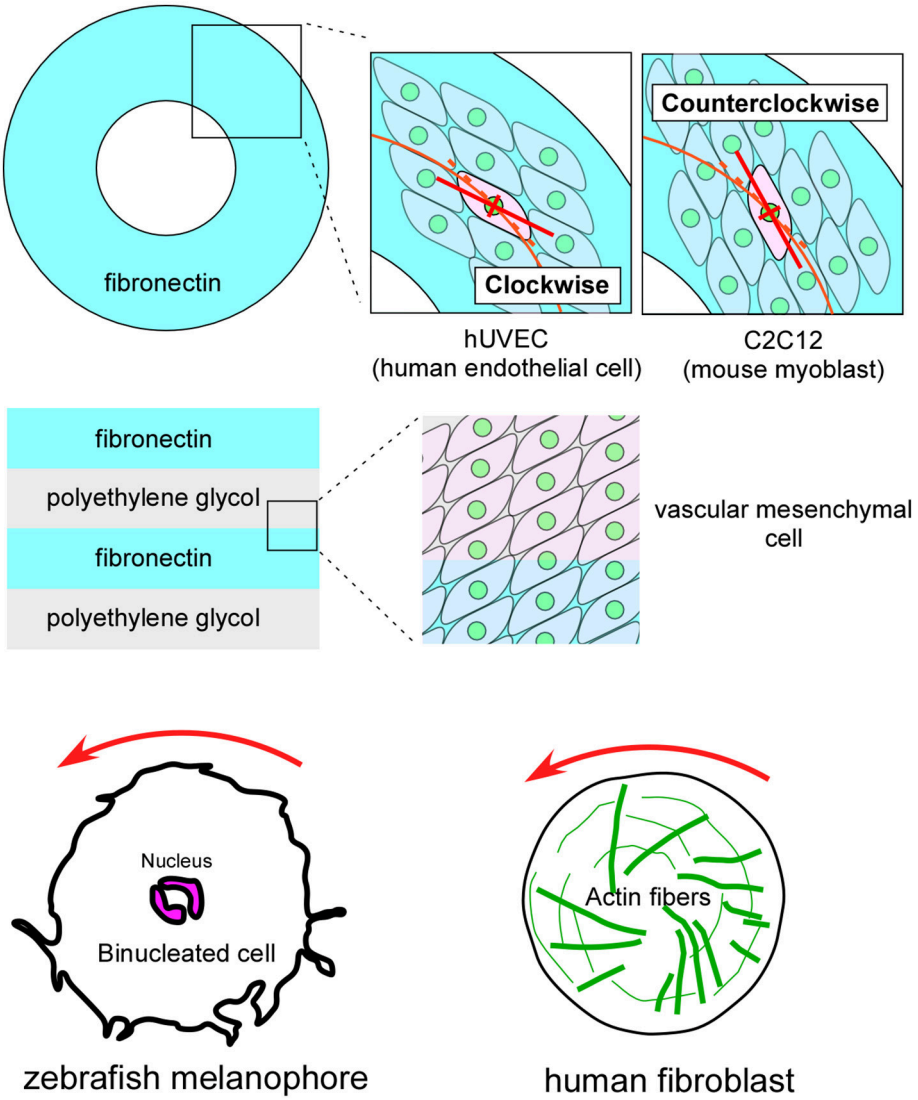

FIGURE 5 | Vertebrate cultured cells exhibit intrinsic cell chirality. **(Top)** Cultured human endothelial (hUVEC) and mouse myoblast (C2C12) cells are arranged in clockwise and counterclockwise spiral patterns on a substrate (Fibronectin) with a ring micropattern (Wan et al., 2011). **(Middle)** Vascular mesenchymal cells exhibit intrinsic chirality when plated on a substrate with a stripe micropattern (Fibronectin and polyethylene glycol) (Chen et al., 2012). **(Bottom)** A counterclockwise rotation of the nucleus is observed in cultured zebrafish melanophores **(Left)** (Yamanaka and Kondo, 2015). Human fibroblasts cultured on a micropattern substrate show chiral swirling **(Right)** (Tee et al., 2015). These figures are partly adapted from Inaki et al. (2016) with permission.

blood cells (dHL60) show leftward biased directional movement in the absence of directional chemotactic cues (Xu et al., 2007). Cell chirality is also observed in the dynamics of intracellular structures. Cultured zebrafish melanophores show a counterclockwise rotation of their dinuclei and cytoplasm (**Figure 5**), and the actin cytoskeleton plays a critical role in this chiral behavior (Tee et al., 2015; Yamanaka and Kondo, 2015). Human foreskin fibroblasts seeded on a circle micropattern show a chiral swirling of actin fibers (**Figure 5**; Tee et al., 2015). Intriguingly, in addition to the appropriate actin cytoskeleton structure, Formin activity appears to be required to generate this chiral swirling of actin fibers; similarly, the *formin* gene has an essential role in creating blastomere chirality in a snail (Davison et al., 2016). Although the biological relevance of the vertebrate cell chirality observed *in vitro* remains elusive, many cell lines from various organs show distinct chirality (Wan et al., 2011), suggesting that cell chirality might drive the LR asymmetric morphogenesis of these organs, as in invertebrates.

In addition to these vertebrate cells, chiral cellular behaver was recently reported in *Dictyostelium discoideum* (Tamada and Igarashi, 2017). During their ameboid movement, *Dictyostelium* cells extend filopodia that rotate in a rightward screwlike manner (**Figure 6**; Tamada and Igarashi, 2017). This right-screw rotation

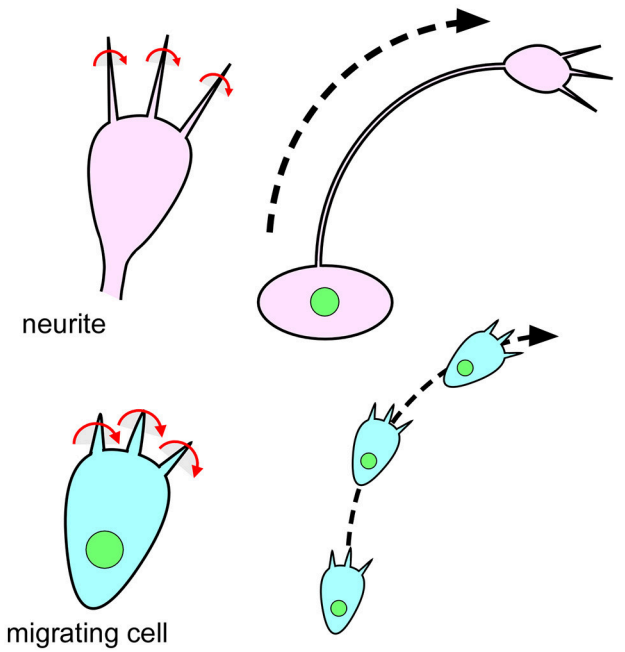

FIGURE 6 | The chiral behavior of filopodia is evolutionarily conserved from single-celled eukaryotic organisms to mammals. **(Top)** Filopodia of the growth cone on mouse neurites rotate in a rightward screwlike manner **(Left)** (Tamada and Igarashi, 2017). The right-screw rotation of filopodia introduces a clockwise growth of neurites **(Right)** (Tamada and Igarashi, 2017). **(Bottom)** Filopodia of *Dictyostelium* cells also show a rightward-screwlike rotation **(Left)** (Tamada and Igarashi, 2017). The right-screw rotation of filopodia leads the cells to migrate in a clockwise direction **(Right)** (Tamada and Igarashi, 2017).

is very similar to the movement of filopodia on the growth cone of mouse neurons (**Figure 6**; Tamada et al., 2010; Tamada and Igarashi, 2017). It was proposed that the right-screw rotation of filopodia introduces the observed clockwise tracks in neurite growth and in cell migration on two-dimensional substrates (**Figure 6**; Tamada and Igarashi, 2017). These findings suggest that cell chirality can be traced back to single-celled eukaryotic organisms.

CONCLUDING REMARKS

Today, it is well-accepted that many animal cells show intrinsic cell chirality. Although the molecular mechanisms of cell chirality formation are still largely unknown, F-actin appears to play critical roles in this process, as revealed in *Drosophila*, snails, *C. elegans*, and vertebrates. In particular, the essential role of Formin family proteins in the cell chirality formation of snail blastomeres and mammalian cells suggests that the axial rotation of F-actin may be one of the origins of chirality (Tee et al., 2015; Davison et al., 2016). In *Drosophila*, Myo31DF may switch the chiral status of the F-actin structure or dynamics, although this possibility remains to be proven.

In *Drosophila*, several lines of evidence show that cell chirality is a common mechanism in this organism for developing LR asymmetric structures. On the other hand, in vertebrates, although cell chirality is broadly found, its functions remain a mystery. A computer simulation predicted that a model cell with cell chirality may have an advantage for passing through a population of cells (Sato et al., 2015b). In addition, it is possible that cell chirality interferes or collaborates with PCP, thereby disrupting or modifying the architecture of the planarly polarized cells. This could occur in two ways: cell chirality itself may be superimposed onto the PCP, or chiral cells may intermingle with PCP-exhibiting cells. By such processes, cell chirality may control various morphogenetic events, not only LR asymmetric development. The investigation of cell chirality is still in its infancy, and many questions, especially about the molecular mechanisms of its formation and biological functions, are still open. Answering these questions will add valuable insight for studies in biology and medicine in the near future.

AUTHOR CONTRIBUTIONS

MI, TS, and KM wrote the review; MI and TS made figures.

FUNDING

This work was supported by JSPS KAKENHI Grant Number 15H05863, 16K07349, and 15K07077.

REFERENCES

Bergmann, D. C., Lee, M., Robertson, B., Tsou, M. F., Rose, L. S., and Wood, W. B. (2003). Embryonic handedness choice in *C. elegans* involves the Galpha protein GPA-16. *Development* 130, 5731–5740. doi: 10.1242/dev.00839

Brown, N. A., and Wolpert, L. (1990). The development of handedness in left/right asymmetry. *Development* 109, 1–9.

Chen, T.-H., Hsu, J. J., Zhao, X., Guo, C., Wong, M. N., Huang, Y., et al. (2012). Left-right symmetry breaking in tissue morphogenesis via cytoskeletal mechanics novelty and significance. *Circ. Res.* 110, 551–559. doi: 10.1161/CIRCRESAHA.111.255927

Coutelis, J. B., Géminard, C., Spéder, P., Suzanne, M., Petzoldt, A. G., and Noselli, S. (2013). Drosophila left/right asymmetry establishment is controlled by the Hox gene abdominal-B. *Dev. Cell* 24, 89–97. doi: 10.1016/j.devcel.2012.11.013

Davison, A., McDowell, G. S., Holden, J. M., Johnson, H. F., Koutsovoulos, G. D., Liu, M. M., et al. (2016). Formin is associated with left-right asymmetry in the pond snail and the frog. *Curr. Biol.* 26, 654–660. doi: 10.1016/j.cub.2015.12.071

Fox, D. T., and Spradling, A. C. (2009). The Drosophila hindgut lacks constitutively active adult stem cells but proliferates in response to tissue damage. *Cell Stem Cell* 5, 290–297. doi: 10.1016/j.stem.2009.06.003

González-Morales, N., Géminard, C., Lebreton, G., Cerezo, D., Coutelis, J.-B., and Noselli, S. (2015). The atypical cadherin dachsous controls left-right asymmetry in Drosophila. *Dev. Cell* 33, 675–689. doi: 10.1016/j.devcel.2015.04.026

Hatori, R., Ando, T., Sasamura, T., Nakazawa, N., Nakamura, M., Taniguchi, K., et al. (2014). Left-right asymmetry is formed in individual cells by intrinsic cell chirality. *Mech. Dev.* 133, 146–162. doi: 10.1016/j.mod.2014.04.002

Hegan, P. S., Ostertag, E., Geurts, A. M., and Mooseker, M. S. (2015). Myosin Id is required for planar cell polarity in ciliated tracheal and ependymal epithelial cells. *Cytoskeleton* 72, 503–516. doi: 10.1002/cm.21259

Hozumi, S., Maeda, R., Taniguchi, K., Kanai, M., Shirakabe, S., Sasamura, T., et al. (2006). An unconventional myosin in Drosophila reverses the default handedness in visceral organs. *Nature* 440, 798–802. doi: 10.1038/nature04625

Inaki, M., Liu, J., and Matsuno, K. (2016). Cell chirality: its origin and roles in left-right asymmetric development. *Philos. Trans. R. Soc. Lond. B Biol. Sci.* 371:20150403. doi: 10.1098/rstb.2015.0403

Kuranaga, E., Matsunuma, T., Kanuka, H., Takemoto, K., Koto, A., Kimura, K., et al. (2011). Apoptosis controls the speed of looping morphogenesis in Drosophila male terminalia. *Development* 138, 1493–1499. doi: 10.1242/dev.058958

Kuroda, R., Endo, B., Abe, M., and Shimizu, M. (2009). Chiral blastomere arrangement dictates zygotic left-right asymmetry pathway in snails. *Nature* 462, 790–794. doi: 10.1038/nature08597

Lengyel, J. A., and Iwaki, D. D. (2002). It takes guts: the Drosophila hindgut as a model system for organogenesis. *Dev. Biol.* 243, 1–19. doi: 10.1006/dbio.2002.0577

McConnell, R. E., and Tyska, M. J. (2010). Leveraging the membrane - cytoskeleton interface with myosin-1. *Trends Cell Biol.* 20, 418–426. doi: 10.1016/j.tcb.2010.04.004

Murakami, R., and Shiotsuki, Y. (2001). Ultrastructure of the hindgut of Drosophila larvae, with special reference to the domains identified by specific gene expression patterns. *J. Morphol.* 248, 144–150. doi: 10.1002/jmor.1025

Naganathan, S. R., Fürthauer, S., Nishikawa, M., Jülicher, F., and Grill, S. W. (2014). Active torque generation by the actomyosin cell cortex drives left–right symmetry breaking. *Elife* 3:e04165. doi: 10.7554/eLife.04165

Nonaka, S. (2013). Visualization of mouse nodal cilia and nodal flow. *Methods Enzymol.* 525, 149–157. doi: 10.1016/B978-0-12-397944-5.00008-0

Nonaka, S., Shiratori, H., Saijoh, Y., and Hamada, H. (2002). Determination of left-right patterning of the mouse embryo by artificial nodal flow. *Nature* 418, 96–99. doi: 10.1038/nature00849

Nonaka, S., Tanaka, Y., Okada, Y., Takeda, S., Harada, A., Kanai, Y., et al. (1998). Randomization of left-right asymmetry due to loss of nodal cilia generating leftward flow of extraembryonic fluid in mice lacking KIF3B motor protein. *Cell* 95, 829–837. doi: 10.1016/S0092-8674(00)81705-5

Nonaka, S., Yoshiba, S., Watanabe, D., Ikeuchi, S., Goto, T., Marshall, W. F., et al. (2005). *De novo* formation of left-right asymmetry by posterior tilt of nodal cilia. *PLoS Biol.* 3:e268. doi: 10.1371/journal.pbio.0030268

Okada, Y., and Hirokawa, N. (1999). A processive single-headed motor: kinesin superfamily protein KIF1A. *Science* 283, 1152–1157. doi: 10.1126/science.283.5405.1152

Okada, Y., and Hirokawa, N. (2009). Observation of nodal cilia movement and measurement of nodal flow. *Methods Cell Biol.* 91, 265–285. doi: 10.1016/S0091-679X(08)91014-1

Okumura, T., Sasamura, T., Inatomi, M., Hozumi, S., Nakamura, M., Hatori, R., et al. (2015). Class I myosins have overlapping and specialized functions in left-right asymmetric development in Drosophila. *Genetics* 199, U1183–U1493. doi: 10.1534/genetics.115.174698

Pelseneer, P. (1920). Les variations et leur heredite chez les Molluques. *Classe Sci.* 5:826.

Petzoldt, A. G., Coutelis, J. B., Géminard, C., Spéder, P., Suzanne, M., Cerezo, D., et al. (2012). DE-Cadherin regulates unconventional Myosin, ID and Myosin IC in Drosophila left-right asymmetry establishment. *Development* 139, 1874–1884. doi: 10.1242/dev.047589

Pruyne, D., Evangelista, M., Yang, C., Bi, E., Zigmond, S., Bretscher, A., et al. (2002). Role of formins in actin assembly: nucleation and barbed-end association. *Science* 297, 612–615. doi: 10.1126/science.1072309

Pyrpassopoulos, S., Feeser, E. A., Mazerik, J. N., Tyska, M. J., and Ostap, E. M. (2012). Membrane-bound myo1c powers asymmetric motility of actin filaments. *Curr. Biol.* 22, 1688–1692. doi: 10.1016/j.cub.2012.06.069

Raymond, M. J., Ray, P., Kaur, G., Singh, A. V., and Wan, L. Q. (2016). Cellular and nuclear alignment analysis for determining epithelial cell chirality. *Ann. Biomed. Eng.* 44, 1475–1486. doi: 10.1007/s10439-015-1431-3

Robertson, C. W. (1936). The metamorphosis of *Drosophila melanogaster,* including an accurately timed account of the principal morphological changes. *J. Morphol.* 59, 351–399.

Rolan-Alvarez, E., and Rolan, E. (1995). Occurrence true symmetry inversion in gastropods: an evolutiony perspective. *Thalassas* 11, 93–104.

Sato, K., Hiraiwa, T., Maekawa, E., Isomura, A., Shibata, T., and Kuranaga, E. (2015a). Left-right asymmetric cell intercalation drives directional collective cell movement in epithelial morphogenesis. *Nat. Commun.* 6:10074. doi: 10.1038/ncomms10074

Sato, K., Hiraiwa, T., and Shibata, T. (2015b). Cell chirality induces collective cell migration in epithelial sheets. *Phys. Rev. Lett.* 115:188102. doi: 10.1103/PhysRevLett.115.188102

Shibazaki, Y., Shimizu, M., and Kuroda, R. (2004). Body handedness is directed by genetically determined cytoskeletal dynamics in the early embryo. *Curr. Biol.* 14, 1462–1467. doi: 10.1016/j.cub.2004.08.018

Spéder, P., Adám, G., and Noselli, S. (2006). Type ID unconventional myosin controls left-right asymmetry in Drosophila. *Nature* 440, 803–807. doi: 10.1038/nature04623

Suzanne, M., Petzoldt, A. G., Spéder, P., Coutelis, J. B., Steller, H., and Noselli, S. (2010). Coupling of apoptosis and L/R patterning controls stepwise organ looping. *Curr. Biol.* 20, 1773–1778. doi: 10.1016/j.cub.2010.08.056

Tamada, A., and Igarashi, M. (2017). Revealing chiral cell motility by 3D Riesz transform-differential interference contrast microscopy and computational kinematic analysis. *Nat. Commun.* 8:2194. doi: 10.1038/s41467-017-02193-w

Tamada, A., Kawase, S., Murakami, F., and Kamiguchi, H. (2010). Autonomous right-screw rotation of growth cone filopodia drives neurite turning. *J. Cell Biol.* 188, 429–441. doi: 10.1083/jcb.200906043

Taniguchi, K., Maeda, R., Ando, T., Okumura, T., Nakazawa, N., Hatori, R., et al. (2011). Chirality in planar cell shape contributes to left-right asymmetric epithelial morphogenesis. *Science* 333, 339–341. doi: 10.1126/science.1200940

Tee, Y. H., Shemesh, T., Thiagarajan, V., Hariadi, R. F., Anderson, K. L., Page, C., et al. (2015). Cellular chirality arising from the self-organization of the actin cytoskeleton. *Nat. Cell Biol.* 17, 445–457. doi: 10.1038/ncb3137

Tzolovsky, G., Millo, H., Pathirana, S., Wood, T., and Bownes, M. (2002). Identification and phylogenetic analysis of *Drosophila melanogaster* myosins. *Mol. Biol. Evol.* 19, 1041–1052. doi: 10.1093/oxfordjournals.molbev.a004163

Wan, L. Q., Ronaldson, K., Park, M., Taylor, G., Zhang, Y., Gimble, J. M., et al. (2011). Micropatterned mammalian cells exhibit phenotype-specific left-right asymmetry. *Proc. Natl. Acad. Sci. U.S.A.* 108, 12295–12300. doi: 10.1073/pnas.1103834108

Wells, R. E., Barry, J. D., Warrington, S. J., Cuhlmann, S., Evans, P., Huber, W., et al. (2013). Control of tissue morphology by Fasciclin III-mediated intercellular adhesion. *Development* 140, 3858–3868. doi: 10.1242/dev.096214

Wood, W. B. (1991). Evidence from reversal of handedness in *C. elegans* embryos for early cell interactions determining cell fates. *Nature* 349, 536–538. doi: 10.1038/349536a0

Worley, K. E., Shieh, D., and Wan, L. Q. (2015). Inhibition of cell-cell adhesion impairs directional epithelial migration on micropatterned surfaces. *Integr. Biol.* 7, 580–590. doi: 10.1039/C5IB00073D

Xu, J., Van Keymeulen, A., Wakida, N. M., Carlton, P., Berns, M. W., and Bourne, H. R. (2007). Polarity reveals intrinsic cell chirality. *Proc. Natl. Acad. Sci. U.S.A.* 104, 9296–9300. doi: 10.1073/pnas.0703153104

Yamanaka, H., and Kondo, S. (2015). Rotating pigment cells exhibit an intrinsic chirality. *Genes Cells* 20, 29–35. doi: 10.1111/gtc.12194

Yang, C. H., Axelrod, J. D., and Simon, M. A. (2002). Regulation of Frizzled by fat-like cadherins during planar polarity signaling in the Drosophila compound eye. *Cell* 108, 675–688. doi: 10.1016/S0092-8674(02)00658-X

Conflict of Interest Statement: The authors declare that the research was conducted in the absence of any commercial or financial relationships that could be construed as a potential conflict of interest.

frontiers in Cell and Developmental Biology

ORIGINAL RESEARCH
published: 19 July 2017
doi: 10.3389/fcell.2017.00066

Wave Propagation of Junctional Remodeling in Collective Cell Movement of Epithelial Tissue: Numerical Simulation Study

Tetsuya Hiraiwa[1], *Erina Kuranaga*[2,3] *and Tatsuo Shibata*[4]*

[1] Department of Physics, Graduate School of Science, University of Tokyo, Tokyo, Japan, [2] Laboratory of Histogenetic Dynamics, Graduate School of Life Sciences, Tohoku University, Sendai, Japan, [3] Laboratory for Histogenetic Dynamics, RIKEN Center for Developmental Biology, Kobe, Japan, [4] Laboratory for Physical Biology, RIKEN Quantitative Biology Center, Kobe, Japan

OPEN ACCESS

Edited by:
Takaaki Matsui,
Nara Institute of Science and Technology, Japan

Reviewed by:
Philippe Marcq,
Université Pierre et Marie Curie, France
Takaki Miyata,
Nagoya University, Japan
René-Marc Mège,
Centre National de la Recherche Scientifique (CNRS), France

***Correspondence:**
Tatsuo Shibata
tatsuo.shibata@riken.jp

Specialty section:
This article was submitted to Cell Adhesion and Migration, a section of the journal Frontiers in Cell and Developmental Biology

Received: 26 March 2017
Accepted: 28 June 2017
Published: 19 July 2017

Citation:
Hiraiwa T, Kuranaga E and Shibata T (2017) Wave Propagation of Junctional Remodeling in Collective Cell Movement of Epithelial Tissue: Numerical Simulation Study. Front. Cell Dev. Biol. 5:66. doi: 10.3389/fcell.2017.00066

During animal development, epithelial cells forming a monolayer sheet move collectively to achieve the morphogenesis of epithelial tissues. One driving mechanism of such collective cell movement is junctional remodeling, which is found in the process of clockwise rotation of *Drosophila* male terminalia during metamorphosis. However, it still remains unknown how the motions of cells are spatiotemporally organized for collective movement by this mechanism. Since these moving cells undergo elastic deformations, the influence of junctional remodeling may mechanically propagate among them, leading to spatiotemporal pattern formations. Here, using a numerical cellular vertex model, we found that the junctional remodeling in collective cell movement exhibits spatiotemporal self-organization without requiring spatial patterns of molecular signaling activity. The junctional remodeling propagates as a wave in a specific direction with a much faster speed than that of cell movement. Such propagation occurs in both the absence and presence of fluctuations in the contraction of cell boundaries.

Keywords: mathematical model, vertex model, mechanobiology, collective cell migration, epithelial cells, cell intercalation

INTRODUCTION

The morphogenesis of embryonic development involves epithelial tissue deformations (Tomer et al., 2012). Epithelial tissue consists of epithelial cells that adhere to each other through cell-cell junctions, such as adherence junctions and tight or septate junctions. These intercellular junctions are connected to the intracellular actin cables of individual cells (Harris and Tepass, 2010; Takeichi, 2014), which generate a mechanical tension that is exerted on the cell-cell junction. The mechanical forces of an individual cell are further transmitted to its neighboring cells through the junctions. Consequently, the cell monolayer achieves mechanical integrity as an epithelial tissue. While maintaining the balance of mechanical forces in the tissue, an epithelial sheet can dynamically deform to elongate and fold during development. Such epithelial deformations are often achieved through the positional rearrangements of epithelial cells (Bertet et al., 2004; Nishimura et al., 2012; Tomer et al., 2012). Such cell rearrangements in a cell sheet occur through the extension and contraction of cell-cell junctions in the apical plane, which lead to junction exchange between

neighboring cells, which is called a T1 transition, while maintaining the monolayer integrity (Bertet et al., 2004; Blankenship et al., 2006; Rauzi et al., 2008). Therefore, the remodeling of the network of cell-cell junctions in the apical plane is a key mechanism by which epithelial tissue achieves a large deformation.

A typical example of a deformation driven by the junctional remodeling is convergent extension, by which a tissue elongates in one direction while shrinking in the perpendicular direction (Tada and Heisenberg, 2012; Collinet et al., 2015). During this process, the cell junctions perpendicular to the extension direction shrink and cells intercalate with each other along the direction of tissue convergence (Munro and Odell, 2002a,b). Consequently, the tissue achieves a large deformation without changing the cell size or shape and thus the internal stress. A well-studied example is the germ band extension (GBE) occurring during *Drosophila* early embryogenesis. During GBE, epithelial cells undergo intercalation directed along the dorso-ventral (DV) axis. A high accumulation of non-muscle myosin II (Myo-II) at the anterior and posterior cell boundaries increases the strength of the junctional contraction, causing a decrease in junctional length. These DV-oriented cell intercalations cause the tissue to narrow along the DV axis and lengthen along the anteroposterior (AP) axis, resulting in GBE. In other examples of large scale morphogenesis driven by the junctional remodeling, mediolaterally oriented cell intercalation contributes to kidney tubule elongation in *Xenopus* (Lienkamp et al., 2012), and polarized apical cell constriction drives neural tube invagination in the chick (Nishimura et al., 2012).

Such cell intercalation accompanied by the junctional remodeling is also a driving mechanism for the collective cell movement of epithelial tissue. During the morphogenesis of *Drosophila* male terminalia, the genitalia undergo a 360° clockwise rotation, which induces dextral spermiduct looping (Suzanne et al., 2010; Kuranaga et al., 2011). The *Drosophila* genitalia rotation (DGR) is achieved by the collective clockwise movement of surrounding epithelial cells. We previously reported that this collective cell movement is driven by polarized cell intercalation at the right oblique cell boundaries in the surrounding epithelial tissue (Sato et al., 2015a). The moving cells intercalate while remaining attached to their neighboring cells. Most of the remodeled cell boundaries form right oblique angles with the AP axis and show Myo-II accumulation. In addition, numerical simulations revealed that such diagonally polarized cell intercalation is sufficient to induce unidirectional cellular movement (Sato et al., 2015a). We also revealed that such left-right asymmetry of the cell boundary motion accompanied by AP asymmetry of the tissue is indispensable for the unidirectional movement (Sato et al., 2015b). Since epithelial cells also have the asymmetry of apico-basal polarity, the left-right asymmetry of Myo-II accumulation and resultant cell boundary motions in the planer plane can be referred to as the chirality, or the handedness, of the cells (Sato et al., 2015b).

Both GBE and DGR are induced by the cell intercalation. However, the dynamicity of cells in the tissues shows a strong contrast between the two situations. GBE is induced by a tissue deformation involving different aspect ratios of singly rearranged cells. In contrast, DGR involves the movement of a cell collective. Specifically, small cells of about 5-μm diameter move a distance of 300 μm or more in over 12 hours (Kuranaga, 2012; Sato et al., 2015a). What makes this difference in the dynamicity of the two systems? One obvious difference is the direction of cell intercalation; it is perpendicular to the direction of cell movement in GBE (Collinet et al., 2015), while diagonal in DGR (see Figure 4 in Sato et al., 2015a). Consequently, the cell intercalation events take place transiently in GBE until the tissue deformation finishes, while in DGR the cell intercalation events can continue to occur. However, this diagonal direction of cell intercalation is not sufficient to explain the collective cell movement that lasts for more than 12 hours. One factor underlying the difference in these processes is predicted to be the spatiotemporal dynamics (time order and distribution) of the cell intercalation. What determines the spatiotemporal dynamics of the cell intercalations?

A molecular signaling activity can regulate the spatiotemporal dynamics of junctional remodeling and cell rearrangement. But, it can also be organized spontaneously through mechanical processes. Here, we referred to such a spontaneous spatiotemporal organization of cell intercalation without relying on molecular signaling activity as self-organization. After a certain period of time, a series of T1 transitions gives a viscous property or plasticity to a tissue that enables large-scale deformation. In contrast, in the shorter term, elastic behavior can appear in response to the T1 transition of an individual cell that is induced by intracellular molecular signaling. When individual T1 transition is induced, mechanical forces are exerted on the surrounding cells. Such forces can be transmitted through the network of cell-cell junctions. The transmission of such a force usually ceases within the distance of a few cells (Farhadifar et al., 2007). If it further triggers another T1 transition, however, the transmission can occur over a longer distance. Consequently, the junctional remodeling and cell rearrangement could spread throughout an entire tissue in a spatiotemporally correlated way. It is therefore possible that the large scale reorganization of epithelial tissue is not only instructed by molecular signaling activity of axis information, but also involves self-organization through mechanical coupling among cells. However, such self-organized spatiotemporal dynamics of cell intercalations have not been described in our previous study. Therefore, the question that we address in this paper is whether the transmission of mechanical forces due to the cell intercalation can occur without spatiotemporal signal instruction, and how the cell rearrangements by junction remodeling are spatiotemporally organized during the collective epithelial cell movement in DGR.

In this paper, we investigated theoretically the spatiotemporal dynamics of cell movement in the ring-like epithelial tissue that surrounds the male genitalia, using a mathematical model that we described previously (Sato et al., 2015a,b). We show for the first time that the T1 transitions and cell rearrangement propagate in space in the same direction of the collective cell movement, leading to the propagation of cell velocity change in space with speed faster than the collective cell movement.

MODEL AND METHODS

Numerical Model of the Epithelial Cell Monolayer with Left–Right Cell Asymmetry

We describe the model for the rotational motion of *Drosophila* genital disc that we have introduced in the previous work (Sato et al., 2015a). We use a vertex cell model in two-dimensional space to simulate the in-plane motions of cells in an epithelial monolayer tissue (Nagai and Honda, 2001; Farhadifar et al., 2007). When we look at the epithelial cell monolayer from the apical side (**Figure 1A**), individual cells exhibit a polygonal shape. Based on this observation, the cell shapes are described as polygons with vertices and edges (**Figure 1B**). A polygon in the model is specified by the location of the i th vertex, $\mathbf{r}_i = (x_i, y_i)$, and the bond $\langle kl \rangle$ that connects vertices k and l. By considering the force balance between the potential force $-\partial E(\{\mathbf{r}_i\}_i, \{\gamma_{kl}\}_{\langle kl \rangle})/\partial \mathbf{r}_i$ and the friction force of the simplest form $-\eta_i \mathbf{r}_i/dt$, the time evolution equation of the vertex model is given by

$$\frac{d\mathbf{r}_i}{dt} = -\frac{1}{\eta_i} \frac{\partial E(\{\mathbf{r}_i\}_i, \{\gamma_{kl}\}_{\langle kl \rangle})}{\partial \mathbf{r}_i}\Big|_{\gamma_{kl} = \hat{\gamma}(\theta_{kl})} \tag{1}$$

Here, the potential function E is given by

$$E(\{\mathbf{r}_i\}_i, \{\gamma_{kl}\}_{\langle kl \rangle}) = E_\mathrm{p} + E_\mathrm{t} + E_\mathrm{b}. \tag{2}$$

The first term on the right hand side of Equation (2), E_p, is the contribution from the hydrostatic pressure within a single cell given by

$$E_\mathrm{p} = \frac{K_a}{2} \sum_{\alpha=1}^{N} (A_\alpha/A_0 - 1)^2, \tag{3}$$

with the actual area A_α of the α-th cell, the preferred area A_0, and the coefficient K_a controlling the strength of the pressure. The integer N indicates the total number of cells. The second term E_t is the potential function for the total tension on cell-cell adhesions, given by

$$E_\mathrm{t} = \frac{K_p}{2} \sum_{\alpha=1}^{N} (L_\alpha/L_0 - 1)^2 + \sum_{\langle ij \rangle} \gamma_{ij}(t)\, \ell_{ij}. \tag{4}$$

The first term is the contribution due to the mismatch between the actual perimeter L_α of the α-th cell and the preferred perimeter L_0, with the coefficient K_p controlling the tension strength. The second term is another contribution due to the cell's spontaneous and bond-specific transport of molecules, such as myosin II and cadherin, which exert tension with the bond-specific tension strength γ_{kl} (**Figure 1C**), which can be time dependent, as described in detail below.

The last term E_b is the potential function describing the boundaries of the system as explained below. The epithelial monolayer forms a ring-like tissue. It is flanked by two circular walls with different radii (R_out and R_in for the outer and inner walls, respectively), both of which are centered at the origin $(0, 0)$. These walls mimic the concentric ring-like tissue structure that surrounds the *Drosophila* male genitalia at the larval stage (Sato et al., 2015a). We assume that additional forces are exerted on the vertices i located along the outer wall ($i \in \mathcal{O}$) and the inner wall ($i \in J$), described by the potential function as

$$E_\mathrm{b} = \frac{k_\mathrm{out}}{2} \sum_{i \in \mathcal{O}} (r_i - R_\mathrm{out})^2 + \frac{k_\mathrm{in}}{2} \sum_{i \in J} (r_i - R_\mathrm{in})^2, \tag{5}$$

where $r_i = \sqrt{x_i^2 + y_i^2}$ is the distance of the i th vertex from the origin (0,0), and k_out and k_in are coefficients. We also assume that the friction coefficients η_i are different between vertices along the outer and inner walls.

The bond-specific tension γ_{kl} includes regulatory processes that are cell-autonomous and not described by potential functions. We thus consider that the force in Equation (1) is given as a derivative with respect to the position $\mathbf{r}_i$ under the condition that γ_{kl} is independent of $\mathbf{r}_i$. After deriving the force, we consider that the tension strength γ_{kl} depends on the direction θ_{kl} of the bond $\langle kl \rangle$ around the AP axis of the tissue, as $\gamma_{kl}(t) = \hat{\gamma}[\theta_{kl}(\mathbf{r}_k, \mathbf{r}_l)]$. This consideration breaks the conservation of the potential E in Equation (2), and keeps the system from relaxing

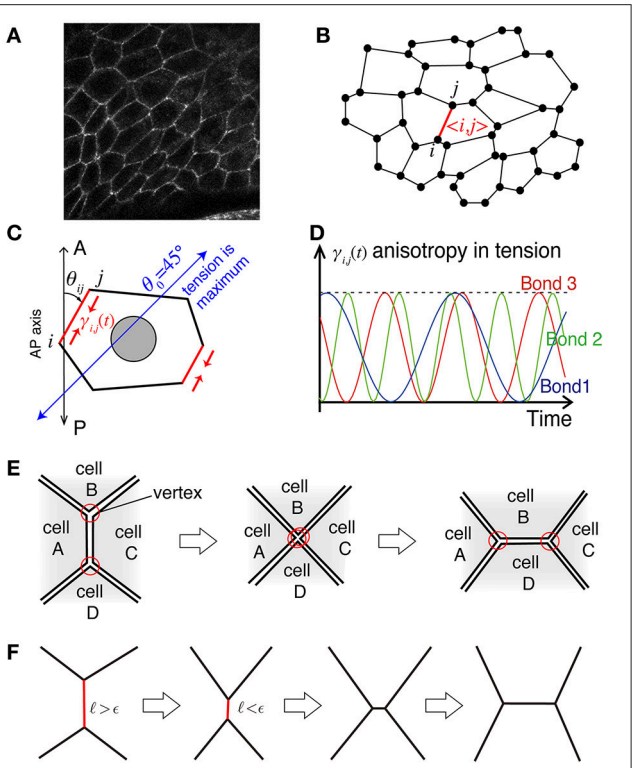

FIGURE 1 | Illustration of the mathematical model. **(A)** Actual cell–cell junctions visualized with E-cadherin. The epithelial cell monolayer resembles polygons whose shared sides correspond to cell–cell junctions. **(B)** The cell vertex model in two dimensions, modeling the polygon-like structure of the network of cell–cell junctions. The vertex index is indicated by i and j, and the bond index is given by $\langle i, j \rangle$. **(C)** Bond-dependent tension strength. When the bond is tilted in the clockwise direction by $\theta_0 = 45°$ from the AP axis, the line tension of the bond is maximum. **(D)** The heterogeneity in line tension strength in the model. **(E)** Process of junctional remodeling, called a T1 transition. Lines indicate the edges of cells. **(F)** T1 transition process in the numerical simulation.

to the equilibrium state (Sato et al., 2015b). The specific form of $\gamma_{kl}(t)$ in this article is given by

$$\gamma_{kl}(t) = \gamma_c \cos^2(\theta_{kl}(t) - \theta_0), \quad (6)$$

where $\theta_0 = +45^\circ$ and γ_c is a constant giving the maximum tension. We define the sign of the angle θ_{kl} in the clockwise direction around the AP axis. We also consider the case in which temporal fluctuations are present in the tension $\gamma_{kl}(t)$, given by

$$\gamma_{kl}(t) = \gamma_c \cos^2\left(2\pi f_{kl} t + \delta_{kl}\right) \cos^2(\theta_{kl}(t) - \theta_0), \quad (7)$$

where f_{kl} is the frequency and δ_{kl} is the initial phase of the bond $\langle kl \rangle$. The frequency and initial phase are given by uniformly distributed random numbers in $f_{kl} \in [0, 1]$ and $\delta_{kl} \in [0, 2\pi]$ in the presence of temporal fluctuations (**Figure 1D**).

When the length of a bond becomes shorter than a threshold ϵ during the time evolution according to Equation (1), the bond rotates 90 degrees around its midpoint, and the five bonds of the two vertices at the rotated bond reconnect to achieve a T1 transition (**Figure 1E**).

The numerical simulation is performed based on Equations (1)–(5) by the simple Euler method with time discretization of the increment $dt = 0.001$. The T1 transition occurs when the length ℓ_{kl} of the bond $\langle kl \rangle$ becomes shorter than a given length $\epsilon = 0.005$ (see also **Figure 1F**). The friction constant is set to be $\eta_i = 1$ except for the outer and inner walls. We choose the units of length and time so that the radius of outer wall and the coefficient for tension are given by $R_{\rm out} = 1$ and $\gamma_c = 1$ ($\eta_i R_{\rm out}/\gamma_c = 1$), respectively. The friction at the outer wall is given by $\eta_i = 100$, and at the inner wall as $\eta_i = 10$. The total number of cells is given by $N = 450$. Additional parameter values are given by $R_{\rm in} = 0.5$, $k_{\rm out} = 100$, $k_{\rm in} = 100$, $K_a = 10$, $A_0 = (\pi R_{\rm out}^2 - \pi R_{\rm in}^2)/N \sim 0.0052$, and $L_0 = \sqrt{4\pi A_0} \sim 0.26$. The strength of the tension K_p is shown in the figures. This set of parameter values are basically comparable with our previous work (Sato et al., 2015a) except for the total number N of cells, which was 168 in the previous work. By increase of N, we are able to investigate the mechanical processes during the collective cell movement by measuring spatiotemporal distributions and correlations of the velocity fluctuations of cell motility and the T1 transition frequency.

Note that the collective cell migration of genital disc of *Drosophila* is considered to be driven mainly by the activity at the apical side (Sato et al., 2015a). Therefore, in our model active processes were considered for the apical processes, such as the remodeling of cell-cell junctions. For basal processes, only a passive resistance force was considered between cells and the basal extracellular matrix and cells. A collective migration of epithelial cells may also be induced by protrusive activities along the basement membrane. Motivated by such basal processes, directional driving forces of individual cells have been introduced to a cell vertex model in self-propelled Voronoi model (Li and Sun, 2014; Garcia et al., 2015; Bi et al., 2016).

Analysis of Simulation Results

In the following sections, from numerical simulations, we determine the cell angular velocity v, the elliptical cell shape anisotropy s, the frequency of T1 transition, $n_{\rm T1}$, and the bond chirality c. The angular velocity v_α of the α-th cell is given by $v_\alpha = d\psi_\alpha(t)/dt$ around the origin (0,0) (genital disc center), where ψ_α is the angular position of the α-th cell around the origin, and the cell position is given by the centroid of the polygonal cell. The angular velocity v_α is positive when the cell moves in clockwise direction. Then, v is given as the average of v_α among the cells. For the elliptical cell anisotropy s_α of the α-th cell, we first quantify the moment matrix of inertia $\mathbf{M}$ of the polygonal cell, and s_α is obtained by the half difference of the two eigenvalues of $\mathbf{M}$. Thus, s_α measures the deviation of the cell shape from that of a circle. The variable s is given as the average of s_α among the cells. For the frequency of T1 transition, $n_{\rm T1}$, we count the number of T1 transition per unit time. For the bond chirality c, we count the number of tilted cell-cell junctions as described previously (Sato et al., 2015a). In this article, it is given by $c \equiv N_{\rm cl}/N_{\rm ccl} - N_{\rm ccl}/N_{\rm cl}$, where $N_{\rm cl}$ and $N_{\rm ccl}$ are the numbers of cell-cell junctions tilted clockwise and counterclockwise, respectively, from the AP axis. When the distribution of the bond directions is uniform with respect to the AP axis, c is zero, while c is not zero when the bond directions are biased. The mathematical details of these quantities are given in the Appendix.

RESULTS

Oscillation in Collective Cell Movement

As reported previously, the entire ring-like epithelial tissue that surrounds the genitalia rotates in the clockwise direction (**Figure 2A**, **Supplementary Movie 1**). To see the dynamics of collective cell movement quantitatively, we first measured the global angular velocity for the case without temporal fluctuation in the tension, as plotted over time in **Figure 2B**. Here, the global angular velocity is the average of the angular velocity of all the cells. The global angular velocity exhibited a dependence on K_p as reported previously (Sato et al., 2015b). In **Figure 2C** (red symbols), the global angular velocity averaged over time was plotted against K_p. The global angular velocity showed a maximum value at around $K_p = 5$. As K_p increased further, the state is discontinuously changed from the rotating state to a state without rotation at around $K_p \approx 15$. Such an abrupt change is called subcritical transition. This subcritical characteristic of the transition was also seen in the hysteresis curves (blue and green lines).

How are the cell motions organized during the collective movement? One possibility would be that the cells would move at the same speed. Another possibility would be that they move in the clockwise direction randomly without a cell-cell correlation. Interestingly, the global angular velocities exhibited temporal oscillatory behaviors as shown in **Figure 2B**, indicating that some temporal organization is present in the cell movements. To examine this oscillatory behavior more closely, in addition to the global angular velocity, we plotted the time series of the T1 transition frequency, $n_{\rm T1}(t)$, the cell shape distortion $s(t)$, and the bond chirality $c(t)$ in **Figure 3A** (see Appendix for the detailed explanation of these quantities). To see the oscillatory behavior more statistically, the temporal auto-correlation functions were plotted in **Figure 3B** for the four quantities. The auto-correlation

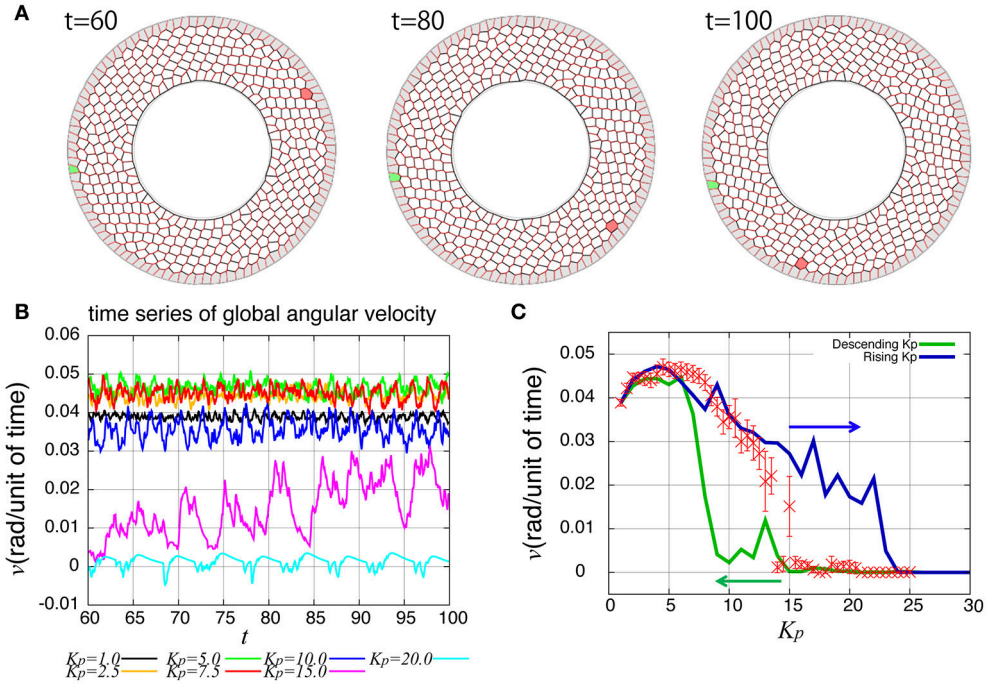

FIGURE 2 | Rotational motion of the genital disc in the absence of line tension fluctuation. **(A)** Time-lapse images of genital disc rotation. **(B)** Time evolution of global angular velocity for various values of K_D. **(C)** K_D-dependence of the global angular velocity. The angular velocity was averaged over the time window from $t = 60$ to 100 (red). Error bars indicate the standard deviation in the time course. Hysteresis curves for the global angular velocity were plotted for increasing and decreasing parameter values (blue and green lines, respectively).

function quantifies the correlation of a quantity at different time points with lag time Δt. This analysis indicated that these quantities exhibit oscillation with the same oscillation period of $t \approx 2$. To determine the temporal order of the events, we next studied the temporal cross-correlation functions among the four quantities, shown in **Figures 3C,D**. The cross-correlation function quantifies the correlation of two quantities at different time points with lag time Δt. This analysis revealed that as the bond chirality c increases, cell distortion is accumulated, as evidenced by the increase in s (green line in **Figure 3D**), accompanied by a decrease in the angular velocity, as indicated by the negative peak with a positive delay time in the blue line in **Figure 3C**. Such cell distortion can be released by T1 transition. **Figure 3D** (blue line) shows that the correlation between n_{T1} and s reaches its maximum positive value when the delay time is zero, indicating that an accumulation of distortion accompanies the increase in the number of T1 transition. Then, the T1 transition enhances the change in cell positions, causing an increase in the angular velocity $v(t)$. The correlation between $v(t)$ and $n_{\mathrm{T1}}(t)$ reaches its maximum value at a small positive delay time (red line in **Figure 3C**).

Spatial Propagation of Cell Rearrangement

So far, we have studied the global quantities averaged over space. To see whether the cell movement is organized spatially, we next examined the cell movement and rearrangements in a local area. In **Figure 4**, the local averages of the angular velocities and the T1 transition frequency, $v(\theta, t)$ and $n_{\mathrm{T1}}(\theta, t)$ are shown in **Figures 4A,B**, respectively (the last 10 units of time are displayed). We found small patches indicating propagations of increase in both angular velocity and T1 transition frequency generated at different positions. We then scrutinized these propagation patterns in more quantitative ways as follows. We first considered the temporal autocorrelations of the local angular velocity v (**Figure 4C**, red line), which also exhibited an oscillatory behavior with period of about 2 units of time, consistent with the case of global velocity (**Figure 3B**). Then, we calculated the spatiotemporal autocorrelation function of the local angular velocity as shown in **Figure 4E** (a schematic explanation of spatiotemporal correlation function is shown in **Supplementary Figure 1**). The peak in the correlation at $t = 0$ and $\Delta\theta = 0$ exhibited a propagation in the clockwise direction $\Delta\theta > 0$ with a velocity of about 2 (rad) per unit time. Interestingly, this propagation speed was much faster than the angular velocity of cell movement, which was at most about 0.05 (rad) per unit time (**Figure 2C**, $K_p = 5$). Considering that in the present model the potential force is balanced with the frictional force that is proportional to the velocity, the propagation of velocity change indicates that the force is transmitted through the tissue as in Introduction.

To see the propagation of the T1 transition statistically, we next plotted the temporal and spatiotemporal auto-correlation functions in **Figure 4C** (green line) and **Figure 4F**, respectively. When compared with the local velocity [**Figure 4C**

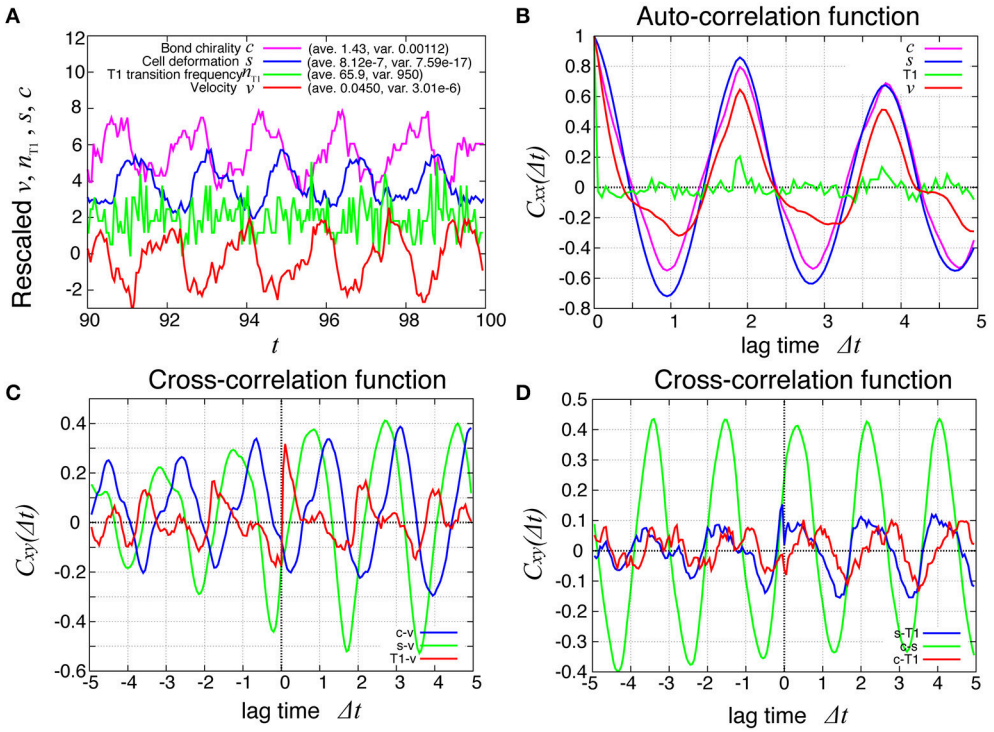

FIGURE 3 | Dynamics and correlation functions for $K_D = 7.5$ in the absence of line tension oscillation, showing oscillations of the rotation velocity, T1 transition frequency, shape deformation and chirality in bond angles and correlations between them with time delays. **(A)** Time evolution of the global angular velocity v, (red), the number of T1 transitions per unit time, n_{T1} (green), elliptical anisotropy s (blue), and bond chirality c (purple). For these quantities of $x = v, n_{T1}, s,$ or c, we plotted the scaled values as $(x - \langle x \rangle)/\sigma_x$ with the average $\langle x \rangle$ and standard deviation σ_x. For visibility, the plots were offset by 2 (n_{T1}), 4 (s), and 6 (c). **(B)** Auto-correlations of v, n_{T1}, s, and c. **(C)** Cross-correlation functions between v and the other quantities, given by $C_{xv}(\Delta t) = \langle \delta x(t) \delta v(t + \Delta t) \rangle / \sigma_x \sigma_v$, where x is n_{T1}, s, or c (red, green, and blue, respectively). Here, the positive time difference Δt means that x precedes v. $\delta x = x - \langle x \rangle$. **(D)** Cross-correlation functions given by $C_{sn_{T1}}(\Delta t) = \langle \delta s(t) \delta n_{T1}(t + \Delta t) \rangle / \sigma_s \sigma_{n_{T1}}$, $C_{cs}(\Delta t) = \langle \delta c(t) \delta s(t + \Delta t) \rangle / \sigma_c \sigma_s$, and $C_{cn_{T1}}(\Delta t) = \langle \delta c(t) \delta n_{T1}(t + \Delta t) \rangle / \sigma_c \sigma_{n_{T1}}$.

(red line) and **Figure 4E**], the oscillation and propagation of the T1 transitions were not so evident. Then, the cross-correlation function clearly indicated a correlation between the local quantities (**Figures 4D,G**), indicating the oscillation and propagation behaviors of the T1 transition. The temporal cross-correlation function reached a maximum value with a small positive lag time (**Figure 4D**), and the correlation propagated spatially in the clockwise direction (**Figure 4G**). This analysis of cross-correlation functions indicated that after the propagation of the T1 transition passes through, the propagation of the increase in angular velocity occurs.

To see the mechanism of the global oscillation in **Figure 3**, we next considered the relationship between this spatial propagation of cell rearrangement and the global oscillation. For both the global and local angular velocities, the auto-correlation functions without normalization by their variances were plotted in **Figures 5A,B** for $K_p = 2.5$ and 7.5, respectively. We found that the peak correlations at $\Delta t \sim 1.9$ and 3.7 as well as the variances ($\Delta t = 0$) of the local velocity (blue lines) were about 10 times larger than those of the global velocity (red line). We then examined the K_p-dependence of the global and local velocities. In **Figure 5C**, for various K_p values, we plotted the coefficient of variation $\sigma_v / \langle v \rangle$ (CV) for the global and local velocities as red crosses and blue circles, respectively. Here, σ and $\langle v \rangle$ were the standard deviation and the temporal average of velocity, respectively. As shown in **Figure 2C**, the global angular velocity decreased as K_p decreased below $K_p = 5$. The CV for the local velocity was about ten times larger than that for the global velocity. These differences in both the auto-correlation functions and CV could stem from the propagation of cell rearrangement. Changes in the local velocity showed temporal oscillatory fluctuations, which propagated spatially. Because of this propagation, the phase of oscillation in the velocity was distributed through the entire system. Therefore, the amplitude of oscillation in the global velocity was averaged out by the summation of local velocities in the entire system. The proportion of the different phases of oscillation in the entire system was time-dependent. Such time-dependence might arise due to the fact that the system size is incommensurate with the wavelength. For a sufficiently large system, the oscillation in the global velocity may become negligible. Such inconsistency was clearly seen in the spatiotemporal profile of the local velocity shown in **Figure 4A**, where continuous propagations were interrupted by a sudden change in the phase of oscillation.

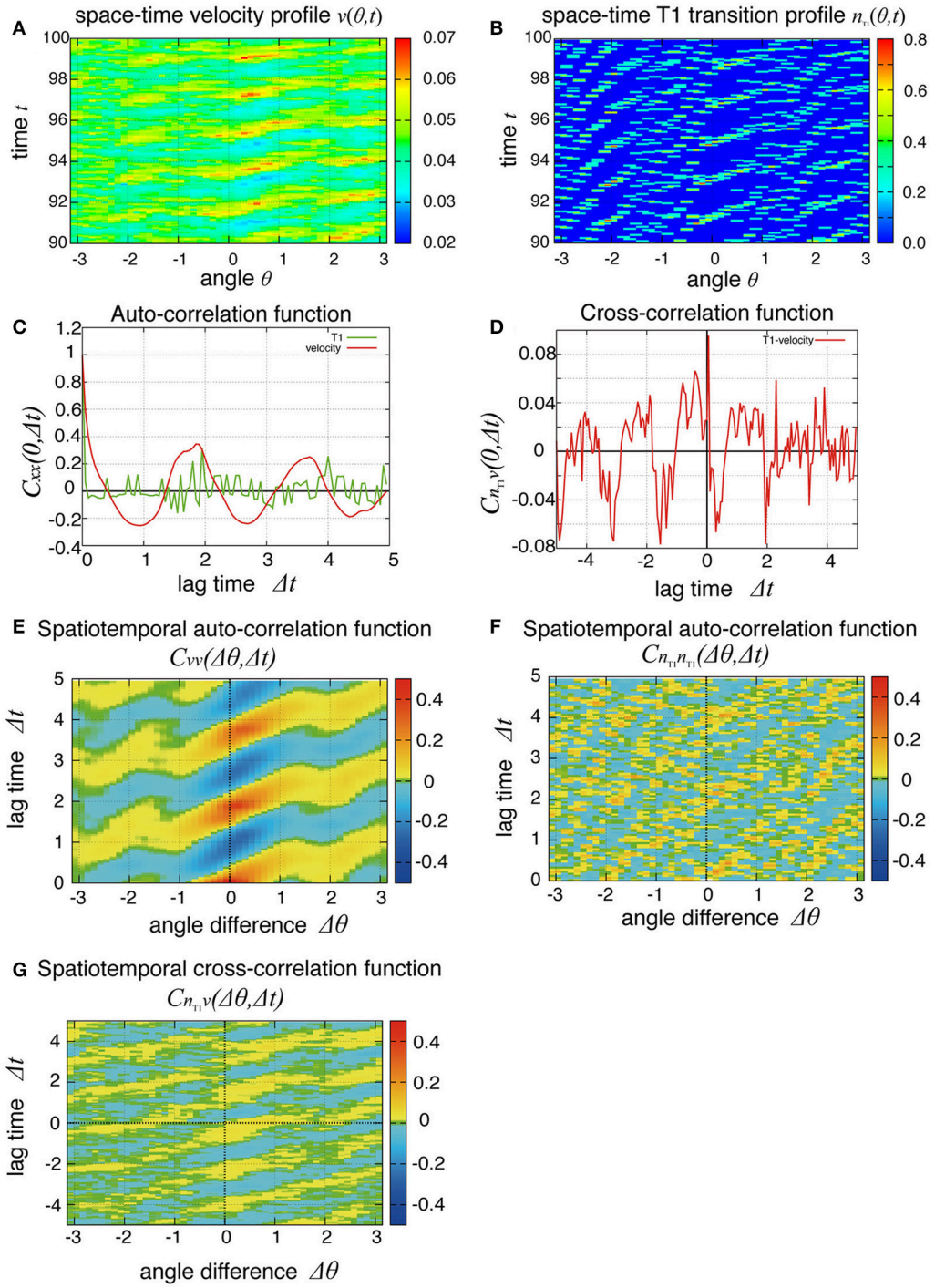

FIGURE 4 | Spatial propagations of cellular motility and T1 transition frequency. **(A,B)** Spatiotemporal distributions of local angular velocities **(A)** and frequency of T1 transitions **(B)** for $K_p = 7.5$. **(C–G)** Spatiotemporal correlation functions for $K_p = 7.5$ in the absence of oscillation of chiral line tension. A schematic explanation of spatiotemporal correlation function is shown in **Supplementary Figure 1**. **(C)** Temporal auto-correlation of the local angular velocity (red line) and the T1 transition (green line). **(D)** Temporal cross-correlation function. **(E)** Spatiotemporal auto-correlation of the local angular velocity. **(F)** Spatiotemporal auto-correlation of the local frequency of T1 transition. The max/min color was plotted when the color value exceeded the max/min of the color bar. **(G)** Spatiotemporal cross-correlation $C_{n_{T1}v}(\Delta\theta, \Delta t) = \langle \delta n_{T1}(\theta, t)\, \delta v(\theta + \Delta\theta, t + \Delta t)\rangle / \sigma_{n_{T1}} \sigma_V$ between fluctuations of the local angular velocity and the frequency of T1 transition. θ and $\Delta\theta$ here are defined in the clockwise direction. **(F,G)** The auto-correlations **(F)** and the cross-correlations **(G)** along the time axis of $\Delta\theta = 0$.

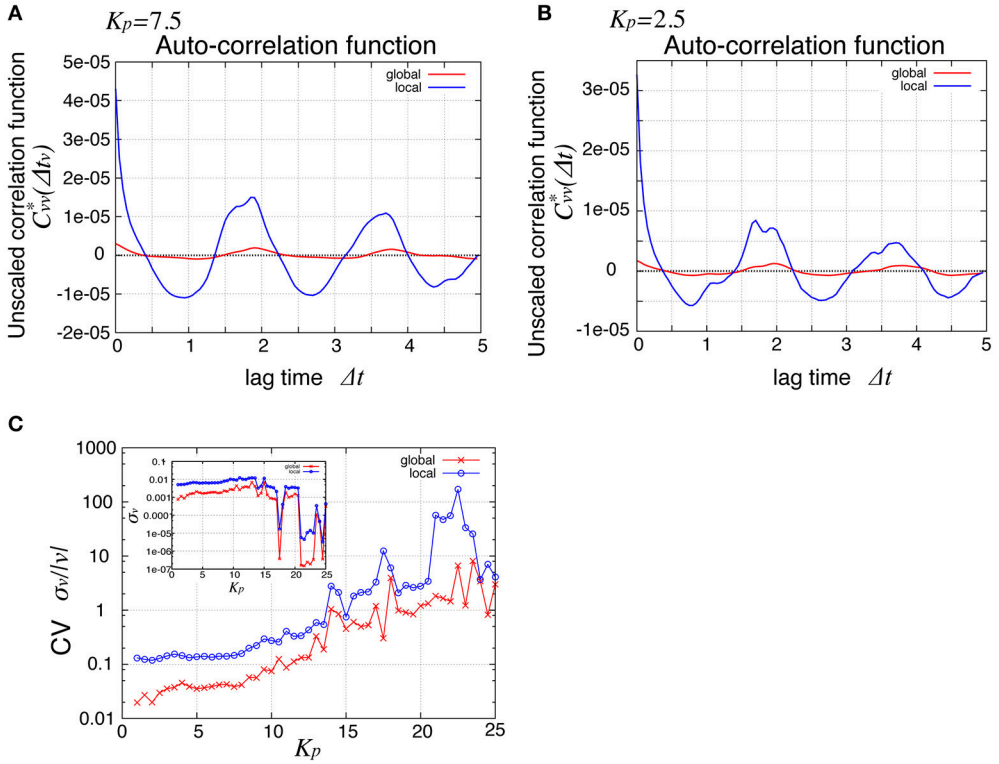

FIGURE 5 | Comparison of global and local behaviors, suggesting the relationship between the spatial propagation and the global oscillation of cell rearrangements. **(A,B)** Auto-correlation functions $C^*_{vv}(\Delta t) = \langle \delta v(t)\delta v(t+\Delta t)\rangle$ of the angular velocities for $K_p = 7.5$ **(A)** and $K_p = 2.5$ **(B)**. **(C)** Standard deviation scaled by the average time courses of the angular velocity. Red symbols, for global velocity; blue symbols, local velocity. Inset shows their standard deviation.

Propagation of Cell Rearrangement Depends on the Chirality

The direction of the collective cell movement depends on the chiral property θ_0 in tension in Equation (6). **Figure 6A** shows that the angular velocity v and the bond chirality c exhibited their maximum and minimum values at $\theta_0 = 45°$ and $\theta_0 = 135°$, respectively, and that the T1 transitions occurred most frequently at both these angles, as reported previously (Sato et al., 2015b). The bond chirality c disappeared at $\theta_0 = 0, 90, 180°$, as did the angular velocity and T1 transition. In **Figures 6B–D**, the spatiotemporal correlations of the local angular velocities were plotted. We found that the propagation speed of the spatiotemporal correlation in local velocity fluctuations depended on the chiral property θ_0 in tension.

The Cell Rearrangement Propagates through the System with Tension Fluctuations

During the rotation of *Drosophila* genital disc, the contraction of the cell-cell junctions has been shown to be accompanied by temporal fluctuations (Sato et al., 2015a). The myosin II intensity at the junctions has also exhibited temporal fluctuations in an inversely correlated way. Therefore, we next asked whether the same propagation of velocity change and T1 transitions occur in the collective cell movement of epithelial cells under this condition. To consider the fluctuating contraction, we introduced a temporal fluctuation in the tension γ_{kl} as shown in Equation (7). The numerical simulation of the case with tension fluctuation is shown in **Supplementary Movie 2**. We found that an oscillation of the global angular velocities also occurred in this condition with tension fluctuation (**Figure 7A**), although the oscillation was more irregular than in the case without tension fluctuation (**Figure 2B**). As K_p increased, the global angular velocity continuously decreased without an apparent transition (**Figure 7B**, in contrast to the previous case without fluctuations in **Figure 2C**).

In **Figure 8A** (red line), the temporal evolution of the global angular velocity was plotted. As evident from the auto-correlation functions in **Figure 8B**, the rotating motion was more irregular compared to the case without tension fluctuation (**Figure 3**). The temporal cross-correlation between v and n_{T1} (red line in **Figure 8C**) indicated that the angular velocity increased or decreased suddenly after the frequency of T1 transition increased or decreased, respectively. The cross-correlation between s and n_{T1} reached its positive maximum value with a negative delay time (blue line in **Figure 8D**), suggesting that the cell distortion increased or decreased after the frequency of T1 transition increased or decreased, respectively.

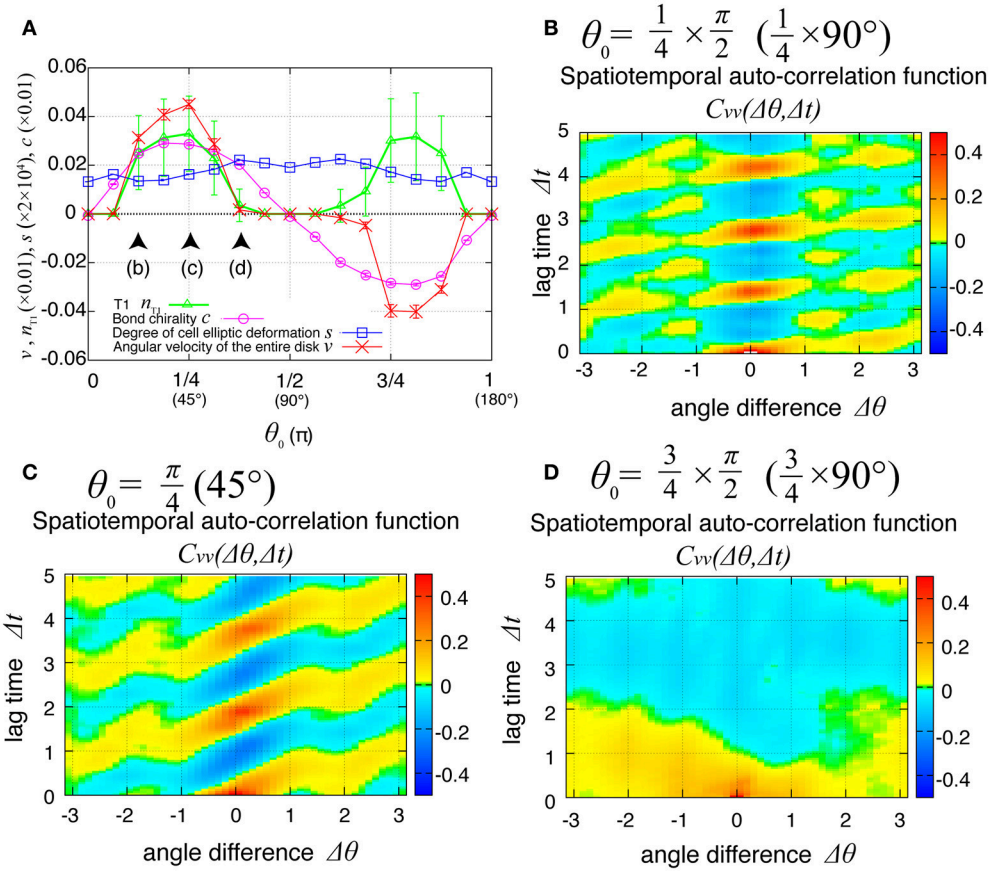

FIGURE 6 | Dependence of collective cell movement on the chirality in the absence of tension fluctuation. **(A)** Dependence of average quantities on the angle θ_0 in Equation (6): v (red), n_{T1} (green), s (blue), and c (purple). To calculate the K_p-dependence of the angular velocity, the time window from $t = 60$ to 100 was used for this average. Vertical bars indicate standard deviation in the time course. **(B–D)** Dependency of spatiotemporal correlation functions of fluctuations in locally averaged cell angular velocity $C_{vv}(\Delta\theta, \Delta t) = \langle \delta v(\theta, t)\delta v(\theta + \Delta\theta, t + \Delta t)\rangle / \sigma_v^2$ for $K_p = 7.5$ in the absence of oscillation of chiral line tension; **(B)** for $\theta_0 = 22.5°$, **(C)** for $\theta_0 = 45°$, and **(D)** for $\theta_0 = 67.5°$.

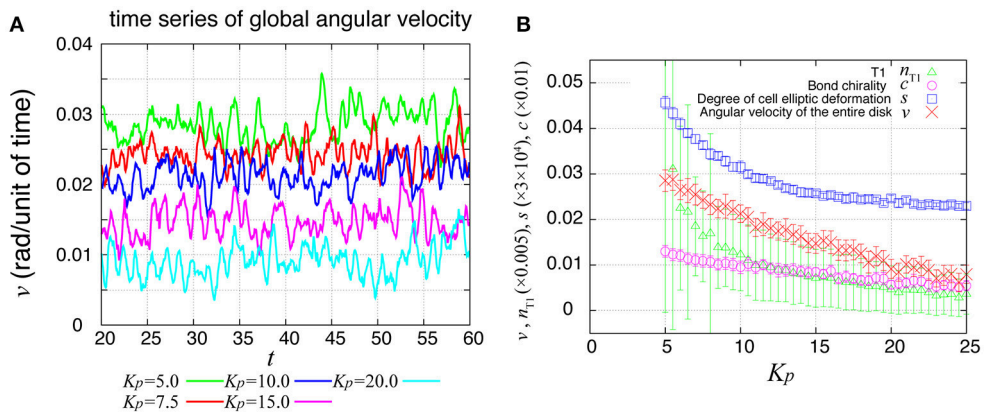

FIGURE 7 | Global angular velocity in the presence of line tension fluctuation. **(A)** Time evolution of the global angular velocity of an entire ring-like tissue for various values of K_p. **(B)** K_p-dependence of the global angular velocity. To calculate the K_p-dependence, the angular velocity was averaged over the time window from $t = 20$ to 60. Error bars indicate standard deviation in the time course.

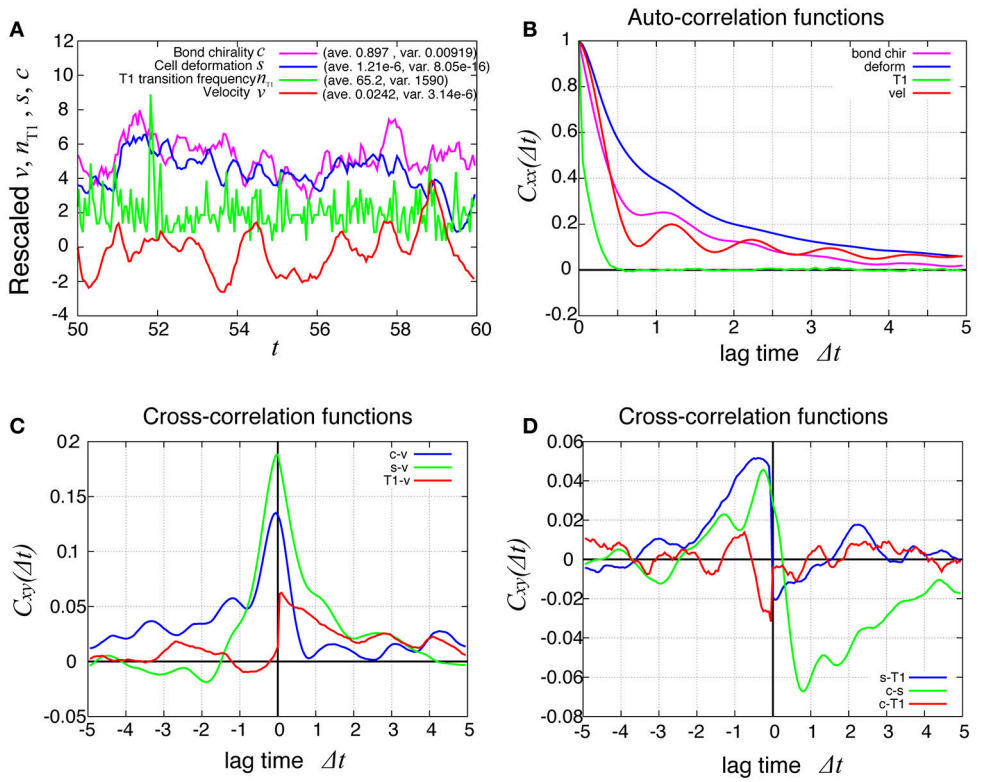

FIGURE 8 | Dynamics and correlation functions for $K_p = 7.5$ in the presence of line tension fluctuation, showing a weak oscillation in cell motility and the correlations with other quantities. **(A)** Time evolutions of the average angular velocity (red curve), the number of T1 transitions per unit time (green curve), the average s (blue curve), and the bond chirality c (purple curve) in the time window from $t = 50$ to 60. The quantities $x = v, n_{T1}, s, c$ plotted in this figure were rescaled as $(x - \langle x \rangle)/\sigma_x$, respectively, with the average $\langle x \rangle$ and standard deviation σ_x. The plots are offset by 2 (n_{T1}), 4 (s), and 6 (c), for visibility. **(B)** Auto-correlations of v, n_{T1}, s, and c. **(C)** Cross-correlation functions between v and the other quantities, given by $C_{xv}(\Delta t) = \langle \delta x(t) \delta v(t + \Delta t) \rangle / \sigma_x \sigma_v$, where x is n_{T1}, s, or c (red, green, and blue, respectively). Here, the positive time difference Δt means that x precedes v. $\delta x = x - \langle x \rangle$. **(D)** Cross-correlation functions given by $C_{sn_{T1}}(\Delta t) = \langle \delta s(t) \delta n_{T1}(t + \Delta t) \rangle / \sigma_s \sigma_{n_{T1}}$, $C_{cs}(\Delta t) = \langle \delta c(t) \delta s(t + \Delta t) \rangle / \sigma_c \sigma_s$, and $C_{cn_{T1}}(\Delta t) = \langle \delta c(t) \delta n_{T1}(t + \Delta t) \rangle / \sigma_c \sigma_{n_{T1}}$.

To examine the propagation of velocity fluctuation, the temporal auto-correlation functions of the local angular velocity v was depicted in **Figure 9A**; it quickly decayed with oscillation with a period of about 1.2, which agreed with the small peak in the auto-correlation function of the global angular velocity in **Figure 9B** (red line). In **Figure 9C**, although the peak at the origin also decayed quickly in space, it exhibited a propagation in both clockwise and counter-clockwise directions, in contrast to the previous case without tension fluctuation. The propagation in the counter-clockwise direction ceased in about one unit of time and 1 rad. In contrast, the propagation in the clockwise direction, seen as the yellow region, continued for more than five units of time ($\Delta t = 5$). The propagation speed was much slower than in the previous case without tension fluctuation. The spatiotemporal auto-correlation function of the local frequency of T1 transition did not indicate a clear propagation behavior (**Figure 9D**). However, the integral of the correlation function with respect to time showed that the correlated behavior was seen more in the clockwise direction than the other (**Figure 9F**). The cross-correlation between the angular velocity and the T1 transition was plotted (**Figure 9E**), and showed that the correlated behavior indicated by yellow was more evident in the clockwise direction. Although the propagation speed was much slower than in the case without tension fluctuation, it was still much faster than the angular velocity of cell movement (about 0.025 rad per unit time for $K_p = 7.5$). We conclude that the propagation of the cell rearrangement is a robust property of the epithelial cells' collective cell movement.

Finally, we examined the dependence of the collective cell movement on the chiral property θ_0 in tension in Equation (6) in the presence of tension fluctuation. As shown in **Figure 10A**, the angular velocities v, the bond chirality c, the T1 transition n_{T1}, and the cell shape deformation s exhibited smooth dependences on the chiral direction θ_0 with the same tendency as in the case without tension fluctuation shown in **Figure 6A**. In **Figures 10B–D**, the spatiotemporal correlation of the local angular velocities was plotted for different values of θ_0, and showed that the propagation of the fluctuation in the local velocity fluctuations occurred in the clockwise direction for these cases.

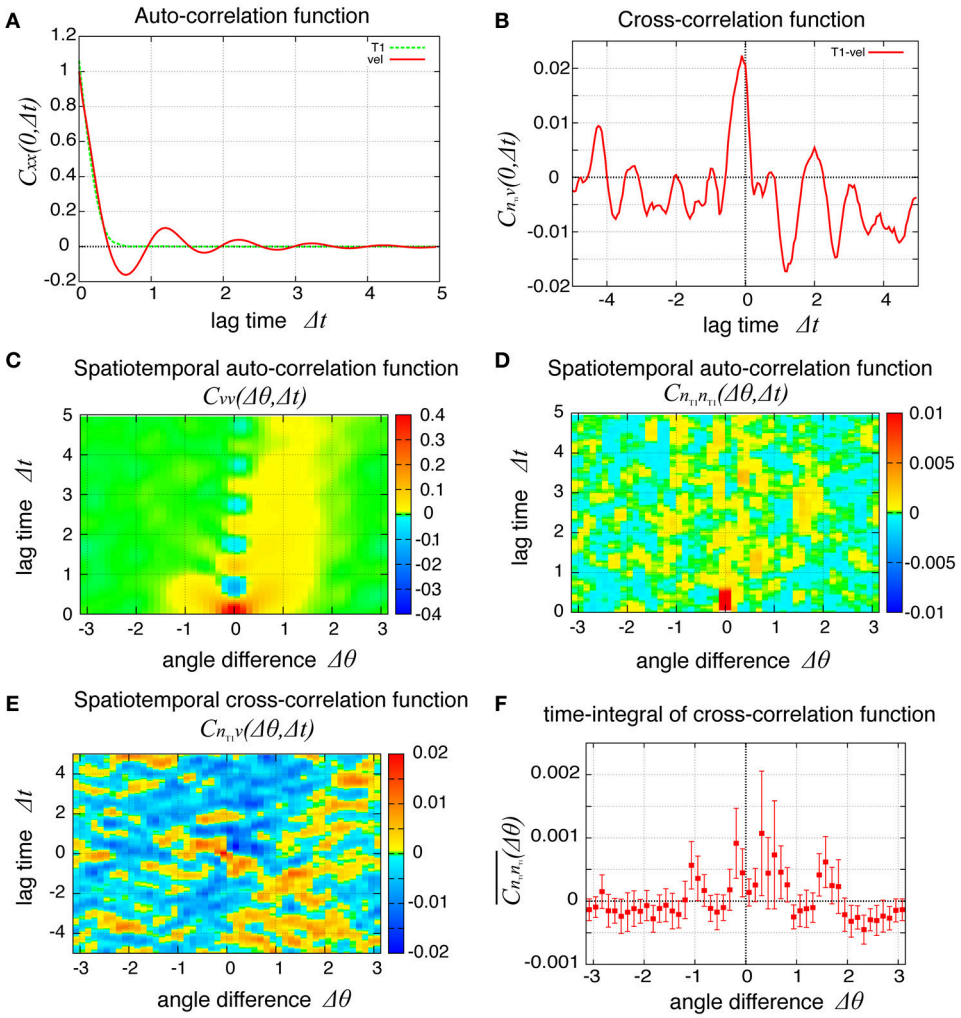

FIGURE 9 | Spatiotemporal correlation functions for $K_p = 7.5$ in the presence of chiral line tension fluctuation, showing the spatial propagation of cell rearrangements. **(A)** Temporal auto-correlation function of the local angular velocity and the local frequency of T1 transitions (red and green lines, respectively). **(B)** Temporal cross-correlation function between the two quantities. **(C,D)** Spatiotemporal correlation function of the local angular velocity **(C)** and the local frequency of T1 transition **(D)**. **(E)** Spatiotemporal correlation function between the two quantities. **(F)** Integrated spatiotemporal correlation $\overline{C_{n_{T1}n_{T1}}}(\Delta\theta)$ of **(D)** along the time difference between $\Delta t = 1$ and $\Delta t = 5$, given by $\overline{C_{n_{T1}n_{T1}}}(\Delta\theta) = \int_1^5 C_{n_{T1}n_{T1}}(\Delta\theta, \Delta t)\, d(\Delta t)$, where C is the spatiotemporal correlation function. To obtained the plot, 132 simulations were carried out with different values of the random parameters, the frequency f_{kl} and the initial phase δ_{kl} of tension fluctuation. The integration $\overline{C_{n_{T1}n_{T1}}}(\Delta\theta)$ was first performed for each simulation. Then, the means over the 132 simulations were plotted (marks) against the angle difference $\Delta\theta$. Vertical bars indicate 95 percent confidence intervals of the means among the 132 simulations.

DISCUSSION

In this study, we investigated the spatiotemporal self-organization of junctional remodeling and cell rearrangement in the collective cell movement of epithelial cells based on a numerical cellular vertex model. For this analysis, we focused on the rotating motion of a ring-like tissue composed of epithelial cells that exhibit a chiral contraction of cell-cell junctions. In the absence of spatiotemporal patterns in molecular signaling activity, the spatiotemporal organization of T1 transition occurred uninterruptedly in time, so that the tissue rotated in a specific direction, as we reported previously (Sato et al., 2015a). We further found in this study that the sequence of T1 transitions occurred as a traveling wave in the following way. When a cell changed its position owing to contraction and T1 transitions, it increased stress at the surrounding cells, leading to an increase in the frequency of T1 transition at the neighboring cells. Chiral contraction could bias the propagation direction by modulating this frequency in a direction-dependent manner. Consequently, the cell rearrangements propagated in a specific direction as a traveling wave, which drove the rotation of the epithelial ring-like tissue. This traveling wave behavior occurred in both the absence and presence of tension fluctuation.

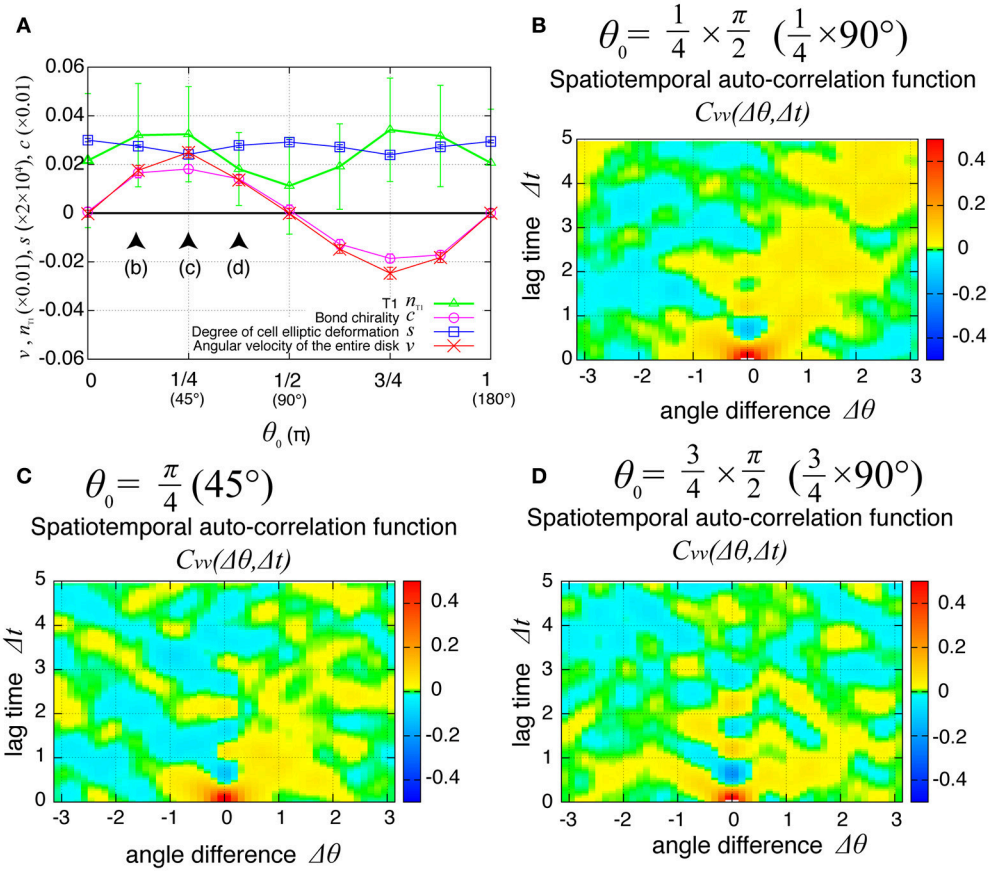

FIGURE 10 | Dependence of collective cell movement on chirality in the presence of tension fluctuation. **(A)** Dependencies of average quantities on the angle θ_0 in Equation (6). **(B–D)** Dependence of spatiotemporal correlation functions of fluctuations in the local angular velocity $C_{vv}(\Delta\theta, \Delta t) = \langle \delta v(\theta, t)\delta v(\theta + \Delta\theta, t + \Delta t)\rangle / \sigma_v^2$ for $K_p = 7.5$, **(B)** for $\theta_0 = 22.5°$, **(C)** for $\theta_0 = 45°$, and **(D)** for $\theta_0 = 67.5°$. See **Figure 6** for details.

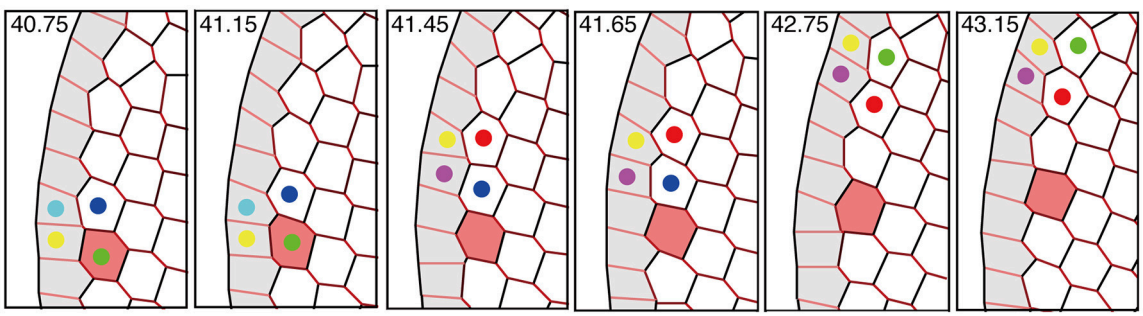

FIGURE 11 | Propagation of T1 transition and cell rearrangements. T1 transition occurs between cells (indicated by colored dots) that undergo cell intercalation. The propagation of T1 transition is much faster than the cell movement (see red-colored cell). This figure was obtained from our numerical simulation in the absence of tension fluctuations ($Kp = 7.5$).

Interestingly, the speed of the traveling wave of T1 transition and cell rearrangement in this mechanism was found to be much faster than the motile speed of individual cells, as shown in **Figure 11** and **Supplementary Movie 1**. This finding indicates that in some developmental processes, morphogenetic information may be transmitted much faster and farther through the mechanical coupling reported in this article than through cell movement alone.

Our simulation result naturally arises a question as to whether the similar traveling wave behavior can be observed experimentally, in particular, the genitalia rotation in *Drosophila* male terminalia (Sato et al., 2015a). In the presence of tension

fluctuation, the propagation of velocity change is difficult to be seen in a single time course as shown in **Supplementary Movie 2**, contrasting to the case without tension fluctuation as shown in **Supplementary Movie 1**. To see the traveling wave behaviors in the spatiotemporal correlation function, we had to take statistics for sufficiently enough number of samples. This is also the case for experimental situations, where fluctuations are inevitably present. To confirm whether the traveling wave behavior occurs in the tissue, a statistical analysis for several samples with image segmentation needs to be carried out, which remains to be a future topic for the study of tissue morphogenesis dynamics.

Another mechanism of collective epithelial cell movement is observed in *Drosophila* follicular epithelium (Haigo and Bilder, 2011; Cetera et al., 2014; Chen et al., 2016; Barlan et al., 2017). Elongating follicles are known to rotate circumferentially around their long axes driven by the epithelial cell migration (Haigo and Bilder, 2011). For this, the cells use the mechanism taking advantage of basal protrusion activities, which is explained in the Model and Method section. The same mechanism of collective epithelial cell movement is reported for the *in-vitro* monolayer sheet of MDCK cells (Serra-Picamal et al., 2012). Interestingly, a mechanical wave propagation, such as propagations of cellular velocities, rate of cell deformation and monolayer stresses, has been observed also in such a system (Serra-Picamal et al., 2012). In contrast to these examples, the *Drosophila* genitalia rotation relies not on the basal protrusive activity but only on the contraction activity of apical junctions (Sato et al., 2015a), as considered in the present paper. Whether a further generic principle for collective cell migrations underlies both apical and basal mechanisms is an intriguing future topic in both studies of biophysics and tissue morphogenesis.

Our model predicts that a non-uniform spatiotemporal patterning of the motile behaviors of cells including locomotion and T1 transition can be observed in the epithelial dynamics. We found that, accompanied by the transmission of an increase or decrease in the frequency of T1 transition (**Figures 4F**, **9D**), the transmission of an increase or decrease in the local locomotion velocity of cells was observed (**Figures 4E**, **9C**). Here we refer to the transmission of an increase or decrease in local locomotion velocity as "motility transmission." This phenomenon may have analogies in the motion of particles, granules, or other elements in a crowded situation. A typical example is a traffic jam, where the congestion at the rear end spreads in time and space, which has been extensively studied in the field of physics (Sugiyama et al., 2008). Collective cellular motions in crowded situations and their spatiotemporal motility patterns have also been studied for human bronchial epithelial cell (HBEC) monolayers and numerical models of epithelial cells spontaneously migrating on a substrate (Garcia et al., 2015; Bi et al., 2016). A challenging future problem will be to reveal the general rules that determine the directionality and speed of motility transmissions, by comparing the dynamics of transmission and the spreading of motility in various crowded situations. The biological functions and possible applications of this phenomenon are also important future topics.

AUTHOR CONTRIBUTIONS

TH and TS conceived the project and designed the numerical simulations. TH performed the numerical simulations. TH, EK, and TS wrote the manuscript.

FUNDING

This work was supported by MEXT KAKENHI Grant Number JP26114003 (EK), and the JSPS KAKENHI, grant numbers JP16K17777 (TH), JP24687027 (EK), JP16H04800 (EK), JP15KT0086 (TS).

SUPPLEMENTARY MATERIAL

The Supplementary Material for this article can be found online at: http://journal.frontiersin.org/article/10.3389/fcell.2017.00066/full#supplementary-material

Supplementary Figure 1 | Schematic explanation of spatiotemporal correlation function.

Supplementary Movie 1 | Numerical simulation of the vertex model without tension fluctuations corresponding to **Figure 3**.

Supplementary Movie 2 | Numerical simulation of the vertex model with tension fluctuations corresponding to **Figure 8**.

REFERENCES

Aigouy, B., Farhadifar, R., Staple, D. B., Sagner, A., Röper, J.-C., Jülicher, F., et al. (2010). Cell flow reorients the axis of planar polarity in the wing epithelium of *Drosophila*. *Cell* 142, 773–786. doi: 10.1016/j.cell.2010.07.042

Barlan, K., Cetera, M., and Horne-Badovinac, S. (2017). Fat2 and lar define a basally localized planar signaling system controlling collective cell migration. *Dev. Cell* 40, 467–477. doi: 10.1016/j.devcel.2017.02.003

Bertet, C., Sulak, L., and Lecuit, T. (2004). Myosin-dependent junction remodelling controls planar cell intercalation and axis elongation. *Nature* 429, 667–671. doi: 10.1038/nature02590

Bi, D., Yang, X., Marchetti, M. C., and Manning, M. L. (2016). Motility-driven glass and jamming transitions in biological tissues. *Phys. Rev. X* 6:021011. doi: 10.1103/physrevx.6.021011

Blankenship, J. T., Backovic, S. T., Sanny, J. S. P., Weitz, O., Zallen, J. A., and Zallen, J. A. (2006). Multicellular rosette formation links planar cell polarity to tissue morphogenesis. *Dev. Cell* 11, 459–470. doi: 10.1016/j.devcel.2006.09.007

Cetera, M., Ramirez-San Juan, G. R., Oakes, P. W., Lewellyn, L., Fairchild, M. J., Tanentzapf, G., et al. (2014). Epithelial rotation promotes the global alignment of contractile actin bundles during *Drosophila* egg chamber elongation. *Nat. Commun.* 5:5511. doi: 10.1038/ncomms6511

Chen, D.-Y., Lipari, K. R., Dehghan, Y., Streichan, S. J., and Bilder, D. (2016). Symmetry breaking in an edgeless epithelium by Fat2-regulated microtubule polarity. *Cell Rep.* 15, 1125–1133. doi: 10.1016/j.celrep.2016.04.014

Collinet, C., Rauzi, M., Rauzi, M., Lenne, P.-F., and Lecuit, T. (2015). Local and tissue-scale forces drive oriented junction growth during tissue extension. *Nat. Cell Biol.* 17, 1247–1258. doi: 10.1038/ncb3226

Farhadifar, R., Röper, J.-C., Aigouy, B., Eaton, S., and Jülicher, F. (2007). The influence of cell mechanics, cell-cell interactions, and proliferation on epithelial packing. *Curr. Biol.* 17, 2095–2104. doi: 10.1016/j.cub.2007.11.049

Garcia, S., Hannezo, E., Elgeti, J., Joanny, J.-F., Silberzan, P., and Gov, N. S. (2015). Physics of active jamming during collective cellular motion in a monolayer. *Proc. Natl. Acad. Sci. U.S.A.* 112, 15314–15319. doi: 10.1073/pnas.1510973112

Haigo, S. L., and Bilder, D. (2011). Global tissue revolutions in a morphogenetic movement controlling elongation. *Science* 331, 1071–1074. doi: 10.1126/science.1199424

Harris, T. J. C., and Tepass, U. (2010). Adherens junctions: from molecules to morphogenesis. *Nat. Rev. Mol. Cell Biol.* 11, 502–514. doi: 10.1038/nrm2927

Kuranaga, E. (2012). Beyond apoptosis: caspase regulatory mechanisms and functions *in vivo*. *Genes Cells* 17, 83–97. doi: 10.1111/j.1365-2443.2011.01579.x

Kuranaga, E., Matsunuma, T., Kanuka, H., Takemoto, K., Koto, A., Kimura, K.-I., et al. (2011). Apoptosis controls the speed of looping morphogenesis in *Drosophila* male terminalia. *Development* 138, 1493–1499. doi: 10.1242/dev.058958

Li, B., and Sun, S. X. (2014). Coherent motions in confluent cell monolayer sheets. *Biophys. J.* 107, 1532–1541. doi: 10.1016/j.bpj.2014.08.006

Lienkamp, S. S., Liu, K., Karner, C. M., Carroll, T. J., Ronneberger, O., Wallingford, J. B., et al. (2012). Vertebrate kidney tubules elongate using a planar cell polarity–dependent, rosette-based mechanism of convergent extension. *Nat. Genet.* 44, 1382–1387. doi: 10.1038/ng.2452

Munro, E. M., and Odell, G. (2002a). Morphogenetic pattern formation during ascidian notochord formation is regulative and highly robust. *Development* 129, 1–12.

Munro, E. M., and Odell, G. M. (2002b). Polarized basolateral cell motility underlies invagination and convergent extension of the ascidian notochord. *Development* 129, 13–24.

Nagai, T., and Honda, H. (2001). A dynamic cell model for the formation of epithelial tissues. *Philos. Mag. B* 81, 699–719. doi: 10.1080/13642810108205772

Nishimura, T., Honda, H., and Takeichi, M. (2012). Planar cell polarity links axes of spatial dynamics in neural-tube closure. *Cell* 149, 1084–1097. doi: 10.1016/j.cell.2012.04.021

Rauzi, M., Rauzi, M., Verant, P., Lecuit, T., and Lenne, P.-F. (2008). Nature and anisotropy of cortical forces orienting *Drosophila* tissue morphogenesis. *Nat. Cell Biol.* 10, 1401–1410. doi: 10.1038/ncb1798

Sato, K., Hiraiwa, T., Maekawa, E., Isomura, A., Shibata, T., and Kuranaga, E. (2015a). Left-right asymmetric cell intercalation drives directional collective cell movement in epithelial morphogenesis. *Nat. Commun.* 6:10074. doi: 10.1038/ncomms10074

Sato, K., Hiraiwa, T., and Shibata, T. (2015b). Cell chirality induces collective cell migration in epithelial sheets. *Phys. Rev. Lett.* 115:188102. doi: 10.1103/PhysRevLett.115.188102

Serra-Picamal, X., Trepat, X., Conte, V., Anon, E., Vincent, R., Tambe, D. T., et al. (2012). Mechanical waves during tissue expansion. *Nat. Phys.* 8, 628–634. doi: 10.1038/nphys2355

Sugiyama, Y., Fukui, M., Kikuchi, M., Hasebe, K., Nakayama, A., Nishinari, K., et al. (2008). Traffic jams without bottlenecks—experimental evidence for the physical mechanism of the formation of a jam. *New J. Phys.* 10:033001. doi: 10.1088/1367-2630/10/3/033001

Suzanne, M., Petzoldt, A. G., Spéder, P., Coutelis, J.-B., Steller, H., and Noselli, S. (2010). Coupling of apoptosis and L/R patterning controls stepwise organ looping. *Curr. Biol.* 20, 1773–1778. doi: 10.1016/j.cub.2010.08.056

Tada, M., and Heisenberg, C. P. (2012). Convergent extension: using collective cell migration and cell intercalation to shape embryos. *Development* 139, 3897–3904. doi: 10.1242/dev.073007

Takeichi, M. (2014). Dynamic contacts: rearranging adherens junctions to drive epithelial remodelling. *Nat. Rev. Mol. Cell Biol.* 15, 397–410. doi: 10.1038/nrm3802

Tomer, R., Khairy, K., Amat, F., and Keller, P. J. (2012). Quantitative high-speed imaging of entire developing embryos with simultaneous multiview light-sheet microscopy. *Nat. Meth.* 9, 755–763. doi: 10.1038/nmeth.2062

Conflict of Interest Statement: The authors declare that the research was conducted in the absence of any commercial or financial relationships that could be construed as a potential conflict of interest.

APPENDIX

We calculated various quantities for our analyses as follows.

Average cell angular velocity $v(t) = \langle d\psi_\alpha/dt\rangle_{\rm global}$ *among the entire tissue.* Cell angular velocity is defined in this article as the increase in the angle of the α-th cell location in the clock-wise direction in unit time $d\psi_\alpha/dt$ around the center of the ring-like tissue. ψ_α is given by the angle between an arbitrary direction and the direction of the center of the cell seen from the center of the disc, *i.e.*, through the relationships $\cos(-\psi_\alpha) = X/\sqrt{X^2+Y^2}$ and $\sin(-\psi_\alpha) = Y/\sqrt{X^2+Y^2}$ with the position vector $(X,\ Y)$ of the center of mass of the cell from the origin $(0,0)$ at the disc center. We calculate the center of mass of the cell consisting of vertices $i = 1,2,\cdots,I$ designated in the counter-clockwise direction by

$$X = \frac{1}{6A}\sum_{i=1}^{I}\left(\mathbf{r}_i \times \mathbf{r}_{i+1}\right)\left(x_i + x_{i+1}\right), \tag{A1}$$

and

$$Y = \frac{1}{6A}\sum_{i=1}^{I}\left(-\mathbf{r}_i \times \mathbf{r}_{i+1}\right)\left(y_i + y_{i+1}\right), \tag{A2}$$

with the position vector $\mathbf{r}_i = (x_i, y_i)$ of the i-th vertex from an arbitrary position and the cell area A. The cell area is calculated by

$$A = \frac{1}{2}\sum_{i=1}^{I}\left(\mathbf{r}_i \times \mathbf{r}_{i+1}\right). \tag{A3}$$

The $i = (I+1)$-th vertex is identified with the $i = 1$-th vertex. The symbol $\times$ indicates a cross product in two dimensions, i.e., $(a_1, a_2) \times (b_1, b_2) = a_1 b_2 - b_1 a_2$. The average $\langle\cdot\rangle$ is performed among all the cells.

Local average $\theta(t) = \langle d\psi_\alpha/dt\rangle_{{\rm local}(\theta)}$ *of the cell angular velocity.* We assign the angle θ of an arbitrary position $(x,\ y)$ into J grids of the width $2\pi/J$, as $2\pi(j-1/2)/J \le \theta < 2\pi(j+1/2)/J$ with $j = 1,2,\cdots,J$. The grid number is set at $J = 50$. The angle θ is defined by $\cos(-\theta) = x/\sqrt{x^2+y^2}$ and $\sin(-\theta) = y/\sqrt{x^2+y^2}$. Furthermore, we take the average $\langle\cdot\rangle_{\rm Local}$ of the angular velocity among the cells whose center of mass $(X,\ Y)$ is located within each grid, $2\pi(j-1/2)/J \le \psi_\alpha(X,\ Y) < 2\pi(j+1/2)/J$, at a later time step to define the velocity. Here, the angle ψ_α of the α-th cell location direction is defined as above.

Total number $n_{T1}(t)$ *of T1 transition events that occur between two adjacent time steps.* We define $n_{T1}(t)$ by counting the total number of T1 transitions that occur between two adjacent time steps and dividing it by the step size dt of time.

Number density $n_{T1}(\theta,\ t)$ *of T1 transitions at time t.* We assign the spatial angle into grids as described above and count the number of T1 transitions that occur within each grid, $2\pi(j-1/2)/J \le \phi < 2\pi(j+1/2)/J$ in the time interval from t to $t+dt$. The grid number is set as $J = 50$ as above. The angle ϕ of the bond location is defined by $\cos(-\phi) = X/\sqrt{X^2+Y^2}$ and $\sin(-\phi) = Y/\sqrt{X^2+Y^2}$ of the midpoint $(X,\ Y)$ of the bond being examined. The number density $n_{T1}(\theta,t)$ is given by dividing the number of T1 transitions by the time step size dt.

Elliptical anisotropy $s(t)$ *in the shape of each cell.* We define the amplitude s of the elliptical deformation in the following way. First, we calculate the moment of inertia M for a uniformly thin plate, the mass density of which per area is scaled to be 1, taking the same shape as the cell being examined (Aigouy et al., 2010).

$$\mathbf{M} = \begin{pmatrix} M_{xx} & M_{xy} \\ M_{yx} & M_{yy} \end{pmatrix} = \begin{pmatrix} \int\limits_V d^2\mathbf{r}(\Delta y)^2 & -\int\limits_V d^2\mathbf{r}\Delta x\Delta y \\ -\int\limits_V d^2\mathbf{r}\Delta x\Delta y & \int\limits_V d^2\mathbf{r}(\Delta x)^2 \end{pmatrix}. \tag{A4}$$

Here, $(\Delta x,\ \Delta y)$ is the position vector of each point from the center of mass of the plate (cell), $d^2\mathbf{r} = d(\Delta x)d(\Delta y)$, and the integral $\int\limits_V$ runs for the entire plate. This tensor $\mathbf{M}$ is calculated through the following formulae:

$$M_{xx} = \frac{1}{12}\sum_{i=1}^{I}\left(\Delta\mathbf{r}_i \times \Delta\mathbf{r}_{i+1}\right)\left(\Delta y_i^2 + \Delta y_i\Delta y_{i+1} + \Delta y_{i+1}^2\right), \tag{A5}$$

$$M_{xy} = M_{yx} = -\frac{1}{24}\sum_{i=1}^{I}\left(\Delta\mathbf{r}_i \times \Delta\mathbf{r}_{i+1}\right)\left[\Delta x_i\left(2\Delta y_i + \Delta y_{i+1}\right) + \Delta x_{i+1}\left(\Delta y_i + 2\Delta y_{i+1}\right)\right],$$

and

$$M_{yy} = \frac{1}{12}\sum_{i=1}^{I}\left(\Delta\mathbf{r}_i \times \Delta\mathbf{r}_{i+1}\right)\left(\Delta x_i^2 + \Delta x_i\Delta x_{i+1} + \Delta x_{i+1}^2\right), \tag{A6}$$

with the position vector $\Delta\mathbf{r}_i = (\Delta x_i, \Delta y_i)$ of each vertex (i-th vertex) from the center of mass of the plate (cell). Here, the cell is assumed to consist of the vertices $i = 1,2,\cdots,I$ designated in counter-clockwise order of the position seen from the cell's center, and the $i = 1$-th vertex is identified with the $i = (I+1)$-th vertex. The symbol $\times$ indicates a cross product in two dimensions, i.e., $(a_1, a_2) \times (b_1, b_2) = a_1 b_2 - b_1 a_2$. From this analysis, we define the elliptical cell anisotropy s_α of α-th cell as the half difference of two eigenvalues of the tensor $\mathbf{M}$, which is given by

$$s_\alpha = \sqrt{(M_{xx} - M_{yy})^2 + 4M_{xy}M_{yx}}. \tag{A7}$$

This quantity s_α is 0 when the plate is set to be a circle, and when the plate has an elliptically deformed shape from the circle, s_α has non-zero value. Therefore, we use s_α to quantify how the cell shape is elliptically deformed. Finally, the variable s is given as the average of s_α among the cells.

Bond chirality $c(t)$. At each time step, we count the numbers $N_{\rm cl}(t)$ and $N_{\rm ccl}(t)$ of cell-cell junctions tilted clockwise and counterclockwise from the AP axis, respectively. We then define the bond chirality $c(t)$ by $c(t) \equiv N_{\rm cl}(t)/N_{\rm ccl}(t) - N_{\rm ccl}(t)/N_{\rm cl}(t)$. If the system has no chirality, $N_{\rm cl}(t)/N_{\rm ccl}(t) = N_{\rm ccl}(t)/N_{\rm cl}(t)$ with the statistical average $\langle\cdot\rangle$, and hence $\langle c(t)\rangle = 0$.

frontiers in Cell and Developmental Biology

MINI REVIEW
published: 05 February 2018
doi: 10.3389/fcell.2018.00004

Dancing Styles of Collective Cell Migration: Image-Based Computational Analysis of JRAB/MICAL-L2

*Ayuko Sakane[1], Shin Yoshizawa[2], Hideo Yokota[2] and Takuya Sasaki[1]**

[1] Department of Biochemistry, Tokushima University Graduate School of Medical Sciences, Tokushima, Japan, [2] Image Processing Research Team, RIKEN Center for Advanced Photonics, RIKEN, Wako, Japan

Collective cell migration is observed during morphogenesis, angiogenesis, and wound healing, and this type of cell migration also contributes to efficient metastasis in some kinds of cancers. Because collectively migrating cells are much better organized than a random assemblage of individual cells, there seems to be a kind of order in migrating clusters. Extensive research has identified a large number of molecules involved in collective cell migration, and these factors have been analyzed using dramatic advances in imaging technology. To date, however, it remains unclear how myriad cells are integrated as a single unit. Recently, we observed unbalanced collective cell migrations that can be likened to either precision dancing or *awa-odori*, Japanese traditional dancing similar to the style at Rio Carnival, caused by the impairment of the conformational change of JRAB/MICAL-L2. This review begins with a brief history of image-based computational analyses on cell migration, explains why quantitative analysis of the stylization of collective cell behavior is difficult, and finally introduces our recent work on JRAB/MICAL-L2 as a successful example of the multidisciplinary approach combining cell biology, live imaging, and computational biology. In combination, these methods have enabled quantitative evaluations of the "dancing style" of collective cell migration.

Keywords: rab GTPases, JRAB/MICAL-L2, conformational change, collective cell migration, computational analysis, optical flow

OPEN ACCESS

Edited by:
Takaaki Matsui, Nara Institute of Science and Technology, Japan

Reviewed by:
Thomas Fath, University of New South Wales, Australia
Zhizhan Gu, Albert Einstein College of Medicine, United States

****Correspondence:***
Takuya Sasaki
sasaki@tokushima-u.ac.jp

Specialty section:
This article was submitted to Cell Adhesion and Migration, a section of the journal Frontiers in Cell and Developmental Biology

Received: *30 October 2017*
Accepted: *19 January 2018*
Published: *05 February 2018*

Citation:
Sakane A, Yoshizawa S, Yokota H and Sasaki T (2018) Dancing Styles of Collective Cell Migration: Image-Based Computational Analysis of JRAB/MICAL-L2. Front. Cell Dev. Biol. 6:4. doi: 10.3389/fcell.2018.00004

COLLECTIVE CELL MIGRATION

Cell migration is a fundamental cellular function involved in various biological processes. Broadly speaking, there are two kinds of cell movement: single-cell and collective migration. In the latter, cells form a cluster via adhesion and move as a group. The cells at the migrating front generate a strong force that pulls the mass behind them, whereas the rear cells maintain adhesion and communicate with their neighbors. At the tip of the multicellular group, complete-epithelial to mesenchymal transition (EMT) or partial-EMT is often observed, resulting in the migration mode switch between single-cell and collective cell migration (Friedl and Wolf, 2010; Friedl and Alexander, 2011). In another mode of cell migration with intermediate phenotype, individual cells move one after each other using the same path, which is referred to as multicellular streaming (Friedl and Wolf, 2010; Friedl and Alexander, 2011). Collective cell migration is observed during

morphogenesis, angiogenesis, and wound healing (Friedl and Gilmour, 2009; Gray et al., 2010; Mayor and Carmona-Fontaine, 2010; Rørth, 2012; Theveneau and Mayor, 2012) and contributes to efficient metastasis in some kinds of cancers (Sahai, 2005; Friedl and Gilmour, 2009). In other words, this type of cell migration is important in both physiological and pathological contexts. Thus, it has been extensively studied in the field of cell biology (Ladoux and Mège, 2017) and simulation-based biophysics (Ionides, 2001; Woods et al., 2014; Te Boekhorst et al., 2016; George et al., 2017; van Helvert et al., 2018). Collectively migrating cells are much better organized than a random assemblage of individual cells, indicating that one or more factors imposes an order that allows myriad cells to behave as a single unit. Collective cell migration involves multiple molecules [including the Rho family of small GTPases, which regulates actin cytoskeletal reorganization; the Rab family of small GTPases, which regulates membrane trafficking; and extracellular signal-related kinase (ERK), a component of the ERK/MAPK signaling pathway], which are predicted to engage in a complex interplay; Rac and Rho, two members of the Rho family, along with the regulators of their activity, GDP/GTP exchange proteins and GTPase-activating proteins, spatiotemporally regulate actomyosin contractility in moving cell groups (Zegers and Friedl, 2014). Rab5 and Rab11, two members of the Rab family, control the level of Rac activity via intracellular trafficking of receptor tyrosine kinases, resulting in the organization of individual cells during collective cell migration (Ramel et al., 2013). Intracellular propagation waves of ERK activation are observed in groups of cells during collective cell migration (Aoki et al., 2017). The waves induce collective cell migration in the opposite direction. In addition, advances in imaging technology have helped to understand the regulatory systems underlying the complex, higher-order cell functions involved in collective migration. Even with these, however, the whole picture of the regulatory system has not been fully elucidated.

IMAGE-BASED COMPUTATIONAL ANALYSIS ON CELL MIGRATION

Various computational tools have been employed for quantitative studies of cell migration. Due to rapid advances in live-cell imaging technology, such data-driven approaches have become popular and important tools for understanding migration dynamics. Model-based analyses, such as statistical or mechanical simulations for directional cell migration (Ionides, 2001; Woods et al., 2014; George et al., 2017), also rely on analysis of data, including images, for verification and calibration of models and parameters.

Although the purpose of quantitative analysis strongly depends on the individual research subjects, useful intermediate information computed from cell migration images can be abstracted for various biological purposes. Hence, image-based analysis yields statistical information about the geometry, topology, and kinematics of individual cells or cell groups, including spatial and temporal descriptors (Cordelières et al., 2013) such as shape, velocity, and motion pattern. Computational frameworks designed to obtain such information usually involve registration/calibration of imaging, filtering (noise reduction, restoration, super-resolution, etc.), segmentation and tracking of cells (or target fluorescent tags), and motion estimation/analysis. For image-based motion analyses of collective cell migration dynamics, the difficulties lie in the segmentation and tracking approaches. The reader is directed to excellent surveys (Castañeda et al., 2014; Masuzzo et al., 2016) for further information about general computational methods and software packages applied to analyses of cell migration.

Motion analysis based on segmentation and tracking approaches has been often applied to phase-contrast and fluorescence images of cell migration, which visualize the cytoplasm, nuclei, or plasma/nuclear membranes. For example, trajectories of individual cell nuclei have been studied in *Drosophila* gastrulation (Supatto et al., 2009), embryogenesis in zebrafish (Khairy and Keller, 2011), and the *Drosophila* border cell system (Cliffe et al., 2017) by linking segmented nuclear regions in adjacent time-lapse images. At the cellular and subcellular scales, the cell and its nucleus are both topologically equivalent to a sphere (i.e., a topological disk/ball), except during cell division. Therefore, finding a pair of corresponding segmented cells/nuclei in adjacent time-lapse images is easier than in cases with no topological restrictions. The ellipsoidal shapes of cells and nuclei in collective cell migration are also favorable for region extraction. Thus, popular unsupervised segmentation methods, such as discriminant analysis (HUVEC: human umbilical vein endothelial cells Huang et al., 2012), active contours (monolayer of cultured pig epithelial cells Bunyak et al., 2006), mean shift [HUVEC, astrocytoma, melanoma, and colon carcinoma cells (Debeir et al., 2005) and human melanoma cells (Cordelières et al., 2013)], and supervised machine learning techniques (Masuzzo et al., 2016) have been employed for motion analysis. The mathematical and algorithmic aspects of these methods were imported from computer science, especially computer vision, pattern recognition, and image processing, and have been adapted to processing of migration images in cell biology. Unfortunately, objects (organelles, cytoskeleton, structures on plasma/nuclear membranes such as pores and receptors, and proteins of interest) in cell images are usually much more complex, and undergo spatiotemporal changes in both their geometry and topology. Objects of this type have not been extensively examined by conventional computer science. In addition, because manually generating sets of teaching images is tedious and time-consuming, it is difficult to acquire enough teaching images containing segmented/tracked regions for use with state-of-the art deep learning techniques. Also, once a training set has been obtained then automatic segmentation (and tracking) based on machine learning techniques could become irrelevant, as quantitative information could be obtained from the teaching images. Although some *a priori* knowledge about cell migration can be incorporated into these computations, this valuable knowledge is the very information that we hope to obtain from image-based computational analysis in the first place. Thus, segmentation and tracking approaches are limited in terms of their applicability for tags for objects other than the

cytoplasm and nucleus, such as intracellular structures (hereafter, referred to as general-target tags), especially in the analysis of collective cell migration.

Motion estimation without segmentation/tracking of target shapes has been applied to cell migration analysis, e.g., a damped harmonic oscillator model often employed in fluid dynamics and a particle image velocimetry software were applied to extract motion fields of cells (cell populations) in (Angelini et al., 2011) and (Jang et al., 2017), respectively. The most common technique employed in such motion analyses [including intracellular logistics at the Golgi apparatus (Ben-Tekaya et al., 2005)] is Optical Flow (OF), which estimates a motion field consisting of a velocity vector at each pixel of a live-cell image (see middle images of **Figure 1** as examples of motion fields with their corresponding live images). Although many OF models have been developed [see (Delpiano et al., 2012) for some of these models applied to point signals in fluorescence images], the general idea is based on the hypothesis that the intensity/texture of local regions in time-varying images is approximately constant under motion, at least over short timescales. This hypothesis leads to the so-called OF constraint equation, consisting of the spatial gradient and temporal first-order partial derivative (speed) of the image intensity; see seminal surveys (Beauchemin and Barron, 1995; Fortun et al., 2015) for more information on mathematical formulation, computational methodology, and applications. Once motion fields are obtained, spatial and temporal descriptors (Castañeda et al., 2014) are usually extracted to represent quantitative and salient features of the target tags, as well as visualizing the vector field along with its corresponding cell migration image. The trajectories of the target tags are obtained by averaging velocity vectors within a local or segmented image region.

OPTICAL FLOWS IN COLLECTIVE CELL MIGRATION ANALYSIS

OF is also popular for analysis of collective cell migration images consisting of cytoplasm or nuclei (Breen and Williams, 1994; Siegert et al., 1994; Ronot et al., 2000; Dubin-Thaler et al., 2008; Amat et al., 2013; Boric et al., 2013; Kappe et al., 2016), despite the fact that segmentation and tracking approaches work well on such images.

Breen and Williams developed an OF-based digital imaging vision system and applied it to ventral cellular layers of the migrating *Dictyostelium discoideum* slug (Breen and Williams, 1994). Their system characterized the speed of the layers and migrating tips of the slug based on velocity profiles and the corresponding cross-correlation analysis. Siegert et al. reported an OF-based image processing method and demonstrated its use on phase-contrast images of the *Dictyostelium* developmental cycle (Siegert et al., 1994). Their analysis, based on velocity profiles, the color-coded velocity map, and cell trajectories, showed that *Dictyostelium* development from the aggregation stage onwards, is governed by rotational movement. Ronot et al. proposed an OF-based image analysis approach and used it to study cell movement in phase-contrast images of HeLa monolayers undergoing wound healing (Ronot et al., 2000). Their approach estimated the velocity profiles and affine transformation coefficients of the monolayers, and then quantified the various phases of the wound repair process and wound closure dynamics in multiple cell lines. Dubin-Thaler et al. studied single-cell motility during cell spreading, based on velocity fraction histograms and auto-correlation of velocity maps calculated from OF-based image analysis (Dubin-Thaler et al., 2008). They proposed that regulatory pathways provide some combination of local motility modules that contribute to the overall motility function of the cell. Boric et al. developed an assay for analyzing and quantifying migration of cranial neural crest cells in zebrafish based on OF-based image analysis (Boric et al., 2013). Specifically, they characterized cell migration patterns of normal and ethanol-exposed embryos, based on directional histograms with a polar coordinate system, hue color visualization of velocity vectors, and displacement factors over time.

OF-based analysis has also been tailored to the specific characteristics of 3D time-lapse light-sheet microscopy datasets, especially for images of the nucleus, e.g., in *Drosophila* and zebrafish development (Amat et al., 2013) and *Drosophila* gastrulation (Kappe et al., 2016). On the other hand, OF is rarely applied to general-target fluorescent tags in collective cell migration analyses, even though (as mentioned above) it is suitable for such images. In contrast to these studies, images of a single molecule called JRAB/MICAL-L2 and its mutants labeled with such general-target tags were quantitatively analyzed using an OF technique, revealing its pivotal role in the "dancing styles" of collective cell migration (Sakane et al., 2016). The rest of the review focuses on JRAB/MICAL-L2 and how it affects migration dynamics.

JRAB/MICAL-L2 MAY CONTROL COLLECTIVE DYNAMICS

JRAB (Junctional Rab13-binding protein)/MICAL-L2 (molecules interacting with CasL-like 2) is an effector protein of Rab13 (Terai et al., 2006), a member of the Rab family of small GTPases, that serves as a molecular switch in the regulation of membrane trafficking (Takai et al., 2001; Zerial and McBride, 2001; Hutagalung and Novick, 2011). Several studies, including our own, have shown that Rab13–JRAB/MICAL-L2 is involved in the transport of cell adhesion molecules and thereby regulates cell–cell adhesion in epithelia (Zahraoui et al., 1994; Marzesco et al., 2002; Morimoto et al., 2005; Terai et al., 2006; Yamamura et al., 2008; Sakane and Sasaki, 2015). Furthermore, JRAB/MICAL-L2 engages in an intramolecular interaction between its N-terminal and C-terminal regions, and binding of Rab13 releases this interaction, resulting in a conformational change from the closed to open form (Sakane et al., 2010). This change is also involved in the spatiotemporal regulation of actin dynamics during epithelial junctional development (Sakane et al., 2012). A structural model of JRAB/MICAL-L2 based on an approach combining bioinformatics and biochemistry (Sakane

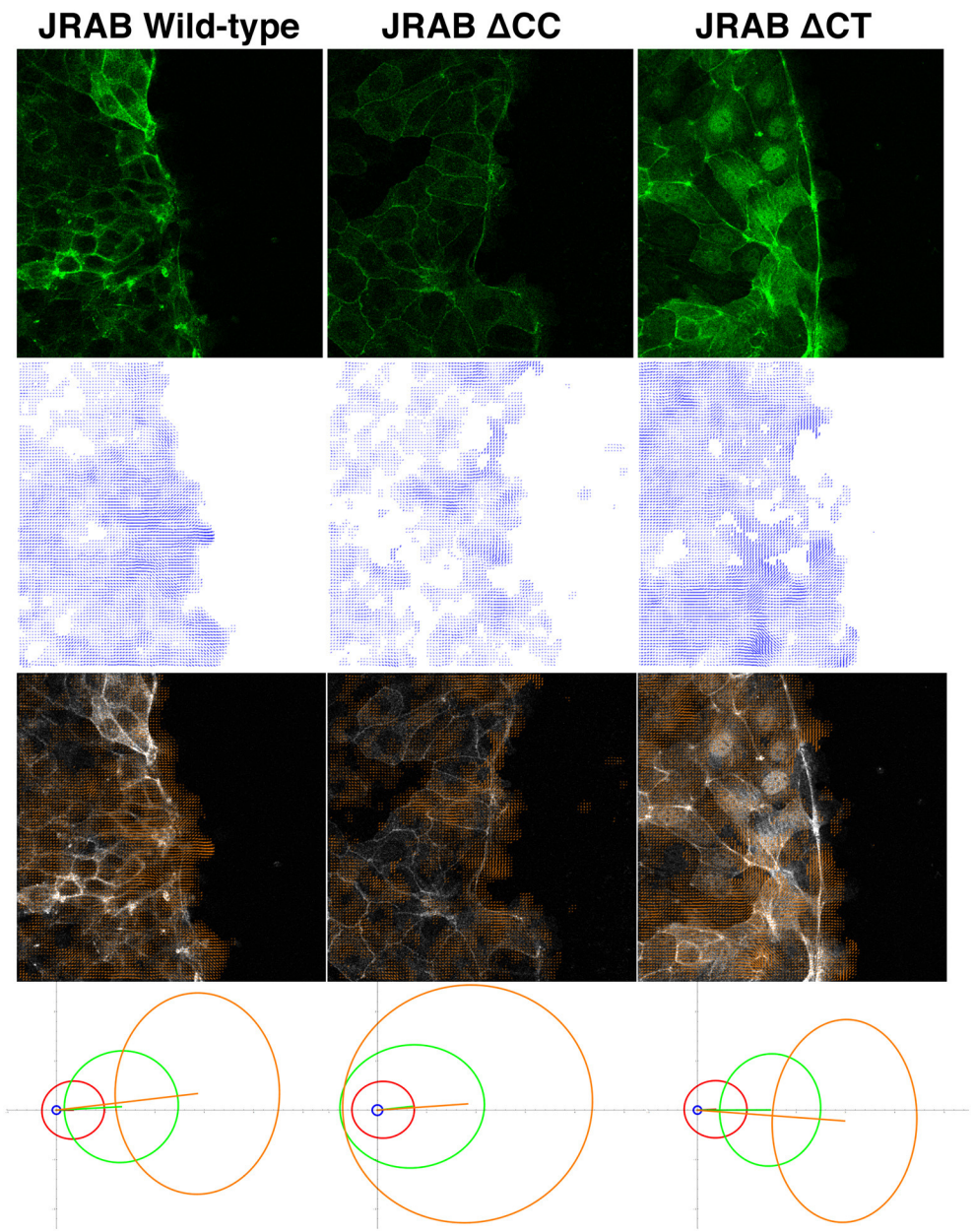

FIGURE 1 | Example of OF analysis of collective cell migration. Top row: live-cell images of cell groups expressing GFP-tagged JRAB wild-type and two mutants. Second row: estimated velocity fields obtained via OF, corresponding to the images in the top row. Third row: overlays of the top and second-row images. Fourth row: PCA results (four different subsets of velocity vectors) corresponding to the datasets represented by the top-row images. More than two billion vectors extracted from 27 time-lapse sets consisting of 7,700 images were employed in the PCA. Each ellipse shows how magnitude and direction of the corresponding velocity vector set varies in 2D space. Coordinate origin represents no movement, and increasing distance from the origin indicates greater velocity. Hence, each ellipse in JRABwt (bottom-left image), especially the two ellipses in the high-speed region, is more concentrated toward the left, which is the direction of cell migration. Thus, JRABwt is more efficient than the other mutants. For more detailed statistical analysis and discussion, see our recent work (Sakane et al., 2016); these figures were adapted from that paper with permission from ASCB.

et al., 2016) has also provided firm evidence for a conformational change induced by Rab13.

These observations raise the possibility that JRAB/MICAL-L2, through its conformational change, coordinates cell–cell adhesion and individual cell migration during collective cell migration.

CONFORMATIONAL CHANGE OF JRAB/MICAL-L2 IN THE CELL

To test the above hypothesis, we generated JRAB mutants fixed in a specific conformation: open form, JRABΔCC; closed form, JRABΔCT (Sakane et al., 2010). Further investigations (Sakane

et al., 2016) of individual cells expressing GFP-JRABΔCC or GFP-JRABΔCT provided the following observations and biological results.

JRABΔCT enhanced the formation of the thick F-actin bundle along the free edge. In addition, radial actin filaments extended from the F-actin bundle, resulting in the maturation of focal adhesions. By contrast, neither the thick F-actin bundle nor mature focal adhesions were observed at front cells expressing JRABΔCC. These differences may explain the results of the biomechanical analyses showing that JRABΔCT generates a traction force at the free edge of the cell population, whereas JRABΔCC impairs this force (Sakane et al., 2016).

We also examined the follower cells, and found that the cells expressing JRABΔCT were larger in size at the junctional level than those expressing JRABΔCC. Moreover, in cells expressing JRABΔCT, many more stress fibers were observed at the basal level than in cells expressing JRABΔCC. These findings imply that JRABΔCT shifts the actin cytoskeleton from cell–cell adhesion to cell–matrix adhesion, thereby increasing the area of the cell at the junctional level. On the contrary, JRABΔCC maintains an appropriate cell area at the junctional level, probably via the formation of stable cell–cell junctions. The results of hanging-drop culture assays support the idea that JRABΔCC maintains more stable cell–cell adhesion, resulting in larger spheroids than those formed by control cells or those expressing JRABΔCT. Taken together, these observations indicate that at the front, the closed form of JRAB/MICAL-L2 plays a role in the generation of traction force that pulls the population in a certain direction, whereas the open form of JRAB/MICAL-L2 contributes to formation and maintenance of stable cell–cell adhesion between follower cells, enabling them to behave as a single unit.

QUANTIFICATION OF "DANCING STYLES" VIA OPTICAL FLOW

In wound healing assays using epithelial MTD-1A cells expressing these mutants, different conformations of JRAB/MICAL-L2 exhibited distinctive "dancing styles" based on the regulation of actin dynamics (Sakane et al., 2016). Groups of cells expressing GFP-JRABΔCT moved strongly in a fixed direction, akin to precision dancing (top-right image of **Figure 1**). By contrast, remarkable ruffles were observed along the front line of clusters of cells expressing JRABΔCC, which migrated in random directions (top-center image of **Figure 1**), resembling *awa-odori*, a Japanese form of traditional dancing similar to the style observed at the Rio Carnival. Groups of cells expressing GFP-JRABwt exhibited an intermediate phenotype (top-left image of **Figure 1**; Sakane et al., 2016).

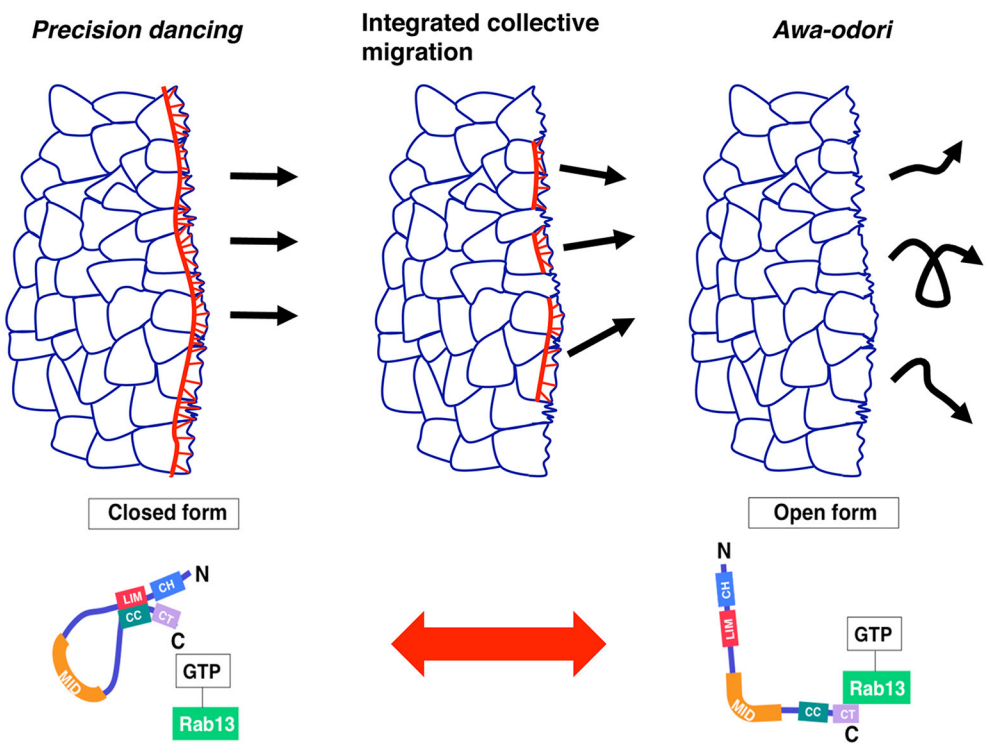

FIGURE 2 | Model: collective cell migration regulated by JRAB/MICAL-L2 conformational plasticity. A cell population expressing only the closed form of JRAB exhibits precision dancing (left), whereas a population expressing only the open form exhibits movement analogous to *awa-odori* (right). For integrated collective cell migration, JRAB/MICAL-L2 must be able to change its conformation freely depending on the situation (middle). This figure was reproduced from our recent work (Sakane et al., 2016) with permission from ASCB.

Because GFP fusions of wild-type JRAB/MICAL-L2, JRABΔCC, and JRABΔCT are general-target fluorescent tags, as discussed above, OF is suitable for characterizing their associated dancing styles from live images and performing quantitative analyses. Hence, we applied an OF technique to study distinctive features of GFP-tagged wild-type JRAB/MICAL-L2 and its conformational mutants during collective cell migration (Sakane et al., 2016). Principal component analysis (PCA) was applied to a subset of velocity vectors classified by speed magnitude based on the extracted OF motion fields (bottom images of **Figure 1**); in this context, PCA provided a set of linearly uncorrelated directions and corresponding magnitudes of a set of time-lapse motion fields. We found that the high-speed motions of JRABwt were more concentrated in the direction corresponding to cell migration than those of the mutants. Thus, wild-type JRAB/MICAL-L2, which can change its structure between the open and closed forms, allows cells to behave as an effective unit. By contrast, mutants locked in the open or closed form did not exhibit this behavior.

CONCLUDING REMARKS

In this review, two different but linked topics were discussed: image-based computational methods and the functional role of JRAB/MICAL-L2 in collective cell migration. Although JRAB/MICAL-L2 was expected to be a key player in migration dynamics, conventional molecular, and cell biology approaches were not sufficient to establish its importance. To address this issue, we used a robust approach combining cell biology, live imaging, and computational analysis (especially OF methods) to evaluate the "dancing style" of migrating cells expressing JRAB/MICAL-L2 or its variants. The results provided valuable insight into a longstanding question concerning how several cells are organized in a moving cell population. Indeed, recent advances in computational analysis provides us with a simple model in which conformational plasticity of a single molecule, JRAB/MICAL-L2, generates the order underlying the integrated movements associated with collective cell migration (**Figure 2**).

OF-based methods and software systems will continue to expand in terms of methodology and application (Delpiano et al., 2012; Fortun et al., 2015; Masuzzo et al., 2016). Also integrating the obtained motion fields with model-based computational analyses such as mechanical and biochemical simulations of cell migrations (Te Boekhorst et al., 2016; van Helvert et al., 2018) is useful and promising future work. Consequently, biologists may be able to choose from among existing tools in order to obtain motion fields in their target images. On the other hand, spatial and temporal descriptors in motion field analysis of collective cell migration images remain rather simple in comparison with those developed in computational fluid dynamics, medical image processing, and computer graphics. Therefore, in the future, the more advanced mathematical tools of vector field analysis, such as vector field topology (Theisel et al., 2005; Wang et al., 2013), Hodge decomposition (Bhatia et al., 2013), and ridge creases (Tricoche et al., 2008; Schultz et al., 2010) could be useful, and such sophisticated methods might become popular in cell biology.

AUTHOR CONTRIBUTIONS

All authors listed have made a substantial, direct and intellectual contribution to the work, and approved it for publication.

ACKNOWLEDGMENTS

We thank the reviewers of this review for their valuable comments. This work was supported by MEXT KAKENHI Grant Number 15H05954 (HY) and JSPS KAKENHI Grant Numbers 26460370, 17K08636 (AS).

REFERENCES

Amat, F., Myers, E. W., and Keller, P. J. (2013). Fast and robust optical flow for time-lapse microscopy using super-voxels. *Bioinformatics* 29, 373–380. doi: 10.1093/bioinformatics/bts706

Angelini, T. E., Hannezo, E., Trepat, X., Marquez, M., Fredberg, J. J., and Weitz, D. A. (2011). Glass-like dynamics of collective cell migration. *Proc. Natl. Acad. Sci. U.S.A.* 108, 4714–4719. doi: 10.1073/pnas.1010059108

Aoki, K., Kondo, Y., Naoki, H., Hiratsuka, T., Itoh, R. E., and Matsuda, M. (2017). Propagating wave of ERK activation orients collective cell migration. *Dev Cell* 43, 305.e5–317. e5. doi: 10.1016/j.devcel.2017.10.016

Beauchemin, S. S., and Barron, J. L. (1995). The computation of optical flow. *ACM Comput. Surv.* 27, 433–466. doi: 10.1145/212094.212141

Ben-Tekaya, H., Miura, K., Pepperkok, R., and Hauri, H. P. (2005). Live imaging of bidirectional traffic from the ERGIC. *J. Cell Sci.* 118, 357–367. doi: 10.1242/jcs.01615

Bhatia, H., Norgard, G., Pascucci, V., and Bremer, P. T. (2013). The helmholtz-hodge decomposition–a survey. *IEEE Trans. Vis. Comput. Graph.* 19, 1386–1404. doi: 10.1109/TVCG.2012.316

Boric, K., Orio, P., Viève, T., and Whitlock, K. (2013). Quantitative analysis of cell migration using optical flow. *PLoS ONE* 8:e69574. doi: 10.1371/journal.pone.0069574

Breen, E. J., and Williams, K. L. (1994). Optical flow analysis of the ventral cellular layer of the migrating *Dictyostelium discoideum* slug. *Microbiology* 140 (Pt 5), 1241–1252. doi: 10.1099/13500872-140-5-1241

Bunyak, F., Palaniappan, K., Nath, S. K., Baskin, T. I., and Dong, G. (2006). "Quantitative cell motility for in vitro wound healing using level set-based active contour tracking," in *Proceedings IEEE International Symposium on Biomedical Imaging* (Arlington, VA: IEEE), 1040–1043.

Castañeda, V., Cerda, M., Santibáñez, F., Jara, J., Pulgar, E., Palma, K., et al. (2014). Computational methods for analysis of dynamic events in cell migration. *Curr. Mol. Med.* 14, 291–307. doi: 10.2174/1566524014666140128113952

Cliffe, A., Doupé, D. P., Sung, H., Lim, I. K., Ong, K. H., Cheng, L., et al. (2017). Quantitative 3D analysis of complex single border cell behaviors in coordinated collective cell migration. *Nat. Commun.* 8:14905. doi: 10.1038/ncomms14905

Cordelières, F. P., Petit, V., Kumasaka, M., Debeir, O., Letort, V., Gallagher, S. J., et al. (2013). Automated cell tracking and analysis in phase-contrast videos (iTrack4U): development of Java software based on combined mean-shift processes. *PLoS ONE* 8:e81266. doi: 10.1371/journal.pone.0081266

Debeir, O., Van Ham, P., Kiss, R., and Decaestecker, C. (2005). Tracking of migrating cells under phase-contrast video microscopy with combined mean-shift processes. *IEEE Trans. Med. Imaging* 24, 697–711. doi: 10.1109/TMI.2005.846851

Delpiano, J., Jara, J., Scheer, J., Ramírez, O. A., Ruiz-Del-Solar, J., and Härtel, S. (2012). Performance of optical flow techniques for motion analysis of

fluorescent point signals in confocal microscopy. *Mach. Vis. Appl*. 23, 675–689. doi: 10.1007/s00138-011-0362-8

Dubin-Thaler, B. J., Hofman, J. M., Cai, Y., Xenias, H., Spielman, I., Shneidman, A. V., et al. (2008). Quantification of cell edge velocities and traction forces reveals distinct motility modules during cell spreading. *PLoS ONE* 3:e3735. doi: 10.1371/journal.pone.0003735

Fortun, D., Bouthemy, P., and Kervrann, C. (2015). Optical flow modeling and computation: a survey. *Comput. Vis. Image Underst*. 134, 1–21. doi: 10.1016/j.cviu.2015.02.008

Friedl, P., and Alexander, S. (2011). Cancer invasion and the microenvironment: plasticity and reciprocity *Cell* 147, 992–1009. doi: 10.1016/j.cell.2011.11.016

Friedl, P., and Gilmour, D. (2009). Collective cell migration in morphogenesis, regeneration and cancer. *Nat. Rev. Mol. Cell Biol*. 10, 445–457. doi: 10.1038/nrm2720

Friedl, P., and Wolf, K. (2010). Plasticity of cell migration: a multiscale tuning model. *J. Cell Biol*. 188, 11–19. doi: 10.1083/jcb.200909003

George, M., Bullo, F., and Campàs, O. (2017). Connecting individual to collective cell migration. *Sci. Rep*. 7:9720. doi: 10.1038/s41598-017-10069-8

Gray, R. S., Cheung, K. J., and Ewald, A. J. (2010). Cellular mechanisms regulating epithelial morphogenesis and cancer invasion. *Curr. Opin. Cell Biol*. 22, 640–650. doi: 10.1016/j.ceb.2010.08.019

Huang, G., Kim, J., Huang, X., Zheng, G., and Tokuta, A. (2012). A statistical framework for estimation of cell migration velocity. *J. WSCG* 20, 29–36.

Hutagalung, A. H., and Novick, P. J. (2011). Role of Rab GTPases in membrane traffic and cell physiology. *Physiol. Rev*. 91, 119–149. doi: 10.1152/physrev.00059.2009

Ionides, E. (2001). *Statistical Analysis of Cell Motion*. Ph.D. thesis, University of Calfornia.

Jang, H., Notbohm, J., Gweon, B., Cho, Y., Park, C. Y., Kee, S. H., et al. (2017). Homogenizing cellular tension by hepatocyte growth factor in expanding epithelial monolayer. *Sci. Rep*. 8:45844. doi: 10.1038/srep45844

Kappe, C. P., Schütz, L., Gunther, S., Hufnagel, L., Lemke, S., and Leitte, H. (2016). Reconstruction and visualization of coordinated 3D cell migration based on optical flow. *IEEE Trans. Vis. Comput. Graph*. 22, 995–1004. doi: 10.1109/TVCG.2015.2467291

Khairy, K., and Keller, P. J. (2011). Reconstructing embryonic development. *Genesis* 49, 488–513. doi: 10.1002/dvg.20698

Ladoux, B., and Mège, R. M. (2017). Mechanobiology of collective cell behaviours. *Nat. Rev. Mol. Cell Biol* 18, 743–757. doi: 10.1038/nrm.2017.98

Marzesco, A. M., Dunia, I., Pandjaitan, R., Recouvreur, M., Dauzonne, D., Benedetti, E. L., et al. (2002). The small GTPase Rab13 regulates assembly of functional tight junctions in epithelial cells. *Mol. Biol. Cell* 13, 1819–1831. doi: 10.1091/mbc.02-02-0029

Masuzzo, P., Van Troys, M., Ampe, C., and Martens, L. (2016). Taking aim at moving targets in computational cell migration. *Trends Cell Biol*. 26, 88–110. doi: 10.1016/j.tcb.2015.09.003

Mayor, R., and Carmona-Fontaine, C. (2010). Keeping in touch with contact inhibition of locomotion. *Trends Cell Biol*. 20, 319–328. doi: 10.1016/j.tcb.2010.03.005

Morimoto, S., Nishimura, N., Terai, T., Manabe, S., Yamamoto, Y., Shinahara, W., et al. (2005). Rab13 mediates the continuous endocytic recycling of occludin to the cell surface. *J. Biol. Chem*. 280, 2220–2228. doi: 10.1074/jbc.M406906200

Ramel, D., Wang, X., Laflamme, C., Montell, D. J., and Emery, G. (2013). Rab11 regulates cell-cell communication during collective cell movements. *Nat. Cell Biol*. 15, 317–324. doi: 10.1038/ncb2681

Ronot, X., Doisy, A., and Tracqui, P. (2000). Quantitative study of dynamic behavior of cell monolayers during *in vitro* wound healing by optical flow analysis. *Cytometry* 41, 19–30. doi: 10.1002/1097-0320(20000901)41:1<19::AID-CYTO3>3.0.CO;2-X

Rørth, P. (2012). Fellow travellers: emergent properties of collective cell migration. *EMBO Rep*. 13, 984–991. doi: 10.1038/embor.2012.149

Sahai, E. (2005). Mechanisms of cancer cell invasion. *Curr. Opin. Genet. Dev*. 15, 87–96. doi: 10.1016/j.gde.2004.12.002

Sakane, A., Abdallah, A. A., Nakano, K., Honda, K., Ikeda, W., Nishikawa, Y., et al. (2012). Rab13 small G protein and junctional Rab13-binding protein (JRAB) orchestrate actin cytoskeletal organization during epithelial junctional development. *J. Biol. Chem*. 287, 42455–42468. doi: 10.1074/jbc.M112.383653

Sakane, A., and Sasaki, T. (2015). "Roles of Rab family small G proteins in formation of the apical junctional complex in epithelial cells," in *Cell Polarity* ed K. Ebnet. (Germany: Springer), 349–374. doi: 10.1007/978-3-319-14463-4_15

Sakane, A., Honda, K., and Sasaki, T. (2010). Rab13 regulates neurite outgrowth in PC12 cells through its effector protein, JRAB/MICAL-L2. *Mol. Cell. Biol*. 30, 1077–1087. doi: 10.1128/MCB.01067-09

Sakane, A., Yoshizawa, S., Nishimura, M., Tsuchiya, Y., Matsushita, N., Miyake, K., et al. (2016). Conformational plasticity of JRAB/MICAL-L2 provides "law and order" in collective cell migration. *Mol. Biol. Cell* 27, 3095–3108. doi: 10.1091/mbc.E16-05-0332

Schultz, T., Theisel, H., and Seidel, H. P. (2010). Crease surfaces: from theory to extraction and application to diffusion tensor MRI. *IEEE Trans. Vis. Comput. Graph*. 16, 109–119. doi: 10.1109/TVCG.2009.44

Siegert, F., Weijer, C. J., Nomura, A., and Miike, H. (1994). A gradient method for the quantitative analysis of cell movement and tissue flow and its application to the analysis of multicellular Dictyostelium development. *J. Cell Sci*. 107(Pt 1), 97–104.

Supatto, W., McMahon, A., Fraser, S. E., and Stathopoulos, A. (2009). Quantitative imaging of collective cell migration during *Drosophila* gastrulation: multiphoton microscopy and computational analysis. *Nat. Protoc*. 4, 1397–1412. doi: 10.1038/nprot.2009.130

Takai, Y., Sasaki, T., and Matozaki, T. (2001). Small GTP-binding proteins. *Physiol. Rev*. 81, 153–208. doi: 10.1152/physrev.2001.81.1.153

Te Boekhorst, V., Preziosi, L., and Friedl, P. (2016). Plasticity of cell migration *in vivo* and *in silico*. *Annu. Rev. Cell Dev. Biol*. 32, 491–526. doi: 10.1146/annurev-cellbio-111315-125201

Terai, T., Nishimura, N., Kanda, I., Yasui, N., and Sasaki, T. (2006). JRAB/MICAL-L2 is a junctional Rab13-binding protein mediating the endocytic recycling of occludin. *Mol. Biol. Cell* 17, 2465–2475. doi: 10.1091/mbc.E05-09-0826

Theisel, H., Weinkauf, T., Hege, H. C., and Seidel, H. P. (2005). Topological methods for 2D time-dependent vector fields based on stream lines and path lines. *IEEE Trans. Vis. Comput. Graph*. 11, 383–394. doi: 10.1109/TVCG.2005.68

Theveneau, E., and Mayor, R. (2012). Cadherins in collective cell migration of mesenchymal cells. *Curr. Opin. Cell Biol*. 24, 677–684. doi: 10.1016/j.ceb.2012.08.002

Tricoche, X., Kindlmann, G., and Westin, C. F. (2008). Invariant crease lines for topological and structural analysis of tensor fields. *IEEE Trans. Vis. Comput. Graph*. 14, 1627–1634. doi: 10.1109/TVCG.2008.148

van Helvert, S., Storm, C., and Friedl, P. (2018). Mechanoreciprocity in cell migration. *Nat. Cell Biol*. 20, 8–20. doi: 10.1038/s41556-017-0012-0

Wang, C., Shen, H.-W., Weiskopf, D., Peterka, T., and Chen, G. (2013). State-of-the-art flow field analysis and visualization. 2013 IEEE VIS Tutorials.

Woods, M. L., Carmona-Fontaine, C., Barnes, C. P., Couzin, I. D., Mayor, R., and Page, K. M. (2014). Directional collective cell migration emerges as a property of cell interactions. *PLoS ONE* 9:e104969. doi: 10.1371/journal.pone.0104969

Yamamura, R., Nishimura, N., Nakatsuji, H., Arase, S., and Sasaki, T. (2008). The interaction of JRAB/MICAL-L2 with Rab8 and Rab13 coordinates the assembly of tight junctions and adherens junctions. *Mol. Biol. Cell* 19, 971–983. doi: 10.1091/mbc.E07-06-0551

Zahraoui, A., Joberty, G., Arpin, M., Fontaine, J. J., Hellio, R., Tavitian, A., et al. (1994). A small rab GTPase is distributed in cytoplasmic vesicles in non polarized cells but colocalizes with the tight junction marker ZO-1 in polarized epithelial cells. *J. Cell Biol*. 124, 101–115. doi: 10.1083/jcb.124.1.101

Zegers, M. M., and Friedl, P. (2014). Rho GTPases in collective cell migration. *Small GTPases* 5:e28997. doi: 10.4161/sgtp.28997

Zerial, M., and McBride, H. (2001). Rab proteins as membrane organizers. *Nat. Rev. Mol. Cell Biol*. 2, 107–117. doi: 10.1038/35052055

Conflict of Interest Statement: The authors declare that the research was conducted in the absence of any commercial or financial relationships that could be construed as a potential conflict of interest.

frontiers in Cell and Developmental Biology

ORIGINAL RESEARCH
published: 03 August 2017
doi: 10.3389/fcell.2017.00068

Inference of Cell Mechanics in Heterogeneous Epithelial Tissue Based on Multivariate Clone Shape Quantification

Alice Tsuboi[1†], Daiki Umetsu[2†], Erina Kuranaga[2] and Koichi Fujimoto[1*]*

[1] *Laboratory of Theoretical Biology, Department of Biological Sciences, Osaka University, Toyonaka, Japan,* [2] *Laboratory of Histogenetic Dynamics, Graduate School of Life Sciences, Tohoku University, Sendai, Japan*

Cell populations in multicellular organisms show genetic and non-genetic heterogeneity, even in undifferentiated tissues of multipotent cells during development and tumorigenesis. The heterogeneity causes difference of mechanical properties, such as, cell bond tension or adhesion, at the cell–cell interface, which determine the shape of clonal population boundaries via cell sorting or mixing. The boundary shape could alter the degree of cell–cell contacts and thus influence the physiological consequences of sorting or mixing at the boundary (e.g., tumor suppression or progression), suggesting that the cell mechanics could help clarify the physiology of heterogeneous tissues. While precise inference of mechanical tension loaded at each cell–cell contacts has been extensively developed, there has been little progress on how to distinguish the population-boundary geometry and identify the cause of geometry in heterogeneous tissues. We developed a pipeline by combining multivariate analysis of clone shape with tissue mechanical simulations. We examined clones with four different genotypes within *Drosophila* wing imaginal discs: wild-type, *tartan* (*trn*) overexpression, *hibris* (*hbs*) overexpression, and *Eph* RNAi. Although the clones were previously known to exhibit smoothed or convoluted morphologies, their mechanical properties were unknown. By applying a multivariate analysis to multiple criteria used to quantify the clone shapes based on individual cell shapes, we found the optimal criteria to distinguish not only among the four genotypes, but also non-genetic heterogeneity from genetic one. The efficient segregation of clone shape enabled us to quantitatively compare experimental data with tissue mechanical simulations. As a result, we identified the mechanical basis contributed to clone shape of distinct genotypes. The present pipeline will promote the understanding of the functions of mechanical interactions in heterogeneous tissue in a non-invasive manner.

Keywords: cell mechanics, PCA, heterogeneity, tumor, cell sorting, cell mixing, *Drosophila*, vertex model

OPEN ACCESS

Edited by:
Takaaki Matsui,
Nara Institute of Science and Technology, Japan

Reviewed by:
René-Marc Mège,
Centre National de la Recherche Scientifique (CNRS), France
Francois Graner,
Centre National de la Recherche Scientifique (CNRS), France

***Correspondence:**
Daiki Umetsu
umetsu@tohoku.ac.jp
Koichi Fujimoto
fujimoto@bio.sci.osaka-u.ac.jp

[†]These authors have contributed equally to this work.

Specialty section:
This article was submitted to Cell Adhesion and Migration, a section of the journal Frontiers in Cell and Developmental Biology

Received: *28 March 2017*
Accepted: *05 July 2017*
Published: *03 August 2017*

Citation:
Tsuboi A, Umetsu D, Kuranaga E and Fujimoto K (2017) Inference of Cell Mechanics in Heterogeneous Epithelial Tissue Based on Multivariate Clone Shape Quantification. Front. Cell Dev. Biol. 5:68. doi: 10.3389/fcell.2017.00068

INTRODUCTION

There are intrinsic differences among cells within any population, even in genetically uniform populations such as, clonal populations of bacteria, yeasts, and undifferentiated plant and animal cells (Elowitz, 2002; Raser, 2004; Raj and van Oudenaarden, 2008; Eldar and Elowitz, 2010; Itzkovitz et al., 2011; Meyer and Roeder, 2014). The non-genetic (isogenic) heterogeneity stems

from intrinsic noise due to stochastic fluctuations in gene expression and extrinsic noise due to stochastic changes in upstream signal transduction (Paulsson, 2004; Shibata and Fujimoto, 2005). Theoretical and experimental discrimination between intrinsic and extrinsic noise (Elowitz, 2002; Swain et al., 2002) promoted an understanding of not only the molecular mechanisms but also the functional significance of the non-genetic heterogeneity (Raj and van Oudenaarden, 2008; Eldar and Elowitz, 2010). Genetic heterogeneity in tissues arises from spontaneous mutations in cell lineages. The emergence of cellular heterogeneity in epithelial tissues alters the morphology of the boundaries between neighboring populations and thereby affects the cellular geometry in the tissue. Alterations of the geometrical cellular configuration between clonal populations (clones) often have physiological consequences. Clonal segregation caused by Eph receptors has been shown to play a tumor-suppressive role in colorectal cancer by compartmentalizing the cancer cells and thereby limiting their invasion into normal tissues (Cortina et al., 2007; Porazinski et al., 2016). In the context of the cell competition, known as the tissue homeostatic system, to eliminate unfit cells from heterogeneous populations (Vincent et al., 2013; Amoyel and Bach, 2014; Morata and Ballesteros-Arias, 2015), the intermingling of cells at clonal boundaries facilitates the competition by increasing the contact length between competing genotypes, so-called winner and loser cells (Levayer et al., 2015; Levayer and Moreno, 2016). Those insights suggest the potential to predict physiological consequences (e.g., tumor malignancy) based on the quantification of clone shapes. Therefore, the establishment of a pipeline that combines the quantification of clone shapes with an analysis of the physical mechanisms underlying the clone shapes would be beneficial.

A major contributing factor for clone shape is mechanical interactions at the cell–cell interface. Cell–Cell adhesion mediated by adhesion molecules and contractility exerted by the actomyosin network contribute to the tension on the cell–cell interface (Lecuit and Lenne, 2007). The differential adhesion and contractility among genetically heterogeneous cells have been experimentally shown to play a major role in cell segregation by driving or guiding cell rearrangements (Nose et al., 1988; Krieg et al., 2008; Maitre et al., 2012; Maître et al., 2016). The role of such mechanical cell–cell interactions on cell sorting has been also theoretically studied using computer simulations of tissue mechanics (Graner and Glazier, 1992; Brodland, 2002). More recently, experimental evidence in combination with models has shown that the alteration of boundary morphology can be explained by the tissue anisotropy of mechanical tension at the cell–cell interface (Landsberg et al., 2009; Monier et al., 2010; Aliee et al., 2012; Rudolf et al., 2015). The relative strength of such mechanical tension (or stress) has been estimated non-invasively from time lapse of cell shape dynamics (Brodland et al., 2010; Chiou et al., 2012; Ishihara and Sugimura, 2012; Nier et al., 2016) or images of fixed tissue (Brodland et al., 2014), and invasively using physical perturbation (e.g., laser ablation of cell junctions) (Sugimura et al., 2016, and reference therein). Moreover, a recent study showed that the "clone tension," which is defined by the average strength of the junctional tension inside and on the border of the clone relative to that on the outside, uniquely distinguishes smoothed and convoluted clone shapes (Bosveld et al., 2016a). Hence, reliable quantification of clone shape should make it possible to identify the averaged strength of tensions in heterogeneous tissue.

Although several quantification methods for clone shape, such as, circularity (Milán et al., 2002; Chang et al., 2011) and cell mixing index (Umetsu et al., 2014a; Levayer et al., 2015), have been established, each has been applied only independently. It is not known whether those methods can be applied to any clone shape or are suited for some particular clone shape. Moreover, it has been unknown whether such methods are sufficient to distinguish clone shapes or the other methods (e.g., cell area) are required. The combinatorial use of multiple quantitative methods would more reliably evaluate the clone shapes of various genotypes.

In this study, we provide a pipeline to quantify the clone shape difference and identify the cause of the difference by combining a multivariate quantitative analysis of clone shape with computer simulations of tissue mechanics (**Figure 1A**). Using fixed *Drosophila* wing imaginal discs, we examined four genotypes [wild-type control, *tartan* (*trn*) overexpression, and *Eph* RNAi, *hibris* (*hbs*) overexpression], which exhibit smoothed or convoluted clone morphologies yet have unknown cell mechanical properties. Clones that overexpress *Drosophila trn*, which encodes leucine rich repeat-containing transmembrane proteins (Milán et al., 2001, 2002; Sakurai et al., 2007), adopt a smooth shape. The knockdown of *Eph*, which encodes tyrosine kinases of the Eph receptor protein family, also generates round clones (Umetsu et al., 2014b). In contrast, the overexpression of *hbs*, an immunoglobulin superfamily member, leads to the separation of the *hbs*-overexpressing cells and their partial mixing into surrounding cells (Bao et al., 2010), resulting in a convoluted clone morphology. We used multiple cell-based criteria to quantify the clone morphology. While no single criterion alone was able to distinguish all four genotypes, by combinatorial use of multiple criteria, we distinguished the four genotypes with optimal criteria. Based on the quantitative criteria, we compared experimental results with vertex model simulations, which we explored in a wide range of differential tensions. The comparison enabled us to estimate different contribution of clone tensions and tension parameters to clone morphologies of distinct genotypes, noting that the force inference of individual cells over entire tissue is beyond the scope of the present paper. The present multivariate clone shape quantification could be extended to estimate genetic and non-genetic cell mechanics of heterogeneous populations (e.g., tumorigenic environment) in a non-invasive manner.

MATERIALS AND METHODS

Drosophila Strains and Genetics

We used *y w hs-flp; DE-Cad::GFP; Act>CD2>GAL4, UAS-DsRed* as the tester-stock genotype in our experiments. We crossed the tester stock with RNAi lines and raised the offspring at 25°C for 3 days. We then subjected the offspring to heat shock at 37°C for 40 min to induce somatic clones (**Figure 1K**). We subsequently

kept the larvae at 25°C for 3 days before dissection. We used the following transgenic strains in our study: UAS-*trn* (Sakurai et al., 2007), UAS-*hbs* (Dworak et al., 2001), and UAS-ds-*Eph* (Vienna stock center, 4771). Hereafter, we refer to the *Drosophila* tester-stock clone as the wild-type.

Immunohistochemistry

We hand dissected larvae to obtain wing imaginal discs, which we fixed in PBS with 4% formaldehyde for 40 min at room temperature. We washed the fixed samples three times with PBT (PBS with 0.1% triton) and mounted them on a glass slide.

Imaging and Image Processing

We obtained images with a Leica SP8 confocal scanning microscope with a 40 × NA 1.30oil objective. We visualized adherens junctions with the localization of a GFP knock-in for DE-Cadherin (Huang et al., 2009) and used them for image segmentation. We manually selected the GFP signals derived from columnar cells of the wing pouch before making a z-stack projection. We projected the z-stack images by the maximum projection in Fiji (http://fiji.sc) and used them for further quantitative analysis. Average pixel size for each cell junction was 8.4 (Supplementary Figure S11).

Clone Shape Quantification

We performed segmentation, cell tracking, and bond tracking (**Figures 1P–S**) using the Fiji plugin Tissue Analyzer (Aigouy et al., 2016). We projected the clones onto the segmented images and identified cells in the clones using Tissue Analyzer. We roughly estimated possible error rates by having 5 unexperienced individuals hand-correct a segmentation mask for one of the images we used in this study. We estimated the error rate in 4 ways as follows (Supplementary Figure S4); (1) the mean rate of hand-corrections made after auto-segmentation (0.84% of all cell junctions), (2) the mean rate of hand-corrections made by another person after the 1st round of hand-correction (0.28% of all cell junctions), (3) the mean rate of hand-correction made by 1st and 2nd round of hand-correction in total (1.12% of all cell junctions), and 4) the mean final discrepancy rate between 2 individuals (0.23%, max. 0.44%). We note that the correction rate highly depends on original image quality therefore the rate would be variable among images.

We quantified the clone shapes using multiple criteria. Circularity is a measure that calculates the ratio between the perimeter and the area of a clone and has been used to evaluate clone shapes (**Figure 1C**). We also used the following cell-based criteria: cell area (**Figure 1D**), cell edge length (**Figure 1E**), clone boundary angle (**Figure 1F**), and three types of cell mixing index (**Figure 1G**) [i.e., mutant (MT; **Figure 1H**), boundary of mutant (BDMT; **Figure 1I**), and boundary of wild-type (BDWT; **Figure 1J**)].

Principal Component Analysis (PCA)

We performed PCA of the multi-dimensional criteria for clone shape using the R environment for statistical computing (R Development Core Team, 2015) with the "prcomp" function. We plotted the results using the "ggbiplot" function (R package version 0.55. http://github.com/vqv/ggbiplot). We applied PCA to both open and closed clones in the wing imaginal discs using the six criteria (**Figures 1D–F,H–J**) excluding circularity. We standardized the variables to have zero mean and unit variance before the analysis. Factor loadings (**Figure 3K**), which were given by the correlation coefficient between observed variables (criteria) and principal components (PCs), represent the contribution of criteria on PCs. The range of the value is −1.0 to 1.0. The value of −1.0 and 1.0 for the criteria indicates a perfect negative and positive correlation with the PCs, respectively.

Cell Vertex Model

The cell vertex model quantitatively accounts for the packing geometry of normal epithelial cells and predicts the forces that act at cell–cell interfaces, where cell configurations are described as polygons whose vertices form tri-cellular junctions subjected to mechanical force (Honda, 1983; Farhadifar et al., 2007; Gibson et al., 2011). The model can reproduce stable force balance configurations of the adherens junctions network, which depend on mechanical parameters characterizing the cell bond tension and apical area contraction. Cells change their shape based on the force balance of cell packing. The model is represented by balance of three types of mechanical force exerted on a vertex (Farhadifar et al., 2007):

$$\frac{d\overrightarrow{x_i}}{dt} = F_{area\ elastisity} + F_{tension} + F_{contractility} = -\frac{\partial E}{\partial \overrightarrow{x_i}}$$

$$E = \frac{1}{2}\sum\nolimits_{\alpha}(a_\alpha - 1)^2 + \gamma \sum\nolimits_{<i,j>} l_{ij} + \frac{\eta}{2}\sum\nolimits_{\alpha} {l_\alpha}^2, \quad (1)$$

where x_i and E are the position vector of each vertex and the energy function. $F_{area\ elasticity}$ denotes the area elasticity, which decreases as the area of cell α (a_α) approaches the normalized preferred area of unity. The line tension ($F_{tension}$) between vertices i and j (l_{ij}) is provided by the cell–cell adhesion mediated by adhesion molecules and the contractility exerted by actomyosin. The contraction ($F_{area\ elasticity}$) of the cell perimeter l_α is provided by actomyosin ring. We set the contractility parameter $\eta = 0.04$ and the line tension parameter $\gamma = 0.12$ as the control values to account for the cell packing geometry in *Drosophila* wild-type clones (Farhadifar et al., 2007). The line tension at the clone boundary (γ_b) and at the inner clonal edges (γ_c) can differ from γ. Each clone was generated from a single cell by dividing them to be 40 cells in total, which is close to the average number of cells in *Drosophila* wild-type clones. We performed 5 independent simulations for each parameter by changing the seed of the random number generator.

We integrated the vertex model numerically using the Euler method with free boundary conditions. To achieve a mechanical equilibrium of the tissue state, we calculated the position vector of each vertex after each step until the total velocity of all vertices dropped below a threshold of 1.0. The cell division time (cell cycle) t of each cell in the cell vertex model obeys a Gamma distribution with the following probability densities: $p(t) = t^{k-1}exp(-kt/\bar{T})(\bar{T}/k)^{-k}/\Gamma(k)$, where $\Gamma(k)$ is the gamma

function with $k = 25.0$ (Wartlick, 2011). The average and standard deviation are given by $\bar{T}$ and $\bar{T}/\sqrt{k}$, with $\bar{T} = 6$. Cells were divided when the residence times in the cell cycle became zero. Although the cell area decreases to half the original cell area after cell division, it increases as the cell achieves a mechanical equilibrium of energy [Equation (1)]. The mitotic cleavage-plane orientation obeys the long axis rule (Gibson et al., 2011; Bosveld et al., 2016b), where the plane passing through the shorter axis is defined by calculating the inertial tensor of each cell using the positions of the vertices (Fletcher et al., 2013). Cell intercalation (T1 transition) was incorporated when the edge length dropped below a threshold of 0.01. Apoptosis (T2 transition) was introduced into triangular cells (containing 3 vertices) whose area became below a threshold of 0.03 to replace them by a single vertex. In addition, cells which were squeezed and reduced their cell area below a threshold of 0.001 were eliminated by repeating the cell topological changes (T1 and T2 transition) even if the cells containing more than 3 vertices. The number of apoptotic events (during proliferation of a clone from a single cell to 40 cells) depends on the model parameters as seen in earlier studies on homogeneous tissue (Farhadifar et al., 2007). The apoptotic rate (number of apoptotic events/cell cycle) was 0 ($\gamma_b/\gamma = 0.5$, $\gamma_c/\gamma = 1.8$, **Figure 4Ai**), 1.5 ($\gamma_b/\gamma = 1.0$, $\gamma_c/\gamma = 1.8$, **Figure 4Aii**), 0 ($\gamma_b/\gamma = 0.5$, $\gamma_c/\gamma = 1.0$, **Figure 4Aiii**), 0 ($\gamma_b/\gamma = 1.0$, $\gamma_c/\gamma = 1.0$, **Figure 4Aiv**), 0.08 ($\gamma_b/\gamma = 1.6$, $\gamma_c/\gamma = 1.0$, **Figure 4Av**), 0 ($\gamma_b/\gamma = 1.0$, $\gamma_c/\gamma = 0$, **Figure 4Avi**), 0 ($\gamma_b/\gamma = 1.6$, $\gamma_c/\gamma = 0$, **Figure 4Avii**).

Clone Tension

Clone tension is given by the balance of line tension parameters [Equation (1)] at the three types of edges represented by γ, γ_b, and γ_c (Bosveld et al., 2016a):

$$\hat{\sigma} = \frac{\partial E}{\partial L} = \gamma_b - \frac{\gamma + \gamma_c}{2}. \quad (2)$$

It represents the energy cost E [Equation (1)] per unit length of changes in the clone boundary length L (**Figure 1C**) followed by cell intercalation. Because the differential of elastic energy $\partial E/\partial L$ should be negative to satisfy a stable equilibrium, the sign of the clone tension $\hat{\sigma}$ influences the evolution of the clone boundary length L. At negative $\hat{\sigma}$, boundary length change δL should be positive to increase the contact between different cell populations, leading to a convoluted clone boundary. In contrast, at positive $\hat{\sigma}$, δL should be negative to decrease the contact between different cell populations, leading to a smoothed clone boundary. We used dimensionless clone tension $\sigma = \hat{\sigma}/\gamma$ (Bosveld et al., 2016a) in this study.

Projection of the Simulation Data onto the PCA Space of the Experimental Data

To quantitatively compare the multivariate clone shape data from genetic experiments with the vertex model simulations in the PCA space constructed from the experimental data (**Figure 1A**), the simulation clones (See Section Cell Vertex Model for induction of clones) were quantified by an identical set of quantitative criteria with experiments (**Figures 1D–F,H–J**). Subsequently, we subtracted the clone shape dataset for each criterion in simulations from the mean of that in the four genotypes and divided the subtracted values by the standard deviation of that in the genotypes. We calculated the first PC scores (Y_1) of the scaled simulation data (X_1, X_2, ..., X_n) by $Y_1 = a_{11}X_1 + a_{12}X_2 + ... + a_{1n}X_n$, where a_{11}, a_{12}, ..., a_{1n} are the weights (Supplementary Table S1) of four genotypes with $n = 6$ (number of criteria; **Figures 1D–F,H–J**). The weights are given by the first column of the PC matrix, which contains variable loadings whose values are returned by "rotation" in the prcomp function in R. The second PC scores are given in the same way by using the second column of the matrix. We projected the calculated first and second PC scores onto the experimental PCA space using the "ggplot2" function in R (Wickham, 2009). The PC scores in simulation were averaged over the clones categorized by the number of consisting cells (every 5 cells) since the clone size was varied due to fragmentation of a single clone caused by T1 transitions in a simulation.

Estimation of the Mechanical Parameters of the Genetic Experiments in the PCA Space

We determined the estimated mechanical parameters by simulation plots inside a confidence ellipse, which we drew by assuming that the experimental plots of each genotype followed the multivariate normal distribution. We selected the best representative parameters for each genotype by identifying the shortest Mahalanobis distance from the center of the confidence ellipse.

RESULTS

Clone Shape Quantification

We adopted several geometrical indicators (**Figures 1B–J** and Supplementary Figures S1, S2) to quantitatively evaluate the shape of mosaic clones of distinct genotypes induced in the wing discs (**Figures 1K–O**). First, we calculated the circularity of each clone (Section Clone Shape Quantification; **Figures 1C**, **2**), and Supplementary Figure S1). The average circularity of the *trn*-overexpression clones, which exhibited a round shape with a smooth border (**Figure 1M**), was significantly greater than that of the wild-type clones, as reported previously (**Figure 3A**; Milán et al., 2002). In the other genotype, *hbs*-overexpression clones, circularity was distinct from that of the wild-type clones (**Figure 3A**). The cells overexpressing *hbs*, however, scattered into many single-cell clones (**Figure 1O** and Supplementary Figure S3), so the circularity of the single-cell clones represented merely the shape of cells, and not that of clones. Moreover, circularity cannot be applied to open clones located at the edges of the images, because the perimeter length and area of those clones cannot be precisely determined (**Figure 2**, uppermost panels and white-colored clone in Circularity panels). Circularity can be applied only for clones with closed circumference and is therefore measurable only for those clones with a relatively small number of cells located in the middle of the tissue, and

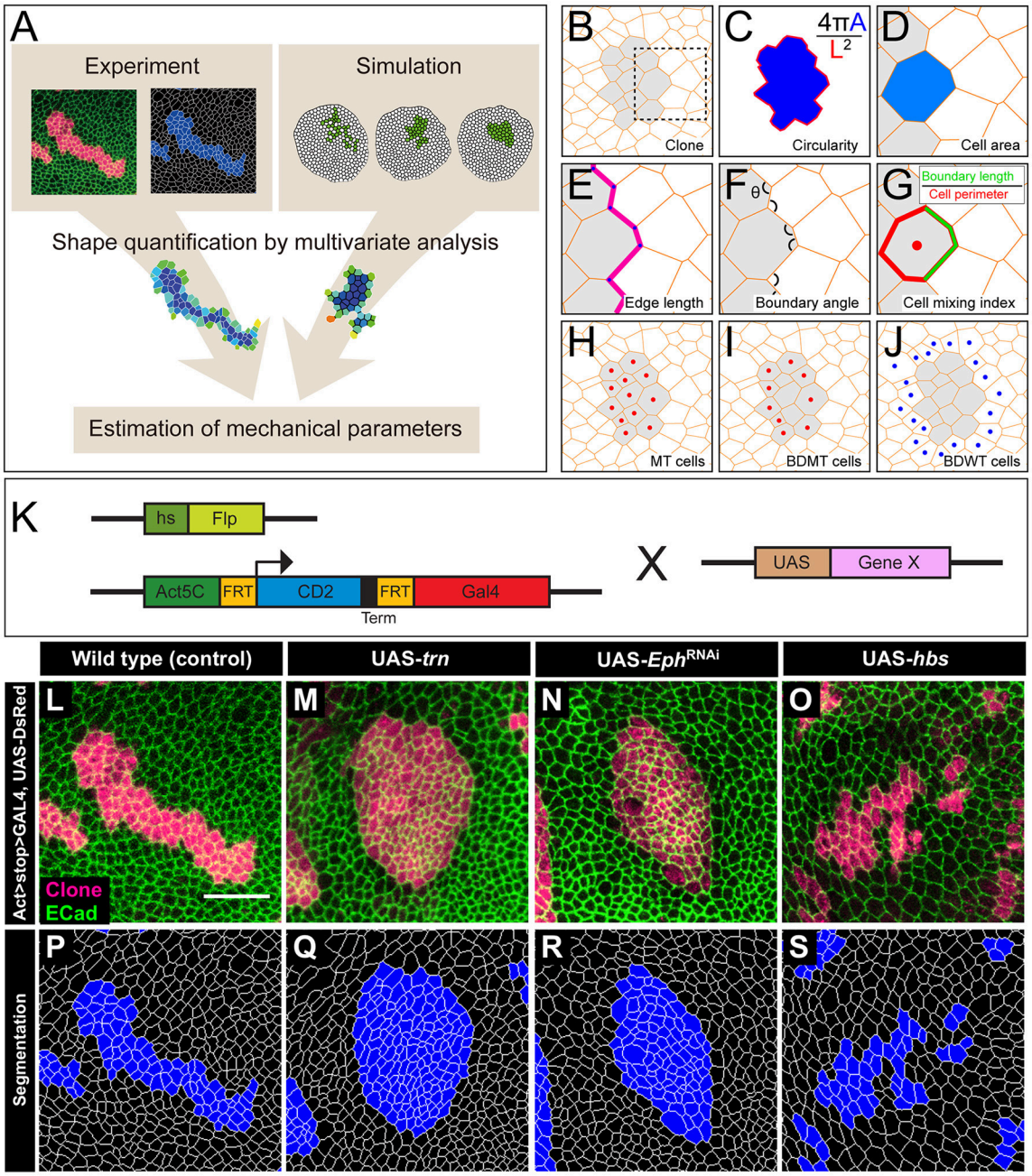

FIGURE 1 | The multivariate estimation pipeline using quantitative evaluation of clone shape. **(A)** Schematic summary of the inference procedure. **(B–J)** Criteria used for the evaluation of clone shape. Circularity **(C)** was measured only for closed clones, while the other six cell-based criteria **(D–J)** were measured for both closed clones and open clones. The cell-based criteria **(D–J)** were calculated for each edge, tri-cellular junction, or cell, and the values were averaged over each clone. **(B)** Scheme for a clone. Orange lines represent adherens junctions, and cells within a clone are shaded. **(C)** Circularity calculated as 4π A/(L^2), where "A" represents the area of the clone, and "L" is the perimeter length of the clonal interface. The circularity of a perfect circle should be 1. **(D–G)** Magnified images of the box in **(B)**. **(D)** Area of a cell within a clone normalized by that of all wild-type cells surrounding the clone in a disc. **(E)** Length of edges (cell junctions between neighboring vertices) at the clone boundary normalized by that of edges between wild-type cells. **(F)** Boundary angle, which is the smaller angle (<180°) between neighboring junctions along the clone boundary at every tri-cellular junction (three-way vertices). **(G)** Cell mixing index, which is the fraction of the perimeter of a cell that is shared with cells from the other side of the clone boundary. **(H–J)** The cells used to calculate the average cell mixing index for MT, BDMT, and BDWT are marked by red dots in (**H**, all cells within the clone) (**I**, clonal cells beside the clone boundary) and blue dots in (**J**, wild-type cells beside the clone boundary), respectively. **(K)** Scheme for genetic manipulation used to generate the clones. GAL4 is expressed only when the CD2 cassette, which includes a transcription termination sequence and is flanked by FRT sites, is excised upon Flippase (Flp) induction by heat shock. Once expressed, GAL4 binds to the UAS sequence and drives expression of the downstream gene. **(L–O)** Clones expressing a marker for wild-type **(L)**, *trn* **(M)**, double-strand RNA against *Eph* **(N)**, and *hbs* **(O)**. **(P–S)** Segmentation of the cell junctions in **(L–O)**.

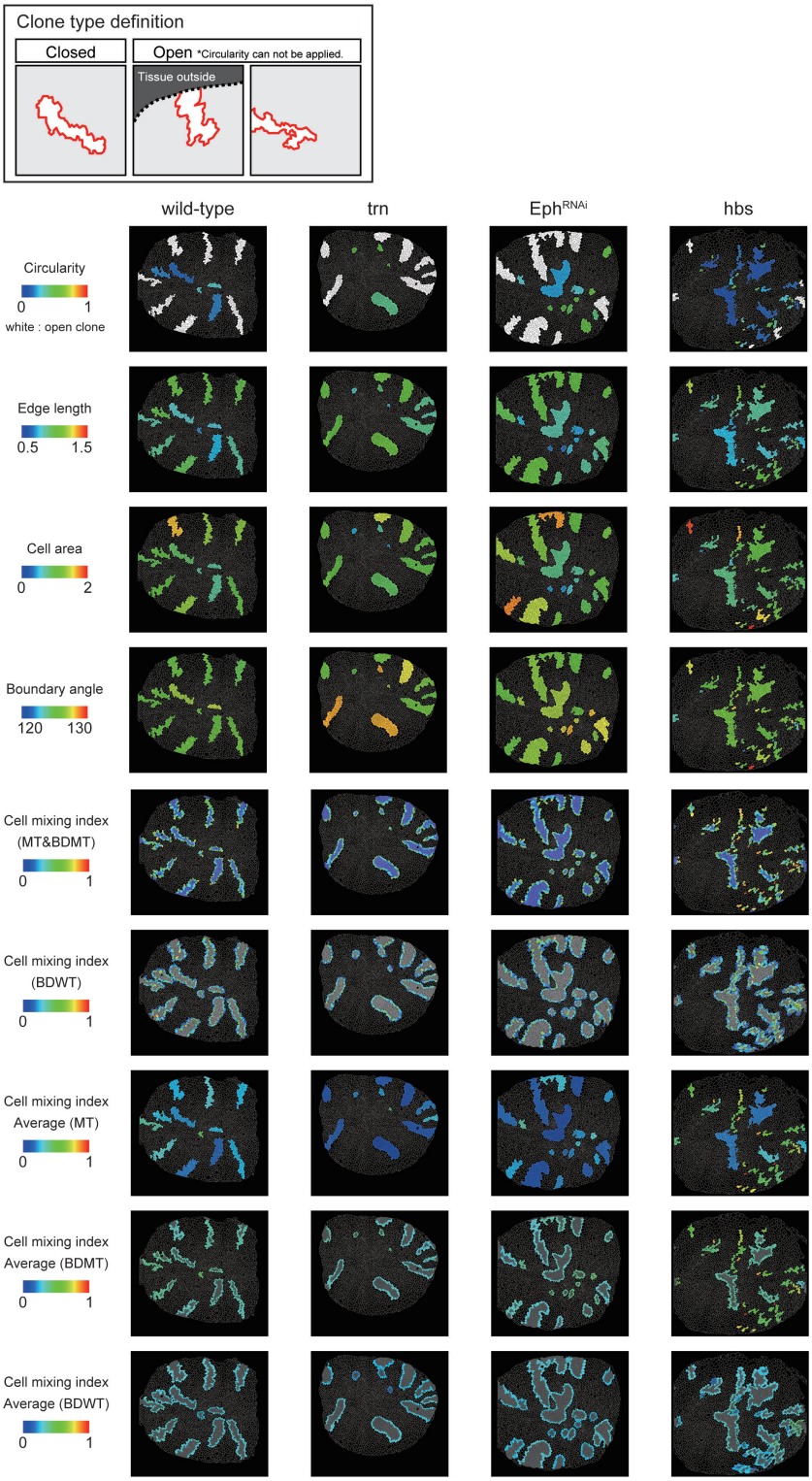

FIGURE 2 | Clone shape quantifications in wing discs. Uppermost panels: Definition of clone type. "Closed" clone is completely enclosed by wild-type cells (left), while "Open" clone contains an invisible portion due to its location at the distal region of the tissue (middle) or image frame (right). Visualization of individual criteria (**Figures 1C–J**) for the examined clones of four genotypes (**Figures 1L–O**). For open clones, circularity was not measurable, so they were filled by a white color.

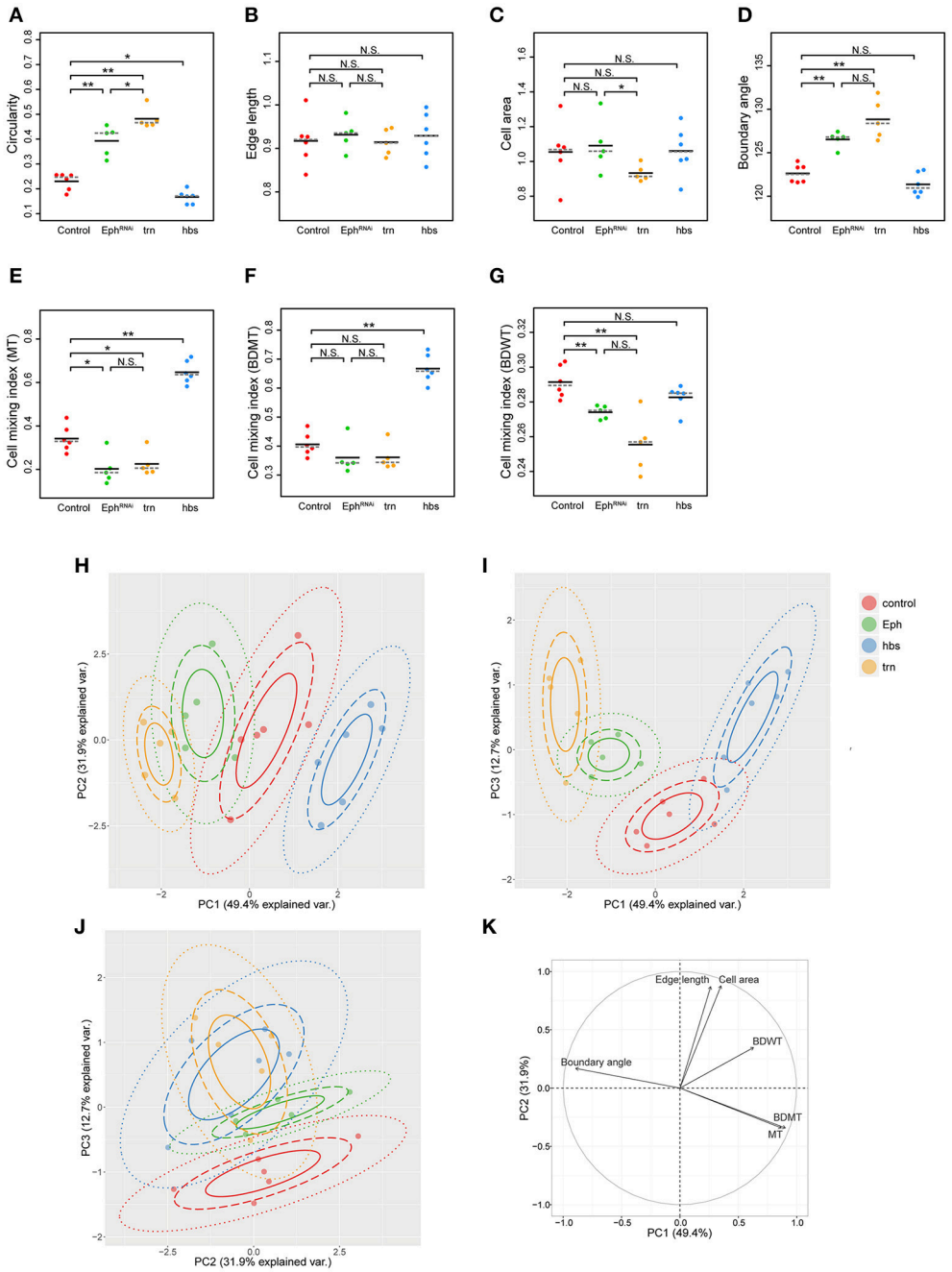

FIGURE 3 | Principal component analysis of clone shape indicators for four genotypes. **(A–G)** Plots for circularity **(A)**, edge length **(B)**, cell area **(C)**, boundary angle **(D)** and cell mixing index of MT cells **(E)**, BDMT cells **(F)**, and BDWT cells **(G)** of clones of four genotypes including wild-type (red), *Eph* RNAi (green), *trn* overexpression (yellow), and *hbs* overexpression (blue). The plotted data were obtained from clones with averaging within a disc. Black solid lines and gray broken lines represent the average and median values, respectively. Wilcoxon rank sum test, $n = 6$ for control and *hbs* overexpression; $n = 5$ for *Eph* RNAi and *trn* overexpression. $^{**}P < 0.01$, $^{*}P < 0.05$ and $P > 0.05$ (N.S., Not Significant). **(H–J)** Results of principal component analysis using six criteria (edge length, cell area, boundary angle, and cell mixing index of MT cells, BDMT cells, and BDWT cells) are plotted for PC1 vs. PC2 **(H)**, PC1 vs. PC3 **(I)**, and PC2 vs. PC3 **(J)**. **(K)** Quantified contribution (factor loadings; Section Principal Component Analysis (PCA) for definition) of each criterion on PC1 and PC2. The arrow length represents the sum of the squared correlation coefficient of PC1 and PC2, noting that the sum of all PCs is equal to 1.

the entire clone should lie within the image frame (**Figure 2**, uppermost panels). In the *Drosophila* wing discs, which are frequently used for mosaic clone analysis, approximately half of the clones were open clones (46.4% for wild-type clones). Therefore, a cell-based analysis to quantify the clone shape was needed.

In order to quantify clone shape at the single-cell level, we precisely traced (segmented) the individual cell shapes and labeled the cells using Tissue Analyzer (Aigouy et al., 2016; Section Clone Shape Quantification; **Figures 1P–S**), which has a sufficiently low error rate of image segmentation (Supplementary Figure S4). For the segmented images, we measured the cell mixing index, which has been used to quantitatively evaluate how much a single cell shares junctions with a neighboring population (Umetsu et al., 2014a; Levayer et al., 2015) (**Figures 1G–J**, **2**; and Supplementary Figure S1; MT, BDMT, and BDWT). Remarkably, the MT and BDMT of the *hbs*-overexpression clones were significantly higher than those of the wild-type clones (**Figures 3E,F**). In order to test whether the cell mixing index is sensitive enough to distinguish clone shapes with different smoothness, we compared *Eph*-RNAi clones (**Figures 1N,R**) with *trn*-overexpression clones (**Figures 1M,Q**); however, none of the indices (MT, BDMT, and BDWT) was able to distinguish between the *Eph*-RNAi clones and the *trn*-overexpression clones (**Figures 3E–G**). The boundary angle (**Figure 1F**) was also unable to separate the *Eph*-RNAi and *trn*-overexpression clones, although it could distinguish the *Eph*-RNAi or *trn*-overexpression clones from the wild-type clones (**Figures 2**, **3D**). The edge length (**Figure 1E**) was not able to distinguish between any pair of genotypes (**Figures 2**, **3B**). The cell area (**Figure 1D**) could uniquely distinguish the *Eph*-RNAi clones from the *trn*-overexpression clones but not from the wild-type clones (**Figure 3C**). In summary, there was no single cell-based criterion that could separate the four genotypes. The combinatory use of multiple criteria may provide a better resolution to distinguish the clone shapes of the genotypes, which could ultimately infer mechanical parameters of each genotype (**Figure 1A**).

PCA Separated Sources of Phenotypic Heterogeneity

The combinatorial use of multivariate (6-dimensional) dataset increases information of data sets required for the complete separation, while the multi-dimensional information is too complex for us to intuitively extract some important criteria for the efficient separation. Therefore, multi-dimensional analysis generally has a trade-off between the merits and demerits. The principal component analysis (PCA) can optimize the trade-off: It can provide criteria to maximize the variance of the data and compresses multi-dimensional information into lower dimensions while retaining most of the original information. PCA has been extensively developed in the field of morphometrics of individual cells (Lacayo et al., 2007; Pincus and Theriot, 2007), organs (Iwata, 2002; Klingenberg, 2011), and individual bodies (Zelditch et al., 2012), but not of clones in multicellular tissue. We applied PCA to the data set of the six criteria for the four genotypes ($n = 84$ clones from six discs for wild-type, $n = 61$ clones from five discs for *Eph* RNAi, $n = 53$ clones from five discs for *trn* overexpression, $n = 215$ clones from six discs for *hbs* overexpression; **Figures 3H–K** and Supplementary Figures S5, S6). We averaged over the set of clones in each wing disc before applying PCA to analyze genetic variation separately from non-genetic variation. We found that more than 80% of the information was compressed into only two principal components (PC1 = 49.4%, PC2 = 31.9%, PC3 = 12.7%; **Figures 3H–J**). Each genotype was separated mainly in PC1 without overlap (**Figure 3H**), while the *Eph*-RNAi and *trn*-overexpression clones were also efficiently separated in PC2 and PC3 (**Figures 3H–J**). The major criteria with higher factor loading on PC1 [>0.85; See Section Principal Component Analysis (PCA) for the definition of factor loading] were MT, BDMT, and boundary angle, while some other criteria such as, cell area and edge length showed a high contribution on PC2, and BDWT contributed relatively on PC1 and PC3 (**Figure 3K** and Supplementary Figure S5). Both the separation of genotypes mainly in PC1 and the contribution of each criterion on PC1–PC2 were nearly the same "with averaging" or "without averaging" within the discs (**Figures 3H–K** and Supplementary Figure S6).

Note that PCA without averaging within the discs showed that the variation within a genotype was mainly distributed in PC2, while each genotype was separated in parallel with PC1 (Supplementary Figure S6A). Since the variation occurred in an identical combination of clone (e.g., *Eph* RNAi) and non-clone genotypes (wild-type), hereafter we call it "non-genetic" heterogeneity (Supplementary Figures S1, S7A, middle panels). Interestingly, PC2 had a positive correlation with the distance from the center of the disc (Supplementary Figure S7B), indicating that the non-genetic heterogeneity in PC2 encoded the positional information of each clone. That might be caused by spatial gradients of the expression of several genes in the *Drosophila* wing pouch (e.g., *spalt*, *optomotor-blind*, *Distalless*, and *vestigial*; Milán et al., 2002; Affolter and Basler, 2007; Swarup and Verheyen, 2012). Therefore, genetic as well as non-genetic heterogeneities were efficiently segregated in lower dimensions in the PC space, allowing us to estimate the mechanical basis of the genetic heterogeneity using PCA.

Vertex Model Simulations with Differential Line Tension

We analyzed how the mechanical cell–cell interactions contribute to the characteristic clone shapes (**Figures 1L–S**) by comparing *Drosophila* experiments to computer simulations (**Figure 1A**). We utilized the cell vertex model, which quantitatively accounts for the packing geometry of epithelial cells [Section Cell Vertex Model, Equation (1)]. Clone shape has been shown to be modulated mainly by the combination of line tension parameters at three types of edges: γ [default tension in Equation (1)], γ_b (clone boundary tension), and γ_c (inner clonal tension; **Figure 4A**, right bottom panel for the classification of edges) (Graner, 1993; Graner and Sawada, 1993; Brodland, 2002). Therefore, as a pilot study for the multivariate inference of mechanical parameters for each genotype, we presupposed that γ_b and γ_c relative to γ are the main causes of clone formation, although other parameters such as, the rate of cell proliferation might potentially influence the clone boundary shape (see Supplementary Figure S3 for detailed data on the numbers

of cells and clones). We numerically explored the role of the different combinations of line tension parameters γ_b and γ_c in the formation of clones. As the tension parameter for clone boundary γ_b increased relative to the control tension parameter γ, cells were sorted out so that the clone boundary became smoothly rounded (Box1 in **Figure 4C**), as seen previously (Landsberg et al., 2009; Monier et al., 2010; Aliee et al., 2012; Rudolf et al., 2015; Bosveld et al., 2016a). We observed a similar tendency to generate smooth clones by decreasing the inner clonal tension parameter γ_c relative to γ, which is equivalent to increasing adhesion between the inner clonal cells (Box2 in **Figure 4C**). Conversely, cell mixing occurred to form convoluted clones as

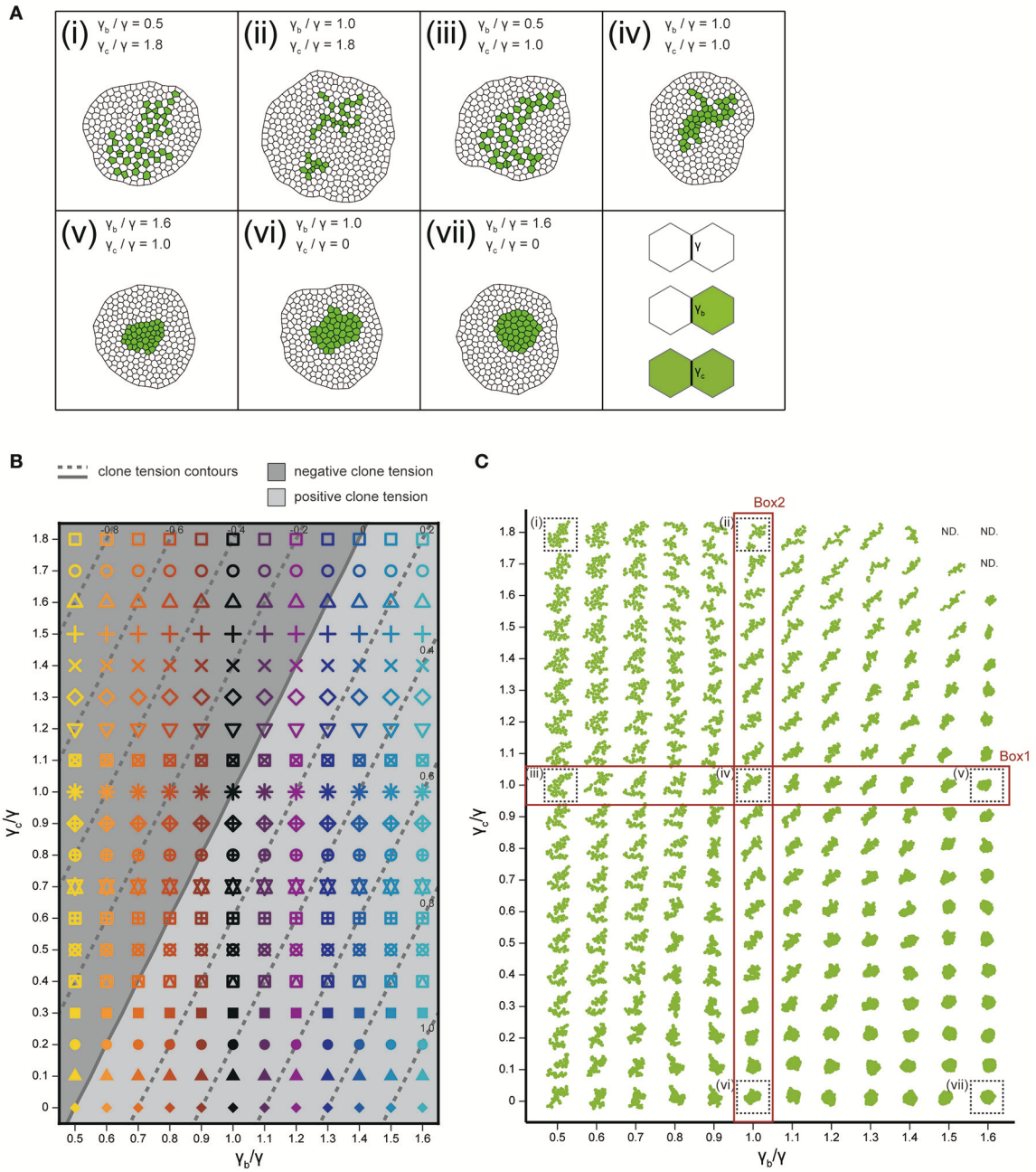

FIGURE 4 | Cell vertex model simulations. **(A)** Right bottom: The classification of line tension parameters: γ [default tension at edges between non-clonal cells (white)], γ_b (clone boundary tension at edges on the clone boundary), and γ_c [inner clonal tension at edges between clonal cells (green)]. **(i–vii)** Snapshots of simulated clones when the total number of green cells is 40. **(B)** Parameter space of normalized line tension (γ_b/γ and γ_c/γ) with contour lines of clone tension σ (See Section Clone Tension for definition). Each symbol denotes different combinations of parameters (γ_b/γ, γ_c/γ). **(C)** Representative form of the clones for all simulation parameters in **(B)**, noting that the model did not work at the three parameter points indicated by "ND." Clones enclosed within black dashed boxes are the same as those in **(i–vii)**.

γ_b decreased or γ_c increased relative to γ (**Figure 4C**). Those results indicate the differences between the default tension (γ) and the one at the clone boundary and inside the clone (γ_b and γ_c) reflect cell sorting and cell mixing. As a measure to distinguish between cell sorting and mixing, we examined the dimensionless clone tension, which is represented by γ, γ_b, and γ_c (σ in Section Clone Tension) (Bosveld et al., 2016a). We confirmed that negative and positive values of the clone tension (**Figure 4B**, gray and light-gray, respectively) mainly distinguished convoluted and rounded clone morphologies, respectively (**Figure 4C**).

Inference of Tension Parameters by Comparison between Experiments and Simulations in the PC Space

We quantitatively compared the clone shapes generated by vertex model simulations using the control parameters ($\gamma = \gamma_b = \gamma_c$, **Figure 4Aiv**) to those of *Drosophila* wild-type clones by projecting the simulated clones onto the PC1 and PC2 space of the experimental data (**Figure 3H**). The simulated control clones (**Figure 5A**, black octagonal asterisk at PC1 $\sim$ 1.07, PC2 $\sim$ 0.56) were consistently similar to the wild-type clones in the PC space (**Figure 5A**, red confidence ellipse). We inferred the wild-type tension parameters from the simulations plotted inside the 68% confidence ellipse of the wild-type clones (Section Estimation of the Mechanical Parameters of the Genetic Experiments in the PCA Space). The estimated parameters of the wild-type clones were distributed around the control parameters of the simulation (**Figure 5B**, red), where the clone tension was nearly zero (**Figure 5B**, solid line, and **Figure 5C**, red), indicating that the vertex model could closely coordinate with the PCA of static tissue images to non-invasively estimate the mechanical parameters of the wild-type clone based only on the clone morphology.

Likewise, when we simultaneously projected simulation data from a wide range of tension parameter sets (all marks in **Figure 4B**) onto the PC space, we found that the two-dimensionality of the parameter space of the line tension (γ_c/γ and γ_b/γ; **Figure 4B**) was maintained in the PC1-PC2 space (**Figure 5A**), indicating a quantitative link between the tension parameters at the cell–cell interface and the clone boundary geometry of heterogeneous populations. Therefore, following the methods applied to the wild-type clone, we estimated the mechanical parameters of the other three genotypes (*Eph* RNAi, *trn* overexpression, and *hbs* overexpression). We found that the estimated regions of the mechanical parameters for each genotype (plotted inside the 68% confidence ellipses in **Figure 5A**) were distributed in parallel to the contour lines of the clone tension (**Figure 5B**). For the *Eph*-RNAi and *trn*-overexpression clones, which had a rounded morphology (**Figures 1M,N**), the tension of both clones was higher than that of the wild-type clone (**Figure 5C**). The *hbs*-overexpression clones had a negative value for clone tension (**Figure 5C**), which was consistent with their convoluted morphology (**Figure 1O**). The ascending order of clone tension (*hbs* overexpression < wild-type < *Eph* RNAi < *trn* overexpression; **Figure 5C**) perfectly agreed with that of PC1 (**Figure 3H**), indicating that the value of PC1 reflects the difference in clone tension. To more directly relate the clone tension to the PCA, we projected the PC scores onto the parameter space of the vertex model simulations (**Figure 5D**). The contour of the PC1 scores was almost parallel to that of the clone tension (**Figure 5D**, red solid line), whereas that of the PC2 scores was rather perpendicular to that of the clone tension (**Figure 5D**, dark gray solid line), indicating that the clone tension was the mechanical basis of PC1.

To better estimate the tension parameters γ_b and γ_c, we defined the simulation plots closest to the centers of the confidence ellipses (**Figure 5A**) as the best representative combinations of line tension parameters for each genotype (pentagonal asterisks in **Figures 5B**, **6**). We confirmed that the representative parameters γ_b and γ_c in simulations quantitatively reproduced experiments of each genotype according to all clone shape criteria used in PCA (Supplementary Figures S8A, S9A, left most panels). The representative parameters indicated that the cause of the higher clone tension was different between the *Eph*-RNAi clones and the *trn*-overexpression clones. The difference was mainly caused by dominantly reduced γ_c relative to γ for the *Eph*-RNAi genotype and both reduced γ_c and increased γ_b relative to γ for the *trn*-overexpression genotype (**Figure 5B**). The lower clone tension of the *hbs*-overexpression clones was caused by dominantly increased γ_c relative to γ (pentagonal asterisk in **Figure 5B**).

At a constant clone tension for each genotype estimated by PC1, PC2 is sensitive to the combination of γ_b and γ_c (e.g., $-4 \leqq$ PC2 $\leqq 2$ at clone tension $= -0.2$ in **Figure 5D**), so that the dominant change of γ_b or γ_c relative to γ was determined according to PC2 value of each genotype. The underlying mechanics how PC2 distinguished the dominance can be understood from the mechanical equilibrium of vertex model; edge length at clone boundary and cell area inside clones, which had higher contribution to PC2 (**Figure 3K**), become smaller as line tension strength γ_b and γ_c at constant clone tension increase in simulations (Supplementary Figure S10). Thus, the mutual projection of the mechanical parameter space and the PC space could efficiently and quantitatively estimate the distinct mechanics of the various clone morphologies.

DISCUSSION

Multivariate Analysis of Clone Shapes

We first developed a PCA of clone shapes in heterogeneous cell populations, which efficiently segregated clones of each genotype in the PC space. No single cell-based criterion of clone shape was able to perfectly segregate all four genotypes (**Figure 3**). In addition, because most of the conventional ways to quantify clone shape used in previous studies can only apply to closed clones (e.g., circularity, **Figure 1C**), much information regarding open clones (e.g., white clones in **Figure 2**) was previously lost during the quantification process. Open clones are frequently observed, however, in tissue specimens. The cell-based criteria that we used (**Figures 1D–J**) can apply to not only closed clones but also open clones, so we can use them widely and independently on the clone shapes and its location in the tissue. Furthermore, the average

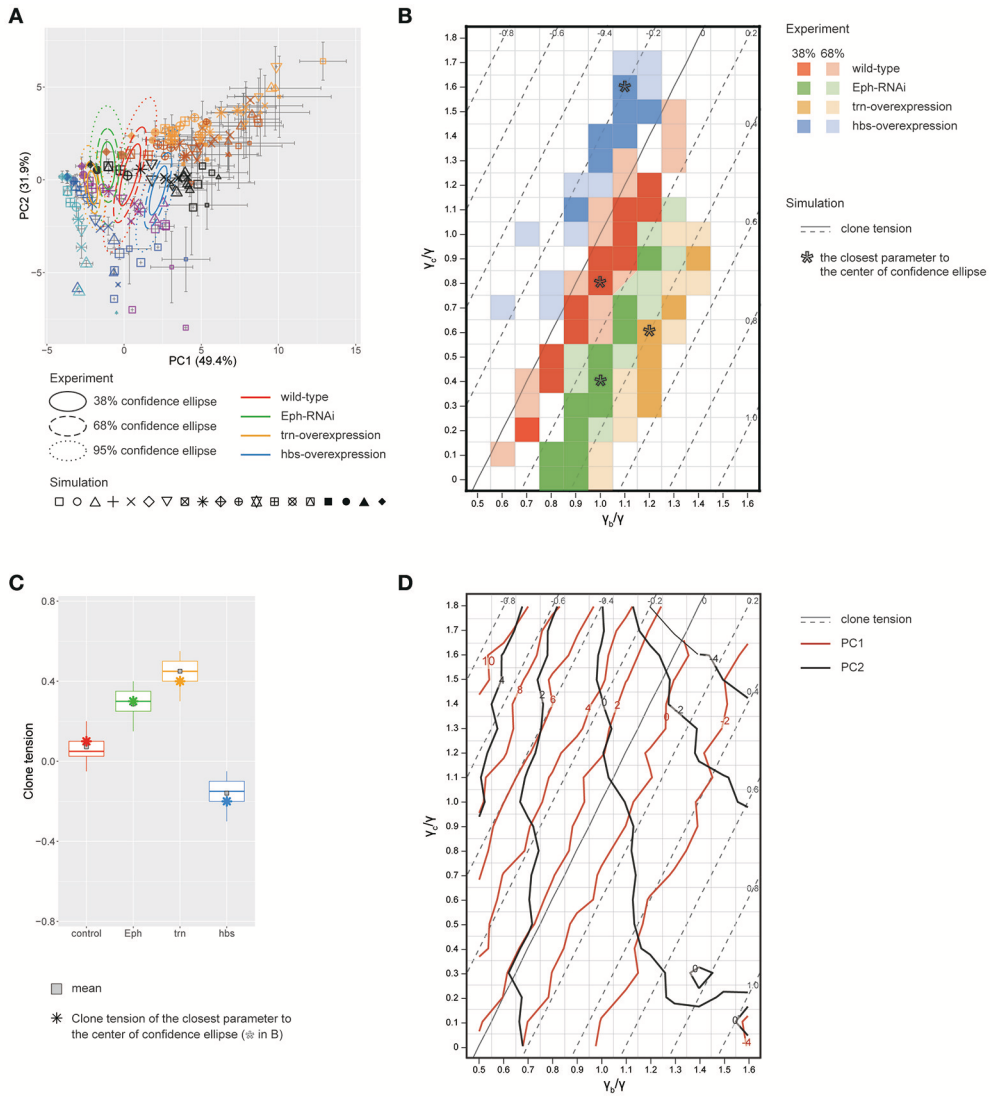

FIGURE 5 | Inference of tension parameter and clone tension of four genotypes. **(A)** Projection of simulated clones onto the PC space of *Drosophila* experiments (See Section Projection of the Simulation Data onto the PCA Space of the Experimental Data for Projection; Symbols denote parameter values given in **Figure 4B**). A limited set of simulation points are plotted for visibility (see Supplementary Figure S12 for the projection of the entire simulated dataset). The experimental confidence ellipses were identical to those in **Figure 3H**. The averaged PC scores were plotted with symbol size proportional to the number of cells within a clone and error bar representing standard deviation. **(B)** Estimated mechanical parameters of four genotypes. Mechanical parameters within the 38 and 68% confidence ellipses in **(A)** are shown by dark and light colors, respectively. Pentagon asterisks (*) mark the best representative parameters, which are the closest to the center of each confidence ellipse. **(C)** Estimated clone tension of four genotypes calculated by the estimated mechanical parameters within the 68% confidence ellipse [dark and light colors in **(B)**]. The upper/lower hinge and thick middle line represent the 25th/75th and 50th percentiles, respectively. Gray squares show the averaged clone tension. Octagonal asterisks are the clone tension of the best representative parameters [pentagonal asterisks in **(B)**]. **(D)** Projection of the contour lines of PC1 and PC2 scores onto the parameter space of vertex model simulations.

pixel size for each cell junction was only 8.4 (Supplementary Figure S11), suggesting the relatively low resolution imaging data is sufficient to distinguish clones of different genotypes with a minimal manual correction (1.12%, Section Clone Shape Quantification and Supplementary Figure S4). Therefore, our cell-based quantification provides a robust method for the clone shape quantification.

Both genetic and non-genetic heterogeneities influence tumorigenesis (Cortina et al., 2007; Porazinski et al., 2016), cell competition, and other events. Elimination of loser cells at the clone boundary during cell competition has been shown to be driven by genetic heterogeneity (Vincent et al., 2013; Amoyel and Bach, 2014; Morata and Ballesteros-Arias, 2015), while not all of loser cells are eliminated indicating the non-genetic heterogeneity due to local cell–cell contacts and gene expression levels in tissues might affect the elimination [e.g., Figure 1 in Levayer et al. (2015); (Froldi et al., 2010; Chen et al., 2012; Kajita et al., 2014)]. The PCA applied to individual clones efficiently

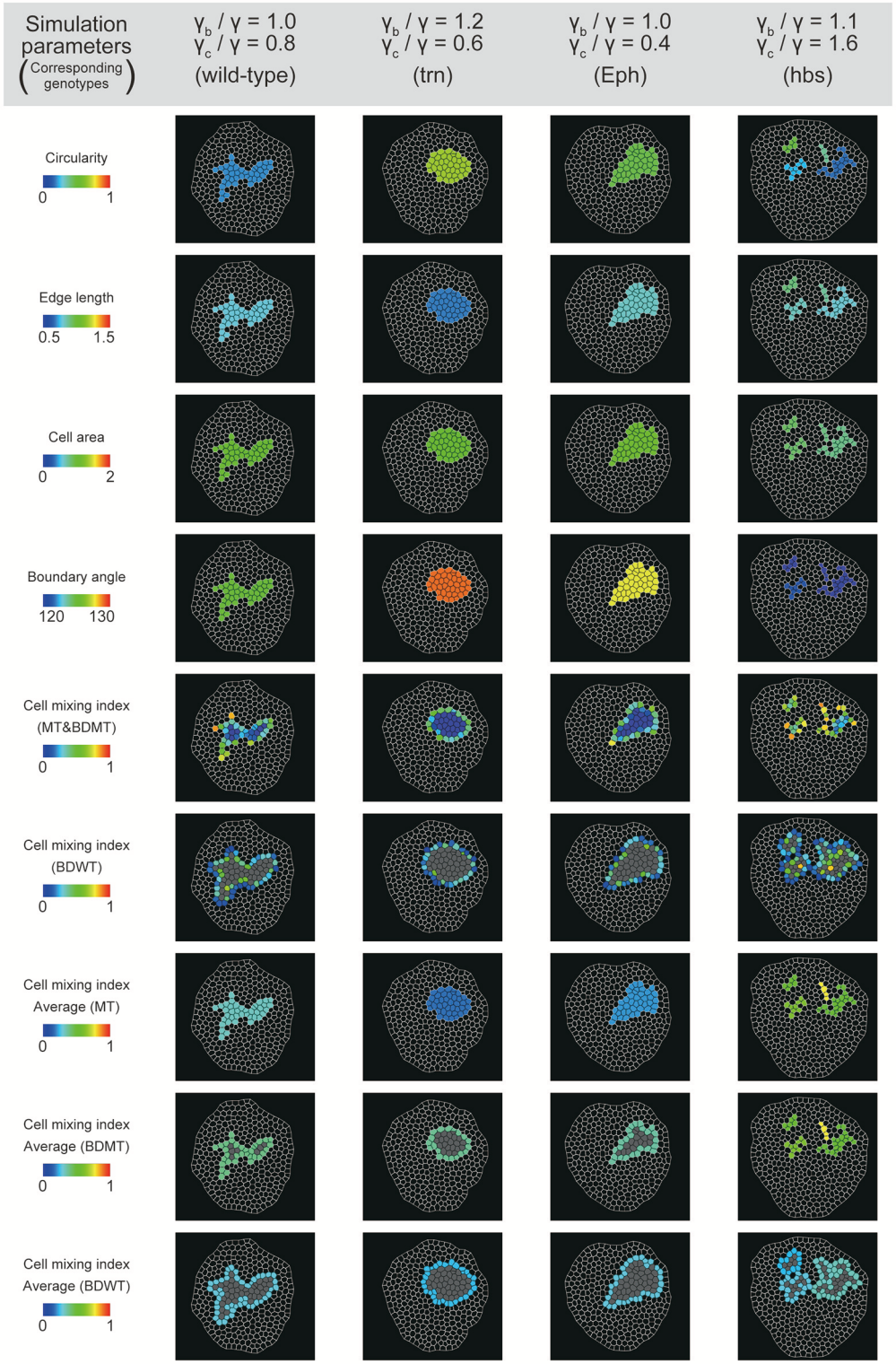

FIGURE 6 | Simulation clones corresponding to the experimental clones. Visualization of individual criteria for the four simulated clones, which correspond to the best representative combination of line tension parameters for the four genotypes (pentagon asterisks in **Figure 5B**).

separated the genetic heterogeneity mainly in PC1, while the non-genetic heterogeneity was distributed in PC2 (Supplementary Figures S6, S7), indicating that PC1 and PC2 encode genetic and non-genetic heterogeneities, respectively. That in turn indicates that the criteria with high contributions on PC1 (BDMT, MT, and boundary angle; Supplementary Figure S6D) and PC2 (BDWT, cell area, and edge length; Supplementary Figure S6D) optimally indicate the genetic and non-genetic heterogeneity, respectively, for the four genotypes in our study. The determination of whether those criteria commonly distinguish between genetic and non-genetic heterogeneity in other genotypes in the future will give clues as to how to separately evaluate genetic and non-genetic contributions to physiological functions of heterogeneous tissue.

Non-invasive Estimation of Cell Mechanics

We non-invasively estimated the mechanical parameters (i.e., clone tension and line tensions) of each genotype by integrating in a PC space the results of vertex model simulations and the quantified clone shapes in static images of cells (**Figure 5A** and Supplementary Figure S12). As a case study for rounded clones, we revealed that *trn*-overexpression clones have greater clone tension than *Eph*-RNAi clones (**Figure 5C**). Despite the patterned expression and the known, spatially graded function of *trn* in the wing pouch (Milán et al., 2002), our method successfully captured the characteristic features of *trn* overexpression, which are significantly distinct from those of *Eph* knockdown (**Figures 3H–K**). That suggests that our method can be applied to the coarse classification of clones with distinct genotypes even in the presence of non-genetic variation derived from a spatial gradient.

We also confirmed that the clone tension of the wild-type was nearly zero (**Figure 5C**). In addition, the range of clone tension for the other genotypes was also close to that measured previously ($0 < \sigma < 0.6$) (Bosveld et al., 2016a), despite the fact that we used different genotypes (**Figure 5C**). In addition, difference of the estimated clone tension (asterisk of **Figure 5C**) among genotypes was larger than the variation within each genotype (box height of each plot in **Figure 5C**), which was also confirmed by the estimation precision of clone tension [± 0.15 (wild-type), under ± 0.1 (*Eph*), ± 0.1 (*hbs*), ± 0.2 (*trn*) calculated from estimation precision of γ_b and γ_c in Supplementary Figures S8, S9 using Equation (2)]. The results indicate that our estimated values were roughly correct and that our method works well to estimate the mechanics. Moreover, we first showed *in vivo* that negative clone tension causes a convoluted morphology by inducing *hbs*-overexpression clones (**Figure 5C**).

Our study revealed the cell mechanics, relative contributions of γ_b or γ_c to the increase or decrease in clone tension. By examining the underlying cell mechanics, we found that the relative contributions of the line tension parameters γ_b and γ_c were different among genotypes, even when the sign of the clone tension was the same. Estimation precision of γ_b/γ for each genotype was evaluated by a limit to how much shift of γ_b/γ from the best representative (pentagonal asterisks in **Figure 5B**) simulation could reproduce experimental data; It was at most ± 0.2 [under ± 0.1 (*Eph, hbs*), ± 0.1 (wild-type), and ± 0.2 (*trn*)] (Supplementary Figure S8), whereas estimation precision of γ_c/γ was at most ± 0.3 [± 0.1 (*Eph*), ± 0.2 (*hbs, trn*), and ± 0.3 (wild-type)] (Supplementary Figure S9). The estimated parameter variation of γ_b/γ and γ_c/γ for each genotype (68% confidence, dark and light colors in **Figure 5B**) was consistently smaller than difference of the best representative parameters between genotypes (pentagonal asterisks in **Figure 5B**). The *Eph*-RNAi clone had decreased bulk line tension, whereas the *trn*-overexpression clone had both increased boundary tension γ_b and decreased γ_c (pentagonal asterisks in **Figure 5B**), resulting in positive clone tension. The *hbs*-overexpression clone, which showed cell mixing due to negative clone tension, mainly had increased γ_c (pentagonal asterisk in **Figure 5B**). Cell mixing caused by increased γ_c was reported previously in *myc*-induced cell competition (Levayer et al., 2015). Our inference on the dominance of γ_b or γ_c for each genotype should be verified by estimation of the mechanical tension by physical perturbation in the future (e.g., laser cutting of the three types of edges in **Figure 4A**, right bottom panel).

Molecular Mechanisms of Cell Sorting and Mixing Mechanics

The present estimation provides mechanical insights of the previously reported molecular functions in cell sorting (**Figure 5B**): *Drosophila trn* and its paralog *capricious* (*caps*) encode leucine rich repeat containing transmembrane proteins that have a function in controlling cell affinity and the regulation of cell communication for cell survival (Milán et al., 2001, 2002; Sakurai et al., 2007). The mammalian homolog, Lrrn1 is required for the formation of the midbrain-hindbrain boundary by regulating cell affinity (Tossell et al., 2011). Eph kinases comprise a large protein family of receptor protein tyrosine kinases. Eph receptors are activated by binding to ephrins, their membrane-anchored ligands, to transduce signals that play diverse roles in axon guidance, neural crest-cell migration, and boundary formation of rhombomeres through their function in repulsive cell–cell interactions (Sela-Donenfeld and Wilkinson, 2005; Fagotto et al., 2014). In addition, mammalian EphB signaling plays a tumor-suppressive role by compartmentalizing cancer cells, potentially through cell-repulsive activity by means of actin cytoskeleton reorganization (Cortina et al., 2007). Our result showing decreased line tension at homotypic cell junctions (γ_c) within the *Eph*-RNAi clones (**Figure 5B**) is consistent with the previously proposed repulsive functions of Eph receptors. Therefore, our method was consistent with the previously reported cell functions. Given the common and uncommon biological functions between *trn* and *Eph*, it would be interesting to investigate how the difference in cell mechanics between the *trn*-overexpression clone and *Eph*-RNAi clone contributes to biological functions of those genes.

Our analysis showed that the overexpression of *hbs* alone can result in negative clone tension (**Figure 5C**), which leads to convoluted clonal morphology and cell scattering. The main contribution to the negative clone tension was the increase of γ_c (**Figure 5B**), which would be a reflection of either an increase in cortical contractility or a decrease

in adhesion at homotypic cell junctions within the clone [Equation (2)]. That suggests that the scattered morphology of the *hbs*-overexpression clones was derived from increased cell bond tension at the *hbs*–*hbs* cell interface, which is independent of the interaction between heterotypic cell junctions at the wild-type–*hbs* interface. The mechanical basis of *hbs* function has been poorly understood, except for its heterophilic interaction with the other nephrin family proteins Roughest and Kirre. Our result therefore provides a new mechanical insight into the cell mixing mechanisms mediated by those proteins.

Future Problems

In addition to line tension parameters, the clone boundary shape could be affected by inter-clonal differences in other parameters such as, the cell proliferation rate, apoptosis rate, and cell division orientation, which we will incorporate into the vertex model in the future. For example, the proliferation rate appeared to be increased more often in *Eph*-RNAi cells than in wild-type cells (Supplementary Figure S3B). Differential proliferation rates induced by such mutants are known to cause not only clone boundary smoothing [e.g., Ras^{V12}-expressing (constitutively active form) cells (Prober and Edgar, 2000) and tkv^{Q253D}-expressing (activated form of Dpp receptor) cells (Nellen et al., 1996)] but also the mechanical elongation of slower-dividing cells at the clone boundary and the compaction of faster-dividing cells [e.g., *Hippo* mutant clones in wild-type tissue (LeGoff et al., 2013; Mao et al., 2013; Pan et al., 2016)], so that cell shape anisotropy, which is a new criterion for cell elongation (LeGoff et al., 2013; Mao et al., 2013), as well as BDWT, clonal cell area, and other parameters might be reliable criteria for differential proliferation. The regulation of cell division orientation depends on the pathway of planar cell polarity, morphogen gradient, and mechanical cell stretching (Gillies and Cabernard, 2011; di Pietro et al., 2016; Stooke-Vaughan et al., 2017). Specifically, misoriented or directionally oriented cell division inside or at the periphery of the clone results in a rounded or convoluted shape of the clone boundary (Li et al., 2009; Mao et al., 2011; Kale et al., 2016). Taken together, the incorporation of additional criteria is required (e.g., cell shape anisotropy) in order to precisely infer the most responsive parameters of genotypes.

According to the increasing dimensions of the parameter space, parameter estimation should be performed in the higher dimensions of the PC space. While we used the PC1-PC2 space containing 80% of the information for the current estimation (**Figure 5A**), PC3 contained about 10% of the information, which segregated *Eph*-RNAi clones from *trn*-overexpression clones (**Figures 3I,J**). Additionally, we could narrow down the estimated parameter region by combining our current analysis with other analyses, such as, a distribution of several criteria as in the parameter estimation of homogeneous epithelial tissue (Farhadifar et al., 2007; Aegerter-Wilmsen et al., 2010). For example, *hbs*-overexpression clones showed an anomalous distribution of cell numbers within clones due to an increasing fraction of clones with smaller numbers of cells (Supplementary Figures S3A,C), while wild-type clones show coherent morphologies (**Figure 1L**) due to the remarkable lack of cell rearrangement in imaginal discs (Gibson et al., 2006). That indicates that the combinatorial use of the clone size distribution (Supplementary Figure S13B) with PCA could estimate the parameters for *hbs*-overexpression clones in a narrower range (Supplementary Figure S13A, parameters covered by both blue and gray oblique lines). Future studies should also clarify the limits and applicability of the multivariate inference of cell mechanics by exploring more complex systems as well as a wider variety of genotypes.

The pipeline based on cell shape quantification developed in this study may be extended to an image-based cancer diagnosis. High-throughput microscopy image-based cancer prognosis has been developed and is expected to provide useful prognostic information for precision medicine (Yu et al., 2016). In addition to the potential contribution to such a classification of the cancer subtype or grade, our method has a potential to provide the mechanistic understanding of tumor development. Elucidation of mechanistic ground of tumor morphology may help cancer treatment planning. Moreover, manipulation of the clone tension at the interface between normal cells and cancer cells (γ_b) as well as of that between cancer cells (γ_c) can be an alternative clinical approach to suppress cancer progression either by limiting tumor invasion or by promoting cell competition.

AUTHOR CONTRIBUTIONS

Conceived and designed the experiments: AT, DU, EK, and KF. Performed genetic experiments: DU. Performed statistical analysis and computer simulations: AT. Analyzed the data: AT, DU, and KF. Wrote the paper: AT, DU, and KF.

FUNDING

AT is a JSPS Research Fellow (15J01837). This work was supported by Grants-in-Aid for Scientific Research from MEXT to DU (15K18536, 17K07402, 17H02939), EK (JP26114003, JP16H04800, 17K19884), and KF (15H01490, 17H05619).

ACKNOWLEDGMENTS

We thank K. Matsushita and K. Hironaka for discussions; Dr. S. Hayashi, Dr. Y. Hong, Dr. H. Sink, and the Bloomington *Drosophila* Stock Center for fly stocks; N. Iijima, T. Iwatsuki, and S. Hoshika for the hand-correction of the segmentation of experimental images; S. Fujita, H. Furukawa, R. Hara, K. Ikeguchi, and Y. Tanaka for participating the segmentation error estimation test.

SUPPLEMENTARY MATERIAL

The Supplementary Material for this article can be found online at: http://journal.frontiersin.org/article/10.3389/fcell.2017.00068/full#supplementary-material

REFERENCES

Aegerter-Wilmsen, T., Smith, A. C., Christen, A. J., Aegerter, C. M., Hafen, E., and Basler, K. (2010). Exploring the effects of mechanical feedback on epithelial topology. *Development* 137, 499–506. doi: 10.1242/dev.041731

Affolter, M., and Basler, K. (2007). The Decapentaplegic morphogen gradient: from pattern formation to growth regulation. *Nat. Rev. Genet.* 8, 663–674. doi: 10.1038/nrg2166

Aigouy, B., Umetsu, D., and Eaton, S. (2016). Segmentation and quantitative analysis of epithelial tissues. *Methods Mol. Biol.* 1478, 227–239. doi: 10.1007/978-1-4939-6371-3_13

Aliee, M., Röper, J.-C., Landsberg, K. P., Pentzold, C., Widmann, T. J., Jülicher, F., et al. (2012). Physical Mechanisms shaping the *Drosophila* dorsoventral compartment boundary. *Curr. Biol.* 22, 967–976. doi: 10.1016/j.cub.2012.03.070

Amoyel, M., and Bach, E. A. (2014). Cell competition: how to eliminate your neighbours. *Development* 141, 988–1000. doi: 10.1242/dev.079129

Bao, S., Fischbach, K.-F., Corbin, V., and Cagan, R. L. (2010). Preferential adhesion maintains separation of ommatidia in the *Drosophila* eye. *Dev. Biol.* 344, 948–956. doi: 10.1016/j.ydbio.2010.06.013

Bosveld, F., Guirao, B., Wang, Z., Rivière, M., Bonnet, I., Graner, F., et al. (2016a). Modulation of junction tension by tumor suppressors and proto-oncogenes regulates cell-cell contacts. *Development* 143, 623–634. doi: 10.1242/dev.127993

Bosveld, F., Markova, O., Guirao, B., Martin, C., Wang, Z., Pierre, A., et al. (2016b). Epithelial tricellular junctions act as interphase cell shape sensors to orient mitosis. *Nature* 530, 495–498. doi: 10.1038/nature16970

Brodland, G. W. (2002). The Differential Interfacial Tension Hypothesis (DITH): a comprehensive theory for the self-rearrangement of embryonic cells and tissues. *J. Biomech. Eng.* 124, 188. doi: 10.1115/1.1449491

Brodland, G. W., Conte, V., Cranston, P. G., Veldhuis, J., Narasimhan, S., Hutson, M. S., et al. (2010). Video force microscopy reveals the mechanics of ventral furrow invagination in *Drosophila*. *Proc. Natl. Acad. Sci. U.S.A.* 107, 22111–22116. doi: 10.1073/pnas.1006591107

Brodland, G. W., Veldhuis, J. H., Kim, S., Perrone, M., Mashburn, D., and Hutson, M. S. (2014). CellFIT: a cellular force-inference toolkit using curvilinear cell boundaries. *PLoS ONE* 9:e99116. doi: 10.1371/journal.pone.0099116

Chang, L.-H., Chen, P., Lien, M.-T., Ho, Y.-H., Lin, C.-M., Pan, Y.-T., et al. (2011). Differential adhesion and actomyosin cable collaborate to drive Echinoid-mediated cell sorting. *Development* 138, 3803–3812. doi: 10.1242/dev.062257

Chen, C.-L., Schroeder, M. C., Kango-Singh, M., Tao, C., and Halder, G. (2012). Tumor suppression by cell competition through regulation of the Hippo pathway. *Proc. Natl. Acad. Sci. U.S.A.* 109, 484–489. doi: 10.1073/pnas.1113882109

Chiou, K. K., Hufnagel, L., and Shraiman, B. I. (2012). Mechanical stress inference for two dimensional cell arrays. *PLoS Comput. Biol.* 8:e1002512. doi: 10.1371/journal.pcbi.1002512

Cortina, C., Palomo-Ponce, S., Iglesias, M., Fernández-Masip, J. L., Vivancos, A., Whissell, G., et al. (2007). EphB–ephrin-B interactions suppress colorectal cancer progression by compartmentalizing tumor cells. *Nat. Genet.* 39, 1376–1383. doi: 10.1038/ng.2007.11

di Pietro, F., Echard, A., and Morin, X. (2016). Regulation of mitotic spindle orientation: an integrated view. *EMBO Rep.* 17, 1106–1130. doi: 10.15252/embr.201642292

Dworak, H. A., Charles, M. A., Pellerano, L. B., and Sink, H. (2001). Characterization of *Drosophila* hibris, a gene related to human nephrin. *Development* 128, 4265–4276.

Eldar, A., and Elowitz, M. B. (2010). Functional roles for noise in genetic circuits. *Nature* 467, 167–173. doi: 10.1038/nature09326

Elowitz, M. B. (2002). Stochastic gene expression in a single cell. *Science* 297, 1183–1186. doi: 10.1126/science.1070919

Fagotto, F., Winklbauer, R., and Rohani, N. (2014). Ephrin-Eph signaling in embryonic tissue separation. *Cell Adh. Migr.* 8, 308–326. doi: 10.4161/19336918.2014.970028

Farhadifar, R., Röper, J.-C., Aigouy, B., Eaton, S., and Jülicher, F. (2007). The influence of cell mechanics, cell-cell interactions, and proliferation on epithelial packing. *Curr. Biol.* 17, 2095–2104. doi: 10.1016/j.cub.2007.11.049

Fletcher, A. G., Osborne, J. M., Maini, P. K., and Gavaghan, D. J. (2013). Implementing vertex dynamics models of cell populations in biology within a consistent computational framework. *Prog. Biophys. Mol. Biol.* 113, 299–326. doi: 10.1016/j.pbiomolbio.2013.09.003

Froldi, F., Ziosi, M., Garoia, F., Pession, A., Grzeschik, N. A., Bellosta, P., et al. (2010). The lethal giant larvae tumour suppressor mutation requires dMyc oncoprotein to promote clonal malignancy. *BMC Biol.* 8:33. doi: 10.1186/1741-7007-8-33

Gibson, M. C., Patel, A. B., Nagpal, R., and Perrimon, N. (2006). The emergence of geometric order in proliferating metazoan epithelia. *Nature* 442, 1038–1041. doi: 10.1038/nature05014

Gibson, W. T., Veldhuis, J. H., Rubinstein, B., Cartwright, H. N., Perrimon, N., Brodland, G. W., et al. (2011). Control of the mitotic cleavage plane by local epithelial topology. *Cell* 144, 427–438. doi: 10.1016/j.cell.2010.12.035

Gillies, T. E., and Cabernard, C. (2011). Cell division orientation in animals. *Curr. Biol.* 21, R599–R609. doi: 10.1016/j.cub.2011.06.055

Graner, F. (1993). Can surface adhesion drive cell-rearrangement? Part I: biological cell-sorting. *J. Theor. Biol.* 164, 455–476. doi: 10.1006/jtbi.1993.1167

Graner, F., and Glazier, J. A. (1992). Simulation of biological cell sorting using a two-dimensional extended Potts model. *Phys. Rev. Lett.* 69, 2013–2016. doi: 10.1103/PhysRevLett.69.2013

Graner, F., and Sawada, Y. (1993). Can surface adhesion drive cell rearrangement? Part II: a geometrical model. *J. Theor. Biol.* 164, 477–506. doi: 10.1006/jtbi.1993.1168

Honda, H. (1983). Geometrical models for cells in tissues. *Int. Rev. Cytol.* 81, 191–248. doi: 10.1016/S0074-7696(08)62339-6

Huang, J., Zhou, W., Dong, W., Watson, A. M., and Hong, Y. (2009). Directed, efficient, and versatile modifications of the *Drosophila* genome by genomic engineering. *Proc. Natl. Acad. Sci. U.S.A.* 106, 8284–8289. doi: 10.1073/pnas.0900641106

Ishihara, S., and Sugimura, K. (2012). Bayesian inference of force dynamics during morphogenesis. *J. Theor. Biol.* 313, 201–211. doi: 10.1016/j.jtbi.2012.08.017

Itzkovitz, S., Lyubimova, A., Blat, I. C., Maynard, M., van Es, J., Lees, J., et al. (2011). Single-molecule transcript counting of stem-cell markers in the mouse intestine. *Nat. Cell Biol.* 14, 106–114. doi: 10.1038/ncb2384

Iwata, H. (2002). SHAPE: a computer program package for quantitative evaluation of biological shapes based on elliptic fourier descriptors. *J. Hered.* 93, 384–385. doi: 10.1093/jhered/93.5.384

Kajita, M., Sugimura, K., Ohoka, A., Burden, J., Suganuma, H., Ikegawa, M., et al. (2014). Filamin acts as a key regulator in epithelial defence against transformed cells. *Nat. Commun.* 5:4428. doi: 10.1038/ncomms5428

Kale, A., Rimesso, G., and Baker, N. E. (2016). Local cell death changes the orientation of cell division in the developing drosophila wing imaginal disc without using fat or dachsous as orienting signals. *PLoS ONE* 11:e0167637. doi: 10.1371/journal.pone.0167637

Klingenberg, C. P. (2011). MorphoJ: an integrated software package for geometric morphometrics. *Mol. Ecol. Resour.* 11, 353–357. doi: 10.1111/j.1755-0998.2010.02924.x

Krieg, M., Arboleda-Estudillo, Y., Puech, P.-H., Käfer, J., Graner, F., Müller, D. J., et al. (2008). Tensile forces govern germ-layer organization in zebrafish. *Nat. Cell Biol.* 10, 429–436. doi: 10.1038/ncb1705

Lacayo, C. I., Pincus, Z., VanDuijn, M. M., Wilson, C. A., Fletcher, D. A., Gertler, F. B., et al. (2007). Emergence of large-scale cell morphology and movement from local actin filament growth dynamics. *PLoS Biol.* 5:e233. doi: 10.1371/journal.pbio.0050233

Landsberg, K. P., Farhadifar, R., Ranft, J., Umetsu, D., Widmann, T. J., Bittig, T., et al. (2009). Increased cell bond tension governs cell sorting at the *Drosophila* anteroposterior compartment boundary. *Curr. Biol.* 19, 1950–1955. doi: 10.1016/j.cub.2009.10.021

Lecuit, T., and Lenne, P.-F. (2007). Cell surface mechanics and the control of cell shape, tissue patterns and morphogenesis. *Nat. Rev. Mol. Cell Biol.* 8, 633–644. doi: 10.1038/nrm2222

LeGoff, L., Rouault, H., and Lecuit, T. (2013). A global pattern of mechanical stress polarizes cell divisions and cell shape in the growing *Drosophila* wing disc. *Development* 140, 4051–4059. doi: 10.1242/dev.090878

Levayer, R., Hauert, B., and Moreno, E. (2015). Cell mixing induced by myc is required for competitive tissue invasion and destruction. *Nature* 524, 476–480. doi: 10.1038/nature14684

Levayer, R., and Moreno, E. (2016). How to be in a good shape? The influence of clone morphology on cell competition. *Commun. Integr. Biol.* 9:e1102806. doi: 10.1080/19420889.2015.1102806

Li, W., Kale, A., and Baker, N. E. (2009). Oriented cell division as a response to cell death and cell competition. *Curr. Biol.* 19, 1821–1826. doi: 10.1016/j.cub.2009.09.023

Maitre, J.-L., Berthoumieux, H., Krens, S. F. G., Salbreux, G., Julicher, F., Paluch, E., et al. (2012). Adhesion functions in cell sorting by mechanically coupling the cortices of adhering cells. *Science* 338, 253–256. doi: 10.1126/science.1225399

Maître, J.-L., Turlier, H., Illukkumbura, R., Eismann, B., Niwayama, R., Nédélec, F., et al. (2016). Asymmetric division of contractile domains couples cell positioning and fate specification. *Nature* 536, 344–348. doi: 10.1038/nature18958

Mao, Y., Tournier, A. L., Bates, P. A., Gale, J. E., Tapon, N., and Thompson, B. J. (2011). Planar polarization of the atypical myosin Dachs orients cell divisions in *Drosophila*. *Genes Dev.* 25, 131–136. doi: 10.1101/gad.610511

Mao, Y., Tournier, A. L., Hoppe, A., Kester, L., Thompson, B. J., and Tapon, N. (2013). Differential proliferation rates generate patterns of mechanical tension that orient tissue growth. *EMBO J.* 32, 2790–2803. doi: 10.1038/emboj.2013.197

Meyer, H. M., and Roeder, A. H. K. (2014). Stochasticity in plant cellular growth and patterning. *Front. Plant Sci.* 5:420. doi: 10.3389/fpls.2014.00420

Milán, M., Pérez, L., and Cohen, S. M. (2002). Short-range cell interactions and cell survival in the *Drosophila* wing. *Dev. Cell* 2, 797–805. doi: 10.1016/S1534-5807(02)00169-7

Milán, M., Weihe, U., Tiong, S., Bender, W., and Cohen, S. M. (2001). msh specifies dorsal cell fate in the *Drosophila* wing. *Development* 128, 3263–3268.

Monier, B., Pélissier-Monier, A., Brand, A. H., and Sanson, B. (2010). An actomyosin-based barrier inhibits cell mixing at compartmental boundaries in *Drosophila* embryos. *Nat. Cell Biol.* 12, 60–65. doi: 10.1038/ncb2005

Morata, G., and Ballesteros-Arias, L. (2015). Cell competition, apoptosis and tumour development. *Int. J. Dev. Biol.* 59, 79–86. doi: 10.1387/ijdb.150081gm

Nellen, D., Burke, R., Struhl, G., and Basler, K. (1996). Direct and long-range action of a DPP morphogen gradient. *Cell* 85, 357–368. doi: 10.1016/S0092-8674(00)81114-9

Nier, V., Jain, S., Lim, C. T., Ishihara, S., Ladoux, B., and Marcq, P. (2016). Inference of internal stress in a cell monolayer. *Biophys. J.* 110, 1625–1635. doi: 10.1016/j.bpj.2016.03.002

Nose, A., Nagafuchi, A., and Takeichi, M. (1988). Expressed recombinant cadherins mediate cell sorting in model systems. *Cell* 54, 993–1001. doi: 10.1016/0092-8674(88)90114-6

Pan, Y., Heemskerk, I., Ibar, C., Shraiman, B. I., and Irvine, K. D. (2016). Differential growth triggers mechanical feedback that elevates Hippo signaling. *Proc. Natl. Acad. Sci. U.S.A.* 113, E6974–E6983. doi: 10.1073/pnas.1615012113

Paulsson, J. (2004). Summing up the noise in gene networks. *Nature* 427, 415–418. doi: 10.1038/nature02257

Pincus, Z., and Theriot, J. A. (2007). Comparison of quantitative methods for cell-shape analysis. *J. Microsc.* 227, 140–156. doi: 10.1111/j.1365-2818.2007.01799.x

Porazinski, S., de Navascués, J., Yako, Y., Hill, W., Jones, M. R., Maddison, R., et al. (2016). EphA2 drives the segregation of Ras-transformed epithelial cells from normal neighbors. *Curr. Biol.* 26, 3220–3229. doi: 10.1016/j.cub.2016.09.037

Prober, D. A., and Edgar, B. A. (2000). Ras1 promotes cellular growth in the *Drosophila* Wing. *Cell* 100, 435–446. doi: 10.1016/S.0092-8674(00)80679-0

Raj, A., and van Oudenaarden, A. (2008). Nature, nurture, or chance: stochastic gene expression and its consequences. *Cell* 135, 216–226. doi: 10.1016/j.cell.2008.09.050

Raser, J. M. (2004). Control of stochasticity in eukaryotic gene expression. *Science* 304, 1811–1814. doi: 10.1126/science.1098641

R Development Core Team (2015). *R: A Language and Environment for Statistical Computing* Vienna: R Foundation for Statistical Computing. Available online at: http://www.R-project.org/

Rudolf, K., Umetsu, D., Aliee, M., Sui, L., Jülicher, F., and Dahmann, C. (2015). A local difference in Hedgehog signal transduction increases mechanical cell bond tension and biases cell intercalations along the *Drosophila* anteroposterior compartment boundary. *Development* 142, 3845–3858. doi: 10.1242/dev.125542

Sakurai, K. T., Kojima, T., Aigaki, T., and Hayashi, S. (2007). Differential control of cell affinity required for progression and refinement of cell boundary during *Drosophila* leg segmentation. *Dev. Biol.* 309, 126–136. doi: 10.1016/j.ydbio.2007.07.001

Sela-Donenfeld, D., and Wilkinson, D. G. (2005). Eph receptors: two ways to sharpen boundaries. *Curr. Biol.* 15, R210–R212. doi: 10.1016/j.cub.2005.03.013

Shibata, T., and Fujimoto, K. (2005). Noisy signal amplification in ultrasensitive signal transduction. *Proc. Natl. Acad. Sci. U.S.A.* 102, 331–336. doi: 10.1073/pnas.0403350102

Stooke-Vaughan, G. A., Davidson, L. A., and Woolner, S. (2017). Xenopus as a model for studies in mechanical stress and cell division. *Genesis* 55:e23004. doi: 10.1002/dvg.23004

Sugimura, K., Lenne, P.-F., and Graner, F. (2016). Measuring forces and stresses *in situ* in living tissues. *Development* 143, 186–196. doi: 10.1242/dev.119776

Swain, P. S., Elowitz, M. B., and Siggia, E. D. (2002). Intrinsic and extrinsic contributions to stochasticity in gene expression. *Proc. Natl. Acad. Sci. U.S.A.* 99, 12795–12800. doi: 10.1073/pnas.162041399

Swarup, S., and Verheyen, E. M. (2012). Wnt/Wingless signaling in *Drosophila*. *Cold Spring Harb. Perspect. Biol.* 4, a007930–a007930. doi: 10.1101/cshperspect.a007930

Tossell, K., Andreae, L. C., Cudmore, C., Lang, E., Muthukrishnan, U., Lumsden, A., et al. (2011). Lrrn1 is required for formation of the midbrain-hindbrain boundary and organiser through regulation of affinity differences between midbrain and hindbrain cells in chick. *Dev. Biol.* 352, 341–352. doi: 10.1016/j.ydbio.2011.02.002

Umetsu, D., Aigouy, B., Aliee, M., Sui, L., Eaton, S., Jülicher, F., et al. (2014a). Local increases in mechanical tension shape compartment boundaries by biasing cell intercalations. *Curr. Biol.* 24, 1798–1805. doi: 10.1016/j.cub.2014.06.052

Umetsu, D., Dunst, S., and Dahmann, C. (2014b). An RNA interference screen for genes required to shape the anteroposterior compartment boundary in *Drosophila* identifies the Eph receptor. *PLoS ONE* 9:e114340. doi: 10.1371/journal.pone.0114340

Vincent, J.-P., Fletcher, A. G., and Baena-Lopez, L. A. (2013). Mechanisms and mechanics of cell competition in epithelia. *Nat. Rev. Mol. Cell Biol.* 14, 581–591. doi: 10.1038/nrm3639

Wickham, H. (2009). *ggplot2 Elegant Graphics for Data Analysis*. New York, NY: Springer-Verlag. doi: 10.1007/978-0-387-98141-3

Wartlick, O., Mumcu, P., Kicheva, A., Bittig, T., Seum, C., Jülicher, F., et al. (2011). Dynamics of Dpp signaling and proliferation control. *Science* 331, 1154–1159. doi: 10.1126/science.1200037

Yu, K., Zhang, C., Berry, G. J., Altman, R. B., Ré, C., Rubin, D. L., et al. (2016). Predicting non-small cell lung cancer prognosis by fully automated microscopic pathology image features. *Nat. Commun.* 7:12474. doi: 10.1038/ncomms12474

Zelditch, M., Swiderski, D. L., and Sheets, H. D. (2012). *Geometric Morphometrics for Biologists, 2nd Edn*. Available online at: http://www.sciencedirect.com/science/book/9780123869036 (Accessed March 8, 2017).

Conflict of Interest Statement: The authors declare that the research was conducted in the absence of any commercial or financial relationships that could be construed as a potential conflict of interest.

frontiers in Cell and Developmental Biology

ORIGINAL RESEARCH
published: 25 November 2016
doi: 10.3389/fcell.2016.00139

Differences in the Mechanical Properties of the Developing Cerebral Cortical Proliferative Zone between Mice and Ferrets at both the Tissue and Single-Cell Levels

Arata Nagasaka[1], Tomoyasu Shinoda[1], Takumi Kawaue[1], Makoto Suzuki[2], Kazuaki Nagayama[3], Takeo Matsumoto[4†], Naoto Ueno[2], Ayano Kawaguchi[1] and Takaki Miyata[1]*

[1] Department of Anatomy and Cell Biology, Graduate School of Medicine, Nagoya University, Nagoya, Japan, [2] Division for Morphogenesis, Department of Developmental Biology, National Institute for Basic Biology, Okazaki, Japan, [3] Micro-Nano Biomechanics Laboratory, Department of Intelligent Systems Engineering, Ibaraki University, Hitachi, Japan, [4] Biomechanics Laboratory, Department of Mechanical Engineering, Nagoya Institute of Technology, Nagoya, Japan

OPEN ACCESS

Edited by:
Takaaki Matsui,
Nara Institute of Science and Technology, Japan

Reviewed by:
Takayuki Suzuki,
Nagoya University, Japan
Yoichi Kosodo,
Korea Brain Research Institute, South Korea

***Correspondence:**
Takaki Miyata
tmiyata@med.nagoya-u.ac.jp

†Present Address:
Takeo Matsumoto,
Department of Mechanical Science and Engineering, Nagoya University, Nagoya, Japan

Specialty section:
This article was submitted to Cell Adhesion and Migration, a section of the journal Frontiers in Cell and Developmental Biology

Received: 29 September 2016
Accepted: 11 November 2016
Published: 25 November 2016

Citation:
Nagasaka A, Shinoda T, Kawaue T, Suzuki M, Nagayama K, Matsumoto T, Ueno N, Kawaguchi A and Miyata T (2016) Differences in the Mechanical Properties of the Developing Cerebral Cortical Proliferative Zone between Mice and Ferrets at both the Tissue and Single-Cell Levels. Front. Cell Dev. Biol. 4:139. doi: 10.3389/fcell.2016.00139

Cell-producing events in developing tissues are mechanically dynamic throughout the cell cycle. In many epithelial systems, cells are apicobasally tall, with nuclei and somata that adopt different apicobasal positions because nuclei and somata move in a cell cycle–dependent manner. This movement is apical during G2 phase and basal during G1 phase, whereas mitosis occurs at the apical surface. These movements are collectively referred to as interkinetic nuclear migration, and such epithelia are called "pseudostratified." The embryonic mammalian cerebral cortical neuroepithelium is a good model for highly pseudostratified epithelia, and we previously found differences between mice and ferrets in both horizontal cellular density (greater in ferrets) and nuclear/somal movements (slower during G2 and faster during G1 in ferrets). These differences suggest that neuroepithelial cells alter their nucleokinetic behavior in response to physical factors that they encounter, which may form the basis for evolutionary transitions toward more abundant brain-cell production from mice to ferrets and primates. To address how mouse and ferret neuroepithelia may differ physically in a quantitative manner, we used atomic force microscopy to determine that the vertical stiffness of their apical surface is greater in ferrets (Young's modulus = 1700 Pa) than in mice (1400 Pa). We systematically analyzed factors underlying the apical-surface stiffness through experiments to pharmacologically inhibit actomyosin or microtubules and to examine recoiling behaviors of the apical surface upon laser ablation and also through electron microscopy to observe adherens junction. We found that although both actomyosin and microtubules are partly responsible for the apical-surface stiffness, the mouse<ferret relationship in the apical-surface stiffness was maintained even in the presence of inhibitors. We also found that the stiffness of single, dissociated neuroepithelial cells is actually greater in mice (720 Pa) than in ferrets (450 Pa). Adherens

junction was ultrastructurally comparable between mice and ferrets. These results show that the horizontally denser packing of neuroepithelial cell processes is a major contributor to the increased tissue-level apical stiffness in ferrets, and suggest that tissue-level mechanical properties may be achieved by balancing cellular densification and the physical properties of single cells.

Keywords: neuroepithelium, apical surface, elasticity, neural progenitor cell, interkinetic nuclear migration, atomic force microscopy, actomyosin, cell density

INTRODUCTION

The formation of mammalian central nervous system structures (i.e., brains and spinal cord) begins with the emergence of the neuroepithelium, which is derived from the ectoderm, and consists of undifferentiated neural progenitor cells. Cross-sectionally, neuroepithelia (50–100 μm thick in early embryonic mice) are sandwiched by, apically, a fluid-filling space (called the ventricle) and, basally, the mesenchyme-derived component that will differentiate into meninges. As the brain walls thicken (~200 μm, in mid-embryonic mouse cerebrum), a new zone where neurons accumulate in large number is added outside the original neuroepithelial part that is thereafter called the ventricular zone (VZ) (~100 μm) (**Figure 1**) (Götz and Huttner, 2005; Miyata, 2008; LaMonica et al., 2012; Taverna et al., 2014).

The apical surface of developing brain walls is formed by tangential assembly of the apical endfeet of neuroepithelial or VZ cells, and this assembly can be visualized as meshes immunopositive for molecules enriched in adherens junction, like ZO-1 (**Figure 1C**) or cadherins (Kosodo et al., 2004). Neuroepithelial and VZ cells are apicobasally elongated, with narrow (<10 μm^2) apices (Nishizawa et al., 2007, in embryonic mouse cerebrum) (**Figure 1C**). As in a variety of epithelial cells, the apex of neuroepithelial or VZ cells is contractile in an actomyosin-dependent manner, and the entire apical surface is under tangential tension. This apical-surface contractility thereby bends or curls the walls toward the apical side (Nishimura et al., 2012; Suzuki et al., 2012; Kadoshima et al., 2013; Okamoto et al., 2013, as shown in **Figure 3A**), causing the developing cerebral hemispheric walls to take on a dome-like, apically concave shape (**Figures 1A,B**). Despite such qualitative understanding of the apical surface's physical property, as well as the potential importance of periventricular mechanical factors in the overall neuroepithelial dynamics (Norden et al., 2009; Kosodo et al., 2011; Leung et al., 2011; Okamoto et al., 2013), quantitative assessments that focus on the elasticity provided by the apical surface and nearby cellular structures have not been made.

The neuroepithelium and the VZ are both pseudostratified, which means that although most of the cells are connected to both apical and basal surfaces of the brain wall to form an epithelial monolayer, their nuclei and somata adopt different apicobasal positions (**Figure 1C**). The reason for the diffusely staggered nuclear and somal positioning (**Figures 1B,C**, scanning electron microscopy) is that proliferative cells move their nuclei and somata apically during G2 phase of the cell cycle before they divide at the apical surface and their daughter cells move nuclei/somata basally during G1, using their apicobasally elongated morphology (**Figure 1C**). These cell-cycle phase-dependent nuclear/somal movements are collectively called interkinetic nuclear migration (INM) (reviewed in Miyata, 2008; Taverna and Huttner, 2010; Kosodo, 2012; Lee and Norden,

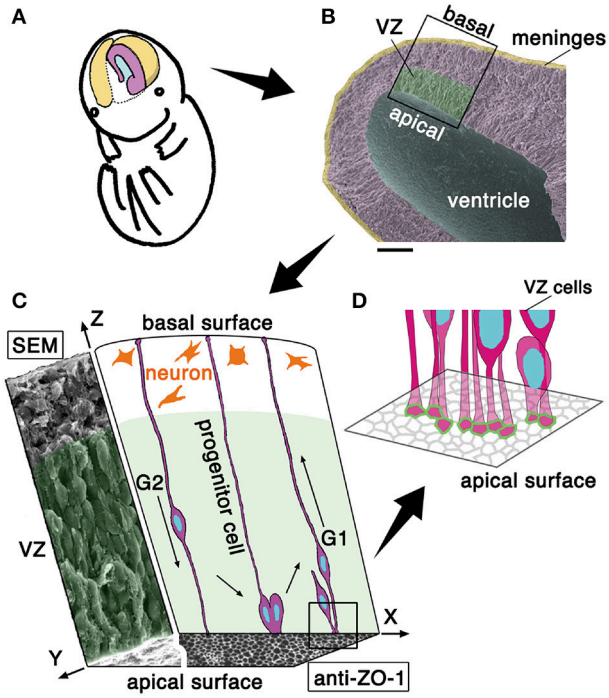

FIGURE 1 | Schematic representation of the embryonic cerebral wall subjected to the present mechanical measurement. (A) Illustration of the cerebral hemispheric wall (colored). **(B)** Scanning electron micrograph picture of a cerebral wall isolated from an embryonic day (E) 13 mouse. Scale bar, 100 μm. **(C)** 3D illustration of a portion of the cerebral wall. In the xz plane, the cross-sectional schematic view depicts progenitor cells spanning apicobasally across the wall and neurons accumulating in the outer zone. In the yz plane, the cross-sectional view obtained by scanning electron microscopy (SEM) shows an apparent stratification of cell bodies. The xy plane (an *en face* view of the ventricular or apical surface of the wall) consists of a SEM portion (left) and an immunohistochemically stained portion (right). While the outer neuronal territory is really stratified, the inner progenitor territory, called the ventricular zone, VZ is "pseudostratified," with each nucleus migrating in a cell cycle–dependent manner within an elongated progenitor cell whose apical endfoot is integrated into the adherens junction meshwork visualized by anti–ZO-1 immunostaining. Note that VZ is filled with somata and cellular processes with no gaps. **(D)** Schematic illustration the apical-most microzone, showing the tangential assembly of the apical processes of VZ cells and the formation of a junctional meshwork (green, corresponding to ZO-1 immunoreactivity in **C**).

2013). The neuroepithelium and the VZ are filled with moving somata and apicobasally oriented processes, with minimal gaps and extracellular spaces (Hinds and Ruffett, 1971).

Analogously to industrial production events in human society that rely heavily on the trafficking or movement of materials and products, INM may contribute to the successful systematic production of cells at the apical surface, thereby supporting overall brain formation (Smart, 1972). Indeed, we recently found that experimental inhibition of basalward INM resulted in nuclear/somal overcrowding on the subapical surface (∼30 μm from the surface), which in turn induced the abnormal detachment of proliferative cells from the apical surface and the disruption of histogenesis (Okamoto et al., 2013). This finding suggests that proliferative cells may sense and respond to excessive mechanical stress generated in the subapical space. It also raises the possibility that similar sensing and responses to mechanical factors might also occur under physiological (non-overcrowded) conditions, possibly coordinating heterogeneous nuclear and somal movements (Miyata et al., 2015; Strzyz et al., 2016). We chose to focus on a microzone near (∼10 μm from) the apical surface, where multiple mechanical events, such as mitosis, resultant duplication of nuclear and somal flow, as well as apical constriction, take place. We decided that this location was a good candidate for where the sensing of mechanical factors by VZ cells occurs. Given increasing necessity of studying the mechanical control of nervous system development (Franze, 2013), measuring physical parameters at or near the apical surface thus provides a platform for studying previously unexplored aspects of brain development, namely intra-neuroepithelial mechanics and crowd dynamics.

To establish a technical basis for dissecting the possible links between intra-neuroepithelial nuclear/somal traffic and physical parameters that proliferative cells face in the subapical space, we sought to compare the stiffness on or near the apical surface of the embryonic cerebral VZ between mice and ferrets in a quantitative manner (**Figure 2**). We had recently found that in ferrets, a microzone containing the apical surface is horizontally denser in terms of the apical process of VZ cells (39.6 apices per 100 μm^2) than in mice (27.6 apices 100 μm^2) (**Figure 2A**), and also that INM behaviors were different between mice and ferrets (i.e., apicalward movement of G2-phase cells' nuclei/somata was slower in ferrets, while basalward movement of early G1-phase cells nuclei/somata was quicker in ferrets than in mice, **Figure 2A**) (Okamoto et al., 2014). The cerebral cortex of adult ferrets, which has gyri and sulci as in primates including humans, is larger than that of mice, which lack gyri and sulci. Moreover, the total volume of the embryonic cerebral cortical VZ is greater in ferrets than in mice (**Figure 2A**). The present mouse-ferret comparison will thus provide insights into possible mechanical modulations that have occurred during evolutionary expansion of the neuroepithelium or VZ.

Our measurements using atomic force microscopy revealed that the apical surface of the mouse VZ was stiffer than that of the ferret VZ. We systematically analyzed factors underlying the apical-surface stiffness through experiments to pharmacologically inhibit actomyosin or microtubules and to examine recoiling behaviors of the apical surface upon laser ablation. We found that although both actomyosin and microtubules are partly responsible for the apical-surface stiffness, the greater stiffness of the ferret apical surface compared with mice is largely explained by the denser lateral assembly of apical endfeet in ferrets. We also found that the stiffness of single dissociated VZ cells was greater in mice than in ferrets. Electron microscopy revealed that adherens junction was comparable between the mouse VZ and ferret VZ. Furthermore, non-somal cellular elements (apical processes) showed greater (76% in ferrets and 60% in mice) occupancy than nuclei/somata in the apicalmost zone (∼5 μm from the surface). These results provide a solid basis for further biomechanical understanding of mechanisms underlying the development of brains.

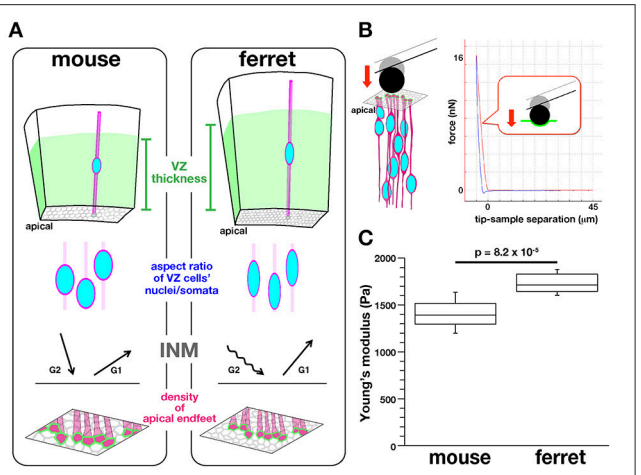

FIGURE 2 | Background, experimental design, and results of AFM measurements made on the apical surface of cerebral walls. (A) Previously reported mouse–ferret differences in the thickness of the VZ (top), the aspect ratios of the nuclei and somata of VZ cells (second row), the pattern of INM (third row), and the density of VZ cell apices (bottom) (Okamoto et al., 2014). **(B)** Illustration showing AFM indentation measurement on the apical surface of cerebral walls (left) and a typical force–distance curve obtained (right). **(C)** Graph showing that the elastic modulus measured vertically on the apical surface was greater for ferret VZ ($n = 12$) than for mouse VZ, $n = 11$ ($p = 8.2 \times 10^{-5}$, Mann-Whitney U-test).

RESULTS

Apical Surface Is Stiffer in the Ferret VZ than in the Mouse VZ

Mouse and ferret VZ cells have recently been found to differ in the degree of pseudostratification (i.e., VZ thickness), the nuclear/somal aspect ratio (ferret VZ cells are more slender), the horizontal/tangential packing density (ferret VZ cells are more densely packed), and the INM behaviors (Okamoto et al., 2014) (**Figure 2A**). To quantitatively determine whether they are under different mechanical conditions on or near the apical surface, we first performed indentation measurement to infer the stiffness using an atomic force microscope (AFM) (Franze, 2011; Iwashita et al., 2014; Gautier et al., 2015). Fresh cerebral walls (200–300 μm thick in mice, 300–400 μm thick in ferrets) were prepared from embryonic mice and ferrets at equivalent

developmental stages (E13 in mice and E28–30 in ferrets) (Clancy et al., 2001), and placed on gel-coated dishes with the apical surface facing up. The apical surface was pushed with a spherical bead (20 μm diameter) attached to the tip of a cantilever (with an indentation depth of 5 μm) (**Figure 2B**). From the force–distance curves obtained subsequently, the elastic (Young's) moduli were determined. As shown in **Figure 2C**, the elastic modulus obtained vertically on the apical surface of the ferret VZ was significantly greater (1734.3 ± 49.9 Pa, $n = 12$) than that obtained for the mouse VZ (1398.8 ± 99.8 Pa, $n = 11$) ($p = 8.2 \times 10^{-5}$, Mann-Whitney U-test), indicating that the apical surface and the nearby microzone are stiffer in ferrets than in mice.

Pharmacological Studies of Apical Surface Stiffness

As a first approach to identifying the basis for the mouse–ferret difference in the elastic modulus at/near the apical surface of VZ, we coupled AFM indentation measurements with pharmacological experiments. Inhibiting myosin with either blebbistatin or Y-27632 (a rho-kinase inhibitor) reduces contractility along the apical surface (Kinoshita et al., 2008), thereby leading to the loss of apical bending/curling of cerebral walls (**Figure 3A**), although our live observation of the apical surface visualized with ZO1-EGFP before and after blebbistatin or Y-27632 showed that apical mesh size did not change (**Figure 3C**). Similar actomyosin-dependent bending/curling occurred in ferret cerebral walls (data not shown). Under actomyosin-inhibited conditions, we found that the elastic moduli decreased (by 30–50%) in both mice and ferrets, but significant mouse–ferret differences were observed even in the presence of blebbistatin ($p = 0.0004$) or Y-27632 ($p = 4.2 \times 10^{-5}$), as in the control (1% DMSO, $p = 0.0002$, Mann-Whitney U-test) (**Figure 4**).

Microtubules play a role in the apicobasal elongation of neuroepithelial cells (Karfunkel, 1971; Miyata and Ogawa, 2007; Suzuki et al., 2012). It is also known that the loss of microtubules and resultant reduction of the neuroepithelial height leads to an increase in the neuroepithelial width (Schoenwolf and Powers, 1987). The addition of nocodazole resulted in thinning and lateral expansion of cerebral walls (**Figures 3A,B**), with horizontal separation between sporadically fluorescent labeled neural progenitor cells (**Figures 3B,C**), as well as increased apical mesh size (**Figure 3C**), which implies that microtubules loss would decrease the tangential/horizontal packing density of neuroepithelial cells. In these nocodazole-treated cerebral walls, the elastic modulus at the apical surface decreased in both mice and ferrets. This suggests that microtubules, which enable neural progenitors to apicobasally extend and are presumably under compression within each neural progenitor cell's process, may partly contribute to the overall stiffness of the apical surface. Since nocodazole treatment shrinks the morphology of neurons that are abundantly packed in the basal part of cerebral walls, it is also possible that cellular accumulation normally occurring in an expansive manner along the apicobasal axis partly contributes to the apical-surface stiffness. Notably, however, the elastic modulus decreased by a similar extent in both mice and ferrets, maintaining the original mouse<ferret relationship ($p = 0.0002$) (**Figure 4**).

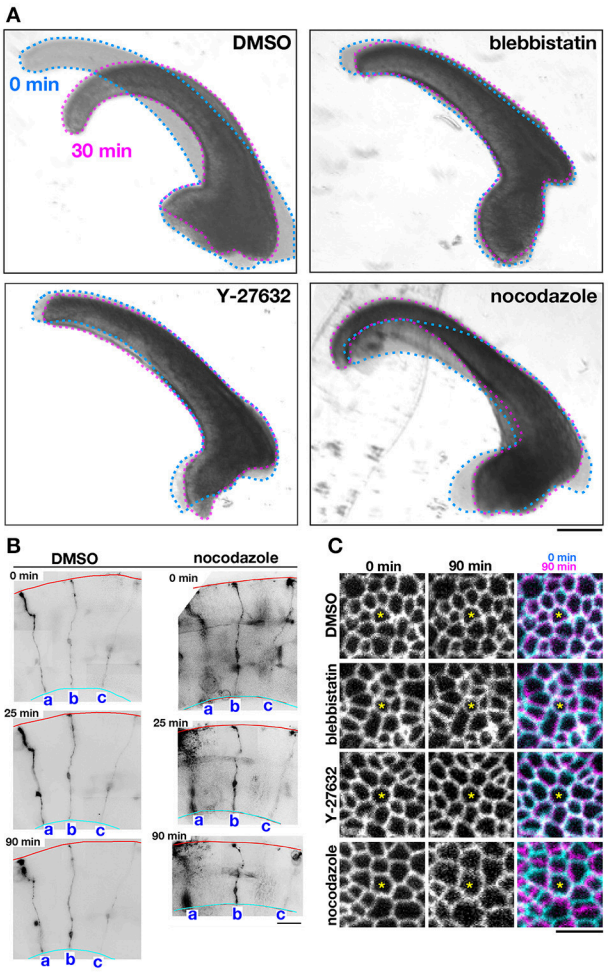

FIGURE 3 | Effects of pharmacological inhibitors on the mechanical behavior of cerebral walls and apical surface. (A) Photomicrographs showing apical bending/curling of E13 mouse cerebral wall slices exposed to DMSO, blebbistatin, Y-27632, or nocodazole. Note that blebbistatin and Y-27632 clearly blocked bending/curling, and also that nocodazole laterally expanded and thinned cerebral walls, making bending/curling less evident. **(B)** Observation of sparsely DiI-labeled three progenitor cells (a-c) in slices treated with DMSO or nocodazole. In the nocodazole-treated slice, thinning and lateral expansion of cerebral wall was coupled with separation between the tracked progenitors. **(C)** Live monitoring of the apical junction mesh using R26-ZO1-EGFP mice. In each set of panels, one endfoot was used as a reference (center, asterisk). While the size of meshes and the distance between meshes did not change in cerebral walls treated with blebbistatin or Y-27632, the nocodazole-treated apical surface showed enlargement of meshes and lateral separation between meshes. Scale bar, 200 μm in **(A)**, 50 μm in **(B)**, 5 μm in **(C)**.

These results suggest that although the stiffness on or near the apical surface of VZ depends on both actomyosin and microtubules, and the observed its mouse–ferret difference may not be sufficiently explained by the difference in dependence on these intracellular factors.

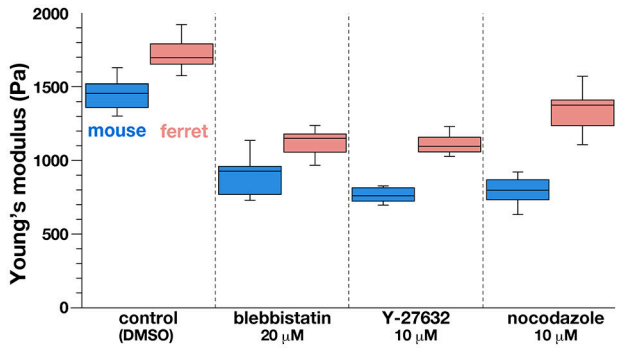

FIGURE 4 | Graph depicting the results of AFM indentation experiments in the presence of pharmacological inhibitors that affect the apical surface. Note that the elastic modulus was reduced by all the inhibitors tested in both mice and ferrets, in keeping with the original mouse<ferret relationship.

Apical Surface Contractility Is Comparable between Mice and Ferrets

The myosin-blocking experiments described above recorded an almost similar reduction in the apical elastic modulus in the mouse and ferret VZs, which suggests that the actomyosin-dependent contractility of the apical surface may be almost identical in both species, and therefore may not contribute much to the overall mouse–ferret difference in apical surface stiffness. To further evaluate this possibility, we performed more direct stress-releasing experiments on the apical surface. Following the visualization of the apices of live VZ cells by transfection with EGFP-ZO-1 (Konno et al., 2008), we subjected *en face* inspected apical surfaces to laser ablation (Hara et al., 2013; Okamoto et al., 2013). We applied a short-pulse laser to the midpoint of a side (boundary line) formed by two polygonal apices of neighboring EGFP-ZO-1–labeled cells, and measured the separation of two vertices at both ends of the laser-targeted side (**Figure 5A**). We did not find significant differences between the velocity of separation of the tracked vertices of mouse ($n = 33$) and those of ferret ($n = 37$) ($p = 0.80$ at 0.5 s; $p = 0.84$ at 1.0 s; $p = 0.73$ at 1.5 s; $p = 0.81$ at 2.0 s, Mann-Whitney U-test) (**Figure 5B**). Hence we verified that the tangential contractility of apical surface is similar in both mice and ferrets.

Adherens Junction Ultrastructure Is Similar in the VZ of both Mouse and Ferret

Following comparative *en face* inspection of immunostained adherens junction (Okamoto et al., 2014), which revealed a difference in the density of apical endfeet (i.e., difference in the horizontal size of each mesh, mouse < ferret), we sought to determine whether the adherens junctions in the mouse VZ and those in the ferret VZ are similar in their vertical size. Specifically, we sought to measure their length along the apicobasal axis using comparative transmission electron microscopy. As shown in **Figure 6**, the measured depth of the adherens junction was similar in both mice (1.06 ± 0.16 μm, $n = 11$) and ferrets (1.03 ± 0.20 μm, $n = 12$) ($p = 0.50$, Mann-Whitney U-test).

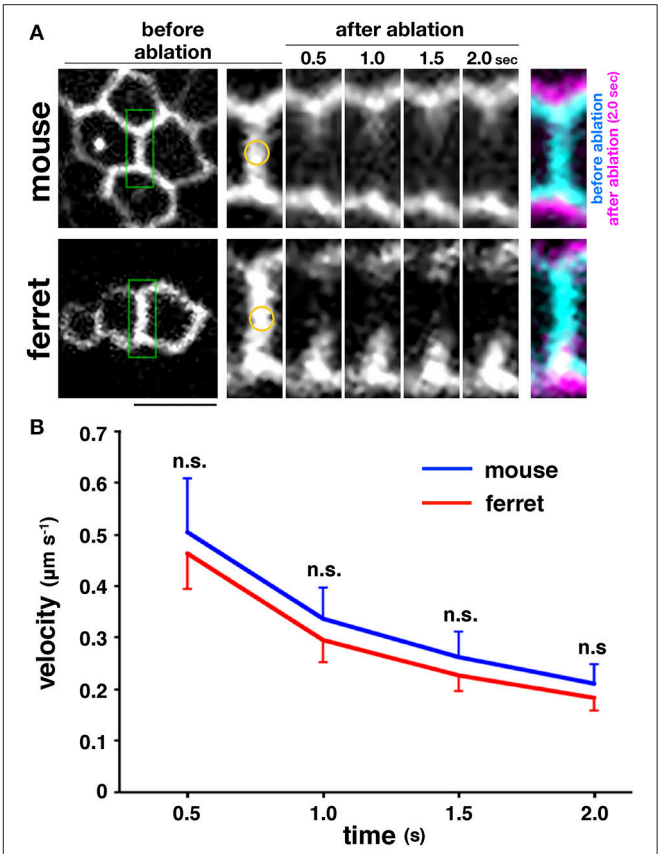

FIGURE 5 | Laser ablation experiments performed on the apical surface of embryonic cerebral walls. (A) *En face* live observed EGFP-ZO-1^{+} endfeet of mouse and ferret VZ cells. A short-pulse laser was applied to the midpoint marked in yellow on the enlarged images of a boundary line enclosed in green formed by two polygonal apices of neighboring EGFP-ZO-1–labeled cells. The centrifugal separation of two vertices at both ends of the laser-targeted side were tracked for 2 s. In the final panels, images at 0 s and at 2 s are superimposed. Scale bar, 5 μm. **(B)** Graph depicting the velocity of time-dependent separation of the vertices tracked, showing that the separation velocity was comparable between mouse and ferret.

Dissociated Mouse VZ Cells Are Stiffer than Ferret VZ Cells

Next, to determine whether the tissue-level difference in stiffness on or near the apical surface between mice and ferrets can be explained by a possible difference in the stiffness of individual VZ cells of the two species, we performed AFM indentation measurements on single, dissociated cells. Most VZ cells were originally bipolar-shaped, and may have lost thin cellular processes, especially basal processes that were much longer than apical processes during microsurgical, enzymatic, and mechanical dissociation steps. Harvested cells were placed in culture dishes and pushed by a spherical bead (5 μm diameter) attached to the tip of a cantilever (with an indentation depth of 1 μm) (**Figure 7A**). Unexpectedly, the elastic modulus was significantly greater in mouse cells (718.7 ± 58.0 Pa, $n = 51$) than in ferret cells (452.7 ± 42.8 Pa, $n = 49$; $p = 1.3 \times 10^{-8}$, Mann-Whitney U-test) (**Figure 7B**). The values obtained for

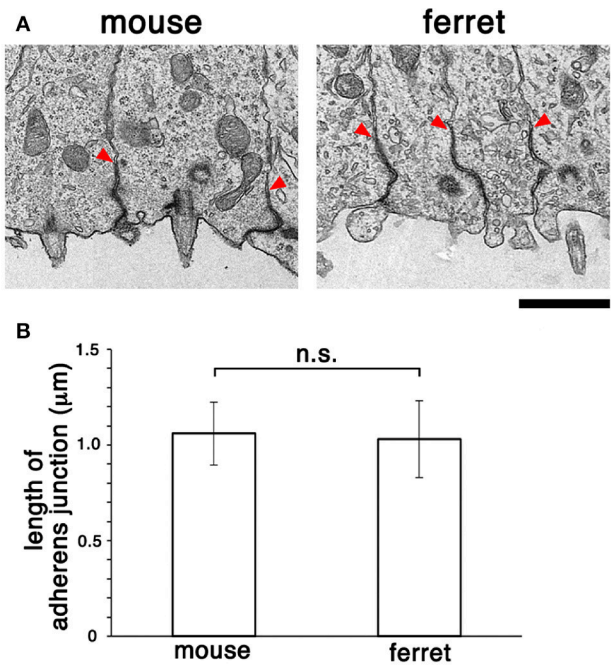

FIGURE 6 | Transmission electron micrographs (A) showing cross-sectional views of adherens junctions, with basal borders indicated by arrowheads, in the VZ of mouse and ferret. **(B)** Graph depicting that the length of adherens junction was similar between the mouse VZ ($n = 11$) and ferret VZ ($n = 12$) ($p = 0.50$, Mann-Whitney *U*-test). Scale bar, 1 μm.

dissociated cells were both much smaller than those obtained for the apical surface of cerebral walls (1399 Pa in mice and 1734 Pa in ferrets). Pharmacological experiments as performed for cerebral walls (blebbistatin, Y-27632, and nocodazole) all reduced elastic moduli of dissociated cells, but interestingly, the mouse–ferret difference in single-cell stiffness (mouse > ferret in control, $p = 5.4 \times 10^{-7}$) was maintained even after inhibitor treatments ($p = 1.4 \times 10^{-8}$ in blebbistatin, $p = 2.3 \times 10^{-6}$ in Y-27632, and $p = 2.8 \times 10^{-8}$ in nocodazole) (**Figure 7C**).

Since LaPlace's law predicts that the pressure within a sealed bubble rises when its radius is reduced (Dai and Sheetz, 1999), we compared the sizes of mouse and ferret cells, expecting mouse cells to be smaller than ferret cells. Contrary to our expectation, the dissociated mouse cells (237 ± 72 μm^3, $n = 55$) were significantly larger than dissociated ferret cells (116 ± 48 μm^3, $n = 75$) ($p = 1.3 \times 10^{-19}$, Mann-Whitney *U*-test) (**Figures 7D,E**) for unknown reasons. These results suggest that the difference in stiffness of single dissociated cells (mouse > ferret) may not directly generate the differential tissue-level stiffness on or near the apical surface (mouse < ferret), and also that it may underlie or be associated with 3D cellular morphology/behaviors in the ferret VZ, namely denser horizontal assembly/packing, more slender nuclear and somal shapes, and a unique INM pattern.

Processes Are Dominant Over Cell Bodies Subapically in Ferrets Compared with Mice

Given that (1) tangential contractility of the apical surface was comparable between mice and ferrets (**Figure 5**), (2) dissociated ferret cells (which may represent cell bodies of ferret VZ cells) were softer than mouse cells (**Figure 7**), and (3) horizontal assembly of apical endfeet was denser in ferrets (Okamoto et al., 2014), we hypothesized that the tangential packing density of VZ cell processes, rather than cell bodies, at or near the apical surface, may be a major contributing factor to the tissue-level mouse–ferret difference in the stiffness on or near the apical surface of VZ.

To further investigate this possibility, we sought to measure the occupancy of apical processes and that of cell bodies in a microzone near (~5 μm from) the apical surface. Cell–cell borders were visualized throughout VZ by labeling plasma membrane with FM4-64 dye. In each horizontal section, which was completely filled with cellular elements and had no clear extracellular spaces, we examined the areal occupancy of either cell bodies (defined so if diameter of each sectional area was >3 μm, highlighted yellow or blue) or processes (seen as mesh) (**Figure 8A**).

At a depth of 5 μm, the occupancy by cell processes was significantly greater than that by cell bodies in both mice and ferrets ($p = 0.0051$, Mann-Whitney *U*-test): 39.7% for cell bodies and 60.3% for processes in mice [$n = 6$ (cerebral walls)]; 23.9% for cell bodies and 76.1% for processes in ferrets [$n = 6$ (cerebral walls)] (**Figure 8B**). At more superficial or apical levels (at 1–2 μm depths), the predominance of processes further increased, approaching >90% (data not shown). Since AFM force–distance curves are generally obtained under a much stronger contribution by the surface of a tested material than that by deeper parts, these results support our proposal that the tissue-level stiffness on or near the apical surface of VZ is best explained by the density of tangentially packed cellular processes, which is significantly greater in ferret (39.6 apices per 100 μm^2) than in mouse (27.6 apices 100 μm^2) (Okamoto et al., 2014).

Stage-Dependent Decrease in Density of Endfeet/Apices Correlated with Reduced Apical-Surface Stiffness in Mice

To further evaluate our model, we compared stage-dependent changes in the apical surface stiffness in mice and examined its possible correlation with changes in the density of apical endfeet. As shown in **Figure 9**, the elastic modulus measured at E14 (1327.4 ± 59.0 Pa, $n = 15$) was significantly smaller than that measured at E12 (1487.3 ± 57.8 Pa, $n = 10$) ($p = 0.0195$, Steel-Dwass test). Additionally, the elastic modulus measured at E13 was between those measured at E12 and E14, although not significantly smaller than at E12, and greater than at E14. We did not detect statistically significant differences between the elastic modulus of dissociated mouse VZ cells at E12 (734.6 ± 45.0 Pa, $n = 64$), E13 (718.7 ± 58.0 Pa, $n = 51$), and E14 (743.8 ± 72.8 Pa, $n = 43$). A previous study reported that the density of apical endfeet decreased during this E12-to-E14 period (35.7 per 100 μm^2 at E12, 20.4 per 100 μm^2 at E13, 12.0 per 100 μm^2 at E14) (Nishizawa et al., 2007). Therefore, during this E12-to-E14 period, the elastic modulus

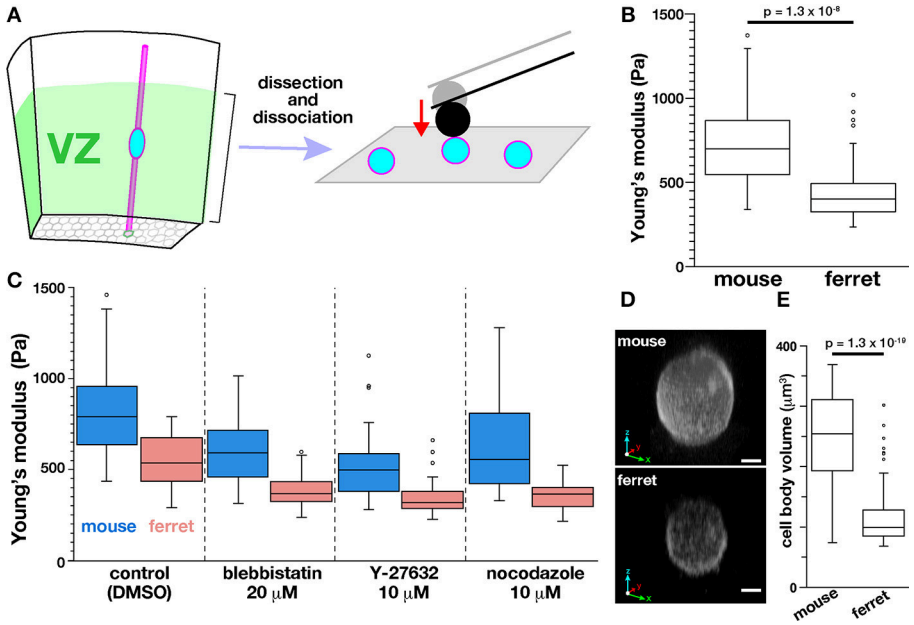

FIGURE 7 | AFM indentation measurements made on dissociated VZ cells. (A) Experimental design. **(B)** Graph showing the elastic modulus of dissociated VZ cells in mice ($n = 51$) and in ferrets ($n = 49$) ($p = 1.3 \times 10^{-8}$, Mann-Whitney U-test). **(C)** AFM measurement made on dissociated cells under pharmacological treatments. **(D)** 3D reconstructed live images of FM4-64–labeled mouse and ferret VZ cells. Scale bar, 2 μm. **(E)** Graph comparing the volume of mouse and ferret VZ cells ($n = 55$ and 75, respectively, $p = 1.3 \times 10^{-19}$, Mann-Whitney *U*-test).

obtained on or near the apical surface and the apical endfoot density both decreased, supporting the idea that horizontal cell-process densification may be a major factor that contributes to an increase in the vertical stiffness on or near the apical surface of the VZ.

DISCUSSION

The primary goal of this study was to determine if there is a measurable physical or mechanical difference between the mouse and ferret VZs. Our previous observation of differential INM behaviors between mice and ferrets (Okamoto et al., 2014) prompted us to speculate that VZ cells may sense and respond to mechanical factors in some way in order to alter their behavior. Motivated by the idea that the sensing of mechanical factors by VZ cells frequently occurs near the apical surface where multiple mechanical events, such as mitosis, resultant duplication of INM flow, and apical constriction, take place, we focused on a microzone close to (~10 μm from) the apical surface of the VZ. Through AFM indentation measurements, we found that the elastic modulus on or near the apical surface of the VZ was greater in ferrets than in mice. Additionally, inhibiting either actomyosin or microtubules partly reduced the apical stiffness of the VZ in both mice and ferrets and maintained the original mouse<ferret relationship. We suggest that the greater stiffness of the ferret apical surface compared with mice is largely explained by the denser lateral assembly of apical endfeet in ferrets. Such difference in stiffness may underlie differential INM behaviors between mice and ferrets.

Lateral Densification of VZ Cells' Apical Processes Increases Stiffness in the Vertical Direction at the Apical Surface

Previous studies have shown that epithelial cells' densification can lead to a variety of cellular responses such as cessation of proliferation and epithelial-to-mesenchymal transitions (detachment from the apical surface) (Halder et al., 2012; Mariani et al., 2012; Mammoto et al., 2013). Assessing the mechanical properties of three-dimensionally developing tissues and microzones is therefore necessary in order to dissect underlying molecular mechanisms that may regulate how cells sense and transduce mechanical stimuli, as well as how they subsequently exhibit outcome behaviors such as proliferation and migration (Heisenberg and Bellaïche, 2013; Mammoto et al., 2013; Iskratsch et al., 2014). A recently reported method of oil droplet–mediated measurement of endogenous mechanical stress in tissues (Campàs et al., 2014) can be an ideal solution, but it also has technical limitations when thin structures such as cellular monolayers are subjected (Campàs, 2016). Preliminary trials for introducing oil droplets into the microzone ~10 μm from the apical surface of the VZ have not succeeded thus far due to its width and proximity to the surface (T. Shinoda, unpublished). As an alternative, we sought to instead measure the elastic modulus of the apical surface of the VZ.

Before beginning this study, we hypothesized that there is a mechanical link between the tangential density of subapically assembled cellular elements (cell bodies and/or processes) and the configuration of the inner/apical surface of the VZ, based on the following past experiences. First, we had previously observed

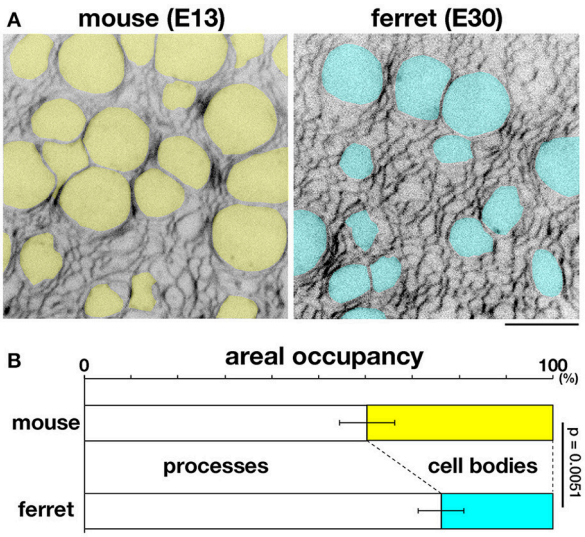

FIGURE 8 | Occupancies of the near-apical microzone by cellular processes and cell bodies. (A) Horizontal confocal sectional live imaging at 5 μm from the apical surface of mouse and ferret VZ (FM4-64–labeled). Cell bodies > 3 μm in diameter at a depth of 5 μm, highlighted in yellow for mouse and blue for ferret, are surrounded by a mesh-like area composed of non-somal elements, i.e., apical processes. Scale bar, 10 μm. **(B)** Graph depicting the ratio of apical processes and cell bodies ($n = 6$, $p = 0.0051$, Mann-Whitney *U*-test).

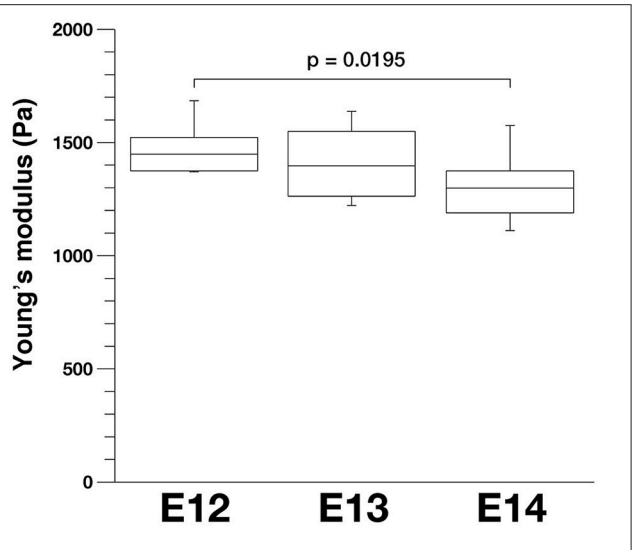

FIGURE 9 | Apical elastic modulus of the mouse VZ measured by AFM indentation at different embryonic days, $n = 10$ for E12, 12 for E13, and 15 for E14 ($p = 0.0195$, Steel-Dwass test).

that focally formed subapical overcrowding due to acute removal of basal processes from VZ cells resulted in apical bulging of that portion. This bulging caused the apical surface contour to become convex in contrast to the original/normal concave line (Okamoto et al., 2013). Second, mechanical simulation using a vertex model, where the volumetric energy within an epithelial-like cell is tightly associated with the apical elastic energy, successfully reproduced physiological and pathological aspects of embryonic mouse cerebral walls' behaviors (Okamoto et al., 2013). Since we found that the apical surface of the ferret VZ was denser than that of the mouse VZ (Okamoto et al., 2014), we expected that if AFM indentation measurement was performed vertically on the apical surface of the ferret VZ, it might yield a different elastic modulus than for mice.

Why is the apical surface vertically stiffer in ferrets than in mice both before (**Figure 2**) and after pharmacological experiments (**Figure 4**), and in a stage-dependent manner in mice (**Figure 9**) when it was tangentially denser in terms of assembled apical endfeet of VZ cells? Assembled apical endfeet form honeycomb structures with cell–cell junctions (adherens junctions) and underlying cytoskeletons. The ultrastructure of adherens junctions are similar in both mice and ferrets (**Figure 6**). We therefore speculate that denser existence of endfeet within the microzone containing the apical surface makes such mesh/honeycomb finer, thereby increasing mechanical resistance against a vertically applied force. It would be important to further compare cell-to-cell adhesiveness between the mouse and ferret VZ. Related to this first model, it is also possible that the apical-most part of the VZ cells' processes, ∼5 μm from the surface, corresponding to the indentation depth in this study, may be more laterally compressed against each other in ferrets than in mice. This could therefore increase the local intracellular or intra-process pressure. Since our laser ablation experiment did not detect significant differences in the velocity of the vertices we tracked at both ends of the laser ablated side between mice and ferrets (**Figure 5**), the results do not directly support this second model. However, if the difference in cellular stiffness measured for dissociated mouse and ferret cells (**Figure 7**) may have affected the recoil behavior of laser-ablated apical-surface elements, the potential compression along the tangential and/or apicobasal directions in the apicalmost ferret VZ could have been partially masked.

Mechanical stimuli presumably sensed at or near the apical surface would function, both in mice and ferrets depending on its degree, as a trigger for activating intracellular signal transduction pathways in VZ cells to potentially regulate their nuclear and somal migration, and/or cell-cycle progression, which could lead to slower nuclear and somal movement in apical-ward G2-phase cells in the ferret VZ, and/or faster nucleokinesis in basalward G1-phase cells (Okamoto et al., 2014). In addition to such a possible cell-intrinsic mechanism, meaning that a VZ cell that senses the tissue-level apical-surface stiffness may regulate its nucleokinesis in an autonomous manner, non-autonomous mechanisms may also exist: VZ cell nuclei and somata that are approaching the apical surface during G2 or those that leave the apical surface during early G1 may be passively influenced (Kosodo, 2012; Lee and Norden, 2013) by tissue-level stiffness at or near the apical surface.

Does Cell Body Stiffness Affect Collective INM in Crowded Neuroepithelia?

Although a densification-induced lateral compression could be a causal mechanical cue for VZ cells in mice and in ferrets to

behave differently, other factors may also exist. Despite a stage-dependent decrease in the density of apices in mice (E12 > E14), VZ cells' INM behaviors do not dramatically change between E12 and E14 (Ochiai et al., 2009; Okamoto et al., 2013). The lower stiffness of dissociated ferret VZ cells compared to mouse VZ cells (**Figure 7**) may contribute to the more slender nuclear and somal shapes of ferret VZ cells compared with mouse VZ cells *in vivo* (Okamoto et al., 2014). Therefore, the lower stiffness may also be associated with quicker basalward nucleokinesis in ferret VZ cells during G1. The mechanisms underlying the mouse–ferret difference in stiffness as well as the nuclear and somal sizes of dissociated cells are currently unknown; however, future measurements of the expression of molecules implicated in regulating nuclear shape and stiffness, such as those associated with the cytoskeleton and/or the nuclear membrane (Nagayama et al., 2014, 2015) in mice and in ferrets may provide useful information.

Our present finding regarding the stiffness, as well as the nuclear and somal sizes of VZ cells is also valuable for comparing the virtual neuroepithelium or the VZ of mice and ferrets. To better understand how INM behaviors of different VZ cells can be coordinated to achieve an ordered pseudostratified structure, we are trying to reproduce the movements of all VZ cells *in silico* by developing new mathematical modeling methods (Shinoda et al., unpublished). Adjusting parameters such as stiffness, as well as nuclear and somal sizes, based on experimental measurements would improve our simulations, which will contribute to fully understanding how neuroepithelium or VZ works as efficiently as possible in collective nuclear and somal traffic to maximize its productivity.

MATERIALS AND METHODS

Animals

To investigate the differences between the ferret and mouse neocortical VZ, we chose a mid-embryonic period during which layer V and layer VI neurons are commonly generated in a variety of mammalian species (Clancy et al., 2001), namely E13 in mice and E28–30 in ferrets as previously described (Okamoto et al., 2014). Pregnant ferrets were obtained from Marshall BioResources while pregnant ICR mice were obtained from SLC. For live visualization of the apical-surface mesh comprised by VZ cells' endfeet, we used a transgenic mouse line (R26-ZO1-EGFP: Accession no. CDB0260K; http://www2.clst.riken.jp/arg/reporter_mice.html) that ubiquitously expresses EGFP fused to mouse ZO-1 under the control of the *ROSA26* locus (Katsunuma et al., 2016). All protocols for animal experiments were approved by the Animal Care and Use Committee of Nagoya University.

Preparation of Cerebral Walls for AFM Measurements at the Apical Surface of VZ

Cerebral hemispheric walls (apicobasally 200–300 μm in mice and 300–400 μm in ferrets) were freshly isolated from embryos, processed (horizontally 400–500 μm × 400–500 μm, 1–2 pieces from a hemisphere) microsurgically in DMEM/F12, and transferred, with 1 ml of DMEM/F12, to a 35 mm dish previously covered partly with AteloCell IAC-30 collagen gel (Koken) at a concentration of 0.3 mg/ml. Cerebral walls were gently placed with their apical surface facing up on top of the gel portion (**Figure 2B**), which was approximately 5 mm thick and 20 mm in diameter (encircled by a silicone rubber ring attached to dish surface). The gel and cerebral walls were completely submerged in DMEM/F12.

Preparation of Dissociated VZ Cells for AFM Measurements and Live Imaging

Cerebral wall slices (coronal) were microsurgically divided into an inner portion corresponding to the VZ and the remaining outer portion. The inner portion (VZ) was treated with trypsin-EDTA (0.05%) (Thermo Fisher Scientific). VZ cells were dissociated by gentle pipetting (**Figure 7A**). Although the majority of the VZ cells were originally bipolar in shape and highly elongated (>100 μm long), the dissociation steps may have removed most of their long processes. It is possible, however, that mouse VZ cells that were stiffer than ferret VZ cells were more resistant to mechanical tearing of their processes. AFM measurements and acquisition of live images were started 30 min after plating of cells and finished within 60 min while cells were still rounded up with no spreading on the dish surface.

AFM Indentation Measurement

All measurements were made with a Cellhesion200 (JPK Instruments) mounted on an IX71 inverted microscope (Olympus), which is equipped with a cantilever with a borosilicate bead (sQUBE, 20 μm diameter for the tissue-level measurement and 5 μm diameter for dissociated cells) (**Figures 2B**, **7A**). The spring constant of each cantilever was determined before measurements were made using the thermal noise method (Hutter and Bechhoefer, 1993) in air (nominal value, 0.2 N/m). The applied forces were 10 nN for the cerebral walls and 1 nN for the VZ cells. The approach and retraction velocities measured were 5 μm/s for the cerebral walls and 1 μm/s for the VZ cells. Each measurement point was set in the central region of the apical surface of a cerebral wall or at the top of each dissociated VZ cell. Force–distance curves (**Figure 2B**) were acquired using the contact mode. Analyses of the obtained force–distance curves were performed with the JPK DP software v.5 (JPK Instruments). Briefly, the Hertz model (Hertz, 1881; Crick and Yin, 2007; Kuznetsova et al., 2007) was applied to calculate Young's modulus as follows:

$$F = \frac{E}{1-\nu^2}\left[\frac{a^2+R^2}{2} ln \frac{R+a}{R-a} - aR\right]$$

where F is the force, E is the Young's modulus, ν is the Poisson's ratio, a is the radius of contact circle, and R is the radius of sphere. The Poisson's ratio was set at 0.5 as previously described (Iwashita et al., 2014). The indentation depth was ∼5 μm for the apical surface of the VZ and ∼1 μm for the dissociated cells.

Although previous studies have reported measurements of the stiffness of different parts of neurons and glia attached on dishes (Lu et al., 2006), the original bipolar morphology of the VZ cells could not be reproduced in 2D culture. Therefore, we

could not perform such cell region–specific AFM measurement. We attempted to measure the elastic modulus of the subapical zone of cross-sectionally prepared cerebral wall slices in which cell layers along the apicobasal axis can be seen, as previously described (Iwashita et al., 2014), but could not obtain reliable force–distance curves in the subapical microzone (∼10 μm from the apical surface) that we focused on in a reproducible manner, probably due to its proximity to the surface. It should also be noted that the spring constant of the cantilever was 0.2 N/m in our study while it was 0.03 N/m in Iwashita et al. (2014).

Pharmacological Experiments

Cerebral wall pieces were treated with DMEM/F12 containing either 1% DMSO (Sigma) (11 pieces from 4 mouse embryos and 9 pieces from 3 ferret embryos), 20 μM blebbistatin (Calbiochem) (14 pieces from 5 mouse embryos and 11 pieces from 3 ferret embryos), 10 μM Y-27632 (Wako) (14 pieces from 5 mouse embryos and 10 pieces from 3 ferret embryos), or 10 μM nocodazole (Wako) (11 pieces from 4 mouse embryos and 9 pieces from 3 ferret embryos) for 30 min before being subject to AFM measurement. Some of the treated mouse cerebral walls were imaged for assessing bending/curling (**Figure 3A**), thinning coupled with lateral expansion (**Figure 3B**), or apical endfeet enlargement (**Figure 3C**) at the indicated timepoints. We examined whether these pharmacological treatments (30 min) affected the density of M-phase cells at the apical surface. While the density of cells positive for phosphohistone-H3 (pH3) was comparable (about 5.8 per 100 μm of the apical surface in coronal cerebral wall sections) between DMSO-, blebbistatin-, or Y-27632–treated E13 mouse hemispheres, it was a little smaller (about 4.2) in nocodazole-treated hemispheres, partly reflecting that occurrence of M-phase (arrival of G2-phase cells) at the apical surface is dependent on microtubules (Tsai et al., 2005; Xie et al., 2007). Based on the lateral expansion of nocodazole-treated cerebral walls (1.2∼1.3-times longer dorsoventrally at the apical surface, **Figures 3A,B**), we obtained a corrected density for $pH3^+$ cells at 5∼5.5. Together, increase of M-phase cells (which would occur when mitosis is arrested) was not observed at the apical surface.

Dissociated cells were treated with DMEM/F12 containing either 1% DMSO (Sigma) (50 mouse cells and 38 ferret cells), 2 μM blebbistatin (43 mouse cells and 36 ferret cells), 1 μM Y-27632 (44 mouse cells and 33 ferret cells), or 1 μM nocodazole (38 mouse cells and 32 ferret cells) for 30 min before being subject to AFM measurement.

Laser Ablation of VZ Cells' Apices Labeled with EGFP-ZO-1

Mouse ZO-1 cDNA fused with EGFP was subcloned from pCAG-EGFP-ZO-1 (gift from F. Matsuzaki) (Konno et al., 2008) into pEFX-LPL (Okamoto et al., 2013; Sakakibara et al., 2014). Sporadic visualization for apices of neural progenitor cells was achieved by transfection with a mixture of conditional expression plasmids, 0.5 μg/μl pEFX-LPL-EGFP-ZO-1 and 0.01 μg/μl pEFX-Cre. Transfection by *in utero* electroporation was performed using pregnant ICR mice as described previously (Okamoto et al., 2013). Briefly, the plasmid solution containing Fast Green was injected into the lateral ventricle of each E12 embryo. 33 V electric pulses were applied four times with forceps-type electrodes (CUY650P3, NEPAGENE). *Exo utero* electroporation was performed using pregnant ferrets as described previously (Okamoto et al., 2014). Briefly, plasmid solution containing Fast Green was injected into the lateral ventricle of E28 embryos, and 55 V electric pulses were applied four times with forceps-type electrodes. For ablation on the apical surface (**Figure 5A**), cerebral walls prepared at E13 (mouse) or E29 (ferret) were mounted apical-side down in a glass-bottomed 35 mm dish using collagen gel. Laser ablation was performed as described previously (Hara et al., 2013) with an IX81 inverted microscope (Olympus) equipped with CSU-X1 (Yokogawa), iXon3 897 EMCCD camera (Andor), 60x objective lens (UPLSAPO 60XW, Olympus), on-stage culture chamber (Tokai Hit), and MicroPoint (Andor) operated with iQ2 live cell imaging software (Andor). The culture chamber was filled with 95% O_2 and 5% CO_2. With image acquisition in 0.5-s intervals, a pulse of 365 nm laser illumination at 16 Hz was simultaneously applied to the cell boundary at the apical surface.

Imaging of Live Cerebral Walls and Dissociated Cells

Low-magnification time-lapse monitoring (**Figures 3A,B**) was performed as described previously (Miyata et al., 2001, 2004; Okamoto et al., 2013). For sparse labeling of neural progenitor cells, cerebral walls were treated with DMEM/F12 containing extremely fine crystals of 1,1-dioctadecyl-3,3,3,3-tetramethylindocarbocyanine perchlorate, DiI C18(3) (D-282; Molecular Probes) for 1–2 min at room temperature. This DiI suspension was made by adding 1 ml of DiI stock solution (10 mg/ml in ethanol) to 10 ml DMEM/F12. DiI-labeled cerebral walls were then coronally sliced, and embedded in AteloCell IAC-30 collagen gel at a concentration of 0.25–0.3 mg/ml. Slices were imaged using an Olympus IX71 [4x (**Figure 3A**) or 20x (**Figure 3B**)] equipped with an Orca ER camera (Hamamatsu Photonics). To measure the volume of each dissociated cell (**Figure 6**), cells were plated on polyethyleneimine-coated glass-bottomed 35 mm dishes (Iwaki) at a density of 5×10^4 / cm^2, and then stained with the styryl dye FM4-64 (Thermo Fisher Scientific) at a concentration of 5 μg/ml for 30 min (Kawaue et al., 2014).

For FM4-64–based 3D imaging of mouse VZ cells to be volume-measured (**Figure 7**), we harvested live VZ cells using Fucci mice, in which differentiated (cell cycle-exited) neurons in the basal region of the cerebral walls are most intensely positive for mKO2-hCdt1, while G1-phase cells in VZ are only weakly positive for mKO2-hCdt1 (Sakaue-Sawano et al., 2008). In our conventional epifluorescence imaging system (an Olympus IX71 equipped with an Orca ER camera), monitoring of mKO2-hCdt1 expressed by G1-phase VZ cells required a very high level of image intensification, which always resulted in over-intensification (image saturation) for neurons. Thus, such clear difference in mKO2-hCdt1 intensity enabled us to easily distinguish cell cycle-exited neurons and cell-cycling VZ cells including G1-phase cells.

We discarded cells that were strongly mKO2-hCdt1-positive (i.e., neurons). The remaining fraction was composed of both cells completely negative for mKO2-hCdt1 expression (S, G2, and M-phase cells) and those showing only very weak mKO2-hCdt1 fluorescence (G1-phase cells). It corresponded to the cell fraction separately obtained from microsurgically harvested VZs (immunocytochemically >90% Sox2-positive). Volume-measured (FM4-64–stained) mouse and ferret cells' VZ identity was confirmed by anti-Sox2 immunostaining immediately after live analysis.

Live confocal images of these stained cells were obtained with an FV1000 laser scanning confocal microscope (Olympus) equipped with a 100x objective lens (UPLSAPO 100XO, Olympus) and an on-stage culture chamber (Tokai Hit) filled with 95% O_2 and 5% CO_2. Confocal images were processed and analyzed with ImageJ. To calculate cell volume, cell diameters were measured along the XY plane and volumes were estimated assuming that the cells form true spheres. Reconstructed 3D images of the dissociated cells were obtained using Volocity (PerkinElmer).

For confocal imaging of all VZ cells in the subapical space (**Figure 8**), processed cerebral hemispheric walls (500 × 500 μm) were stained with 5 μg/ml FM4-64 for 30 min (Kawaue et al., 2014) before being mounted on polystyrene cell culture dish (Corning) using AteloCell IAC-30 collagen gel (Koken). Live confocal images were taken with a BX51W1 microscope (Olympus) equipped with a CSU-X1 laser scanning confocal unit (Yokogawa), a 100x objective lens (LUMPLFL 100XW, Olympus), an iXon+ EMCCD camera (Andor), and an on-stage culture chamber (Tokai Hit) filled with 45% N_2, 40% O_2, and 5% CO_2. Similar preparations were made for cerebral walls prepared from R26-ZO1-EGFP mice (**Figure 3C**).

Immunofluorescence

To visualize the apical junctional meshwork (**Figure 1C**), cerebral walls were fixed in 4% paraformaldehyde prepared in phosphate buffer (pH 7.4) and subject to whole-mount staining with anti–ZO-1 mouse monoclonal antibody (33-9100, Thermo Fisher Scientific), followed by Alexa Fluor 488–labeled anti–mouse IgG antibody (A-11029, Thermo Fisher Scientific). To determine the VZ identity of dissociated cells subjected to AFM measurement or live-cell imaging for volume measurement (**Figure 7**), they were fixed with 4% paraformaldehyde in phosphate buffer (pH 7.4) and immunostained with anti-Sox2 rabbit polyclonal antibody (ab97959, Abcam), followed by Alexa Fluor 488–labeled anti–rabbit IgG antibody (A-11008, Thermo Fisher Scientific). To determine the density of M-phase cells at the apical surface, cerebral walls treated with DMSO, blebbistatin, Y-27632, or nocodazole were coronally frozen-sectioned (16 μm) and immunostained with anti-pH3 (rabbit, 06-570, MILLIPORE, 1:300).

Electron Microscopy

For scanning electron microscopy (**Figure 1**), cerebral hemispheres were fixed in 4% paraformaldehyde in phosphate buffer (pH 7.4), and subsequently in 2.5% glutaraldehyde in phosphate buffer (pH 7.4). The brains were further post-fixed overnight in 2.5% glutaraldehyde at 4°C, followed by 1% OsO4 in PBS and dehydration. The samples were trimmed and coated with osmium and examined under an S-800S SEM (Hitachi). For transmission electron microscopy (**Figure 6**), cerebral hemispheres were fixed with 2% paraformaldehyde and 2.5% glutaraldehyde in cacodylate buffer (pH 7.4), post-fixed with 2% OsO4 in cacodylate buffer, dehydrated, and embedded in Epon 812. Thin sections were mounted on formvar film–coated single-slot copper grids, stained with lead citrate, and examined under a JEM-1400Plus electron microscope (JEOL). We used ImageJ to faithfully measure the length of adherens junctions in each cross-sectional electron micrograph. We traced the entire length of a heavily electron-dense portion (usually started from the apical-most level and ran non-straightly).

AUTHOR CONTRIBUTIONS

AN performed all AFM measurements and pharmacological experiments, and wrote the manuscript. TS carried out 3D imaging and wrote the manuscript. TK performed electronmicroscopy. MS and NU assisted laser ablation experiments. KN and TMa supported AFM measurement. AK supervised the experiments and wrote the manuscript. TMi designed the project, performed DiI-based imaging, and wrote the manuscript.

FUNDING

This work was supported by a Grant-in-Aid for Scientific Research on Innovative Areas, "Cross-talk between moving cells and microenvironment as a basis of emerging order" 22111006 (TMi), from the Ministry of Education, Culture, Sports, Science and Technology of Japan, and 16H02457 (TMi) from Japan Society for the Promotion of Science.

ACKNOWLEDGMENTS

We thank Makoto Masaoka, Hiroshi Imafuku, and Yuji Nishizawa for technical assistance, Toshihiko Fujimori and Sachiko Tsukita for the R26-ZO1-EGFP mouse, and Yasuhiro Inoue and Taiji Adachi for discussion from mechanical viewpoints.

REFERENCES

Campàs, O. (2016). A toolbox to explore the mechanics of living embryonic tissues. *Sem. Cell Dev. Biol.* 55, 119–130. doi: 10.1016/j.semcdb.2016.03.011

Campàs, O., Mammoto, T., Hasso, S., Sperling, R. A., O'Connell, D., Bischof, A. G., et al. (2014). Quantifying cell-generated mechanical forces within living embryonic tissues. *Nat. Methods* 11, 183–189. doi: 10.1038/nmeth.2761

Clancy, B., Darlington, R. B., and Finlay, B. L. (2001). Translating developmental time across mammalian species. *Neuroscience* 105, 7–17. doi: 10.1016/S0306-4522(01)00171-3

Crick, S. L., and Yin, F. C. (2007). Assessing micromechanical properties of cells with atomic force microscopy: importance of the contact point. *Biomech. Model. Mechanobiol.* 6, 199–210. doi: 10.1007/s10237-006-0046-x

Dai, J., and Sheetz, M. P. (1999). Membrane tether formation from blebbing cells. *Biophys. J.* 77, 3363–3370. doi: 10.1016/S0006-3495(99)77168-7

Franze, K. (2011). Atomic force microscopy and its contribution to understanding the development of the nervous system. *Curr. Opin. Genet. Dev.* 21, 530–537. doi: 10.1016/j.gde.2011.07.001

Franze, K. (2013). The mechanical control of nervous system development. *Development* 140, 3069–3077. doi: 10.1242/dev.079145

Gautier, H. O., Thompson, A. J., Achouri, S., Koser, D. E., Holtzmann, K., Moeendarbary, E., et al. (2015). Atomic force microscopy-based force measurements on animal cells and tissues. *Methods Cell Biol.* 125, 211–235. doi: 10.1016/bs.mcb.2014.10.005

Götz, M., and Huttner, W. B. (2005). The cell biology of neurogensis. *Nat. Rev. Mol. Cell. Biol.* 6, 777–788. doi: 10.1038/nrm1739

Halder, G., Dupont, S., and Piccolo, S. (2012). Transduction of mechanical and cytoskeletal cues by YAP and TAZ. *Nat. Rev. Mol. Cell Biol.* 13, 591–600. doi: 10.1038/nrm3416

Hara, Y., Nagayama, K., Yamamoto, T. S., Matsumoto, T., Suzuki, M., and Ueno, N. (2013). Directional migration od leading-edge mesoderm generates physical forces: implication in Xenopus notochord formation. *Dev. Biol.* 382, 482–495. doi: 10.1016/j.ydbio.2013.07.023

Heisenberg, C. P., and Bellaïche, Y. (2013). Forces in tissue morphogenesis and patterning. *Cell* 153, 948–962. doi: 10.1016/j.cell.2013.05.008

Hertz, H. (1881). Über die Berührung faster elastischer Körper. *J. die Reine Angewandte Mathematik* 92, 156–171.

Hinds, J. W., and Ruffett, T. L. (1971). Cell proliferation in the neural tube: an electron microscopic and Golgi analysis in the mouse cerebral vesicle. *Z. Zellforsch Mikrosk Anat.* 115, 226–264. doi: 10.1007/BF00391127

Hutter, J. L., and Bechhoefer, J. (1993). Calibration of atomic-force microscope tips. *Rev. Sci. Instrum.* 64, 1868–1873. doi: 10.1063/1.1143970

Iskratsch, T., Wolfenson, H., and Sheets, M. P. (2014). Appreciating force and shape — the rise of mechanotrunsduction in cell biology. *Nat. Rev. Mol. Cell Biol.* 15, 825–833. doi: 10.1038/nrm3903

Iwashita, M., Kataoka, N., Toida, K., and Kosodo, Y. (2014). Systematic profiling of spatiotemporal tissue and cellular stiffness in the developing brain. *Development* 141, 3793–3798. doi: 10.1242/dev.109637

Kadoshima, T., Sakaguchi, H., Nakano, T., Soen, M., Ando, S., Eiraku, M., et al. (2013). Self-organization of axial polarity, inside-out layer pattern, and species-specific progenitor dynamics in human ES cell-derived neocortex. *Proc. Natl. Acad. Sci. U.S.A.* 110, 20284–20289. doi: 10.1073/pnas.1315710110

Karfunkel, P. (1971). The role of microtubules and microfilaments in neurulation in Xenopus. *Dev. Biol.* 25, 30–56. doi: 10.1016/0012-1606(71)90018-2

Katsunuma, S., Honda, H., Shinoda, T., Ishimoto, Y., Miyata, T., Kiyonari, H., et al. (2016). Synergistic action of nectins and cadherins generates the mosaic cellular pattern of the olfactory epithelium. *J. Cell. Biol.* 212, 561–575. doi: 10.1083/jcb.201509020

Kawaue, T., Sagou, K., Kiyonari, H., Ota, K., Okamoto, M., Shinoda, T., et al. (2014). Neurogenin2-d4Venus and Gadd45-d4Venus transgenic mice: visualizing mitotic and migratory behaviors of cells committed to the neuronal lineag in the developing mammalian brain. *Dev. Growth Differ.* 56, 293–304. doi: 10.1111/dgd.12131

Kinoshita, N., Sasai, N., Misaki, K., and Yonemura, S. (2008). Apical accumulation of Rho in the neural plate is important for neural plate cell shape change and neural tube formation. *Mol. Biol. Cell* 19, 2289–2299. doi: 10.1091/mbc.E07-12-1286

Konno, D., Shioi, G., Shitamukai, A., Mori, A., Kiyonari, H., Miyata, T., et al. (2008). Neuroepithelial progenitors undergo LGN-dependent planar divisions to maintain self-renewability during mammalian neurogenesis. *Nat. Cell Biol.* 10, 93–101. doi: 10.1038/ncb1673

Kosodo, Y. (2012). Interkinetic nuclear migration: beyond a hallmark of neurogenesis. *Cell. Mol. Life Sci.* 69, 2727–2738. doi: 10.1007/s00018-012-0952-2

Kosodo, Y., Röper, K., Haubensak, W., Marzesco, A.-M., Corbeil, D., and Huttner, W. B. (2004). Asymmetric distribution of the apical plasma membrane during neurogenic divisions of mammalian neuroepithelial cells. *EMBO J.* 23, 2314–2324. doi: 10.1038/sj.emboj.7600223

Kosodo, Y., Suetsugu, T., Suda, M., Mimori-Kiyosue, Y., Toida, K., Baba, S. A., et al. (2011). Regulation of interkinetic nuclear migration by cell cycle-coupled active and passive mechanisms in the developing brain. *EMBO J.* 30, 1690–1704. doi: 10.1038/emboj.2011.81

Kuznetsova, T. G., Starodubtseva, M. N., Yegorenkov, N. I., Chizhik, S. A., and Zhdanov, R. I. (2007). Atomic force microscopy probing of cell elasticity. *Micron* 38, 824–833. doi: 10.1016/j.micron.2007.06.011

LaMonica, B. E., Lui, J. H., Wang, X., and Kriegstein, A. R. (2012). OSVZ progenitors in the human cortex: an updated perspective on neurodevelopmental disease. *Curr. Opin. Neurobiol.* 22, 747–753. doi: 10.1016/j.conb.2012.03.006

Lee, H. O., and Norden, C. (2013). Mechanisms controlling arrangements and movements of nuclei in pseudostratified epithelia. *Trend Cell Biol.* 23, 141–150. doi: 10.1016/j.tcb.2012.11.001

Leung, L., Klopper, A. V., Grill, S. W., Harris, W. A., and Norden, C. (2011). Apical migration of nuclei during G2 is a prerequisite for all nuclear motion in zebrafish neuroepithelia. *Development* 138, 5003–5013. doi: 10.1242/dev.071522

Lu, Y.-B., Franze, K., Seifert, G., Steinhäuser, C., Kirchhoff, F., Wolburg, H., et al. (2006). Viscoelastic properties of individual glial cells and neurons in the CNS. *Proc. Natl. Acad. Sci. U.S.A.* 103, 17759–17764. doi: 10.1073/pnas.0606150103

Mammoto, T., Mammoto, A., and Ingber, D. E. (2013). Mechanobiology and developmental control. *Annu. Rev. Cell Dev. Biol.* 29, 27–61. doi: 10.1146/annurev-cellbio-101512-122340

Mariani, E., Mehonic, A., Curran, S., Gale, J., Duke, T., and Baum, B. (2012). Live-cell delamination counterbalances epithelial growth to limit tissue overcrowding. *Nature* 484, 542–545. doi: 10.1038/nature10984

Miyata, T. (2008). Development of three-dimensional architecture of the neuroepithelium: role of pseudostratification and cellular 'community'. *Dev. Growth Differ.* 50(Suppl. 1), S105–S112. doi: 10.1111/j.1440-169X.2007.00980.x

Miyata, T., Kawaguchi, A., Okano, H., and Ogawa, M. (2001). Asymmetric inheritance of radial glial fibers by cortical neurons. *Neuron* 31, 727–741. doi: 10.1016/S0896-6273(01)00420-2

Miyata, T., Kawaguchi, A., Saito, K., Kawano, M., Muto, T., and Ogawa, M. (2004). Asymmetric production of surface-dividing and non-surface-dividing cortical progenitor cells. *Development* 131, 3133–3145. doi: 10.1242/dev.01173

Miyata, T., and Ogawa, M. (2007). Twisting of neocortical progenitor cells underlies a spring-like mechanism for daughter-cell migration. *Curr. Biol.* 17, 146–151. doi: 10.1016/j.cub.2006.11.023

Miyata, T., Okamoto, M., Shinoda, T., and Kawaguchi, A. (2015). Interkinetic nuclear migration generates and opposes ventricular-zone crowding: insight into tissue mechanics. *Front. Cell. Neurosci.* 8:473. doi: 10.3389/fncel.2014.00473

Nagayama, K., Hamaji, Y., Sato, Y., and Matsumoto, T. (2015). Mechanical trapping of the nucleus on micropillared surfaces inhibits the proliferation of vascular smooth muscle cells but not cervical cancer Hela cells. *J. Biomech.* 48, 1796–1803. doi: 10.1016/j.jbiomech.2015.05.004

Nagayama, K., Yamazaki, S., Yashiro, Y., and Matsumoto, T. (2014). Estimation of the mechanical connection between apical stress fibers and the nucleus in vascular smooth muscle cells cultured on a substrate. *J. Biomech.* 47, 1422–1429. doi: 10.1016/j.jbiomech.2014.01.042

Nishimura, T., Honda, H., and Takeichi, M. (2012). Planar cell polarity links axes of spatial dymanics in neural-tube closure. *Cell* 149, 1084–1097. doi: 10.1016/j.cell.2012.04.021

Nishizawa, Y., Imafuku, H., Saito, K., Kanda, R., Kimura, M., Minobe, S., et al. (2007). Survey of the morphogenetic dynamics of the ventricular surface of the developing mouse neocortex. *Dev. Dyn.* 236, 3061–3070. doi: 10.1002/dvdy.21351

Norden, C., Young, S., Link, B. A., and Harris, W. A. (2009). Actomyosin is the main driver of interkinetic nuclear migration in the retina. *Cell* 138, 1195–1208. doi: 10.1016/j.cell.2009.06.032

Ochiai, W., Nakatani, S., Takahara, T., Kainuma, M., Masaoka, M., Minobe, S., et al. (2009). Periventricular Notch activation and asymmetric Ngn2 and Tbr2

expression in pair-generated neocortical daughter cells. *Mol. Cell. Neurosci.* 40, 225–233. doi: 10.1016/j.mcn.2008.10.007

Okamoto, M., Namba, T., Shinoda, T., Kondo, T., Watanabe, T., Inoue, Y., et al. (2013). TAG-1–assisted progenitor elongation streamlines nuclear migration to optimize subapical crowding. *Nat. Neurosci.* 16, 1556–1566. doi: 10.1038/nn.3525

Okamoto, M., Shinoda, T., Kawaue, T., Nagasaka, A., and Miyata, T. (2014). Ferret-mouse differences in interkinetic nuclear migration and cellular densification in the neocortical ventricular zone. *Neurosci. Res.* 86, 88–95. doi: 10.1016/j.neures.2014.03.011

Sakakibara, A., Sato, T., Ando, R., Noguchi, N., Masaoka, M., and Miyata, T. (2014). Dynamics of centrosome translocation and microtubule organization in neocortical neurons during distinct modes of polarization. *Cereb. Cortex* 24, 1301–1310. doi: 10.1093/cercor/bhs411

Sakaue-Sawano, A., Kuroiwa, H., Morimura, T., Hanyu, A., Hama, H., Osawa, H. et al. (2008). Visualizing spatiotemporal dynamics of multicellular cell-cycle progression. *Cell* 132, 487–498. doi: 10.1016/j.cell.2007.12.033

Schoenwolf, G. C., and Powers, M. L. (1987). Shaping of the chick neuroepithelium during primary and secondary neurulation: role of cell elongation. *Anat. Rec.* 218, 182–195. doi: 10.1002/ar.1092180214

Smart, I. H. (1972). Proliferative characteristics of the ependymal layer during the early development of the spinal cord in the mouse. *J. Anat.* 111, 365–380.

Strzyz, P. J., Matejcic, M., and Norden, C. (2016). Heterogeneity, cell biology, and tissue mechanics of pseudostratified epithelia: coordination of cell divisions and growth in tightly packed tissues. *Int. Rev. Cell Mol. Biol.* 325, 89–118. doi: 10.1016/bs.ircmb.2016.02.004

Suzuki, M., Morita, H., and Ueno, N. (2012). Molecular mechanisms of cell shape changes that contribute to vertebrate neural tube closure. *Dev. Growth Differ.* 54, 266–276. doi: 10.1111/j.1440-169X.2012.01346.x

Taverna, E., Götz, M., and Huttner, W. B. (2014). The cell biology of neurogenesis: toward an understanding of the development and evolution of the neocortex. *Annu. Rev. Cell. Dev. Biol.* 30, 465–502. doi: 10.1146/annurev-cellbio-101011-155801

Taverna, E., and Huttner, W. B. (2010). Neural progenitor nuclei in motion. *Neuron* 67, 906–914. doi: 10.1016/j.neuron.2010.08.027

Tsai, J.-W., Chen, Y., Kriegstein, A. R., and Vallee, R. B. (2005). LIS1 RNA interference blocks neural stem cell division, morphogenesis, and motility at multiple stages. *J. Cell Biol.* 170, 935–945. doi: 10.1083/jcb.200505166

Xie, Z., Moy, L. Y., Sanada, K., Zhou, Y., Buchman, J. J., and Tsai, L.-H. (2007). Cep120 and TACCs control interkinetic nuclear migration and neural progenitor pool. *Neuron* 56, 79–93. doi: 10.1016/j.neuron.2007.08.026

Conflict of Interest Statement: The authors declare that the research was conducted in the absence of any commercial or financial relationships that could be construed as a potential conflict of interest.

The reviewer TS declared a shared affiliation, though no other collaboration, with several of the authors AN, TS, TK, KN, TMa, AK, TMi to the handling Editor, who ensured that the process nevertheless met the standards of a fair and objective review.

Advantages of publishing in Frontiers

OPEN ACCESS
Articles are free to read for greatest visibility and readership

FAST PUBLICATION
Around 90 days from submission to decision

HIGH QUALITY PEER-REVIEW
Rigorous, collaborative, and constructive peer-review

TRANSPARENT PEER-REVIEW
Editors and reviewers acknowledged by name on published articles

Frontiers
Avenue du Tribunal-Fédéral 34
1005 Lausanne | Switzerland

Visit us: www.frontiersin.org
Contact us: info@frontiersin.org | +41 21 510 17 00

REPRODUCIBILITY OF RESEARCH
Support open data and methods to enhance research reproducibility

DIGITAL PUBLISHING
Articles designed for optimal readership across devices

FOLLOW US
@frontiersin

IMPACT METRICS
Advanced article metrics track visibility across digital media

EXTENSIVE PROMOTION
Marketing and promotion of impactful research

LOOP RESEARCH NETWORK
Our network increases your article's readership